APPLIED

COMPUTATIONAL

ELECTROMAGNETICS

SOCIETY

JOURNAL

SPECIAL ISSUE ON ADVANCED COMPUTATIONAL ELECTROMAGNETIC METHODOLOGIES AND TECHNIQUES

SPECIAL ISSUE ON NEW DESIGNS OF ANTENNAS AND RF, MICROWAVE, AND WIRELESS STRUCTURES AND SYSTEMS

SPECIAL ISSUE ON CUTTING-EDGE MODELING AND APPLICATIONS OF ELECTROMAGNETIC DEVICES AND FIELDS

Low Rank Matrix Algebra
for the Method of Moments[1]

John Shaeffer

Matrix Compression Technologies, LLC
Marietta, Georgia
john@shaeffer.com

Abstract—**This tutorial presents the use of low rank R_k matrix block formulations for advancing the problem size capability N of the Method of Moments full wave approach to solving Maxwell's integral equations. When MOM unknowns are spatially grouped, the group-group interaction matrix blocks become low rank for electrically large problems. A very significant advantage of this R_k property along with use of the Adaptive Cross Approximation leads to dramatic reduction in memory storage and in operations count. While early R_k approaches focused on iterative approaches, this work shows how R_k methods can be applied to direct solve LU factorization approaches and, for scattering problems, R_k methods can be used to compute the full polarization scattering matrix.**

I. BACKGROUND

Full wave solvers for Maxwell's integral equations are the much-preferred approach when they can be implemented. And direct factor rather than iterative solutions avoids the well-known failures of the latter. However, the direct factor computational cost for N unknowns is immense: N^2 for matrix storage, N^3 for matrix LU factorization and N^2 for each RHS excitation solution.

Researchers in the last 20-30 years have improved on this situation by recognizing that MOM system matrices, when unknowns are spatially grouped, lead to low rank blocks within the overall system matrix. Early researchers developed iterative solvers based on analytic Green's Function expansions (FMM and MLFMM). While these approaches significantly increased problem sizes they suffered from several problems: 1) They required special development of analytical Green's functions; 2) They were not well adapted for multiple RHS problems where the iterative scheme has to restart fresh for each new RHS vector which limits FMM and MLFMM usefulness for backscatter problems with many RHS's; 3) They often have slow and no convergence for the iterative solution for problems involving significant interactions; and 4) They often require matrix preconditioners.

More recently we have seen the development of the Adaptive Cross Approximation (ACA) for computing the low rank UV approximation to system matrix blocks, based on spatial grouping of unknowns. Whole new approaches to solving MOM system matrices has resulted. This includes the author's development in 2006 of Mercury MOM, the first code to LU factor a problem with one million unknowns [1,2] and more recently to five million unknowns [3]. Other researchers have also used R_k methods to extend MOM, each with their own methodology [4,5,6].

Significant ACA advantages over the early FMM/MLFMM approaches are: 1) There is no need for analytic Green's function formulations; 2) The ACA does not require computation of a full matrix block before obtaining its UV R_k approximation as only specific rows and columns of a block need computation; 3) The ACA low rank blocks of a system matrix can be used for iterative as well as direct LU factorizations. In this work a block LU factorization/solve solution is used where all of the Z, L and U factors, V and J are computed and stored in a compressed outer product form.

In the 50 years since the introduction of MOM [7], Moore's law should have suggested a problem size increase N, using factorization, of approximately $(2^{25})^{1/3} = 322$. Assuming a maximum N = 1000 for 1968 computer capability, we should have progressed by technology advance alone to N ~ 322,000. Clearly, we have done 20 to 40 times better. R_k formulations are responsible for this increase. Algorithms count!

This tutorial is organized as follows: II) Cobble stone spatial

grouping; III) What is low rank; IV) A Rank Fraction metric; V) R_k matrix math; VI) Thrill of R_k multiplication; VII) Agony of R_k addition; VIII) Adaptive cross approximation; IX) R_k Addition "Recompression"; X) LU factorization using the ACA; XI) Solve using R_k forms for scattering problems; XII) Mercury MOM scattering code and XIII) Concluding Remarks.

II. COBBLE STONE SPATIAL GROUPING

Spatial grouping of MOM unknowns is the starting point for creating low rank interaction blocks in the MOM system matrix. The key notion is to minimize the solid angle subtended by each pair of test and source groups of unknowns. As the distance between test/source groups increases, the subtended solid angle decreases thus reducing the numerical rank of the interaction, Fig. 2.

With spatial grouping for electrically large problems (as characterized by tens of thousands to several million unknowns with group sizes from 500 to 10,000 unknowns) most all blocks in the system matrix, except for diagonal self-blocks, become R_k. This includes not only Z blocks but also its L and U factors. For scattering problems with many RHS illumination angles, the RHS voltage excitation matrix is R_k as well as the current solution J and/or M:

$$\begin{bmatrix} [Z]_{11} & [Z]_{12} & [Z]_{13} & [Z]_{14} \\ [Z]_{21} & [Z]_{22} & [Z]_{23} & [Z]_{24} \\ [Z]_{31} & [Z]_{32} & [Z]_{33} & [Z]_{34} \\ [Z]_{41} & [Z]_{42} & [Z]_{43} & [Z]_{44} \end{bmatrix} \begin{bmatrix} [J]_1 \\ [M]_2 \\ [J]_3 \\ [M]_4 \end{bmatrix}$$

$$= \begin{bmatrix} I & 0 & 0 & 0 \\ [L]_{21} & I & 0 & 0 \\ [L]_{31} & [L]_{31} & I & 0 \\ [L]_{41} & [L]_{41} & [L]_{41} & I \end{bmatrix} \begin{bmatrix} [U]_{11} & [U]_{12} & [U]_{13} & [U]_{14} \\ 0 & [U]_{22} & [U]_{23} & [U]_{24} \\ 0 & 0 & [U]_{33} & [U]_{34} \\ 0 & 0 & 0 & [U]_{44} \end{bmatrix} \begin{bmatrix} [J]_1 \\ [M]_2 \\ [J]_3 \\ [M]_4 \end{bmatrix} = \begin{bmatrix} [V]_1 \\ [H]_2 \\ [V]_3 \\ [H]_4 \end{bmatrix} . (1)$$

Each R_k matrix block is written as a low rank approximation outer product of a column matrix times a row matrix:

$$\begin{bmatrix} & & \\ & A & \\ & & \end{bmatrix} \cong \begin{bmatrix} Au \end{bmatrix} \begin{bmatrix} Av & \end{bmatrix}. \qquad (2)$$

This R_k form is typically computed using the Adaptive Cross Approximation (ACA) which means that only a few rows/columns of $\mathbf{A}$ are required. The numerical rank k will depend on the desired error tolerance. Each matrix block $\mathbf{A}$ never needs to be computed beforehand, i.e., $\mathbf{A}$ is virtual in the sense that only a subroutine capable of computing ACA required rows/columns of $\mathbf{A}$ is required. The cobble stone grouping algorithm is straight forward: .

- Create a box of all ungrouped unknowns;
- Compute the longest diagonal box vector;
- Pick an arbitrary starting point, typically the end of diagonal box vector;

- Compute distance from this point to all other unknowns;
- Sort these distances from close to far (e.g., Q sort);
- Pick nGroup of closet points to form 1st group; and
- Start over, but now with only ungrouped edges.

The grouping pattern is shown in Fig. 1 results.
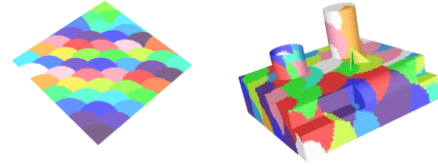
Fig. 1. Cobble stone grouping examples.
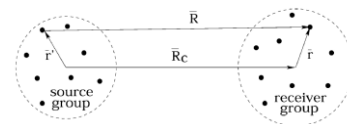
Fig. 2. Spatial source group test group.

III. WHAT IS LOW RANK

Full rank of a (block) matrix is the minimum of the number of rows or columns. In this case each row or column is independent. In the less than full rank R_k case, each row or column is not independent, at least to within some numerical tolerance. In spatially grouped MOM system block matrices, we usually have $R_k \ll R$ and can approximate an (m,n) block as in (2) where the column $\mathbf{U}$ matrix is (m,k) and the row $\mathbf{V}$ matrix is (k,n).

Rank deficient block matrices means that the singular values of a Singular Value Decomposition (SVD) of that matrix drop precipitously. SVD theory is the basis for low rank outer product approximations where a matrix $\mathbf{A}$ is expressed as a product of three matrices $\mathbf{A} = \mathbf{USV}$ where $\mathbf{U}$ and $\mathbf{V}$ are unitary where each column of $\mathbf{U}$ and row of $\mathbf{V}$ are independent and $\mathbf{S}$ is a diagonal only matrix of ordered real singular values. In the example below, let the 3rd singular value be less than some tolerance ε, then $\mathbf{A}$ can be approximated as the outer product of a column matrix times a row matrix:

$$\mathbf{A} = \mathbf{USV} = \begin{pmatrix} u_{11} & u_{12} & u_{13} \\ u_{21} & u_{22} & u_{23} \\ u_{31} & u_{32} & u_{33} \end{pmatrix} \begin{pmatrix} s_{11} & 0 & 0 \\ 0 & s_{22} & 0 \\ 0 & 0 & s_{33} \end{pmatrix} \begin{pmatrix} v_{11} & v_{12} & v_{13} \\ v_{21} & v_{22} & v_{23} \\ v_{31} & v_{32} & v_{33} \end{pmatrix} . (3)$$

With $S_{11} > S_{22} > S_{33}$. If $S_{33} < \varepsilon \sim 0$, then

$$\mathbf{A} = \mathbf{USV} \approx \begin{pmatrix} u_{11} & u_{12} \\ u_{21} & u_{22} \\ u_{31} & u_{32} \end{pmatrix} \begin{pmatrix} s_{11} & \\ & s_{22} \end{pmatrix} \begin{pmatrix} v_{11} & v_{12} & v_{13} \\ v_{21} & v_{22} & v_{23} \end{pmatrix} = \begin{pmatrix} & \\ & \\ & \end{pmatrix} \begin{pmatrix} & & \end{pmatrix} . (4)$$

The numerical rank of $\mathbf{A}$ is the number of singular values greater than some judiciously chosen value or tolerance ε. If the singular values decrease exponentially, as they do in many MOM problems with unknown grouping, then $\mathbf{A}$ is very compressible. Fig. 3 shows the single precision (6 digits)

singular values for a 220 by 214 MOM Z interaction block (rank R = 214) on a $\log_{10}$ scale. There we see that the singular values have decreased to machine precision (6 orders of magnitude) by k = 30.

The next question is how to set the tolerance ε. This involves the Frobenius norm of matrix **A** [8] which is nothing more than the square root of the sum of the squares of all elements of **A**:

$$\|\mathbf{A}\| = \sqrt{\sum_{i=1}^{m} \sum_{j=1}^{n} \|a_{i,j}\|^2} . \qquad (5)$$

The SVD approximation error in the outer product approximation is given in terms of singular values of **A**. Let matrix **A** have rank r and the approximation rank k (using singular values 1 to k). The error involves the remaining singular values from k+1 to r. If $\sigma_k / \sigma_1 \sim 10^{-5}$, the fractional error in the Frobenius norm is small [8]:

$$\frac{\|\mathbf{A} - \mathbf{A}_k\|_F}{\|\mathbf{A}\|_F} = \frac{\sqrt{\sigma_{k+1}^2 + \cdots + \sigma_r^2}}{\sqrt{\sigma_1^2 + \cdots + \sigma_r^2}} . \qquad (6)$$

We see that low rank and tolerance are related and that if the singular values of **A** decrease exponentially, then the compressed form for **A** (2) has significantly less memory requirements and perhaps more importantly, significantly less operations count for matrix multiply operations. The relative norm error then becomes the compressed matrix of approximate rank k minus the full matrix divided by norm of the full matrix:

$$\frac{\|\mathbf{A}_{\text{compressed}}(k) - \mathbf{A}\|}{\|\mathbf{A}\|} = \frac{\|\mathbf{Au\ Av} - \mathbf{A}\|}{\|\mathbf{A}\|} \leq \varepsilon . \qquad (7)$$

Singular Values for a Numerically Low Rank Interaction Matrix
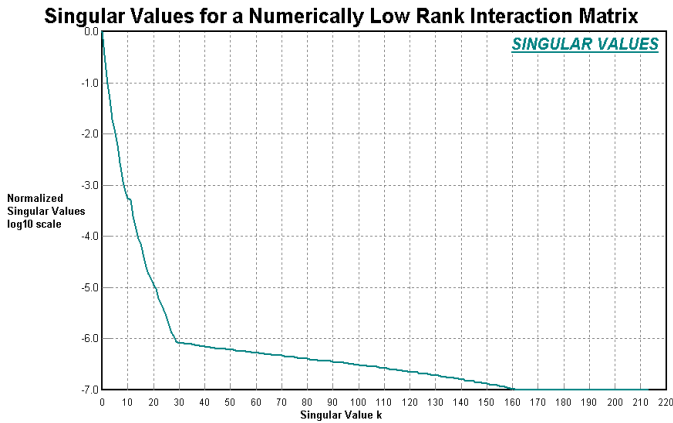
Fig. 3. Singular values for a Rk MOM interaction matrix.

IV. A RANK FRACTION METRIC

An important metric for the compressibility of a matrix is its Rank Fraction (RF) which is defined as the ratio of compressed or approximation memory storage to that of the full matrix. For an m x n matrix with approximation rank k, RF is:

$$RF = \frac{k(m+n)}{mn} . \qquad (8)$$

If m = n, RF = 2k/m. If **A** is 99% compressed with only 1% stored, then RF = 0.01. Often a dB scale is used.

V. R_K MATRIX MATH

The two very significant advantages of R_k formulations are the reduced storage for a (block) matrix and the operations count involving matrix multiplication. For full matrix reference, the storage for an m x n matrix is O(mn) while the operations count for the multiplication of two matrices, one m x k, the other k x n is O(mkn).

R_k matrix math starts by reviewing inner and outer matrix products. The dot or inner product of two vectors, each of k elements, is a row times a column and is characterized by a small operations count of order O(k):

$$r = \mathbf{x} \bullet \mathbf{y} = \begin{bmatrix} x_1 & x_2 & x_3 & x_4 \end{bmatrix} \begin{bmatrix} y_1 \\ y_2 \\ y_3 \\ y_4 \end{bmatrix} , \qquad (9)$$

while a 2 x k row inner product with a k x 2 column matrix has an operations count of O(4k):

$$\begin{bmatrix} \sqrt{\sigma_{\theta\theta}} & \sqrt{\sigma_{\theta\varphi}} \\ \sqrt{\sigma_{\varphi\theta}} & \sqrt{\sigma_{\varphi\varphi}} \end{bmatrix} = \mathbf{R}\ \mathbf{J} = \begin{bmatrix} R_{1\theta} & R_{2\theta} & R_{3\theta} & R_{4\theta} \\ R_{1\varphi} & R_{2\varphi} & R_{3\varphi} & R_{4\varphi} \end{bmatrix} \begin{bmatrix} J_{1\theta} & J_{1\varphi} \\ J_{2\theta} & J_{2\varphi} \\ J_{3\theta} & J_{3\varphi} \\ J_{4\theta} & J_{4\varphi} \end{bmatrix} . \qquad (10)$$

The outer product of a single column times a single row is a full matrix, albeit with rank 1. Let **U** be (m x 1) and **V** (1 x n), then **A** is (m x n), **A** = **U V** with $a_{ij} = u_i v_j$:

$$\begin{bmatrix} u_1 \\ \vdots \\ \vdots \\ u_m \end{bmatrix} \begin{bmatrix} v_1 & \vdots & \vdots & v_n \end{bmatrix} = \begin{bmatrix} a_{11} & \vdots & \vdots & a_{1n} \\ \vdots & \vdots & \vdots & \vdots \\ \vdots & \vdots & \vdots & \vdots \\ a_{m1} & \vdots & \vdots & a_{mn} \end{bmatrix} . \qquad (11)$$

This example dramatically shows the utility of storing a matrix in its **UV** outer product form. The *equivalent* information can be stored in O(m+n) versus O(mn). If m = n, the outer product storage is only 2/m of that required for the full matrix. No additional information can be obtained by storing the full matrix. Matrix algebra involving **A** in its compressed UV form has significantly less operations count.

The sum of two rank 1 outer products is a rank $R_k = 2$ matrix

where $a_{i,j} = u_{i,1} v_{1,j} + u_{i,2} v_{2,j}$:

$$\begin{bmatrix} a_{11} & \vdots & \vdots & a_{1n} \\ \vdots & \vdots & \vdots & \vdots \\ \vdots & \vdots & \vdots & \vdots \\ a_{m1} & \vdots & \vdots & a_{mn} \end{bmatrix} = \sum_{k=1}^{k=2} \begin{bmatrix} u_1 \\ \vdots \\ \vdots \\ u_m \end{bmatrix}_k \begin{bmatrix} v_1 & \vdots & \vdots & v_n \end{bmatrix}_k \quad (12)$$

$$= \begin{bmatrix} u_{11} & u_{12} \\ u_{21} & u_{22} \\ u_{31} & u_{32} \\ u_{41} & u_{42} \end{bmatrix} \begin{bmatrix} v_{11} & v_{12} & v_{13} & v_{14} \\ v_{21} & v_{22} & v_{23} & v_{24} \end{bmatrix}$$

R_k storage is $O(2(m+n))$ or if $m = n$, $O(4m)$ compared to $O(m^2)$, a storage ratio of $4/m$.

The sum of k rank 1 outer products is:

$$\mathbf{A} = \mathbf{UV} = \left(\begin{bmatrix} \mathbf{u} \\ \\ \\ \end{bmatrix} \begin{bmatrix} \mathbf{v} & & \end{bmatrix} \right)_{k=1} + \left(\begin{bmatrix} \mathbf{u} \\ \\ \\ \end{bmatrix} \begin{bmatrix} \mathbf{v} & & \end{bmatrix} \right)_{k=2} + \cdots \left(\begin{bmatrix} \mathbf{u} \\ \\ \\ \end{bmatrix} \begin{bmatrix} \mathbf{v} & & \end{bmatrix} \right)_{k=k}$$

$$= \sum_{i=1}^{i=k} \left(\begin{bmatrix} \mathbf{u}_i \\ \\ \\ \end{bmatrix} \begin{bmatrix} \mathbf{v}_i & & \end{bmatrix} \right)_i \quad (13)$$

$$= \begin{bmatrix} \mathbf{u}_1 & \mathbf{u}_2 & . & \mathbf{u}_k \\ . & . & . & . \\ . & . & . & . \\ . & . & . & . \end{bmatrix} \begin{bmatrix} \mathbf{v}_1 & . & . & . \\ \mathbf{v}_2 & . & . & . \\ . & . & . & . \\ \mathbf{v}_k & . & . & . \end{bmatrix}$$

This is the form for the ACA approximation of k rank 1 outer products used to approximate (compress) $\mathbf{A}$.

The product of a matrix $\mathbf{A}$ with a column vector $\mathbf{y}$ is a column vector $\mathbf{x}$, $\mathbf{x} = \mathbf{A} \mathbf{y}$ which is a matrix vector product:

$$\begin{bmatrix} \mathbf{x} \\ \\ \\ \end{bmatrix} = \begin{bmatrix} & \mathbf{A} & \end{bmatrix} \begin{bmatrix} \mathbf{y} \\ \\ \\ \end{bmatrix}. \quad (14)$$

The product of a row vector with a matrix $\mathbf{A}$ is another row vector, $\mathbf{x}^T = [\mathbf{Ay}]^T = \mathbf{y}^T \mathbf{A}^T$ where $\mathbf{x}^T$ and $\mathbf{y}^T$ are row vectors. This is a vector matrix product:

$$\begin{bmatrix} & \mathbf{x}^t & \end{bmatrix} = \begin{bmatrix} & \mathbf{y}^t & \end{bmatrix} \begin{bmatrix} & \mathbf{A} & \end{bmatrix}^T. \quad (15)$$

VI.   THRILL OF R_K MULTIPLICATION

The product of two or more R_k matrices has a significantly low operations count compared to that for their full-size counterparts. R_k matrix-matrix multiply reduces to one of: a) matrix-vector multiplication; b) vector-matrix multiplication; or c) matrix-vector plus a small matrix-matrix multiply. Let us use three cases.

Let case 1 be $\mathbf{C} = \mathbf{A} \mathbf{B}$ where $\mathbf{A}$ is R_k and $\mathbf{B}$ is full. Then $\mathbf{C}$ is R_k and note that $\mathbf{Cu} = \mathbf{Au}$ and $\mathbf{Cv} = \mathbf{Av} \mathbf{B}$:

$$\begin{bmatrix} \mathbf{Cu} \\ \\ \end{bmatrix} \begin{bmatrix} \mathbf{Cv} & \end{bmatrix} = \begin{bmatrix} \mathbf{Au} \\ \\ \end{bmatrix} \begin{bmatrix} \mathbf{Av} & \end{bmatrix} \begin{bmatrix} & \mathbf{B} & \end{bmatrix} \quad (16)$$

$$\begin{bmatrix} \mathbf{Cu} \\ \\ \end{bmatrix} = \begin{bmatrix} \mathbf{Au} \\ \\ \end{bmatrix}; [\mathbf{Cv} \quad] = \left(\begin{bmatrix} \mathbf{Av} & \end{bmatrix} \begin{bmatrix} & \mathbf{B} & \end{bmatrix} \right)$$

The opts count is that of a row matrix with a full matrix.

For case 2, let $\mathbf{C} = \mathbf{A} \mathbf{B}$ where $\mathbf{A}$ is full and $\mathbf{B}$ is R_k then $\mathbf{C}$ is R_k and note that $\mathbf{Cu} = \mathbf{A} \mathbf{Bu}$ and $\mathbf{Cv} = \mathbf{Bv}$:

$$\begin{bmatrix} \mathbf{Cu} \\ \\ \end{bmatrix} \begin{bmatrix} \mathbf{Cv} & \end{bmatrix} = \left(\begin{bmatrix} \mathbf{A} \\ \\ \end{bmatrix} \begin{bmatrix} \mathbf{Bu} \\ \\ \end{bmatrix} \right) \begin{bmatrix} \mathbf{Bv} & \end{bmatrix} \quad (17)$$

$$\begin{bmatrix} \mathbf{Cu} \\ \\ \end{bmatrix} = \left(\begin{bmatrix} \mathbf{A} \\ \\ \end{bmatrix} \begin{bmatrix} \mathbf{Bu} \\ \\ \end{bmatrix} \right); [\mathbf{Cv} \quad] = [\mathbf{Bv} \quad]$$

Again, the opts count is that of a full matrix with a column matrix.

For case 3 let $\mathbf{C} = \mathbf{A} \mathbf{B}$ where each matrix is R_k and note than $\mathbf{Cu} = \mathbf{Au}$ or $\mathbf{Cv} = \mathbf{Bv}$ depending on which gives the lowest rank for $\mathbf{C}$. Assuming $\mathbf{Au}$ is the lower rank option then:

$$\begin{bmatrix} \mathbf{Cu} \\ \\ \end{bmatrix} \begin{bmatrix} \mathbf{Cv} & \end{bmatrix} = \begin{bmatrix} \mathbf{Au} \\ \\ \end{bmatrix} \begin{bmatrix} \mathbf{Av} & \end{bmatrix} \begin{bmatrix} \mathbf{Bu} \\ \\ \end{bmatrix} \begin{bmatrix} \mathbf{Bv} & \end{bmatrix} \quad (18)$$

$$\begin{bmatrix} \mathbf{Cu} \\ \\ \end{bmatrix} = \begin{bmatrix} \mathbf{Au} \\ \\ \end{bmatrix}; [\mathbf{Cv} \quad] = \left(\begin{bmatrix} \mathbf{Av} & \end{bmatrix} \begin{bmatrix} \mathbf{Bu} \\ \\ \end{bmatrix} \right) \begin{bmatrix} \mathbf{Bv} & \end{bmatrix}$$

For cases 1 and 2 matrix-matrix multiply reduces to matrix-vector multiply. For case 3 we have a low operations count inner product multiply followed by a "small" matrix - row matrix multiply. In each of these cases the operations count involving R_k matrices is significantly lower than their full-size matrix counter parts. When multiplying R_k matrices, one strives to do the low operations count inner products first as suggested in case 3 and then a matrix-vector or vector-matrix multiply. Often the left- or right-hand side of a R_k product is simply either the left or right-hand side $\mathbf{U}$ or $\mathbf{V}$.

VII.   AGONY OF R_K ADDITION

The sum of two or more R_k matrices has undesirable consequences. Let $\mathbf{D} = \mathbf{A} + \mathbf{B} + \mathbf{C}$ where $\mathbf{A}$, $\mathbf{B}$ and $\mathbf{C}$ are R_k:

$$\begin{bmatrix} \mathbf{A}u \\ \\ \end{bmatrix}\begin{bmatrix} \mathbf{A}v & \end{bmatrix} + \begin{bmatrix} \mathbf{B}u \\ \\ \end{bmatrix}\begin{bmatrix} \mathbf{B}v & \end{bmatrix} + \begin{bmatrix} \mathbf{C}u \\ \\ \end{bmatrix}\begin{bmatrix} \mathbf{C}v & \end{bmatrix}$$

$$= \begin{bmatrix} \mathbf{A}u & \mathbf{B}u & \mathbf{C}u \\ & & \\ & & \end{bmatrix}\begin{bmatrix} \mathbf{A}v \\ \mathbf{B}v \\ \mathbf{C}v \end{bmatrix} = \begin{bmatrix} \mathbf{D}u \\ \\ \end{bmatrix}\begin{bmatrix} \mathbf{D}v & \end{bmatrix} \qquad (19)$$

A terrible thing just happened, the R_k rank of **D** is sum of the R_k ranks of **A**, **B**, and **C**. This does not mean that **D** is not low rank, but it does mean that **D** requires "recompression." More on this in section IX.

VIII. ADAPTIVE CROSS APPROXIMATION

A number of techniques can be used to compute the low rank R_k approximation to a (block) matrix **A**. SVD and QR factorizations are possible but they suffer from two very significant drawbacks: a) all of the matrix **A** must be computed beforehand and b) the operations count is prohibitive, typically $O(m^3)$. The Adaptive Cross Approximation (ACA) popularized in [9,11] does not suffer these problems. The ACA operations count is $k^2(m+n)$ and, most significantly, the ACA does not require a prior computation of the full matrix **A**. The ACA only requires various rows and columns of **A**. **A** is virtual in the sense that it only needs to exist as a subroutine which can compute needed rows and columns required by the ACA. It is not compressed in the sense of an SVD or QR.

There are several requirements for successful ACA computation. First, the singular values must drop exponentially which is usually the case for MOM PEC problems with spatially grouped unknowns. Second, the integral operator should have a smooth decay with distance. Our free space Green's function is not quite smooth but the ACA still works well. For the PEC L operator, ACA works very well. For the curl K operator, where the integrand also has geometric terms, ACA may be problematic since sub-blocks can be exactly low rank. In this case special efforts are required to obtain the UV approximation. The ACA is adaptive in the sense that the algorithm always looks for the largest element in a row/column to compute the next k^{th} row/column in the approximation. The ACA terminates when the desired approximation tolerance is obtained.

A six-step algorithm as outlined in [9] starts by writing (block) matrix **A** as the sum of its approximation plus its error and then solving for the error:

$$\mathbf{A} = \mathbf{A}_{approximation} + \mathbf{E}$$
$$\qquad\qquad (20)$$
$$\mathbf{E} = \mathbf{A} - \mathbf{A}_{approximation} = \mathbf{A} - \mathbf{UV}$$

The goal at each step is to make the error as small as possible with each successive rank one **UV** outer product term where

successive terms add columns to **U** and rows to **V**. At the kth step, the error is:

$$\mathbf{E_k} = \mathbf{A} - \mathbf{U_k V_k} = \mathbf{A} - \sum_{p=1}^{k}\left(\begin{bmatrix} \mathbf{u_p} \\ \vdots \\ \vdots \\ \vdots \end{bmatrix}\begin{bmatrix} \mathbf{v_p} & \cdots & \cdots & \cdots \end{bmatrix}\right)_p . \quad (21)$$

The next row/column in the approximation is obtained by setting the pivot row/column error to zero in order to compute the next **UV** outer product term. The choice of row/column is made by finding the maximum element in the last **UV** approximation which is called pivoting. Note that only rows/ columns of **E**, **A** and **UV** are required at each step.

The ACA approximation stops when the norm of the next **UV** term is less than the desired tolerance, where $\mathbf{A}_k$ is a recursive norm computed based only on terms to date [9]:

$$\frac{\|\mathbf{u}_k\|\|\mathbf{v}_k\|}{\|\mathbf{A}_k\|} \le \varepsilon . \qquad (22)$$

Fig. 4 shows the ACA approximation error for a 220 x 214 MOM interaction matrix as a function of the iteration. Convergence to 10^{-4} is achieved by k=20. Also plotted are the corresponding normalized singular values and the true error norm as computed from the full matrix.
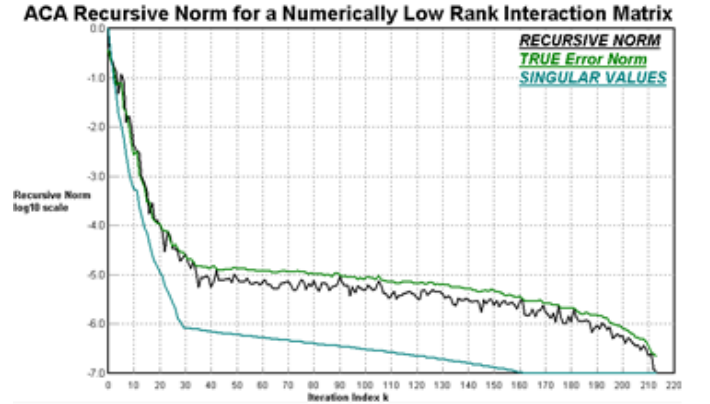
Fig. 4. ACA recursive norm, true error norm and singular values for an R_k MOM interaction matrix.

For a given outer product error tolerance the SVD approximation has the least rank [8]; however, the ACA approach is still quite acceptable.

An example of the Z block rank fraction compression (on a 20 dB scale) achieved by the ACA for an open pipe target with 92,220 unknowns, block size 800, for $\varepsilon = 10^{-5}$ is shown in Fig. 5. The corresponding LU block rank fraction compression is shown in Fig. 6. While there is some fill-in, the LU blocks are never the less very sparse.
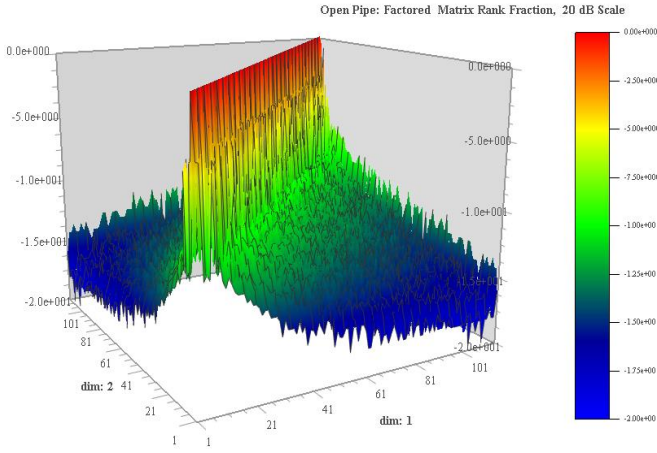
Fig. 5. Rank fraction, 20 dB scale, for block matrices for an LU factored matrix.
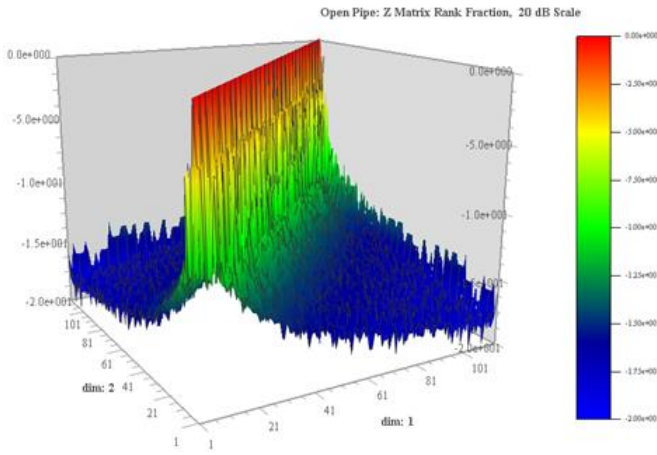
Fig. 6. Rank fraction, 20 dB scale for Z block matrices in system matrix.

IX. R_k ADDITION "RECOMPRESSION"

As we saw in section VII, the sum of a number of R_k terms is itself R_k. However, if we add all terms directly, we end up with the sum R_k equal to sum of the ranks of each term in the sum. This is untenable. A methodology is required to accomplish such R_k sums. Two possible addition "recompression" approaches can be utilized.

Before we outline each approach, let us put into perspective the sizes involved when using either of these techniques when doing block wise LU R_k factorization and solve operations. As an example, let us consider a one million unknown problem where the R_k group size is 5000. This translates into a system matrix of size 200 x 200 blocks with each block 5000 x 5000. The LU factorization and solve formulas (discussed below) have sums involving up to 200 terms of (5000 x k) and (k x 5000) UV terms where k is the rank of each term.

In the 1st approach [2,10] we utilize the ACA to directly compute the R_k form for $\mathbf{D} = \mathbf{UV}$ using the rows/columns from each term S_k in the sum:

$$\mathbf{D} = \mathbf{UV} = \sum_p \left(\begin{bmatrix} \mathbf{S}_u \\ \end{bmatrix} \begin{bmatrix} \mathbf{S}_v & \end{bmatrix} \right)_p . \qquad (23)$$

After choosing an ACA tolerance ε, the required ACA rows are easily computed from the RHS of (23):

$$\begin{bmatrix} \rightarrow & \rightarrow & \rightarrow \end{bmatrix} = \sum \left(\begin{bmatrix} \rightarrow \end{bmatrix} \begin{bmatrix} \downarrow & \downarrow & \downarrow \end{bmatrix} \right)_p , \qquad (24)$$

while the required ACA columns are computed from the RHS of (23) as:

$$\begin{bmatrix} \downarrow \\ \downarrow \\ \downarrow \end{bmatrix} = \sum \left(\begin{bmatrix} \rightarrow \\ \rightarrow \\ \rightarrow \end{bmatrix} \begin{bmatrix} & \downarrow & \end{bmatrix} \right)_p . \qquad (25)$$

This is a speedy process which encompasses a vector-matrix or matrix-vector multiply. In spite of the tedious looking process, it can be accomplished surprising quickly. This procedure is in essence a methodology for computing the R_k sum using the ACA without the necessary requirements for many QR recompressions required when using the 2nd approach. It should be noted that many of these operations can be computed in parallel, OpenMP for outer loops and BLAS libraries for lower level matrix-vector operations.

The 2nd "recompression" approach involves doing a QR factorization of the U and of V components of $\mathbf{D} = \mathbf{UV}$ coupled with an SVD compression using the desired tolerance. Details can be found in [11], but briefly the process involves:

$\mathbf{U} = \mathbf{Q_u R_u} ; \mathbf{V} = \mathbf{Q_v R_v}$ Perform a QR factorizaton on U and V

$$\mathbf{D} = \mathbf{Q_u R_u R_v^T Q_v^T} \qquad . (26)$$

$\mathbf{R_u R_v^T} = \widehat{\mathbf{U}} \Sigma \widehat{\mathbf{V}}$ Perform SVD on the small $\begin{bmatrix} \mathbf{R_u R_v^T} \end{bmatrix}$ matrix

X. LU FACTORIZATION USING THE ACA

The rationale for solving the MOM system matrix via LU factorization is well known [4,12]. In this section we will examine the procedure for a symmetric system matrix and, most importantly, show a technique for performing R_k addition using the ACA which builds on R_k multiplication.

The symmetric matrix factor form [13] is:

$\mathbf{Z} = \mathbf{U^T D U}$

$$= \begin{bmatrix} \mathbf{I} & & & \\ \mathbf{U_{12}^T} & \mathbf{I} & & \\ \mathbf{U_{13}^T} & \mathbf{U_{23}^T} & \mathbf{I} & \\ \mathbf{U_{14}^T} & \mathbf{U_{24}^T} & \mathbf{U_{34}^T} & \mathbf{I} \end{bmatrix} \begin{bmatrix} \mathbf{D_{11}} & & & \\ & \mathbf{D_{22}} & & \\ & & \mathbf{D_{33}} & \\ & & & \mathbf{D_{44}} \end{bmatrix} \begin{bmatrix} \mathbf{I} & \mathbf{U_{12}} & \mathbf{U_{13}} & \mathbf{U_{14}} \\ & \mathbf{I} & \mathbf{U_{23}} & \mathbf{U_{24}} \\ & & \mathbf{I} & \mathbf{U_{34}} \\ & & & \mathbf{I} \end{bmatrix} ,$$

$$(27)$$

which can be recast into standard form as:

$$\mathbf{Z} = \begin{bmatrix} \mathbf{I} & & & \\ \mathbf{L}_{21} & \mathbf{I} & & \\ \mathbf{L}_{31} & \mathbf{L}_{32} & \mathbf{I} & \\ \mathbf{L}_{41} & \mathbf{L}_{42} & \mathbf{L}_{43} & \mathbf{I} \end{bmatrix} \begin{bmatrix} \mathbf{U}'_{11} & \mathbf{U}'_{12} & \mathbf{U}'_{13} & \mathbf{U}'_{14} \\ & \mathbf{U}'_{22} & \mathbf{U}'_{23} & \mathbf{U}'_{24} \\ & & \mathbf{U}'_{33} & \mathbf{U}'_{34} \\ & & & \mathbf{U}'_{44} \end{bmatrix}. \quad (28)$$

The solution for each **U** block [2] is:

$$\mathbf{U}_{iBlk,jBlk} = \mathbf{Z}_{iBlk,jBlk} - \sum_{pBlk=1}^{iBlk-1} \mathbf{L}_{iBlk,pBlk} \mathbf{D}_{pBlk,pBlk}^{-1} \mathbf{U}_{pBlk,jBlk}, \quad (29)$$

where the $\mathbf{D}^{-1}$'s are the dense (not R_k) inverse diagonal blocks (computed using standard LU factorization). Note the sum terms involving R_k forms for $\mathbf{U}^T$ and $\mathbf{U}$. Depending on total number of unknowns, these blocks can range in size from 2500 to 10,000. The R_k form for the **U**'s and **Z**'s (29) becomes:

$$i, j = iBlk, jBlk$$

$$\left(\begin{bmatrix} \mathbf{U}_u \\ \end{bmatrix} [\mathbf{U}_v \quad] \right)_{i,j} = \left(\left(\begin{bmatrix} \mathbf{Z}_u \\ \end{bmatrix} [\mathbf{Z}_v \quad] \right)_{i,j} - \sum_{p=1}^{p=i-1} \left(\begin{bmatrix} \mathbf{L}_u \\ \end{bmatrix} [\mathbf{L}_v \quad] \right)_{i,p} \begin{bmatrix} \mathbf{D} \end{bmatrix}_{p,p}^{-1} \left(\begin{bmatrix} \mathbf{U}_u \\ \end{bmatrix} [\mathbf{U}_v \quad] \right)_{p,j} \right). \quad (30)$$

In this expression, we need to compute the left-hand **U** in R_k form, using the ACA, where all sum terms on the right-hand side are known. In order to accomplish this, the ACA needs rows/columns of the right-hand side. The approach is to recast the RHS as a sum of S matrices in R_k form as shown in section VII:

$$\sum_{p=1}^{k-1} \left(\begin{bmatrix} \mathbf{S}_u \\ \end{bmatrix} [\mathbf{S}_v \quad] \right)_p. \quad (31)$$

Each $\mathbf{S}_p$ matrix in the sum is:

$$\begin{bmatrix} \mathbf{S}_u \\ \end{bmatrix} [\mathbf{S}_v \quad] = \begin{bmatrix} \mathbf{Z}_u \\ \end{bmatrix} [\mathbf{Z}_v \quad] \text{ or}$$

$$\begin{bmatrix} \mathbf{S}_u \\ \end{bmatrix} [\mathbf{S}_v \quad] = \begin{bmatrix} \mathbf{L}_u \\ \end{bmatrix} \left([\mathbf{L}_v \quad] \begin{bmatrix} \mathbf{D} \end{bmatrix}^{-1} \begin{bmatrix} \mathbf{U}_u \\ \end{bmatrix} \right) [\mathbf{U}_v \quad] \quad . (32)$$

Each S_k sum term is computed using R_k multiplication before using the 1st ACA "recompression" approach outlined in section VII.

XI. SOLVE USING R_K FORMS FOR SCATTERING PROBLEMS

For scattering problems, once the LU factored matrix is computed in R_k form, the solution for the currents can be computed in a similar approach where the RHS voltage forcing function and resulting currents may also be expressed block wise in R_k form:

$$\mathbf{V}^{iPol=\theta \text{ or } \varphi} = \begin{bmatrix} v_{1,1}^{\theta \text{ or } \varphi} & \cdots & v_{1,nAng}^{\theta \text{ or } \varphi} \\ & \vdots & \\ v_{k,1}^{\theta \text{ or } \varphi} & & v_{k,nAng}^{\theta \text{ or } \varphi} \end{bmatrix} = \begin{bmatrix} \mathbf{V}u \\ \end{bmatrix} [\mathbf{V}v \quad]. \quad (33)$$

The resulting block wise current solution may also be expressed in R_k from:

$$\mathbf{J}^{iPol=\theta \text{ or } \varphi} = \begin{bmatrix} j_{1,1}^{\theta \text{ or } \varphi} & \cdots & j_{1,nAng}^{\theta \text{ or } \varphi} \\ & \vdots & \\ j_{k,1}^{\theta \text{ or } \varphi} & & j_{k,nAng}^{\theta \text{ or } \varphi} \end{bmatrix} = \begin{bmatrix} \mathbf{J}u \\ \end{bmatrix} [\mathbf{J}v \quad]. \quad (34)$$

The LU block wise forward/back solve formulas [2] are:

$$\mathbf{Y}_i = \left[\mathbf{V}_i - \sum_{p=1}^{i-1} \mathbf{L}_{ip} \mathbf{D}_{pp}^{-1} \mathbf{Y}_p \right], \quad (35)$$

$$\mathbf{J}_i = \mathbf{D}_i^{-1} \left[\mathbf{Y}_i - \sum_{p=n-1}^{i-1} \mathbf{U}_{ip} \mathbf{J}_p \right]. \quad (36)$$

Finally, the full polarization scattering matrix is computed using the R_k forms for the Row measurement matrix [7]. In the backscatter case **R** is the transpose of the monostatic incident block wise plane wave excitation forcing function **V** [7], each is in R_k form:

$$\begin{aligned} \mathbf{R} &= \mathbf{V}^T \\ &= \mathbf{R}_u \mathbf{R}_v = \mathbf{V}_v^T \mathbf{V}_u^T \end{aligned} . \quad (37)$$

The block wise column current solution **J** in R_k form [7] is then used with the row measurement matrix to obtain the full polarization scattering matrix:

$$\begin{bmatrix} \sqrt{\sigma_{\theta\theta}} & \sqrt{\sigma_{\theta\varphi}} \\ \sqrt{\sigma_{\varphi\theta}} & \sqrt{\sigma_{\varphi\varphi}} \end{bmatrix} = \begin{bmatrix} \mathbf{R}_\theta \\ \mathbf{R}_\varphi \end{bmatrix} \begin{bmatrix} \mathbf{J}_\theta & \mathbf{J}_\varphi \\ & \\ & \end{bmatrix}. \quad (38)$$

XII. MERCURY MOM SCATTERING CODE

The computer code MERCURY MOM, [1-3] was built based on the R_k math discussed above. This code is a frequency domain MOM SIE/VIE scattering code which uses RWG triangles and SWG tetrahedrons. SIE boundary conditions include PEC, dielectric, R card, thin dielectric and IBC. Junctions are included between SIE RWG triangles and VIE tetrahedrons. The three EM operators $\mathcal{L}$, $\mathcal{K}$ and $\mathcal{K}$_tilde are utilized to compute three of the four general unknown SIE surface currents: J^+, J^-, M^+. A Galerkin symmetric matrix is utilized, and the full polarization scattering matrix is computed.

Mercury MOM was designed to be run on inexpensive work station class computers located in engineering design environments on an engineers' desk. The computer used by the

author for the five million unknown result [3] was a circa 2013 two socket Intel Xeon processor with 10 cores each (20 total) with a cost of $8900.

XIII. CONCLUDING REMARKS

Spatial grouping / R_k math / ACA / LU factorization-solve techniques have allowed our community to significantly extend the capability of full wave solutions of Maxwell's equations for electrically large bodies, all within the standard MOM framework. This means that increasely large problem sizes can be done in MOM full wave form before we must resort back to problematic and approximate high frequency methods [14] of PO/GO/PTD/GTD/SBR. R_k methods can be implemented on inexpensive workstation class computers located on design engineers' desks and allow a much greater exploration of design space parameters.

The quote in [12] succinctly sums up our quest: "A good computation is one that does the least computation for the right answer" which for practical engineering purposes we might change 'right answer' to 'right/good enough answer.'

REFERENCES

[1] J. Shaeffer, "Direct solve of electrically large integral equations for problem sizes to 1 M unknowns," IEEE Trans. Antennas Propag., vol. 56, no. 8, pp. 2306-2313, Aug. 2008.

[2] J. Shaeffer, "Direct solve of electrically large integral equations for problem Sizes to 1M unknowns," NASA/CR-2008-215353, Sept. 2008

[3] J. Shaeffer, "Five million unknown MOM LU factorization on a PC workstation," Antenna Measurement Techniques Association Meeting, Long Beach, CA, Oct. 11-16, 2015.

[4] A. Heldring, J. Rius, J. M. Tamayo, J. Parron, and E. Ubeda, "Multiscale compressed block decomposition for fast direct solution of method of moments linear system," IEEE Trans. Antennas Propag., vol. 59, no. 2, pp. 526-536, Feb. 2011.

[5] A. Manic, A. Smull, F. H. Rouet, X. S. Li, and B. Notaros, "Efficient scalable parallel higher order direct MOM-SIE method with hierarchically semiseparable structures for 3-d scattering," IEEE Trans. Antennas Propag., vol. 65, no. 5, pp. 2467-2478, May 2017.

[6] H. Guo, Y. Liu, J. Hu, and E. Michielssen, "A butterfly-based direct integral-equation solver using hierarchical LU factorization for analyzing scattering from electrically large conducting objects," IEEE Trans. Antennas Propag., vol. 65, no. 9, pp. 4742-4650, Sept. 2017.

[7] R. F. Harrington, Field Computation by Moment Methods. New York, NY, USA: Macmillan, 1968.

[8] L. Trefethen and D. Bau, Numerical Linear Algebra. Philadelphia, PA: Soc. Indust. Appl Math. (SIAM), 1997.

[9] S. Kurz, O.Rain, and S. Rjasanow, "Application of the adaptive cross approximation technique for the coupled BE-FE solution of electromagnetic problems," Presented at the Int. Association Boundary Element Methods Conf., IABEM 2002, Austin, TX, May 28-30, 2002.

[10] J. F. Shaeffer, "Systems and methods for analysis and design of radiating and scattering objects," United States Patent No. 7,844,407 B1, Nov. 30, 2010.

[11] M. Bebendorf, Hierarchical Matrices. Berlin, Springer-Verlag, 2008.

[12] S. Ambikasaran, "Fast algorithms for dense numerical linear algebra and applications," Ph.D. Dissertation, Stanford University, Aug. 2013.

[13] G. Golub and C. Van Loan, Matrix Computations. 3rd. Baltimore, MD: The John Hopkins Univ. Press, 1996.

[14] E. F. Knott, J. F. Shaeffer, and M. T. Tuley, Radar Cross Section. 2nd Edition, Raleigh, NC: Scitech Publishing, 2004.

A Nyström Discretization of a Broad-Band Augmented-Müller Surface Integral Equation

Nastaran Hendijani [1], Stephen D. Gedney [1], John C. Young [2], and Robert J. Adams [2]

[1] Department of Electrical Engineering
University of Colorado Denver, Denver, CO 80204, USA
stephen.gedney@ucdenver.edu, Nastaran.hendijani@ucdenver.edu

[2] Department of Electrical and Computer Engineering
University of Kentucky, Lexington, KY 40506, USA
john.c.young@uky.edu, robert.adams@uky.edu

Abstract ─ A broad-band Augmented-Müller (A-Müller) surface integral equation method for scattering from material objects is presented. The formulation incorporates surface electric and magnetic charges into the conventional Müller formulation with added constraints on the normal magnetic and electric fields. A new technique to extract the static fields is introduced which improves accuracy of computing scattered near fields at very low frequencies. The (A-Müller) formulation is discretized using the locally corrected Nyström (LCN) method. Numerical results show that the method is high-order accurate and stable over a broad frequency range from arbitrarily low to high frequencies for simply connected, multiply connected, highly lossy, high contrast and complex material geometries. The proposed formulation does not incorporate line charges, charge continuity constraints, or any frequency scaling of the degrees of freedom

Index Terms ─ Locally corrected Nyström method, Müller formulation, surface integral equations.

I. INTRODUCTION

An obstacle to developing accurate and stable surface integral equation formulations for scattering by perfect conducting or penetrable objects is the low frequency breakdown of the electric field integral equation $\mathcal{L}$ operator. Different strategies have been developed to address the instability including Helmholtz decomposition-based and Calderón-based stabilization methods [1, 2]. These methods have been mainly designed for use with only perfect electric conductors and may have drawbacks such as the use of global loops and increased complexity of implementation. Some methods such as the Müller formulation eliminate the low-frequency break down by transforming the hyper-singular kernel to one with a lower singularity [3]. While

the Müller formulation is well conditioned, it provides inaccurate solutions at low frequencies because of catastrophic cancellation in reconstructing the fields.

Other techniques addressing the low frequency instability of the $\mathcal{L}$ operator are called augmented formulations and include surface charges as additional unknowns [4-6]. In this paper, an augmented formulation based on the conventional Müller formulation for scattering by penetrable objects is presented, wherein constraints on tangential and normal components of the fields in both the background media and the scattering media are expressed in terms of surface currents and charges and are combined in Müller form. The resulting A-Müller formulation is accurate, well-conditioned, and stable and does not include line charges, charge continuity constraints, or any frequency-dependent scaling of the unknowns

II. A-MÜLLER FORMULATION

An electromagnetic field radiated by sources in an unbounded region V_1 with material properties (μ_1, ε_1) is incident on a material object with homogeneous material properties (μ_2, ε_2) occupying a finite volume V_2 bound by the surface $S_{1,2}$. Equivalent magnetic $(\vec{M}_{1,2})$ and electric $(\vec{J}_{1,2})$ currents are introduced on $S_{1,2}$ [7]:

$$\vec{M}_{1,2} = \vec{E}_1 \times \hat{n}\big|_{S_{1,2}} \, , \, \vec{J}_{1,2} = \hat{n} \times \vec{H}_1\big|_{S_{1,2}} \, , \qquad (1)$$

where $\vec{E}_1$ and $\vec{H}_1$ are the total electric and magnetic fields on $S_{1,2}$ just inside V_1, and $\hat{n}$ is the unit normal directed into V_1. The magnetic current continuity equation states:

$$\nabla \cdot \vec{M}_{1,2}(\vec{r}) = -j\omega \rho_{m_{1,2}} \, , \qquad (2)$$

where $\rho_{m_{1,2}}$ is the magnetic surface charge density on

$S_{1,2}$ and which satisfies the boundary condition:

$$\rho_{m_{1,2}} = \hat{n} \cdot \mu_1 \vec{H}_1 \Big|_{S_{1,2}} . \tag{3}$$

The electric current continuity equation is defined by applying the duality theorem on (2) and (3) leading to the surface electric charge density $\rho_{e_{1,2}}$. Applying surface electric and magnetic charge continuity constraints leads to the augmented Müller formulation [3, 6]:

$$\mu_{r_1} \eta_0 \vec{T}(\vec{r}) \cdot \vec{H}_1^{inc}(\vec{r}) + \mu_{r_2} \eta_0 \vec{T}(\vec{r}) \cdot \vec{H}_2^{inc}(\vec{r}) =$$

$$\frac{\mu_{r_1} + \mu_{r_2}}{2} \vec{T}(\vec{r}) \cdot \tilde{\vec{J}}_{1,2}(\vec{r}) \times \hat{n}$$

$$- \oiint_{S_{1,2}} \vec{T}(\vec{r}) \cdot \left(\mu_{r_1} \nabla G_1(\vec{r},\vec{r}') - \mu_{r_2} \nabla G_2(\vec{r},\vec{r}') \right) \times \tilde{\vec{J}}_{1,2}(\vec{r}') ds'$$

$$+ j\omega \eta_0 \oiint_{S_{1,2}} \vec{T}(\vec{r}) \cdot \vec{M}_{1,2}(\vec{r}') \left(\mu_{r_1} \varepsilon_1 G_1(\vec{r},\vec{r}') - \mu_{r_2} \varepsilon_2 G_2(\vec{r},\vec{r}') \right) ds' \tag{4}$$

$$+ \eta_0 \oiint_{S_{1,2}} \vec{T}(\vec{r}) \cdot \left(\nabla G_1(\vec{r},\vec{r}') - \nabla G_2(\vec{r},\vec{r}') \right) \tilde{\rho}_{m_{1,2}}(\vec{r}') ds',$$

where $\vec{H}_i^{inc}$ is the incident magnetic field inside V_i, and $\vec{T}(\vec{r})$ is a test vector tangential to $S_{1,2}$. $G_i(\vec{r},\vec{r}')$ is the Green's function in V_i, and $\vec{r}$ is an observation point on $S_{1,2}$. Also, $\tilde{\rho}_{m_{1,2}} = (1/\mu_o) \rho_{m_{1,2}}$, $\tilde{\rho}_{e_{1,2}} = (1/\varepsilon_o) \rho_{e_{1,2}}$, and $\tilde{\vec{J}}_{1,2} = \eta_0 \vec{J}_{1,2}$ are the scaled charge and currents. μ_o, ε_o, and η_o are the free space permeability, permittivity, and characteristic impedance, respectively. Equation (4) is referred to here as the A-Müller Tangential Magnetic Field Integral Equation (TMFIE). Using (2) and (3), and combining the normal constraints on the fields in the two regions in a Müller form, the A-Müller Normal MFIE (NMFIE) can be formed:

$$\mu_{r_1} \eta_0 \hat{n} \cdot \vec{H}_1^{inc}(\vec{r}) + \mu_{r_2} \eta_0 \hat{n} \cdot \vec{H}_2^{inc}(\vec{r}) = \eta_0 \tilde{\rho}_{m_{1,2}}(\vec{r})$$

$$- \oiint_{S_{1,2}} \hat{n}(\vec{r}) \cdot \left(\mu_{r_1} \nabla G_1(\vec{r},\vec{r}') - \mu_{r_2} \nabla G_2(\vec{r},\vec{r}') \right) \times \tilde{\vec{J}}_{1,2}(\vec{r}') ds'$$

$$+ j\omega \eta_0 \oiint_{S_{1,2}} \hat{n}(\vec{r}) \cdot \vec{M}_{1,2}(\vec{r}') \left(\mu_{r_1} \varepsilon_1 G_1(\vec{r},\vec{r}') - \mu_{r_2} \varepsilon_2 G_2(\vec{r},\vec{r}') \right) ds' \tag{5}$$

$$+ \eta_0 \oiint_{S_{1,2}} \hat{n}(\vec{r}) \cdot \left(\nabla G_1(\vec{r},\vec{r}') - \nabla G_2(\vec{r},\vec{r}') \right) \tilde{\rho}_{m_{1,2}}(\vec{r}') ds'.$$

Applying duality leads to the A-Müller TEFIE:

$$\varepsilon_{r_1} \vec{T}(\vec{r}) \cdot \vec{E}_1^{inc} + \varepsilon_{r_2} \vec{T}(\vec{r}) \cdot \vec{E}_2^{inc} = \frac{\varepsilon_{r_1} + \varepsilon_{r_2}}{2} \vec{T}(\vec{r}) \cdot \hat{n} \times \vec{M}_{1,2}$$

$$+ \oiint_{S_{1,2}} \vec{T}(\vec{r}) \cdot \left(\varepsilon_{r_1} \nabla G_1(\vec{r},\vec{r}') - \varepsilon_{r_2} \nabla G_2(\vec{r},\vec{r}') \right) \times \vec{M}_{1,2}(\vec{r}') ds'$$

$$+ j\omega / \eta_0 \oiint_{S_{1,2}} \vec{T}(\vec{r}) \cdot \tilde{\vec{J}}_{1,2}(\vec{r}') \left(\mu_1 \varepsilon_{r_1} G_1(\vec{r},\vec{r}') - \mu_2 \varepsilon_{r_2} G_2(\vec{r},\vec{r}') \right) ds' \tag{6}$$

$$+ \oiint_{S_{1,2}} \vec{T}(\vec{r}) \cdot \left(\nabla G_1(\vec{r},\vec{r}') - \nabla G_2(\vec{r},\vec{r}') \right) \tilde{\rho}_{e_{1,2}}(\vec{r}') ds',$$

and the A-Müller NEFIE:

$$\varepsilon_{r_1} \hat{n} \cdot \vec{E}_1^{inc}(\vec{r}) + \varepsilon_{r_2} \hat{n} \cdot \vec{E}_2^{inc}(\vec{r}) = \tilde{\rho}_{e_{1,2}}(\vec{r})$$

$$+ \oiint_{S_{1,2}} \hat{n}(\vec{r}) \cdot \left(\varepsilon_{r_1} \nabla G_1(\vec{r},\vec{r}') - \varepsilon_{r_2} \nabla G_2(\vec{r},\vec{r}') \right) \times \vec{M}_{1,2}(\vec{r}') ds'$$

$$+ j\omega / \eta_0 \oiint_{S_{1,2}} \hat{n}(\vec{r}) \cdot \tilde{\vec{J}}_{1,2}(\vec{r}') \left(\mu_1 \varepsilon_{r_1} G_1(\vec{r},\vec{r}') - \mu_2 \varepsilon_{r_2} G_2(\vec{r},\vec{r}') \right) ds' \tag{7}$$

$$+ \oiint_{S_{1,2}} \hat{n}(\vec{r}) \cdot \left(\nabla G_1(\vec{r},\vec{r}') - \nabla G_2(\vec{r},\vec{r}') \right) \tilde{\rho}_{e_{1,2}}(\vec{r}') ds'.$$

Equations (4)-(7) represent A-Müller formulation. The equations are discretized using the Locally Corrected Nyström (LCN) method [3, 8-12]. The TMFIE and TEFIE in (4) and (6) are discretized using a divergence–conforming, mixed-order Nyström discretization [10, 13]. The NMFIE and NEFIE in (5) and (7) are discretized using a scalar Nyström discretization. The tangential test vectors in (4) and (6) are unitary vectors sampled at the mixed-order quadrature points [10]. The normal test vectors in (5) and (7) are sampled at scalar quadrature points.

Near interactions must be computed via local corrections [3,8-10,12]. A mixed-order Legendre polynomial basis with order $p \times (p+1)$ is used to represent the current densities [10,13], and p-th order polynomial complete Legendre bases are used to represent the equivalent charge densities [10]. For self-terms, the last integral on the right-hand-side of (4) and (6) and the first integral on the right-hand-side of (5) and (7) require a singularity extraction. This can be accomplished following the procedures outlined in [8-10]

III. EXTRACTING THE STATIC FIELD

As a post–processing step, it is often necessary to compute near or far scattered fields. For example, the magnetic field is calculated as

$$\vec{H}_1^{scat}(\vec{r}) = \oiint_{S_{1,2}} \nabla G_1(\vec{r},\vec{r}') \times \vec{J}_{1,2}(\vec{r}') ds'$$

$$- j\omega \varepsilon_1 \oiint_{S_{1,2}} \vec{M}_{1,2}(\vec{r}') G_1(\vec{r},\vec{r}') ds' \tag{8}$$

$$- \frac{1}{\mu_1} \oiint_{S_{1,2}} \nabla G_1(\vec{r},\vec{r}') \rho_{m_{1,2}}(\vec{r}') ds'.$$

If the material object is non-magnetic, $\vec{H}_1^{scat}$ will decay in amplitude linearly as $O(\omega)$. It can be shown that the integrals involving $\vec{J}_{1,2}$ and $\rho_{m_{1,2}}$ are large valued, but their difference is very small with amplitude decaying as $O(\omega)$. This results in significant numerical errors due to finite precision.

One way to mitigate this is to extract the static solution from the dynamic solution. To this end, the A-Müller formulation in (4)-(7) can be reduced to the static solution setting $\omega = 0$. For example, the static form of the TMFIE from (4) is expressed as:

$$\mu_{r_1}\eta_0 \vec{T}(\vec{r}) \cdot \vec{H}_{1_0}^{inc} + \mu_{r_2}\eta_0 \vec{T}(\vec{r}) \cdot \vec{H}_{2_0}^{inc} =$$

$$\frac{\mu_{r_1}+\mu_{r_2}}{2}\vec{T}(\vec{r}) \cdot \tilde{\vec{J}}_{1,2_0}(\vec{r}) \times \hat{n}$$

$$-\oiint_{S_{1,2}}\vec{T}(\vec{r}) \cdot \left(\mu_{r_1}\nabla G_{1_0}(\vec{r},\vec{r}') - \mu_{r_2}\nabla G_{2_0}(\vec{r},\vec{r}')\right) \times \tilde{\vec{J}}_{1,2_0}(\vec{r}')ds' \quad (9)$$

$$+\eta_0\oiint_{S_{1,2}}\vec{T}(\vec{r}) \cdot \left(\nabla G_{1_0}(\vec{r},\vec{r}') - \nabla G_{2_0}(\vec{r},\vec{r}')\right)\tilde{\rho}_{m_{1,2_0}}(\vec{r}')ds',$$

where G_{i_0}, $i=1,2$, is the static Green function in the i-th medium:

$$G_{1_0} = G_{2_0} = \frac{1}{4\pi|r-r'|} = G_0, \quad (10)$$

$\vec{H}_{i_0}^{inc}$ is the static excitation magnetic field in the i-th medium, and $\tilde{\vec{J}}_{1,2_0}$ and $\tilde{\rho}_{m_{1,2_0}}$ are the static electric current and magnetic charge densities, respectively. The subscript 0 indicates the static solution. Similarly, the static NMFIE from (5) is expressed as:

$$\mu_{r_1}\eta_0\hat{n}\cdot\vec{H}_{1_0}^{inc} + \mu_{r_2}\eta_0\hat{n}\cdot\vec{H}_{2_0}^{inc} = \eta_0\tilde{\rho}_{m_{1,2_0}}(\vec{r})$$

$$-\oiint_{S_{1,2}}\hat{n}(\vec{r}) \cdot \left(\mu_{r_1}\nabla G_{1_0}(\vec{r},\vec{r}') - \mu_{r_2}\nabla G_{2_0}(\vec{r},\vec{r}')\right) \times \tilde{\vec{J}}_{1,2_0}(\vec{r}')ds'$$

$$+\eta_0\oiint_{S_{1,2}}\hat{n}(\vec{r}) \cdot \left(\nabla G_{1_0}(\vec{r},\vec{r}') - \nabla G_{2_0}(\vec{r},\vec{r}')\right)\tilde{\rho}_{m_{1,2_0}}(\vec{r}')ds'. \quad (11)$$

For non-magnetic materials it is assumed that $\mu_{r1} = \mu_{r2} = 1$, and, (9) and (11) reduce to:

$$\eta_0\vec{T}(\vec{r}) \cdot \vec{H}_{1_0}^{inc} + \eta_0\vec{T}(\vec{r}) \cdot \vec{H}_{2_0}^{inc} = \vec{T}(\vec{r}) \cdot \tilde{\vec{J}}_{1,2_0}(\vec{r}) \times \hat{n}, \quad (12)$$

and

$$\hat{n}\cdot\vec{H}_{1_0}^{inc} + \hat{n}\cdot\vec{H}_{2_0}^{inc} = \tilde{\rho}_{m_{1,2_0}}(\vec{r}). \quad (13)$$

Thus, in the static limit, the tangential and normal magnetic fields are proportional to a superposition of the interior and exterior source fields on the boundary.

A post-processing method is proposed to improve the computation of the scattered magnetic field using a static extraction to (8) to compute the scattered magnetic field:

$$\vec{H}_1^{scat}(\vec{r}) = \oiint_{S_{1,2}}\left(\nabla G_1(\vec{r},\vec{r}') - \nabla G_0(\vec{r},\vec{r}')\right) \times \vec{J}_{1,2}(\vec{r}')ds'$$

$$-\frac{1}{\mu_1}\oiint_{S_{1,2}}\left(\nabla G_1(\vec{r},\vec{r}') - \nabla G_0(\vec{r},\vec{r}')\right)\rho_{m_{1,2}}(\vec{r}')ds'$$

$$-j\omega\varepsilon_1\oiint_{S_{1,2}}\vec{M}_{1,2}(\vec{r}')G_1(\vec{r},\vec{r}')ds'$$

$$+\oiint_{S_{1,2}}\nabla G_0(\vec{r},\vec{r}') \times \vec{J}_{1,2}(\vec{r}')ds'$$

$$-\frac{1}{\mu_1}\oiint_{S_{1,2}}\nabla G_0(\vec{r},\vec{r}')\rho_{m_{1,2}}(\vec{r}')ds'. \quad (14)$$

It is also observed for non-magnetic materials that the static current and charge densities radiate zero fields. That is:

$$\oiint_{S_{1,2}}\nabla G_0(\vec{r},\vec{r}') \times \vec{J}_{1,2_0}(\vec{r}')ds'$$

$$-\frac{1}{\mu_1}\oiint_{S_{1,2}}\nabla G_0(\vec{r},\vec{r}')\rho_{m_{1,2_0}}(\vec{r}')ds' = 0. \quad (15)$$

Subtracting (15) from (14) leads to the expression:

$$\vec{H}_1^{scat}(\vec{r}) = \oiint_{S_{1,2}}\left(\nabla G_1(\vec{r},\vec{r}') - \nabla G_0(\vec{r},\vec{r}')\right) \times \vec{J}_{1,2}(\vec{r}')ds'$$

$$-\frac{1}{\mu_1}\oiint_{S_{1,2}}\left(\nabla G_1(\vec{r},\vec{r}') - \nabla G_0(\vec{r},\vec{r}')\right)\rho_{m_{1,2}}(\vec{r}')ds'$$

$$-j\omega\varepsilon_1\oiint_{S_{1,2}}\vec{M}_{1,2}(\vec{r}')G_1(\vec{r},\vec{r}')ds'$$

$$+\oiint_{S_{1,2}}\nabla G_0(\vec{r},\vec{r}') \times \left(\vec{J}_{1,2}(\vec{r}') - \vec{J}_{1,2_0}(\vec{r}')\right)ds'$$

$$-\frac{1}{\mu_1}\oiint_{S_{1,2}}\nabla G_0(\vec{r},\vec{r}')\left(\rho_{m_{1,2}}(\vec{r}') - \rho_{m_{1,2_0}}(\vec{r}')\right)ds'. \quad (16)$$

This extracted formulation provides a stable numerical form for accurately computing the scattered magnetic field at low frequencies. Duality can be applied to derive a stable numerical method for computing low-frequency electric fields scattered from a magnetic material.

IV. NUMERICAL RESULTS

The proposed A-Müller formulation is evaluated by simulating scattering from a number of objects having different geometries and material properties. In all cases, the incident field is a plane wave traveling in the $-z$ direction with its electric field polarized along the x-direction

A. PEC sphere

Initially, the electromagnetic plane-wave scattering from a one-meter radius dielectric sphere is studied. Figures 1 (a) and (b) demonstrate the root mean square (RMS) error in the scattered electric and magnetic fields calculated by the LCN discretized A-Müller formulation at 1 Hz and 50 MHz, respectively, for a surface mesh of the sphere consisting of 96 sixth-order quadrilateral cells. The errors are plotted versus LCN basis order, p, for different values of the relative permittivity ε_r of the dielectric material. The RMS errors are computed as:

$$\text{RMS Error}(x) = \sqrt{\frac{\sum_{i=1}^{N}\left|x^{\text{AMuller}}(\theta_i) - x^{\text{Mie}}(\theta_i)\right|^2}{\sum_{i=1}^{N}\left|x^{\text{Mie}}(\theta_i)\right|^2}}, \quad (17)$$

where $x^{\text{AMuller}}(\theta_i)$ and $x^{\text{Mie}}(\theta_i)$ refer to the scattered vector electric or magnetic fields computed by A-Müller and the analytical Mie series solution at angles $\theta_i = 0^\circ, 1^\circ, \ldots, 180^\circ$ on a semi-circle with radius 1.5 m in the $\varphi = 0^\circ$ plane. The figures demonstrate high-order convergence of the electric and magnetic fields at 1 Hz and 50 MHz for low to high contrast dielectric spheres. It is noted that the static extraction procedure has been applied to accurately calculate magnetic fields at 1 Hz.

Next, we investigate the performance of the A-Müller in comparison to the conventional Müller for scattering from a one-meter radius dielectric sphere over a wide frequency range from 1.0e-8 Hz to 1 GHz. The relative permittivity of the dielectric sphere is $\varepsilon_r = 2.0$. The surface of the sphere is discretized with 2904 fourth-order quadrilateral cells.

Figures 2 (a) and (b) show the RMS error in the electric and magnetic fields scattered by the dielectric sphere. The fields area computed on a semicircle with radius 1.5 m located at $\varphi = 0^\circ$ using both the A-Müller formulation with and without the static extraction and the Müller formulation for LCN basis orders $p = 0$ and p=1. The data exhibits high errors in the Müller formulation at low frequencies due to catastrophic cancellation in reconstructing the electric and magnetic fields. The A-Müller with static extraction has excellent accuracy over a wide frequency range starting from arbitrarily low frequencies. The errors from Müller and A-Müller start to grow at a threshold frequency around 200 MHz where the number of samples per wavelength is 10.

Fig. 1. RMS error in the near magnetic (H) and electric (E) fields computed via the A-Müller method, (a) at 1 Hz and (b) at 50 MHz on a semicircle with radius 1.5 m located at $\varphi = 0^\circ$.
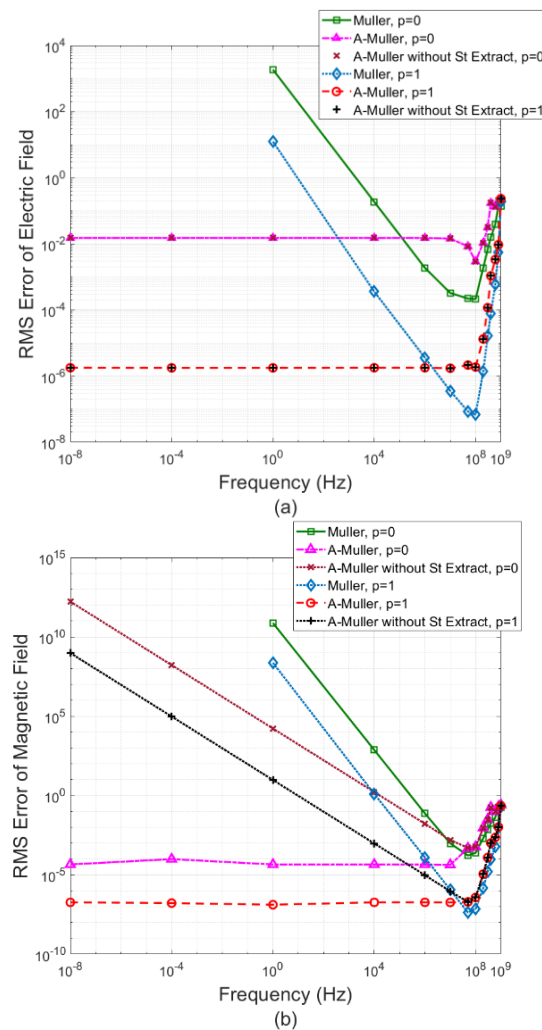
Fig. 2. The RMS error in vector, (a) electric field and (b) magnetic field scattered from a dielectric sphere computed by A-Müller without and with the static extraction (St Extract) and Müller formulations on a semicircle with radius 1.5 m located at $\varphi = 0^\circ$.

Figure 3 plots the condition number of A-Müller and Müller system matrices versus frequency for scattering from the dielectric sphere. The system matrices were pre-conditioned with a left/right iterative diagonal matrix scaling algorithm [14] to eliminate row magnitude disparity. The A-Müller condition number starts oscillating after 400 MHz.

Unlike the Müller and PMCHWT, the VIE provides accurate solutions for exterior scattered electric and magnetic fields at low frequencies. However, one limitation of the VIE is that the condition number of the system matrix at low frequencies grows linearly with increasing material contrast. Figure 4 displays the condition number of the A-Müller and VIE system matrices versus relative permittivity, ε_r, for scattering from a one-meter radius sphere at 1 Hz. The surface of the sphere is meshed with 96 sixth order quadrilateral cells. The LCN basis order is $p = 0$. The figure shows that the condition number of the VIE is increasing linearly with material contrast; however, the condition number of the A-Müller formulation is nearly constant as the relative permittivity increases.
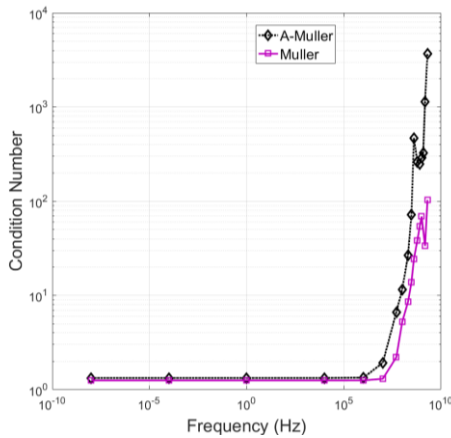
Fig. 3. Condition number of the iteratively scaled A-Müller and Müller system matrices for scattering from the dielectric sphere versus frequency.

B. Dielectric tori

To evaluate the performance of the A-Müller formulation for multiply connected geometries, a nested torus structure consisting of two dielectric tori was simulated. The two torus structure has a z-axis of revolution. The larger torus has a major radius of 1 m and a minor radius of 0.5 m, respectively. The smaller torus has a major radius of 1 mm and a minor radius of 0.5 mm, respectively. The larger and smaller tori surfaces are meshed with quadrilateral cells having average edge lengths, respectively, of 0.2 m and of 0.2 mm for a total of 384 quadratic quadrilateral cells. The dielectric tori both have a relative permittivity $\varepsilon_r = 8.0$.

The LCN basis order is $p = 1$.

Figure 5 demonstrates the radar cross section (RCS) of the two torus structure at 300 MHz computed using A-Müller, Müller, and PMCHWT formulations. The three solutions show excellent agreement. Figures 6 (a) and (b) display the magnitude of the scattered electric and magnetic fields at 1 Hz calculated using A-Müller, Müller, and PMCHWT formulations and using a volume integral equations (VIE) for scattering from the two torus structure. The volume mesh used for the VIE consists of 576 hexahedral cells with an average edge length the same as the applied surface mesh. Very good agreement is observed between the A-Müller and the VIE results. Moreover, the data confirm the low frequency breakdown of the PMCHWT and Müller formulations in reconstructing of the fields at low frequencies.
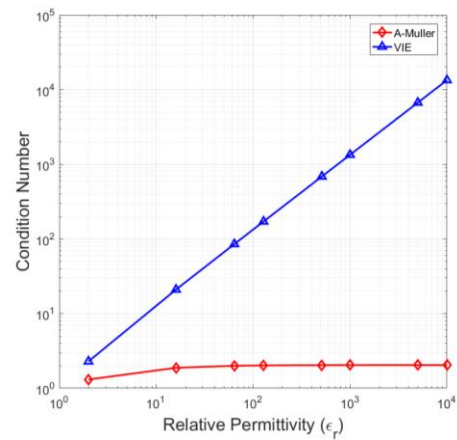
Fig. 4. Condition number of the iteratively scaled A-Müller and VIE system matrices versus relative permittivity, for scattering from a one-meter radius dielectric sphere at 1Hz.
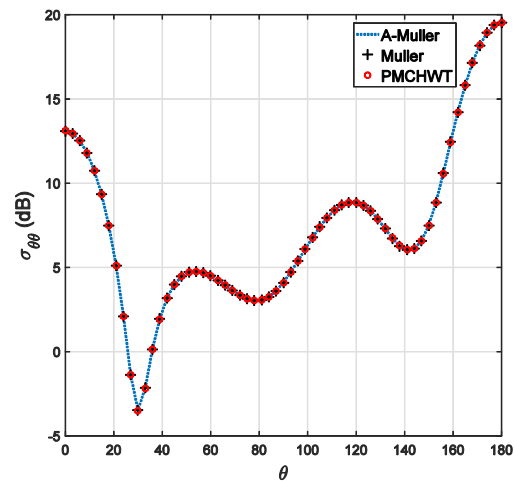
Fig. 5. RCS at 300 MHz for plane wave scattering from the two torus structure.
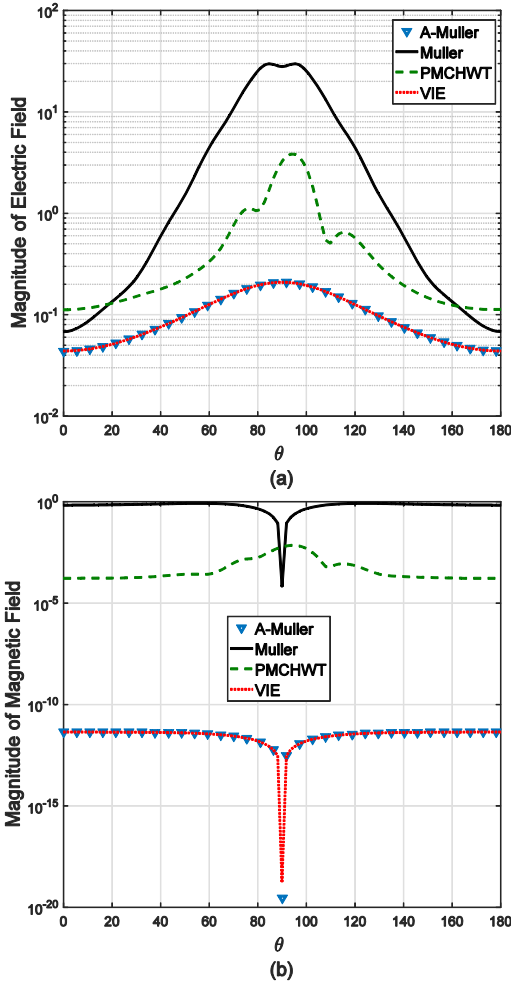
Fig. 6. Scattered (a) electric field and (b) magnetic field at 1 Hz for the two torus structure on a semi-circle with radius 1.5 m at $\varphi = 0°$.

Figures 7 (a) and (b) illustrate the singular values of the A-Müller, Müller, PMCHWT, and VIE system matrices for the two torus configuration at 300 MHz and 1 Hz, respectively. The system matrices are preconditioned using an iterative scaling algorithm [14]. The figures indicate that A-Müller provides a well-conditioned system matrix for multiply connected geometries at both low and high frequencies.

C. Spherical shell of steel

The A-Müller formulation is also compared to a quasi-magnetostatic volume integral equation (VIE) [15] method by simulating the scattering from conducting materials at low frequencies. A spherical shell of steel characterized by electric conductivity $\sigma = 1.37e+6$ S/m and relative permeability $\mu_r = 68.0$. The shell has an inner

radius of 1 cm and outer radius of 3 cm. The mesh cells have an average edge length of 0.35 cm leading to 1160 quadrilateral cells for the A-Müller formulation and 716 hexahedral cells for the VIE.
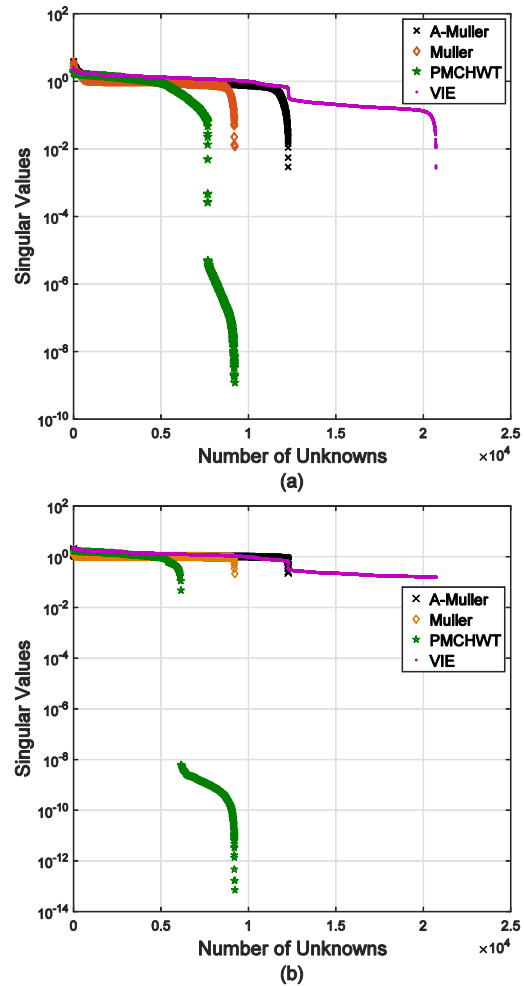
Fig. 7. Singular values of the A-Müller, Müller, PMCHWT, and VIE system matrices for the two torus case at: (a) 300 MHz and at (b) 1Hz.

Figure 8 displays the magnitude of real and imaginary parts of the azimuthal component of the magnetic field (H_φ) scattered from the steel shell computed using the A-Müller formulation and a quasi-magnetostatic VIE at 10 Hz on a semicircle with radius 3.5 cm at $\varphi = 0°$ plane.

The radial and polar (r and θ) components of the magnetic field are not shown since their magnitudes are negligible. Good agreement is observed between the results from the A-Müller formulation and from the quasi-magnetostatic VIE.
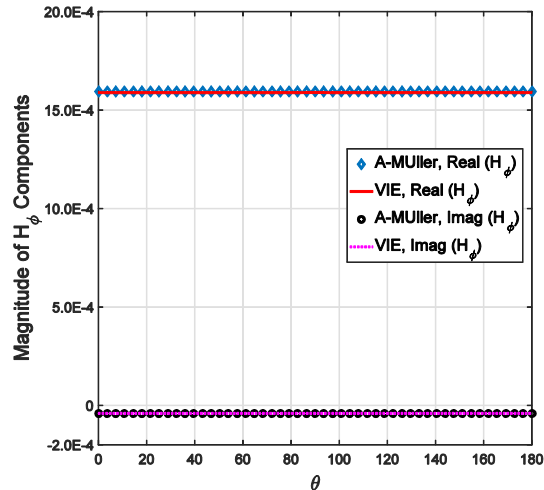
Fig. 8. Magnitude of real and imaginary parts of the azimuthal component of magnetic field scattered from the steel shell computed on a semicircle with radius 3.5 cm at $\varphi = 0°$ plane.

VI. CONCLUSION

In this paper, the LCN discretization of an Augmented-Müller surface integral equation for scattering from material objects was presented. The formulation incorporated surface electric and magnetic charges into the conventional Müller formulation with constraints on the normal magnetic and electric fields on material boundaries. To improve the accuracy of the computation of low-frequency magnetic fields scattered by lossy dielectric structures, a novel static extraction method was introduced. The extraction is applied strictly as a post-processing operation and does not alter the system matrix in any way. Numerical results provided validate that the method is high-order accurate and stable over a broad frequency range from arbitrarily low to high frequencies for simply and multiply connected, lossy, high contrast materials.

ACKNOWLEDGMENT

REFERENCES

[1] F. P. Andriulli, K. Cools, H. Bagci, F. Olyslager, A. Buffa, S. Christiansen, *et al.*, "A multiplicative Calderon preconditioner for the electric field integral equation," *IEEE Transactions on Antennas and Propagation*, vol. 56, pp. 2398-2412, Aug. 2008.

[2] G. Vecchi, "Loop-star decomposition of basis functions in the discretization of the EFIE," *IEEE Transactions on Antennas and Propagation*, vol. 47, pp. 339-346, Feb. 1999.

[3] A. M. Zhu, S. D. Gedney, and J. L. Visher, "A study of combined field formulations for material scattering for a locally corrected Nystrom discretization," *IEEE Transactions on Antennas and Propagation*, vol. 53, pp. 4111-4120, Dec. 2005.

[4] M. Taskinen and P. Yla-Oijala, "Current and charge integral equation formulation," *IEEE Transactions on Antennas and Propagation*, vol. 54, pp. 58-67, Jan. 2006.

[5] T. Xia, H. Gan, M. Wei, W. C. Chew, H. Braunisch, Z. G. Qian, *et al.*, "An integral equation modeling of lossy conductors with the enhanced augmented electric field integral equation," *IEEE Transactions on Antennas and Propagation*, vol. 65, pp. 4181-4190, Aug. 2017.

[6] P. Yla-Oijala and M. Taskinen, "Well-conditioned Muller formulation for electromagnetic scattering by dielectric objects," *IEEE Transactions on Antennas and Propagation*, vol. 53, pp. 3316-3323, Oct. 2005.

[7] R. F. Harrington, "Boundary integral formulations for homogeneous material bodies," *Journal of Electromagnetic Waves and Applications*, vol. 3, pp. 1-15, 1989.

[8] L. F. Canino, J. J. Ottusch, M. A. Stalzer, J. L. Visher, and S. M. Wandzura, "Numerical solution of the Helmholtz equation in 2D and 3D using a high-order Nyström discretization," *Journal of Computational Physics*, vol. 146, pp. 627-663, 1998.

[9] S. D. Gedney, "On deriving a locally corrected Nyström scheme from a quadrature sampled moment method," *IEEE Transactions on Antennas and Propagation*, vol. 51, pp. 2402-2412, Sep. 2003.

[10] S. D. Gedney and J. C. Young, "The locally corrected Nyström method for electromagnetics," in *Computational Electromagnetics: Recent Advances and Engineering Applications*, R. Mittra, Ed., ed New York: Springer, 2013, pp. 149-198.

[11] M. Shafieipour, I. Jeffrey, J. Aronsson, and V. I. Okhmatovski, "On the equivalence of RWG method of moments and the locally corrected Nystrom method for solving the electric field integral equation," *IEEE Transactions on Antennas and Propagation*, vol. 62, pp. 772-782, Feb. 2014.

[12] F. Vico, M. Ferrando-Bataller, A. Valero-Nogueira, and A. Berenguer, "A high-order locally corrected Nystrom scheme for charge-current integral equations," *IEEE Transactions on Antennas and Propagation*, vol. 63, pp. 1678-1685, Apr. 2015.

[13] S. D. Gedney, A. Zhu, and C. C. Lu, "Study of mixed-order basis functions for the locally-corrected Nyström method," *IEEE Transactions on Antennas and Propagation*, vol. 52, pp. 2996-3004,

Nov. 2004.

[14] J. Cheng, R. J. Adams, J. C. Young, and M. A. Khayat, "Augmented EFIE with normally constrained magnetic field and static charge extraction," *IEEE Transactions on Antennas and Propagation*, vol. 63, pp. 4952-4963, Nov. 2015.

[15] J. C. Young and S. D. Gedney, "A locally corrected Nyström formulation for the magnetostatic volume integral equation," *IEEE Transactions on Magnetics*, vol. 47, pp. 2163-2170, Sep. 2011.

Nastaran Hendijani received the B.S. degree in Electrical Engineering from Amirkabir University of Technology (Tehran Polytechnic), Tehran, Iran, in 2003, and the M.S. degree in Electrical Engineering from Iran University of Science and Technology (IUST), Tehran, Iran, in 2006 and the Ph.D. degree in Electrical and Computer Engineering from University of Kentucky, Lexington, KY, in 2015.

From 2009 to 2012, she was a Research Assistant in the Department of Electrical and Computer Engineering at Virginia Polytechnic Institute and State University (Virginia Tech). From 2012 to 2015, she was a Research Assistant in the Department of Electrical and Computer Engineering at the University of Kentucky. Since 2015 she has been a Post-doctoral Researcher in the Department of Electrical and Computer Engineering at the University of Colorado, Denver, CO. Her research interests are in applied and computational electromagnetics, high-performance computing, and radio frequency identification.

Stephen D. Gedney received the B.Eng.-Honors degree from McGill University, in 1985, and the M.S. and Ph.D. degrees in Electrical Engineering from the University of Illinois, Urbana-Champaign, IL, in 1987 and 1991, respectively.

He is currently the Chair and the Don and Karen White Professor of the Electrical Engineering Department at the University of Colorado Denver (UCD). Previously he was a Professor of Electrical Engineering at the University of Kentucky from 1991–2014. He worked for the U.S. Army Corps of Engineers, Champaign, IL ('85-'87). He was a Visiting Professor at the Jet Propulsion Laboratory, (92',93'), HRL Laboratories ('96-'97) and Alpha Omega Electromagnetics ('04-'05). He received the Tau Beta Pi Outstanding Teacher Award in 1995 and 2013. He is a Fellow of the IEEE and Member of Tau Beta Pi.

John C. Young received the B.E.E. degree in Electrical Engineering from Auburn University in 1997, the M.S. degree in Electrical Engineering from Clemson University in 2000, and the Ph.D. degree in Electrical Engineering also from Clemson University in 2002. He received a National Science Foundation Graduate Fellowship in 1998 and served as a Graduate Research Assistant at Clemson University from 1997 to 2002. He is currently an Assistant Professor in the Department of Electrical and Computer Engineering at the University of Kentucky, Lexington, KY. He is a Senior Member of IEEE and a Member of URSI Commission B, Tau Beta Pi, and Eta Kappa Nu.

Robert J. Adams received the B.S. degree from Michigan Technological University, Houghton, MI, USA, in 1993, and the M.S. and Ph.D. degrees in Electrical Engineering from Virginia Tech, Blacksburg, VA, USA, in 1995 and 1998, respectively. From 1999 to 2000, he was a Research Assistant Professor with Virginia Tech. He is currently a Professor with the Department of Electrical and Computer Engineering, University of Kentucky, Lexington, KY, USA. His current research interests include applied and computational electromagnetics.

Provably Stable Local Application of Crank-Nicolson Time Integration to the FDTD Method with Nonuniform Gridding and Subgridding

A. Van Londersele, D. De Zutter, and D. Vande Ginste

Department of Information Technology (INTEC)
Electromagnetics (EM) Group
Ghent University/imec/IDLab, Belgium
arne.vanlondersele@ugent.be, daniel.dezutter@ugent.be, dries.vandeginste@ugent.be

Abstract—This contribution removes some doubts about the stability issues associated with the local and anisotropic use of Crank-Nicolson (CN) time integration in Finite-Difference Time-Domain (FDTD) simulations with spatial irregularities such as nonuniformity and subgridding.

I. INTRODUCTION

To tackle the present-day multiscale electromagnetic problems, Finite-Difference Time-Domain (FDTD) solvers must provide a minimum degree of spatial flexibility, which is typically offered by nonuniform gridding and subgridding techniques. Both techniques allow varying cell sizes that are needed to efficiently resolve the multiscale geometry, but the former preserves the overall tensor-product structure of the grid, whereas the latter supports edge termination as to yield nested tensor-product grids. Although subgridding definitely uses less memory, the more intricate memory organization can cause it to be actually less efficient than nonuniform grids in terms of CPU time depending on the type of problem. Apart from reducing the number of spatial samples, the FDTD algorithm can be further optimized by reducing the number of time samples. However, the time step cannot exceed a certain stability upper bound, better known as the Courant limit, which is proportional to the smallest cell size occurring inside the grid. Conventional subgridding techniques typically assign a local time step, matching the local stability constraint, to each subgrid. This approach virtually always suffers from late-time instability and, although being explicit, the high number of iterations inside each subgrid can be less efficient than applying a (partially) implicit method, such as the Crank-Nicolson (CN) scheme and its Hybrid Implicit-Explicit (HIE) derivatives. Despite some interesting research on this topic, e.g., [1,2], no rigorous stability analysis has been proposed, until the recent publishing of [3], where the local and anisotropic application of CN, Newmark-beta and leapfrog alternating-direction implicit (ADI) schemes to nonuniform grids are thoroughly discussed in terms of stability. Here, we first summarize the key findings of [3] and then extend the stability analysis to a very general class of subgridding schemes with so-called symmetric coupling.

II. NONUNIFORM GRIDDING

With the notations copied from [3, eqns. (2)-(15)], the hybrid explicit-leapfrog implicit-CN FDTD update equation for a general lossless inhomogeneous medium discretized on a nonuniform tensor-product grid is,

$$
\begin{bmatrix} \frac{1}{\Delta t} D_\varepsilon & -\frac{1}{2}(I+\mathcal{P})\hat{\mathcal{V}}\mathcal{C}\hat{\mathcal{W}} \\ \frac{1}{2}\mathcal{V}\mathcal{C}^T\mathcal{W}(I-\mathcal{P}) & \frac{1}{\Delta t} D_\mu \end{bmatrix} x\big|^{n+1} =
$$
$$
\begin{bmatrix} \frac{1}{\Delta t} D_\varepsilon & \frac{1}{2}(I-\mathcal{P})\hat{\mathcal{V}}\mathcal{C}\hat{\mathcal{W}} \\ -\frac{1}{2}\mathcal{V}\mathcal{C}^T\mathcal{W}(I+\mathcal{P}) & \frac{1}{\Delta t} D_\mu \end{bmatrix} x\big|^{n} + s\big|^{n} , \quad (1)
$$

with s the source vector and x the field vector,

$$
x\big|^{n} = \begin{bmatrix} \mathcal{P}\, e(n\,\Delta t) + (I-\mathcal{P})\, e((n-0.5)\,\Delta t) \\ h((n-0.5)\Delta t) \end{bmatrix} , \quad (2)
$$

and $\mathcal{P}$ the diagonal matrix with elements,

$$
[\mathcal{P}]_{i,i} = \begin{cases} 1 & \text{if } e_i \text{ is updated explicitly} \\ 0 & \text{if } e_i \text{ is updated implicitly} \end{cases} . \quad (3)
$$

The FDTD system is exponentially stable if the poles of the z-domain transfer matrix are not located outside the unit disk. Besides, it is also polynomially stable if the repeated poles on the unit circle have linearly independent eigenvectors. An appropriate change of basis shows that the inverse of the transfer matrix belonging to (1) is algebraically similar to,

$$
T(z) = \begin{bmatrix} (z-1)I & -z\,\mathcal{I}_2\,\tilde{\mathcal{C}} \\ \tilde{\mathcal{C}}^T\mathcal{I}_1 & (z-1)I \end{bmatrix} , \quad (4)
$$

with *implicitization operators*,

$$
[\mathcal{I}_1]_{i,i} = \begin{cases} 2 & \text{if } e_i \text{ is updated explicitly} \\ z+1 & \text{if } e_i \text{ is updated implicitly} \end{cases} , \quad (5)
$$

$$
[\mathcal{I}_2]_{i,i} = \begin{cases} 2 & \text{if } e_i \text{ is updated explicitly} \\ 1+z^{-1} & \text{if } e_i \text{ is updated implicitly} \end{cases} , \quad (6)
$$

and modifield curl,

$$
\tilde{\mathcal{C}} = \frac{\Delta t}{2}\left(D_\varepsilon^{-1}\hat{\mathcal{V}}\mathcal{W}\right)^{1/2}\mathcal{C}\left(D_\mu^{-1}\mathcal{V}\hat{\mathcal{W}}\right)^{1/2} . \quad (7)
$$

Hence, the FDTD system is exponentially stable if the roots of the characteristic equation $\det(T(z)) = 0$ satisfy $|z| \leq 1$. A

separate treatment of static and dynamic modes together with a partitioned-matrix rule translates the characterstic equation to,

$$\det\left(z^{-1}(z-1)^2 I_{n_h} + \tilde{\mathcal{C}}^T \mathcal{I}_1 \mathcal{I}_2 \tilde{\mathcal{C}}\right) = 0 . \tag{8}$$

Substitution of $z = (\zeta - 1)/(\zeta + 1)$ allows to interpret (8) as a linear eigenvalue problem. More specifically,

$$\zeta^2 \tilde{\mathcal{C}}^T \tilde{\mathcal{C}} v = \left(\tilde{\mathcal{C}}^T \mathcal{P} \tilde{\mathcal{C}} - I_{n_h}\right) v . \tag{9}$$

Left-multiplying (9) by the hermitian transpose of v and subsequently subtracting/adding the hermitian-transposed equation, yields respectively,

$$\mathrm{Im}(\zeta^2) \, \|\tilde{\mathcal{C}} v\|_2^2 = 0 , \tag{10}$$

$$\mathrm{Re}(\zeta^2) \, \|\tilde{\mathcal{C}} v\|_2^2 = \|\mathcal{P} \tilde{\mathcal{C}} v\|_2^2 - \|v\|_2^2 . \tag{11}$$

As (10) and (11) should hold for any non-zero vector v, the condition $|z| \leq 1$, which is equivalent to $\mathrm{Re}(\zeta) \geq 0$, is satisfied if and only if $\mathrm{Re}(\zeta^2) \leq 0$. A more careful analysis shows that this can only occur for ζ lying on the imaginary axis. In other words, the FDTD system has been proven to be stable if $\mathrm{Re}(\zeta^2) \leq 0$, which upon inspection of (11) yields,

$$\|\mathcal{P} \tilde{\mathcal{C}}\|_2 = \max_{v \neq 0} \frac{\|\mathcal{P} \tilde{\mathcal{C}} v\|_2}{\|v\|_2} \leq 1 . \tag{12}$$

As shown in [3], the limit on Δt imposed by (12) is exact, i.e., it is no overestimation. To avoid polynomial growth the strict inequality should hold. It is clear from (12), that the operator $\mathcal{P}$ can be tuned as to eliminate the smallest cell sizes from the stability limit at the cost of implicit CN computations.

III. SUBGRIDDING

Consider a nonuniform coarse grid that is locally overlapped by a nonuniform subgrid, whose outer edges coincide with coarse primary edges. If the overlapped coarse part would be filled with perfect magnetic conductors, which cannot reduce the time step limit for trivial reasons, the resulting scheme is equivalent to a conventional grid stitching scheme without overlap. Hence, stability with overlap is a sufficient condition for stability without overlap. This insight allows us to detach coarse curl $\mathcal{C}_{\mathrm{c}}$, fine curl $\mathcal{C}_{\mathrm{f}}$ and coupling operator $\mathcal{S}$ from each other, such that, for the subgridding scheme with overlap, (4) translates to,

$$T(z) = \begin{bmatrix} (z-1)I & -2z\,\tilde{\mathcal{C}}_{\mathrm{c}} & & -z\,\mathcal{I}_{2,\mathrm{s}}\,\tilde{\mathcal{S}} \\ 2\tilde{\mathcal{C}}_{\mathrm{c}}^T & (z-1)I & & \\ & & (z-1)I & -z\,\mathcal{I}_{2,\mathrm{f}}\,\tilde{\mathcal{C}}_{\mathrm{f}} \\ \mathcal{N}\,\tilde{\mathcal{S}}^T \mathcal{I}_{1,\mathrm{s}} & & \tilde{\mathcal{C}}_{\mathrm{f}}^T \mathcal{I}_{1,\mathrm{f}} & (z-1)I \end{bmatrix} , \tag{13}$$

where implicitization operators of the form (5)–(6) were added to the subgrid and the coupling. Here, the modified operators are defined as

$$\tilde{\mathcal{C}}_{\mathrm{c}} = \frac{\Delta t}{2} \left(D_{\varepsilon,\mathrm{c}}^{-1} \hat{\mathcal{V}}_{\mathrm{c}} \mathcal{W}_{\mathrm{c}}\right)^{1/2} \mathcal{C}_{\mathrm{c}} \left(D_{\mu,\mathrm{c}}^{-1} \mathcal{V}_{\mathrm{c}} \hat{\mathcal{W}}_{\mathrm{c}}\right)^{1/2} , \tag{14}$$

$$\tilde{\mathcal{C}}_{\mathrm{f}} = \frac{\Delta t}{2} \left(D_{\varepsilon,\mathrm{f}}^{-1} \hat{\mathcal{V}}_{\mathrm{f}} \mathcal{W}_{\mathrm{f}}\right)^{1/2} \mathcal{C}_{\mathrm{f}} \left(D_{\mu,\mathrm{f}}^{-1} \mathcal{V}_{\mathrm{f}} \hat{\mathcal{W}}_{\mathrm{f}}\right)^{1/2} , \tag{15}$$

$$\tilde{\mathcal{S}} = \frac{\Delta t}{2} \left(D_{\varepsilon,\mathrm{c}}^{-1} \hat{\mathcal{V}}_{\mathrm{c}} \mathcal{W}_{\mathrm{c}}\right)^{1/2} \mathcal{S} \left(D_{\mu,\mathrm{f}}^{-1} \mathcal{V}_{\mathrm{f}} \hat{\mathcal{W}}_{\mathrm{f}} \mathcal{N}\right)^{1/2} . \tag{16}$$

The construction of (13) requires the coarse-to-fine coupling operator to be the transposed and row-normalized counterpart of the fine-to-coarse coupling operator. The diagonal operator $\mathcal{N}$ represents this normalization factor. Following the same procedure as for the nonuniform gridding, we end up with a quadratic eigenvalue problem $(\zeta^2 A + \zeta B + C) v = 0$, with

$$A = A^T = \begin{bmatrix} \tilde{\mathcal{C}}_{\mathrm{c}} \tilde{\mathcal{C}}_{\mathrm{c}}^T & 0 \\ 0 & \tilde{\mathcal{C}}_{\mathrm{f}}^T \tilde{\mathcal{C}}_{\mathrm{f}} \end{bmatrix} , \tag{17}$$

$$B = -B^T = \begin{bmatrix} 0 & -\tilde{\mathcal{S}} \\ \tilde{\mathcal{S}}^T & 0 \end{bmatrix} , \tag{18}$$

$$C = \begin{bmatrix} I - \tilde{\mathcal{C}}_{\mathrm{c}} \tilde{\mathcal{C}}_{\mathrm{c}}^T & \mathcal{P}_{\mathrm{s}} \tilde{\mathcal{S}} \\ \tilde{\mathcal{S}}^T \mathcal{P}_{\mathrm{s}} & I - \mathcal{N}^{-1/2} \tilde{\mathcal{C}}_{\mathrm{f}}^T \mathcal{P}_{\mathrm{f}} \tilde{\mathcal{C}}_{\mathrm{f}} \mathcal{N}^{1/2} \end{bmatrix} . \tag{19}$$

Note that $C = C^T$ if $\mathcal{P}_{\mathrm{f}} = 0$, i.e., a fully implicit subgrid, or if $\mathcal{N}$ is a scalar multiple of the identity matrix, i.e., a uniform subgrid. Assuming that the subgrid is either uniform or fully implicit, a quadratic eigenvalue problem with this particular symmetry and with $A \succeq 0$ has roots ζ in the right half-plane if and only if $C \succeq 0$ or, equivalently, if $\lambda_{\max}(I - C) \leq 1$. Separating on- from off-diagonal blocks by means of the triangle inequality yields,

$$\max\left(\|\tilde{\mathcal{C}}_{\mathrm{c}}\|_2^2 , \, \|\mathcal{P}_{\mathrm{f}} \tilde{\mathcal{C}}_{\mathrm{f}}\|_2^2 \right) + \|\mathcal{P}_{\mathrm{s}} \tilde{\mathcal{S}}\|_2^2 \leq 1 . \tag{20}$$

For fully implicit subgrid and coupling updates, the coarse-grid Courant limit is retrieved, as expected.

IV. CONCLUSION

The exact time step limit is provided for nonuniform grids with local and anistropic application of CN time integration. A similar limit, albeit an overestimation, is shown to exist for general symmetric subgridding schemes. The concept of a z-domain implicitization operator in combination with the bilinear transformation can be extended to other stability proofs. A spatial analog may be used to find the stability condition for the hybrid staggered-collocated methods proposed in [4]–[6].

REFERENCES

[1] Z. Huang, G. G. Pan, and K. S. Chen, "A synchronized multigrid time domain method via Huygens subgridding and implicit algorithms," *IEEE Transactions on Antennas and Propagation*, vol. 61, no. 5, pp. 2605–2614, May 2013.

[2] M. R. Cabello, L. D. Angulo, J. Alvarez, I. D. Flintoft, S. Bourke, J. F. Dawson, R. G. Martn, and S. G. Garcia, "A hybrid Crank-Nicolson FDTD subgridding boundary condition for lossy thin-layer modeling," *IEEE Transactions on Microwave Theory and Techniques*, vol. 65, no. 5, pp. 1397–1406, May 2017.

[3] A. Van Londersele, D. De Zutter, and D. Vande Ginste, "An in-depth stability analysis of nonuniform FDTD combined with novel local implicitization techniques," *Journal of Computational Physics*, vol. 342, no. Supplement C, pp. 177–193, 2017.

[4] ——, "A new hybrid implicit-explicit FDTD method for local subgridding in multiscale 2-D TE scattering problems," *IEEE Transactions on Antennas and Propagation*, vol. 64, no. 8, pp. 3509–3520, Aug. 2016.

[5] ——, "A collocated 3-D HIE-FDTD scheme with PML," *IEEE Microwave and Wireless Components Letters*, vol. 27, no. 7, pp. 609–611, July 2017.

[6] ——, "Full-wave analysis of the shielding effectiveness of thin graphene sheets with the 3D unidirectionally collocated HIE-FDTD method," *International Journal of Antennas and Propagation*, vol. 2017, pp. Article ID 5 860 854, 8 pages, July 2017.

FEKO™ Modeling Study of Passive UHF RFID Tags Embedded in Pavement

Sourabh R. Walvekar and Robert J. Burkholder

The Ohio State University ElectroScience Lab
Dept. of Electrical and Computer Engineering
Columbus, U. S. A.
sourabh.w@somaiya.edu, burkholder.1@osu.edu

Abstract—Radio frequency identification (RFID) is investigated as a technology that may be useful for smart cars and autonomous vehicles to read information about local road conditions and geographic location. Passive UHF RFID tags can transmit this data wirelessly to an RFID reader mounted on the vehicle. Coupling between a tag that is on or embedded in pavement, and the reader antenna mounted on the vehicles, is investigated by simulating the tag antenna, reader antenna and local environment in FEKO™. Preliminary simulation results show that it is feasible to implement such a system such that a vehicle traveling up to 200 km/hr. can read the tags as it passes over them.

Keywords—Antennas, autonomous cars, navigation, propagation, RFID.

I. INTRODUCTION

We are close to the days when our cars will become completely autonomous and will not require human input for navigation. GPS is used to get geographical co-ordinates of the current location, and is the primary navigational guidance system for autonomous or self-driving cars, aided by local visual cues and vehicular radar. However, it is difficult to receive GPS signals in tunnels or in "urban canyons" surrounded by high-rises and construction [1]. The vehicle not knowing its precise geographical location and direction of travel for a brief moment of time can be dangerous. During these times RFID tags embedded into the road can provide the vehicle with specific data about the location [2]. Another problem autonomous cars have to deal with is the presence of temporary construction sites on roads. Signs are sufficient for a human driver to take a different path to avoid the area, but may not be sufficient for autonomous cars to make a navigation decision. Even though these cars can recognize road signs using various sensors, any distortion of the signs caused by weather, wear-and-tear, tampering, etc., can put these cars into confusion. Human intervention is still required to maneuver the car in such situations.

Existing RFID technology can help vehicles obtain more information about the local environment. RFID tags can be embedded on the surface of the road or under the first layer of pavement, and the vehicles passing above them with an RFID reader can interrogate the tags and download the information embedded on the tag or associated with the tag ID number. Certain information can be stored directly in the RFID tag's chip, but as discussed in [1], if this is not enough

we can rely on a database system where the data can be retrieved via cellular communication from a database which will have a list of tag IDs and their corresponding data. The advantage of this system is that the data may be updated as road conditions or construction areas change.

The two key issues to be investigated to make a passive UHF RFID system for roads feasible are: 1) read range, and 2) time to read the tag. RFID chips take time to communicate with the reader and this puts a constraint on the speed of the vehicle trying to read the information from the tag. The read range is important because a longer read range means the reader will have more time to communicate with a given tag. These two interdependent issues are investigated here using Altair's FEKO™ computational electromagnetics simulation software.

Section II describes the simulation setup and assumptions made, including information on the reader antenna, the tag antenna, their orientation, and the electrical characteristics of the materials used for simulating the pavement. Section III presents the results obtained from the simulation study and Section IV discusses conclusions on the feasibility of and RFID road system. It also discusses the limitations of the current simulations and proposes future work for improving the simulations and implementation of the system.

II. SIMULATION SETUP

Fig. 1 shows the geometry of a linearly polarized rectangular patch antenna for 915 MHz used as the reader antenna. It is excited by a wire port in FEKO. Most commercially available UHF passive RFID tag antennas have a dipole-like structure and a dipole like gain pattern, hence a small wire dipole antenna matched at 915 MHz is used in the simulations to represent an RFID tag. A single layer 22 cm thick dielectric is used to model the road. Concrete and asphalt roads are chosen for the simulations. The concrete is chosen from the media library of FEKO. The electrical characteristics of asphalt are chosen as follows: permittivity = 6, conductivity = 10^{-4} S/m, and mass density = 2322 kg/m^3 [3]. These parameters represent dry asphalt. The reader antenna facing downward is kept 35 cm above the road. Simulations were performed for tags on the surface and embedded 3 cm into the road. The dipole antenna is oriented to match the polarization of the patch antenna (X-polarized in Fig. 1). Each antenna has a port assigned. The patch

antenna is the active port with 1 W of radiated power.
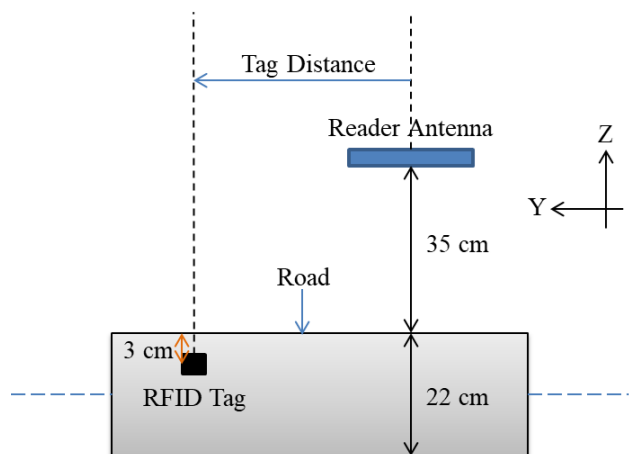
Fig. 1. Side view of the simulation setup. The pavement is infinite in the X and Y directions. The RFID tag antenna and reader antenna are linearly polarized in the X direction.

III. RESULTS

For successful communication between the tag and the reader, a certain amount of RF power must be delivered to the passive RFID tag by the reader antenna. The threshold power for activating the chip is usually specified in the data sheet. For the Impinj Monza 2 RFID chip it is -11.5 dBm (decibels relative to a mW). 1 W of power is fed into the reader antenna, hence the S_{21} between the two ports of the antennas, the wire dipole and the patch antenna, tells us the amount of power received by the wire dipole representing the RFID tag. It is noted that normally the tag antenna is matched to the impedance of the RFID chip, but that is not necessary for the power transfer computations presented here. The tag is moved horizontally away from the reader antenna along the Y-axis in steps of 10 cm. The corresponding S_{21} is computed. The distance where the power reaching the tag falls below the -11.5 dBm threshold is important because this is where the chip will not be activated. Multiplying this distance by two (symmetry on both sides of the Z-axis) gives us the total length of the zone over which the reader can successfully communicate with the tag (because in this zone it is able to deliver sufficient power to the chip for communication). The power delivered to the tag as a function of the Y-distance is plotted in Fig. 2.

According to Chon et al. [1], for successful communication between a tag and a reader, 18 ms are required for transferring 128 bits of data (such as the tag ID number). So the tag and the reader have to be in communication range for at least 18 ms. If we consider a vehicle travelling at 200 km/hr., then in 18 ms it travels 1 m. So the range over which the reader transfers threshold power to the tag should be at least 1 m. We can calculate the communication range for each scenario plotted in Fig. 2 by multiplying by two the distance where the power reaching the tag goes below -11.5 dBm. For example, the communication zone for a tag embedded 3 cm below the concrete pavement is 2 times 50.76, or 101.52 cm. Since this is more than 1 m, all the vehicles travelling at speeds up to 200 km/hr. should be able to successfully communicate with the tags on the road. The communication ranges for the other cases are higher than the one we considered above since the threshold power reaching the tag goes below -11.5

dBm over a greater distance than 50.76 cm. Hence, vehicles travelling at speeds up to 200 km/hr. will certainly be able to communicate with the tags embedded in the roads under the assumed conditions.
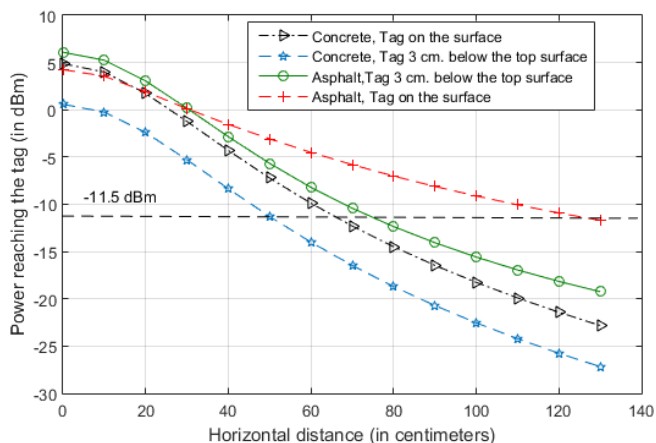
Fig. 2. Power received by the tag antenna as a function of the horizontal distance from the reader antenna for tags on or inside concrete and asphalt pavement. The threshold power of -11.5 dBm is required to activate the RFID chip.

IV. CONCLUSION

Preliminary simulations show that implementing a passive UHF RFID system for concrete or dry asphalt pavement is feasible. The vehicle will not always travel directly over the tag, so more than one reader antenna should be used to make sure that the reader doesn't miss any. Multiple reader antennas are typically connected to a single reader to provide spatial diversity in UHF RFID systems. Placement of these extra antennas will be investigated in the future, as well as various positions and orientations of the tags on the roads. Most importantly, rain, ice and snow will most certainly affect the communication range of the tag and the reader. Therefore, these conditions should be carefully studied in future simulations and experiments.

REFERENCES

[1] H. Chon, S. Jun, H. Jung, and S. An, "Using RFID for accurate positioning," Journal of Global Positioning Systems, vol. 3, no. 1-2, pp. 32-39, 2004.

[2] T. Jing, X. Wei, W. Cheng, M. Guan, L. Ma, Y. Huo, and X. Cheng, "An efficient scheme for tag information update in RFID systems on roads," IEEE Transactions on Vehicular Technology, vol. 65, no. 4, pp. 2435-2444, 2016.

[3] O. Franek, P. Kyritsi, and G. F. Pedersen, "RFID on the road – some considerations about passive tag antennas," in Proc. 5th EuCAP, Rome, Italy, pp. 1203-1207, Apr. 2011.

High-Order Moment-Matching MOR with Impedance Boundaries for Signal Integrity Analysis

Matthew B. Stephanson

ANSYS, Inc., San Jose, California
matt.stephanson@ansys.com

Abstract—This paper presents an extension of high-order moment-matching model order reduction to frequency-dependent impedance boundary conditions. Such boundary conditions are essential for accurately and efficiently modeling conductors at high frequency, where skin effect is significant. These boundary conditions involve complicated transcendental functions, whereas previous MOR methods assume polynomial dependence. Automatic differentiation is used to easily and accurately calculate the higher derivatives of such functions. Substantial improvement is shown, not only compared to discrete frequency sweeps, but also compared to non-moment-matching S matrix interpolation.

I. INTRODUCTION

Model order reduction (MOR) is a frequently-used technique to develop efficient approximations to discretizations of Maxwell's equations that depend on one or more parameters (e.g., frequency or material properties). Although there are many methods to accomplish this, they can broadly be classified according to how well the reduced-order solution matches the full-order solution (order) and how many points in parameter space the two solutions match (single- vs. multi-point). High-order methods, in which not only the value but also the derivatives of the solutions are equal, can be efficient for systems with smooth parameter dependence because the incremental cost of each order is a matrix forward-backward substitution, rather than a factorization [1]. The disadvantage is that the derivatives of the system matrix with respect to the parameters must be known.

For signal integrity (SI) analysis of electronic packages and circuit boards, this presents a problem. Modeling of high-speed interconnects requires analysis up to tens of gigahertz, where losses from skin effect significantly affect performance. One approach to capture this effect is to model the volume inside the conductors with a mesh fine enough to resolve the decaying field. The system matrix entries are then second-order polynomials of frequency and the derivatives are easily calculated. Alternatively, an impedance boundary condition (IBC) can be used, but the matrix entries are no longer polynomials.

This work shows that the accuracy of an IBC can be achieved with the ease-of-implementation of a polynomial formulation by using automatic differentiation to calculate the higher-order derivatives of the surface impedance. This is a method for transforming the computer code of a function so that it not only calculates the value of the function, but also the derivatives with respect to the inputs. In contrast to finite difference methods, there is no discretization error, only round-off error. There are also advantages compared to symbolic differentiation, e.g., it is unnecessary to translate the computer code into a single mathematical expression.

The resulting method has several advantages for network analysis compared to S matrix interpolation. First, the use of higher-order moment-matching allows the same accuracy and bandwidth to be achieved with fewer matrix factorizations. Second, the reduced-order model automatically inherits several desirable properties form the original system, including passivity and stability [2]. Third, although not pursued here, knowledge of the S parameter's exact derivatives could be used to provide better error control choosing the moment-matching points adaptively.

II. BACKGROUND

A. Finite element modeling of SI problems

The finite element method is used to discretize Maxwell's equations, as applied to the problem geometry. For non-dispersive materials and ohmic conductors, this results in a matrix equation of the form:

$$A(s)\mathbf{E} = (S + sY + s^2 M)\mathbf{E} = \mathbf{J}(s), \tag{1}$$

where $s = j\omega$ is the complex frequency, and $\mathbf{J}$ and $\mathbf{E}$ are the current excitation and electric field solution vectors. The matrices S, Y, and M are the stiffness, admittance, and mass matrices, and depend, respectively, on the materials' permeability μ, conductivity σ, and permittivity ε. Inside good conductors, the fields decay exponentially on a length scale given by the skin depth $\delta = \sqrt{2/\omega\mu\sigma}$ (e.g., about $0.3\,\mu\text{m}$ for copper at $40\,\text{GHz}$). With trace cross sections on the order of tens of microns or more, this requires an extremely dense mesh to accurately resolve.

Because the traces and ground planes are typically wide compared to their thickness, it is common to model them with a layered media impedance boundary [3]. For a single layer, this has the form:

$$Z_{IBC} = Z_0 \frac{1 + \Gamma e^{-2\gamma T}}{1 - \Gamma e^{-2\gamma T}}, \tag{2}$$

where $Z_0 = \sqrt{\mu/\varepsilon}$ is the intrinsic impedance, Γ is the reflection coefficient from the surrounding dielectric, $\gamma = j\omega\sqrt{\varepsilon\mu}$ is the propagation constant, and T is the metal thickness. For

good conductors, $\Gamma \approx 1$, $\gamma \approx (1 + j)/\delta$, and $Z_0 \approx \gamma/\sigma$, leading to a rather complicated expression for Z_{IBC}. It is this expression (actually, its inverse) that the matrix entries now depend on and which must be differentiated for moment-matching.

B. Projection-based model order reduction

A projection-based reduced order model is obtained by Galerkin-testing the $N \times N$ system matrix A with the $N \times M$ reduced-order basis vectors V:

$$\widehat{A}(s) = V^H A(s) V. \tag{3}$$

The reduced-order matrix equation is then:

$$\widehat{A}(s)\widehat{\mathbf{E}} = V^H \mathbf{J}, \tag{4}$$
$$\mathbf{E} \approx V\widehat{\mathbf{E}}. \tag{5}$$

Because $M \ll N$, this equation can be solved much more rapidly than the original. In order for $\widehat{\mathbf{E}}$ and $\mathbf{E}$ to match up to the p-th order at frequency s_0, it can be shown that it is sufficient that the column space of V equal $\mathrm{span}\big(\mathbf{E}|_{s_0}, \mathbf{E}'|_{s_0}, \ldots, \mathbf{E}^{(p)}|_{s_0}\big)$ [4]. Applying the Leibnitz product rule to $A\mathbf{E} = \mathbf{J}$ shows that these are given by:

$$\mathbf{E}^{(p)} = A^{-1}\left[\mathbf{J}^{(p)} - \sum_{k=1}^{p}\binom{p}{k}A^{(k)}\mathbf{E}^{(p-k)}\right]. \tag{6}$$

C. Automatic differentiation

Automatic differentiation consists of analyzing each line of code that involves a dependent variable, for example Z_{IBC}, and augmenting it with a line that calculates the derivative with respect to the independent variable (frequency) as well [5]. Thus, for example, calculation of δ would include:

$$\delta'(f) = \left(\frac{1}{f\pi\mu\sigma}\right)^{-1/2} \cdot \frac{-1}{f^2\pi\mu\sigma}. \tag{7}$$

The power of automatic differentiation is that this augmentation can be done automatically, either by source code translation or operator overloading. Furthermore, the process can be applied recursively to obtain arbitrarily high orders.

To see how this can be accomplished, consider first the simplest case, computing only the first derivative. Using the overloading approach, this means that every value u that depends on frequency is replaced by a class that contains both the value and its derivative with respect to frequency: $\langle u, u' \rangle$. Then, the basic mathematical operators are overloaded to use this new class. For example, multiplication and the exponential function become:

$$\langle u, u' \rangle \times \langle v, v' \rangle = \langle uv, uv' + u'v \rangle, \tag{8}$$
$$\exp\langle u, u' \rangle = \langle \exp u, u' \exp u \rangle. \tag{9}$$

To extend this to higher orders, the derivatives themselves can be treated as value were above, up to some maximum order, and the rules applied recursively. This can be illustrated

by working out the exponential function up to second order and verifying that it indeed gives the correct result:

$$\begin{aligned}\exp\langle u, u', u'' \rangle &= \langle \exp u, \langle u', u'' \rangle \times \exp\langle u, u' \rangle\rangle \\ &= \langle \exp u, \langle u', u'' \rangle \times \langle \exp u, u' \exp u \rangle\rangle \quad (10) \\ &= \langle \exp u, u' \exp u, [(u')^2 + u'']\exp u \rangle.\end{aligned}$$

In general, when applying a unary function f to a value and its n first derivatives, the chain rule provides:

$$\begin{aligned}f&\langle u, u^{(1)}, u^{(2)}, \ldots, u^{(n)}\rangle \\ &= \Big\langle f(u), f'\langle u, \ldots, u^{(n-1)}\rangle \times \langle u^{(1)}, \ldots, u^{(n)}\rangle\Big\rangle. \quad (11)\end{aligned}$$

Notice that the argument to f' has one lower order, so that eventually we reach the scalar case the the recursion terminates.

There are two significant advantages to this approach. The first is the ease of understanding and maintaining the code. If we define "reduction" and "differentiation" operators as:

$$\mathbf{u} \equiv \langle u, u^{(1)}, \ldots, u^{(n)}\rangle, \tag{12}$$
$$\mathsf{R}\mathbf{u} \equiv \langle u, u^{(1)}, \ldots, u^{(n-1)}\rangle, \tag{13}$$
$$\mathsf{D}\mathbf{u} \equiv \langle u^{(1)}, \ldots, u^{(n)}\rangle, \tag{14}$$

then many functions can be programmed using expressions that look nearly equivalent to what one might find in a math textbook, for example,

$$\exp\mathbf{u} = \langle \exp u, \exp(\mathsf{R}\mathbf{u}) \cdot \mathsf{D}\mathbf{u}\rangle, \tag{15}$$
$$\sin\mathbf{u} = \langle \sin u, \cos(\mathsf{R}\mathbf{u}) \cdot \mathsf{D}\mathbf{u}\rangle, \tag{16}$$
$$\cos\mathbf{u} = \langle \cos u, -\sin(\mathsf{R}\mathbf{u}) \cdot \mathsf{D}\mathbf{u}\rangle, \tag{17}$$
$$\mathbf{u}^p = \begin{cases}\langle u^p, p \cdot (\mathsf{R}\mathbf{u})^{p-1} \cdot \mathsf{D}\mathbf{u}\rangle & \text{if } p \neq 0 \\ \langle 1, \mathbf{0}\rangle & \text{if } p = 0.\end{cases} \tag{18}$$

The second advantage is ease of testing. Simply comparing the first derivative, calculated using recursive automatic differentiation, with a few values calculated manually is sufficient to verify the code's correctness, because this simple test nonetheless achieves 100% code coverage.

Set against this, the primary disadvantage is efficiency. Multiplication can be done quadratically in terms of the maximum order, using the Leibniz rule, making the entire recursion cubic. There are two ways to mitigate this. One is to obtain and learn one of the many third-party automatic differential libraries, such as those listed at www.autodiff.org [6]. These use more optimized algorithms, but few, if any, support complex numbers, making IBC calculations difficult. The second is to note, as explained in detail below, that derivative calculation can be made a minuscule part of the overall computation, so that an especially efficient implementation is actually unnecessary.

Because many of the system matrix entries have the same frequency dependence, up to a multiplicative constant, it would be inefficient to calculate them entry by entry. Rather, the
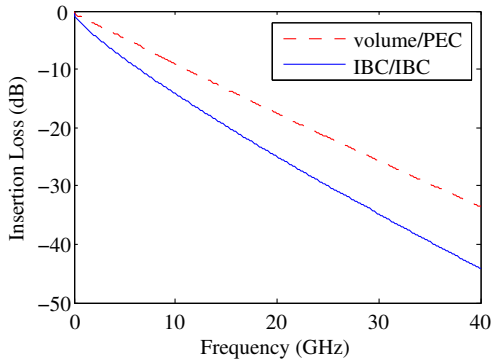
Fig. 1. Insertion loss for two different conductor models: (dashed red) volume conductor for traces, PEC for ground (solid blue) IBC for both.

matrix can be decomposed into a linear combination of scalar functions and constant matrices:

$$A(s) = \sum_i \phi_i(s) A_i. \tag{19}$$

The number of functions is typically less than a few dozen, e.g., one IBC-related function for each unique pair (T, σ). The derivatives $\phi_i^{(p)}$ can therefore be rapidly calculated, even with an unoptimized implementation, at which point evaluating $A^{(p)}(s)$ becomes trivial. Furthermore, this decomposition permits rapid online computation of the reduced-order matrix $\widehat{A}$, by precomputing each $V^H A_i V$.

III. RESULTS AND CONCLUSIONS

A. Long microstrip

To demonstrate the benefit of MOR with IBCs, a simple test project consisting of a very long trace, as might be found on a PCB, is used. The trace is $127 \, \mu m$ wide, $48 \, \mu m$ thick, and $30 \, cm$ long. The ground plane underneath is $33 \, \mu m$ thick, separated by $69 \, \mu m$-thick FR4 ($\varepsilon_r = 4.4$, $\tan \delta = 0.02$). The S parameters are extracted to $40 \, GHz$ using the Sentinel-PSI solver in ANSYS SIwave, which uses a 5th-order moment matching algorithm.

Four different analysis methods are considered. The first is using IBC on both the trace and ground plane and using the MOR with automatic differentiation described above. Second, MOR is also used, but with the simplest conductor modeling that gives a polynomial system matrix and a similar number of unknowns. In particular, the trace is modeled as a volume conductor and the ground plane is PEC; note that the mesh is not heavily refined, so this is expected to result in less loss. Third, IBCs are again used on all metals, but S matrix interpolation is used for the frequency sweep. Finally, for reference, the IBC results are calculated without any fast-sweep algorithm.

The resulting insertion loss is shown in Fig. 1. As expected, the model using volume conductivity and PEC shows significantly less loss at high frequency, up to $10 \, dB$ at $40 \, GHz$. The

Table 1: Performance Results

Model	Sweep Method	Freq. Samples	Time (min.)	Memory (GB)	% Error RMS/Peak
IBC	MOR	33	33.9	9.00	0.06/0.48
σ/PEC	MOR	31	27.6	8.50	65/105
IBC	S interp.	262	112.3	3.93	3.6/18.5
IBC	none	800	344.9	3.95	—/—
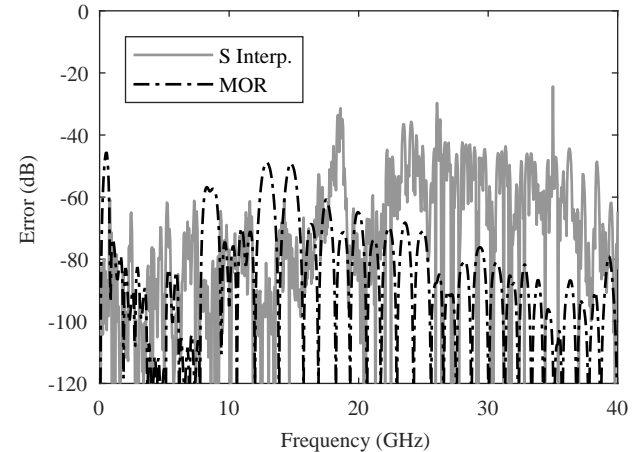
Fig. 2. Error in S matrix for long microstrip, using S matrix interpolation versus high-order moment matching MOR.

performance measurements are shown in Table 1. The error is defined as $||S - S_{ref}||_F / ||S_{ref}||_F$. Two conclusions can be drawn. First, for a problem with a given number of unknowns, the addition of IBCs has no significant impact on the runtime of the MOR algorithm, compared to the polynomial case. Second, the use of higher-order moment matching allows for a significantly reduced number of frequency samples compared to S matrix interpolation. In addition, Fig. 2 shows the error in the two frequency sweep methods. It can be seen that the MOR results has much more spacing between the nulls at the sample points (where the error is exactly zero), demonstrating the utility of high-order moment matching in providing more bandwidth per sample.

B. Flip-chip package

Figure 3 shows a more complicated example, a flip-chip package with four layers, four signal conductors, and three power/ground nets. The fact that some parts of the signal traces lack a nearby ground reference, combined with the many cutouts in the ground plane, lead to many dips in the insertion loss. This is a challenging situation for methods that interpolate the S parameters based on value alone, without any knowledge of the derivatives.

Table 2 shows the performance results, while Figs. 4 and 5 illustrate the insertion loss and S parameter error, respectively. Once more, the superior runtime and accuracy performance, at the cost of more memory, can be seen. In this case, the error nulls at the sample frequencies are not evident because of numerical non-reproducibility, caused by, e.g., differing

unknown ordering and using SIMD instructions on unaligned data [7]. Nevertheless, besides the number of samples being smaller, the fact that the average error level is lower also implies larger bandwidth per sample, because the error does not increase as rapidly when the frequency moves away from a sample. With higher-order moment matching, not only is the error zero at the samples, but its derivatives are also (apart from numerical rounding). It is also worth noting that of the 6.5 minutes spent computing the frequency sweep, a mere 21 ms was spent performing automatic differentiation. This validates the earlier observation that, for this particular application, a simple and understandable implementation may be preferable to a highly-optimized one.

Table 2: Flip-Chip Performance Results

Sweep Method	Frequency Samples	Time (minutes)	Memory (GB)	% Error RMS/Peak
MOR	8	6.5	7.7	0.006/0.06
S interpolation	92	20.6	3.0	0.05/0.7
none	400	91.2	3.1	—/—

(a) First layer   (b) Second layer
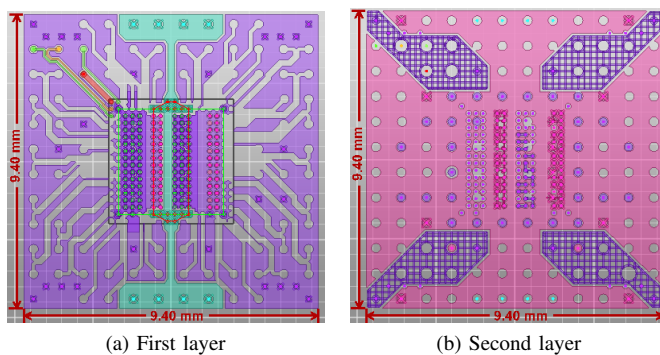
Fig. 3. First two layers of flip-chip package. The four signal nets are in the upper left-hand corner of the first layer. Note the cross-hatched grounds in the corners of the seconds layer, a source of additional reflections.
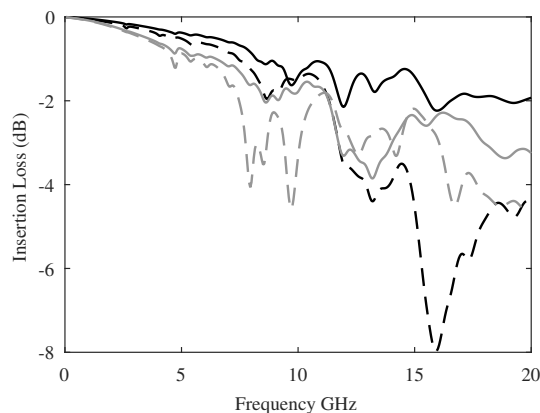
Fig. 4. Package insertion loss for each signal net.
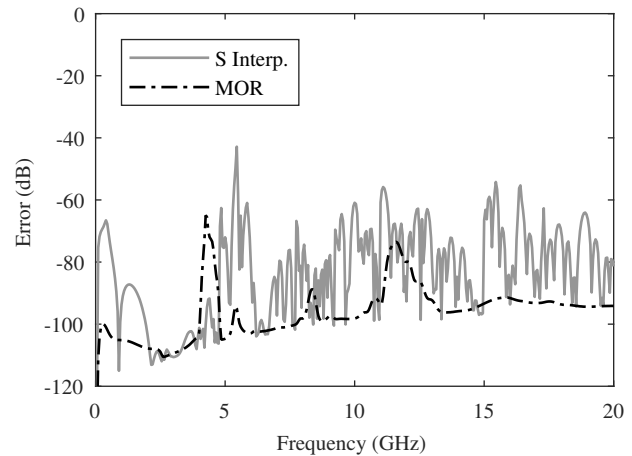
Fig. 5. Error in S matrix for flip-chip package, using S matrix interpolation versus high-order moment matching MOR.

REFERENCES

[1] R. D. Slone, R. Lee, and J.-F. Lee, "Multipoint Galerkin asymptotic waveform evaluation for model order reduction of frequency domain FEM electromagnetic radiation problems," *IEEE Trans. Antennas Propag.*, vol. 49, no. 10, pp. 1504–1513, Oct. 2001.

[2] A. Odabasioglu, M. Celik, and L. T. Pileggi, "PRIMA: Passive reduced-order interconnect macromodeling algorithm," *IEEE Trans. Comput.-Aided Design Integr. Circuits Syst.*, vol. 17, no. 8, pp. 645–654, Aug. 1998.

[3] *HFSS Online Help (Release 19.0)*, ANSYS, Inc., Canonsburg, PA, "Finite conductivity boundaries".

[4] O. Farle and R. Dyczij-Edlinger, "Numerically stable moment matching for linear systems parameterized by polynomials in multiple variables with applications to finite element models of microwave structures," *IEEE Trans. Antennas Propag.*, vol. 58, no. 11, pp. 3675–3684, Nov. 2010.

[5] M. Bartholomew-Biggs, S. Brown, B. Christianson, and L. Dixon, "Automatic differentiation of algorithms," *J. Comput. and Appl. Math.*, vol. 124, no. 1, pp. 171–190, 2000.

[6] Selected AD tools. [Online]. Available: http://www.autodiff.org/?module=Tools

[7] *Intel Math Kernel Library for Windows: Developer Guide (MKL 2018)*, Intel, "Obtaining Numerically Reproducible Results,". [Online]. Available: https://software.intel.com/sites/default/files/managed/35/53/mkl-2018-developer-guide-win.pdf

Whistler Mode Wave Refractive Index in a Finite Temperature Anisotropic Plasma Medium

Marek Gołkowski
Department of Electrical Engineering
University of Colorado Denver
Denver, CO USA
mark.golkowski@ucdenver.edu

Ashanthi Maxworth
Institute of Space and Atmospheric Studies
Department of Physics and Engineering Physics
University of Saskatchewan
Saskatoon, SK, Canada
asm468@mail.usask.ca

Abstract—**Whistler mode waves, which exist in a magnetized plasma, are prevalent in the Earth's magnetosphere in the extremely low frequency (ELF) and very low frequency (VLF) bands (100 Hz - 30 kHz). Due to the impact of whistler mode waves on space weather processes, it is important to accurately predict the propagation trajectory of these waves and their properties. Numerical raytracing determines the power flow path of the whistler mode waves in the anisotropic medium of the magnetosphere based on local calculation of the refractive index. In the majority of previous work, magnetospheric raytracing has been implemented assuming a cold background plasma (0 K). However, a more accurate description of the magnetospheric plasma includes a background temperature of about 1 eV (11600 K). We present solutions to the dispersion relation that include the effects of finite electron and ion temperatures on the wave refractive index using a warm plasma formulation. Finite temperature effects of the background plasma are shown to be most significant for highly oblique wave normal angles where the refractive index is bounded to smaller values than in the ideal cold plasma approximation.**

Keywords—*oblique whistler waves, radiation belts, raytracing, warm plasma, whistler mode*.

I. INTRODUCTION

Whistler mode waves are electromagnetic plasma waves that exists in a magnetized plasma, typically with plasma frequency much greater than electron cyclotron frequency. They are characterized by group and phase velocities much less than the speed of light with significant dispersion and a polarization that is generally right hand elliptically polarized [1]. Whistler mode waves are prominent in certain laboratory plasma applications and also play a key role in the energy dynamics of the near-Earth space environment, which we focus on here. Due to the plasma medium therein and the dominant effect of the geomagnetic field, this region is termed the magnetosphere and hosts a variety of whistler mode waves from diverse sources including manmade transmitters, atmospheric lightning, and local plasma instabilities. The medium is highly anisotropic making the prediction of wave trajectories analytically intractable outside of special cases. The power flow path of whistler mode waves can be determined using numerical raytracing. The magnetosphere contains two distinct populations of plasma, the background low temperature plasma with densities of 1 - 5000 cm^{-3} and a much smaller population of hot plasma with densities below 1 cm^{-3} but

energies in the 10 keV – 1 MeV range. (The hot plasma population is often called the radiation belts.) The hot plasma drives instabilities, but the background low temperature plasma determines the propagation characteristics of waves. The majority of the previous work on magnetospheric raytracing was performed assuming an ideally cold background plasma. However, observations show that the magnetospheric background exhibits finite temperatures of around 1 eV or greater [2]. In this work we investigate how refractive index surfaces change with the inclusion of finite background temperature to electrons and ions. Finite temperature effects become important for highly oblique whistler mode waves. For highly oblique waves near the resonance cone (limit of cold plasma solutions), the warm plasma formulations can be approximated by quasi-electrostatic or electrostatic models for frequencies below the half cyclotron frequency but at higher frequencies the models diverge. The results suggest that warm plasma raytracing codes are able to capture the important wave characteristics for all wave normal angles and are therefore more robust than quasi-electrostatic assumptions and not significantly more computationally expensive than cold plasma raytracing.

II. WARM PLASMA MODEL

A. Refractive Index Surfaces

Numerical ray tracing is the process of determining the power flow path of a whistler wave by solving the Haselgrove equations [3] under a WKB assumption. The medium properties enter the formulation through the refractive index, μ, which is a strong function of wave normal angle θ, which is the angle between the wave normal vector and the geomagnetic field. Under the ideal cold plasma assumption the dispersion relation is fourth order in μ:

$$A_0\mu^4 + B_0\mu^2 + C_0 = 0, \tag{1}$$

where the parameters A_0, B_0, and C_0 are cold plasma parameters defined below [4,5]. With the inclusion of finite temperature, the dispersion relation becomes sixth order:

$$q^T A_1\ \mu^6\left(A_0 + q^T B_1\right)\mu^4 + \left(B_0 + q^T C_1\right)\mu^2 + C_0 = 0, \tag{2}$$

where temperature T_s of each plasma species, *s*, is captured in:

$$q_s^T = \frac{k_B T_s}{m_s c^2}. \tag{3}$$

Where k_B is the Boltzmann constant, m_s is the mass and c is the speed of light. Since in most cases $q^T A_1 << A_0$, the first term in (2) only becomes significant in cases where μ is large. This occurs for highly oblique wave normal angles near the so called resonance cone for which the cold plasma assumption yields μ→∞. If more than one plasma species (i.e., electron and ions) has finite temperature, then (1) becomes a summation over the species s:

$$\left(\sum_s q_s^T A_{1s}\right)\mu^6 + \left(A_0 + \sum_s q_s^T B_{1s}\right)\mu^4 + \left(B_0 + \sum_s q_s^T C_{1s}\right)\mu^2 + C_0 = 0. \tag{4}$$

The remaining parameters are defined below. The dielectric tensor can be defined as having a cold and warm component:

$$\boldsymbol{K} = \boldsymbol{K^0} + \tau \boldsymbol{K^1}.$$

The elements of the cold tensor $\boldsymbol{K^0}$ are the well-known formulations from magneto-ionic theory:

$$\boldsymbol{K^0} = \begin{bmatrix} 1 - \dfrac{X}{1-Y^2} & \dfrac{iXY}{1-Y^2} & 0 \\ \dfrac{-iXY}{1-Y^2} & 1 - \dfrac{X}{1-Y^2} & 0 \\ 0 & 0 & 1-X \end{bmatrix},$$

$$X_s = \frac{\omega_{ps}^2}{\omega^2},$$

$$Y_s = \frac{\omega_{cs}}{\omega},$$

where ω is the wave frequency and ω_{ps} and ω_{cs} are the plasma frequency and cyclotron frequency, respectively for each particle species. The element of the finite temperature tensor $\boldsymbol{K^1}$ tensor are:

$$K_{11s}^1 = \frac{-X_s}{1-Y_s^2}\left[\frac{3sin^2\theta}{1-4Y_s^2} + \frac{1+3Y_s^2}{(1-Y_s^2)^2}cos^2\theta\right],$$

$$K_{22s}^1 = \frac{-X_s}{1-Y_s^2}\left[\frac{1+8Y_s^2}{1-4Y_s^2}sin^2\theta + \frac{1+3Y_s^2}{(1-Y_s^2)^2}cos^2\theta\right],$$

$$K_{33s}^1 = -X_s\left[3cos^2\theta + \frac{sin^2\theta}{1-Y_s^2}\right],$$

$$K_{12s}^1 = -K_{21s}^1 = \frac{iX_sY_s}{1-Y_s^2}\left[\frac{6sin^2\theta}{1-4Y_s^2} + \frac{3+Y_s^2}{(1-Y_s^2)^2}cos^2\theta\right],$$

$$K_{23s}^1 = -K_{32s}^1 = \frac{-iX_sY_s}{(1-Y_s^2)^2}\left(3-Y_s^2\right).sin\theta.cos\theta,$$

$$K_{13s}^1 = K_{31s}^1 = \frac{-2X_s}{(1-Y_s^2)^2}.sin\theta.cos\theta.$$

From the tensor components, the coefficients in (4) can be defined as:

$$A_0 = K_{11}^0 sin^2\theta + K_{33}^0 cos^2\theta,$$

$$B_0 = -[K_{11}^0.K_{22}^0 + (K_{12}^0)^2].sin^2\theta - K_{33}^0[K_{11}^0 + K_{22}^0.cos^2\theta],$$

$$C_0 = K_{33}^0\left[(K_{12}^0)^2 + K_{11}^0.K_{22}^0\right],$$

$$A_{1s} = K_{11s}^1 sin^2\theta + K_{33s}^1 cos^2\theta + 2K_{13s}^1.sin\theta.cos\theta,$$

$$B_{1s} = -[K_{11s}^1.K_{22}^0 + K_{22s}^1.K_{11}^0 + 2K_{12}^0.K_{12s}^1].sin^2\theta - K_{33s}^1[K_{11}^0 + K_{22}^0.cos^2\theta] - K_{33}^0[K_{11s}^1 + K_{22s}^1.cos^2\theta] + 2.sin\theta.cos\theta.[K_{12}^0.K_{23s}^1 - K_{13s}^1.K_{22}^0],$$

$$C_{1s} = K_{33s}^1\left[(K_{12}^0)^2 + K_{11}^0.K_{22}^0\right] + K_{33}^0[2K_{12}^0.K_{12s}^1 + K_{11}^0.K_{22s}^1 + K_{11s}^1.K_{22}^0].$$

Details of derivation of above expressions are provided in [4, 5] and references therein. Fig. 1 shows the refractive index surface for an example case of 3 kHz wave at the geomagnetic equator two Earth radii from the surface ($L = 2$) for various electron and ion temperatures as well as the cold plasma case. It is seen that the finite temperature effects cause the refractive index surface to deviate from the cold plasma value only for highly oblique angles near the resonance cone. The magnitude of refractive index is seen to decrease with temperature.
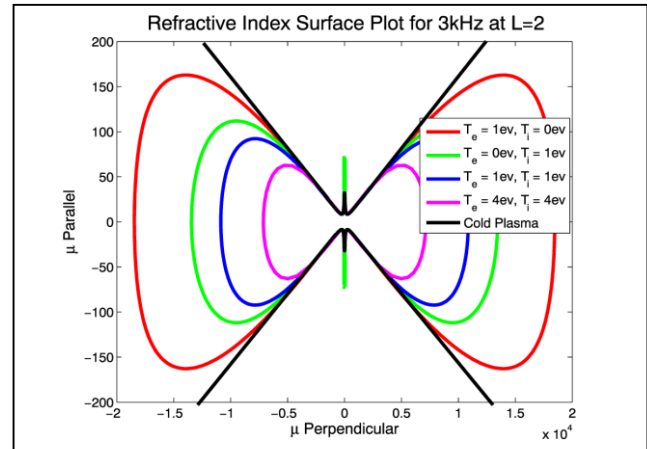
Fig. 1. Refractive index surfaces at the magnetic equator for the cold plasma and finite temperatures for ions and electrons. The refractive indeex is "open" under the cold plasma assumption but closed surfaces when temperature effects are included [5]. Note the disparate scale of the vertical and horizontal axes. The resonance cone angle is 89.1°.

III. COMPARISON WITH QUASI-ELECTROSTATIC AND ELECTROSTATIC APPROXIMATIONS

There has recently been interest in estimating the refractive index for highly oblique whistler mode waves where cold plasma theory is inadequate. Ma *et al.* [6] have employed a quasi-electrostatic assumption and shown reasonable

agreement with spacecraft observations. We perform a comparison of refractive index values obtained under warm plasma assumptions, quasi electrostatic and electrostatic assumptions. Quasi-electrostatic and electrostatic refractive index models of whistler mode refractive index have been presented by *Horne and Sazhin* [8]. In that work two plasma populations were considered: a finite temperature background plasma at 1 eV and a smaller hot plasma population at 200 eV. In the electrostatic and quasi-electrostatic simplified models of *Horne and Sazhin* [8], the two plasma populations each contribute to the refractive index calculation. The warm plasma formulations presented here take the more traditional approach from whistler mode raytracing where the background plasma determines the refractive index and wave trajectory and a hot plasma distribution can later be introduced to calculate resonance effects like wave growth or damping. For this reason and due to the fact that the hot plasma of the radiation belts is very dynamic and hard to generalize, we perform comparisons of the models using the background 1 eV plasma only. Figs. 2-7 present the comparison results obtained from the above three methods, at the equator at $L = 4, 6$ and 6.6, and for two frequencies normalized to the local cyclotron frequency with ratios ω/ω_c of 0.4 and 0.6. The three locations were selected as just-inside the plasma-pause ($L=4$) with background density $N_e = 200$ cm^{-3}, outside the plasma pause ($L=6$) with density $N_e = 8.5$ cm^{-3} and at the geostationary orbit ($L=6.6$) with density $N_e = 1$ cm^{-3}. At all locations the electron and ion temperature is $T_e = T_i = 1$ eV. The three gyro-frequencies corresponding to the equator of $L = 4, 6$ and 6.6 are 12 kHz, 4 kHz and 3 kHz respectively. The electrostatic and quasi electrostatic models are parametrized with the value λ given in (5) as the ratio between the squared sum of background electron plasma frequency and the squared electron gyro-frequency:

$$\lambda = \frac{\omega_p^2}{\omega_c^2}. \tag{5}$$

The refractive index for the quasi-electrostatic model is given by:

$$\mu^2 = \frac{\lambda Y^2 \left[\theta' \pm \left(\theta' - 2\alpha_{00}\beta \right)^{1/2} \right]}{\left[Y^2 - 1 \right]^{1/2} \alpha_{00}\beta}, \tag{6}$$

where

$$\beta = \frac{\omega_p^2 T_e}{\omega_c^2 m_e c^2},$$

$$\alpha_{00} = \frac{Y^2 \left(-11Y^2 + 23 \right)}{\left(Y^2 - 1 \right)^2 \left(4Y^2 - 1 \right)},$$

and where Y is defined as in the previous section and θ', defined as $\theta' = \theta - \theta_R$, where θ is the wave normal angle of the wave, θ_R is the cold plasma resonance cone angle given as:

$$\sin^2 \theta_R = \frac{\left(1 - \lambda Y^2 \right)\left(1 - Y^2 \right)}{\lambda Y^4}. \tag{7}$$

The refractive index for the electrostatic model is given by:

$$\mu^2 = \frac{2\theta' \lambda Y^2}{\left[Y^2 - 1 \right]^{1/2} \alpha_{00}\beta}. \tag{8}$$

Fig. 2 shows the refractive indices calculated using the warm plasma, quasi electrostatic and electrostatic approximations at *L=4* for $\omega/\omega_c = 0.4$ plotted as a function of θ' near the resonance cone where the quasi-electrostatic and electrostatic models have validity and the cold plasma model does not produce a solution. For these oblique wave normal angles there is good agreement between the models. Electrostatic and quasi-electrostatic models agree perfectly when the wave normal angles are higher than the resonance cone angle ($\theta' > 0$). The electrostatic approximation does not provide a solution for $\theta' < 0$. The warm plasma model predicts slightly lower values of refractive index. The near perfect agreement between the electrostatic and quasi-electrostatic models is a feature for all cases considered here though these models give divergent results for higher frequencies near $\omega/\omega_c = 0.8$ [8].

Figs. 3 and 4 show the comparison results of refractive indices at $L = 6$ and 6.6 where the background density is lower. From the plots, a very close agreement between warm plasma assumptions and quasi-electrostatic approximations can be observed for $\theta' < \theta_R$. The warm plasma model again predicts slightly lower values of refractive index when $\theta' > 0$ and this is more pronounced for the $L= 6.6$ location.

Figs. 5-7 show the results obtained at the three selected locations for $\omega/\omega_c = 0.6$. In all figures, warm plasma approximations produce much higher refractive indices compared to the other two approximations.
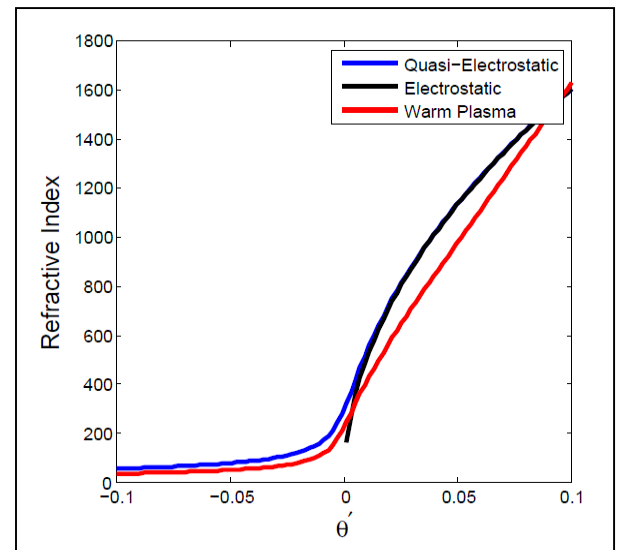
Fig. 2. Comparison of refractive index calculated with quasi-electrostatic, electrostatic and warm plasma models near the resonance cone (θ' = 0) for $L = 4$ ($\lambda = 111$) and $\omega/\omega_c = 0.4$.
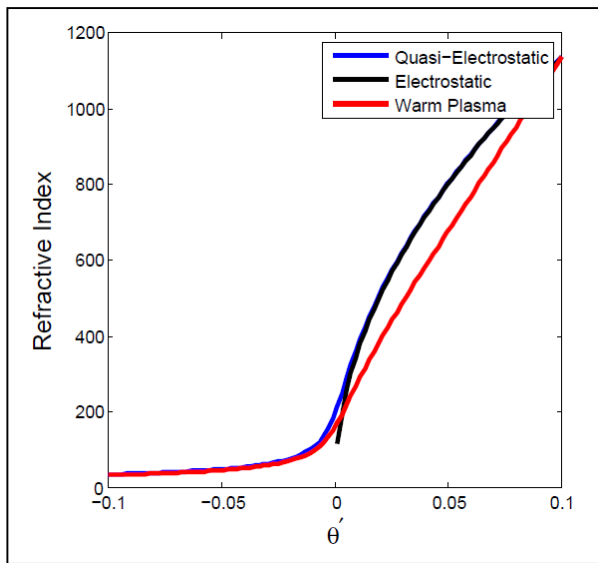
Fig. 3. Comparison of refractive index calculated with quasi-electrostatic, electrostatic and warm plasma models near the resonance cone (θ' = 0) for $L = 6$ ($\lambda = 42.82$) and $\omega/\omega_c = 0.4$.

IV. DISCUSSION

Horne and Sazhin [8], perform a comparison between quasi-electrostatic, electrostatic and what they call hot plasma assumptions that derive from the HOTRAY code [9]. Unfortunately, the details of the hot plasma formulations used for the comparison are not clear [8]. The electrostatic and quasi-electrostatic results shown here differ slightly from *Horne and Sazhin* [8] due to our neglect of the "hot" 200 eV population mentioned above. However, we note that our warm plasma results agree nearly exactly with the *Horne and Sazhin* [8] HOTRAY plasma results for $\omega/\omega_c = 0.4$ at $L=4$, $L=6$. For $\omega/\omega_c = 0.4$ and $L = 6.6$ the agreement is still very good except that the HOTRAY results shows a discontinuity around the resonance cone angle. For the higher frequency cases $\omega/\omega_c = 0.6$ the warm plasma model produces higher refractive index values compared to the HOTRAY code. For the ratio $\frac{\omega}{\Omega} = 0.8$, the values obtained from the warm plasma assumptions are smaller than the values obtained from the HOTRAY code.

For frequencies below the half gyrofrequency, like the cases at $\omega/\omega_c = 0.4$ considered here, there is general agreement between the different models especially at the resonant cone angles and slightly smaller wave normal angles. Therefore, for analysis of oblique lower band chorus phenomena, especially at background densities of 200 cm^{-3} or higher, any of the models can be expected to provide reasonable results. At the same time, it is clear that for lower background densities and higher frequencies, the models discussed here do not show exact agreement. Specific knowledge of the hot plasma distribution and its density may be necessary for accurate estimates of the refractive index of highly oblique waves in such conditions.

One advantage of the warm plasma formulation presented here is that it provides solutions for all wave normal angles and

reduces to the well-known cold plasma solutions for moderately oblique and field aligned waves. Using this formulation a robust raytracing code can be deployed to assess whistler mode trajectories and properties over the full scale of the magnetosphere. Such a raytracing code is presented by *Maxworth and Golkowski* [5]. It can be argued that a full hot plasma kinetic approach to raytracing is the most accurate and preferable approach. However, a full kinetic approach is computationally expensive.
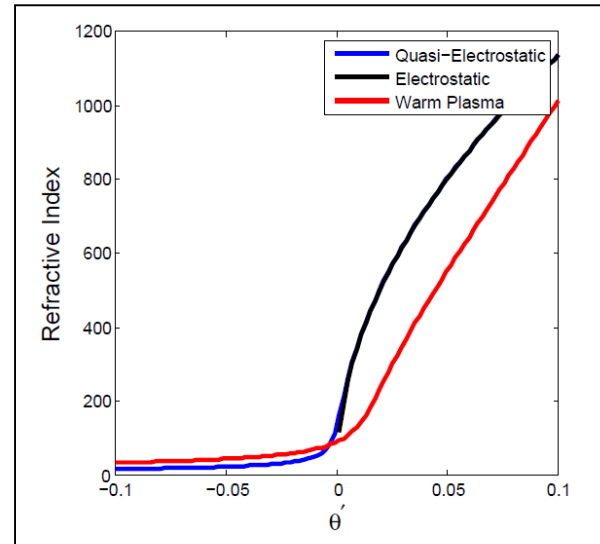
Fig. 4. Comparison of refractive index calculated with quasi-electrostatic, electrostatic and warm plasma models near the resonance cone (θ' = 0) for $L = 6.6$ ($\lambda = 8.96$) and $\omega/\omega_c = 0.4$.
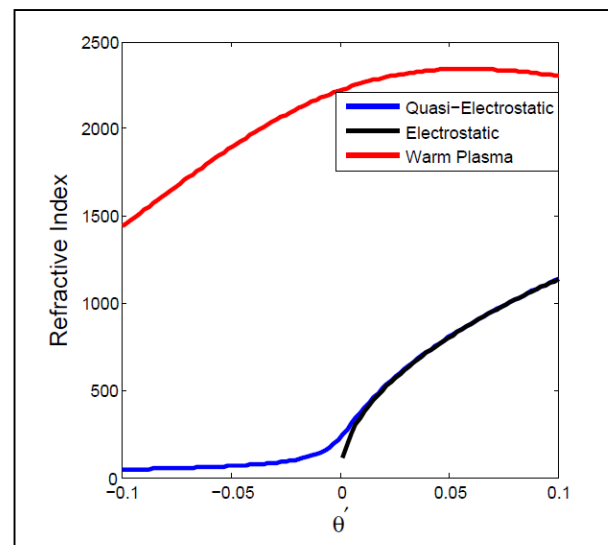
Fig. 5. Comparison of refractive index calculated with quasi-electrostatic, electrostatic and warm plasma models near the resonance cone (θ' = 0) for $L = 4$ ($\lambda = 111.95$) and $\omega/\omega_c = 0.6$.
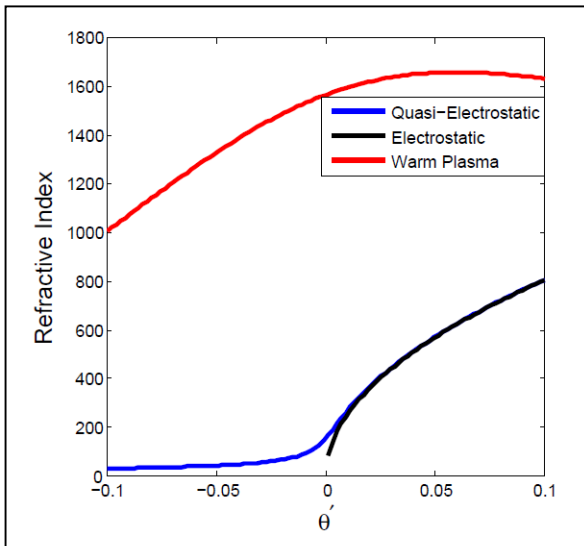
Fig. 6. Comparison of refractive index calculated with quasi-electrostatic, electrostatic and warm plasma models near the resonance cone (θ' = 0) for $L = 6$ ($\lambda = 42.82$) and $\omega/\omega_c = 0.6$.
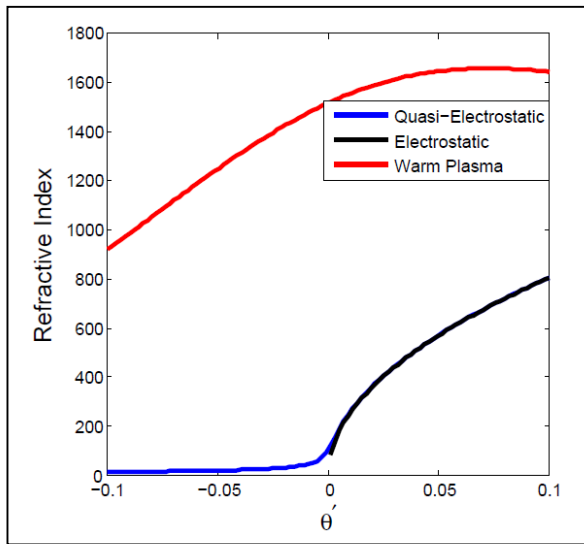
Fig. 7. Comparison of refractive index calculated with quasi-electrostatic, electrostatic and warm plasma models near the resonance cone (θ' = 0) for $L = 6.6$ ($\lambda = 8.96$) and $\omega/\omega_c = 0.6$.

V. CONCLUSIONS

Inclusion of finite temperature of the background plasma changes the refractive index for highly oblique whistler waves. Recent spacecraft observations show a significant presence of such highly oblique whistler mode waves and their role in radiation belt dynamics are still being assessed. A primary effort in space weather research is modeling energetic particle populations using quasi-linear diffusion codes. The upper limit of the refractive index surface has been identified as an important parameter [10]. So even if inclusion of finite temperature does not significantly change a typical whistler wave trajectory from that predicted by cold plasms theory, the implications of refractive index change at oblique wave normal angles can have far reaching effects. The warm plasma theory discussed here allows for calculation of the maximum refractive index outside the resonance cone. The warm plasma approach shows very similar results to quasi electrostatic and electrostatic approximations near the resonance cone for frequency below the half gyrofrequency making the model a robust choice for general whistler mode raytracing problems.

REFERENCES

[1] U. S. Inan, S. Umran, and M. Gołkowski, Principles of Plasma Physics for Engineers and Scientists. Cambridge University Press, 2010.

[2] P. M. E Decreau, C. Beghin, and M. Parret, "Global characteristics f the cold plasma in the equatorial plasmasphere region as deduced from the GEOS 1 mutial impedance probe," J. Geophys. Res A87, 695, 1982.

[3] J. Haselgrove, "Ray theory and a new method for ray tracing," in Physics of the Ionosphere, Physics of the Ionosphere Conference, Cambridge, London, 355-364, 1954.

[4] P. Kulkarni, M. Gołkowski, U. S. Inan, and T. F. Bell, "The effect of electron and ion temperature on the refractive index surface of 1-10 kHz whistler mode waves in the inner magnetosphere," J. Geophys. Res. Space Physics, 120, 1, 581-591, 2015.

[5] A. S. Maxworth and M. Gołkowski, "Magnetospheric whistler mode raytracing in a warm background plasma with finite electron and ion temperature," J. Geophys. Res. Space Physics, 122, 7, 7323-7335, 2017.

[6] Q. Ma, et al., "Very oblique whistler mode propagation in the radiation belts: Effects of hot plasma and Landau damping," Geophys. Res. Lett., 2017.

[7] D. M Malaspina, et al., "The distribution of plasmaspheric hiss wave power with respect to plasmapause location," Geophys. Res. Lett., 43, 15, 7878-7886, 2016.

[8] R. B. Horne and S. S. Sazhin, "Quasielectrostatic and electrostatic approximations for whistler mode waves in the magnetospheric plasma," Planetary and Space Science, vol. 38, iss. 2, 1990.

[9] R. B. Horne "Path-integrated growth of electrostatic waves: The generation of terrestrial myriametric radiation," J. Geophys. Res., 94, A7, 8895-8909, 1989.

[10] J. M. Albert, "Quasi-linear diffusion coefficients for highly oblique whistler mode wave," J. Geophys. Res., 122, 5, 5339-5354, 2017.

Locally Corrected Nyström Discretization for Impressed Current Cathodic Protection Systems

John C. Young [1], Robert A. Pfeiffer [1], Robert J. Adams [1], and Stephen D. Gedney [2]

[1] Department of Electrical and Computer Engineering
University of Kentucky, Lexington, KY 40506, USA
john.c.young@uky.edu, robert.pfeiffer@uky.edu, robert.adams@uky.edu

[2] Department of Electrical and Computer Engineering
University of Colorado-Denver, Denver, CO 80204, USA
stephen.gedney@ucdenver.edu

Abstract — A high-order locally corrected Nyström discretization for analyzing impressed current cathodic protection systems is presented. Non-linear polarization curves are incorporated using a Newton-Raphson scheme. A Schur complement scheme is introduced to handle large domains with small electrodes. The methods are characterized in terms of error convergence and computation time by comparing to the analytic solution for a sphere and hemisphere.

Index Terms — Impressed current cathodic protection systems, integral equations, locally corrected Nyström method.

I. INTRODUCTION

Hull corrosion of marine vessels has been an area of much interest since vessels began to be constructed using metal. Various methods are used to mitigate hull corrosion including painting the hull with an insulating material and using cathodic protection systems. Cathodic protection systems are primarily classified as either sacrificial or impressed current. In a sacrificial system, a more easily corroded metal is used to inject electrons into the electrolyte, whereas in an impressed current system electrons are injected directly using a battery or generator. Cathodic protection system electrodes often exhibit non-linear behavior which can be approximately modeled using polarization curves.

In this paper, an overview of the integral formulation [1-6] for the analysis of an impressed current cathodic protection (ICCP) system is presented. The equation is discretized using the arbitrary-order locally corrected Nyström (LCN) method [7-9]. The Newton-Raphson method is used to handle problems with non-linear polarization curves. A Schur complement-based method is discussed to reduce the computational complexity of the Newton-Raphson iteration when the boundary conditions are mostly constant. Validation and convergence of the method is investigated using a sphere with non-constant boundary conditions.

II. THEORY

A. Formulation

Consider a region V bound by a surface S with inward surface normal $\hat{\mathbf{n}}_i$. The region may represent either an internal or an external region, and, if the region is external, part of S recedes to infinity. Furthermore, let the region be filled with an electrolyte with conductivity σ. Green's second identity relates the electric potential Φ in the electrolyte to the boundary potential Φ and its normal derivative $\hat{\mathbf{n}}_i \cdot \nabla \Phi$ as:

$$\Phi(\mathbf{r}) - \oint_S \Phi' \nabla' G \cdot \hat{\mathbf{n}}_i' ds' - \Phi^\infty$$
$$+ \oint_S G \nabla' \Phi' \cdot \hat{\mathbf{n}}_i' ds' = 0, \quad \mathbf{r} \in V \quad , \quad (1)$$

where the additional unknown Φ^∞ is only included for an external problem. The kernel is the static, homogeneous Green's function:

$$G(\mathbf{r}, \mathbf{r}') = \frac{1}{4\pi |\mathbf{r} - \mathbf{r}'|} . \quad (2)$$

For both the interior and exterior problems, a meaningful solution exists only if the total flux over the boundary S is zero [10]:

$$\oint_S \nabla \Phi \cdot \hat{\mathbf{n}}_i dS = 0 . \quad (3)$$

Furthermore, for the linear interior Neumann problem [10], the additional constraint:

$$\oint_S \Phi dS = C , \quad (4)$$

with constant C (usually zero) is applied. Enforcement of (1) on S produces the integral equation:

$$\frac{1}{2}\Phi(\mathbf{r}) - \text{P.V.}\oint_S \Phi'\nabla'G(\mathbf{r},\mathbf{r}')\cdot\hat{\mathbf{n}}_i'\,ds' - \Phi^\infty$$

$$+ \oint_S G\nabla'\Phi'\cdot\hat{\mathbf{n}}_i'\,ds' = 0, \quad \mathbf{r}\in S \quad (5)$$

The hull surface may be split into three parts: an insulating part S^i on which $\nabla'\Phi'\cdot\hat{\mathbf{n}}_i' = 0$, electrodes S^p on which the potential Φ is known, and electrodes S^f on which the normal derivative (flux) is known $\nabla'\Phi'\cdot\hat{\mathbf{n}}_i'$. Often electrodes S^f are polarized and are specified using a polarization curve P such that,

$$\hat{\mathbf{n}}_i\cdot\nabla\Phi = P(\Phi). \quad (6)$$

B. Locally corrected Nyström discretization

The integral Equation (5) with the conditions (as necessary) (3) and (4) is discretized using an arbitrary-order locally corrected Nyström (LCN) method where the surface is meshed with either triangle or quadrilateral elements of arbitrary order. As an example, the discretization of (3) and (5) for the exterior Neumann problem with polarized electrodes is:

$$\begin{bmatrix} H^e \end{bmatrix}\begin{bmatrix} \Phi^f \\ \Phi^i \\ \Phi^\infty \end{bmatrix} = \begin{bmatrix} H^{ff} & H^{fi} & -1 \\ H^{if} & H^{ii} & -1 \\ 0 & 0 & 0 \end{bmatrix}\begin{bmatrix} \Phi^f \\ \Phi^i \\ \Phi^\infty \end{bmatrix}$$

$$= \begin{bmatrix} G^{ff} & G^{fi} & 0 \\ G^{if} & G^{ii} & 0 \\ S^f & S^i & 0 \end{bmatrix}\begin{bmatrix} P(\Phi^f) \\ 0 \\ 0 \end{bmatrix}, \quad (7)$$

$$= \begin{bmatrix} G^e \end{bmatrix}\begin{bmatrix} P(\Phi^f) \\ 0 \\ 0 \end{bmatrix}$$

where the matrix definitions are determined by comparing (7) to (3) and (5). Note that the additional zero column in the G^e matrix is added so that H^e and G^e are of the same dimensions. Also, the S^x entries are related to the differential surface areas of the elements at the test points and are used to enforce (3).

C. Newton-Raphson method

For a non-constant polarization curve $P(\Phi)$, the Newton-Raphson method [3] is applied with the iterative update $\begin{bmatrix} \Phi^{k+1} \end{bmatrix} = \begin{bmatrix} \Phi^k \end{bmatrix} + \begin{bmatrix} \delta\Phi^k \end{bmatrix}$ such that,

$$\begin{bmatrix} \delta\Phi^k \end{bmatrix} = -\begin{bmatrix} J(\Phi^k) \end{bmatrix}^{-1}\begin{bmatrix} P(\Phi^{f,k}) \end{bmatrix}, \quad (8)$$

where the Jacobian matrix $[J]$ at iteration k is:

$$[J] = \begin{bmatrix} \dfrac{\partial P}{\partial\Phi^k} \end{bmatrix} = \begin{bmatrix} G^e \end{bmatrix}\cdot\text{diag}\left(\begin{bmatrix} P'(\Phi^{f,k}) \\ 0 \\ 1 \end{bmatrix}\right) - \begin{bmatrix} H^e \end{bmatrix}. \quad (9)$$

For large problems in which the electrodes only cover a small portion of the surface, the Schur complement can be applied to avoid factoring a full Jacobian matrix at each iteration. A partitioning of the Jacobian matrix amenable to the Schur complement is:

$$[J] = \begin{bmatrix} G^{nc,nc}\cdot\text{diag}\left(P'\left(\Phi^{nc}\right)\right) - H^{nc,nc} & -H^{nc,co} \\ G^{co,nc}\cdot\text{diag}\left(P'\left(\Phi^{nc}\right)\right) - H^{co,nc} & -H^{co,co} \end{bmatrix} \quad (10)$$

where the superscripts *nc* and *co* indicate those portions of the matrix corresponding to non-constant and constant boundary conditions, respectively. Before the Newton-Raphson iteration begins, the matrix $H^{co,co}$ is pre-factored and stored. Then, at each Newton-Raphson step, a matrix is only factored that has the dimensions of the degrees-of-freedom associated with the electrodes having non-constant polarization curves. The above Schur complement form is also amenable for use in fast-direct solvers.

D. Image plane theory

In the event that one side of the electrolyte is completely bounded by a planar, insulating surface, then image theory may be applied to reduce the computational burden. For external problems, the insulating, planar boundary is often unbounded such as when the electrolyte fills a half-space that is bounded above by an electrolyte-air interface. In this case, the use of image theory greatly reduces the modeling burden and improves accuracy. Otherwise, the half-space must be truncated and placed inside a finite box for computation, which introduces truncation error into the solution. In addition, note that using a truncated box model changes an exterior problem into an interior one.

When image theory is applied, the planar, insulating surface is not meshed and no degrees-of-freedom are assigned to it. Instead an image Green's function,

$$G_{\text{im}}(\mathbf{r},\mathbf{r}') = G(\mathbf{r},\mathbf{r}') + G(\mathbf{r},\mathbf{r}'_{\text{im}}), \quad (11)$$

is used in (1) and (5) in place of G. Here, $\mathbf{r}'_{\text{im}}$ is the reflection of $\mathbf{r}'$ across the image plane. In addition, care must be taken in computing the $\nabla'G(\mathbf{r},\mathbf{r}')\cdot\hat{\mathbf{n}}_i'$ term as well since the normal vector must also be imaged appropriately. The image Green's function produces an electric potential Φ that is an even function about the image plane. This in turn leads to an electrolyte current $\mathbf{J} = -\sigma\nabla\Phi$ whose normal component at the bounding electrolyte-insulator interface is zero.

III. RESULTS

For initial validation, an exterior Neumann problem comprising a one meter sphere with boundary condition [2]:

$$P^f(\Phi) = \frac{\partial \Phi}{\partial n^i} = \Phi + \cos\theta + 3, \quad 0 \le \theta \le \pi, \quad (12)$$

representing a cathodic surface was analyzed. The analytic solution is:

$$\Phi(\mathbf{r}) = -3 - \cos\theta / (3r^2), \quad (13)$$

with $\Phi^\infty = -3$. The discretization in (9) was used and the Newton-Raphson iteration converged in one step. The sphere was discretized with 10th order quadrilateral elements and two meshes of 24 cells and 96 cells were analyzed for various LCN basis orders.

The RMS relative error in the surface potential at the system quadrature points versus basis order is plotted in Fig. 1. The relative error decreases as the basis order increases, but the convergence can stagnate due to the integration of the normal derivative $\nabla' G(\mathbf{r}, \mathbf{r}') \cdot \hat{\mathbf{n}}_i'$ in the self-term on curved surfaces [6, 11]. In practice, lower errors can be achieved if a local adaptive integration error tolerance is used for the problematic integrals and a tighter error tolerance is used elsewhere. The scheme used in this paper is to use a relatively tight error tolerance everywhere and then relax the error tolerance on-the-fly and re-integrate only for those integrals that are observed not to converge.

To validate the image plane method, a one meter sphere centered at the origin and floating in an electrolytic half-space of conductivity $\sigma = 1$ S/m for $z < 0$ and $\sigma = 0$ S/m for $z > 0$ was investigated using the boundary condition:

$$P^f(\Phi) = \frac{\partial \Phi}{\partial n^i} = \Phi - \cos(\phi)\sin(\theta) + 3, \quad (14)$$

for $\frac{\pi}{2} \le \theta \le \pi$. The analytic solution is:

$$\Phi = -3 + \cos(\phi)\sin(\theta) / (3r^2), \quad \frac{\pi}{2} \le \theta \le \pi, \quad (15)$$

where again $\Phi^\infty = -3$. The problem was solved in three ways: imaging the hemisphere so that the model is a full sphere in an infinite electrolyte, modeling the hemisphere only using the image Green's function, and boxing the electrolyte with a larger outer hemispherical surface and treating the problem as an interior problem. In the latter case, as depicted in Fig. 2, the modeled surface includes the original hemispherical surface, an outer hemispherical surface, and an annular surface at the electrolyte-air interface that connects the two hemispheres. The $\cos(\phi)\sin(\theta)$ variation in (14) is used since the $\cos(\theta)$ variation in (12) does not produce a potential Φ that is symmetric about the electrolyte-air interface as required.

The surfaces in each of the three models were meshed using 8th-order quadrilateral elements with

meshes of various densities and the problem was solved using Newton-Raphson iteration for various basis orders. For the boxed-electrolyte model, the problem was solved for outer hemispheres with radii of 8 m, 16 m, 32 m, and 64 m. To keep the problem size manageable, the outer hemispherical surface used a fixed, coarse discretization. The computed electrostatic surface potential and (1) were used to determine the electrostatic potential at various points in the electrolyte.
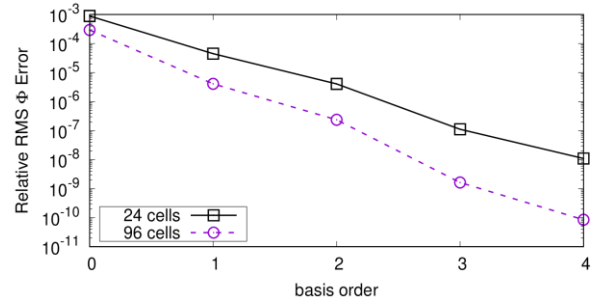
Fig. 1. Relative RMS error between computed and analytic surface potential Φ solutions versus basis order for a one meter sphere meshed with 10th order quadrilateral elements.
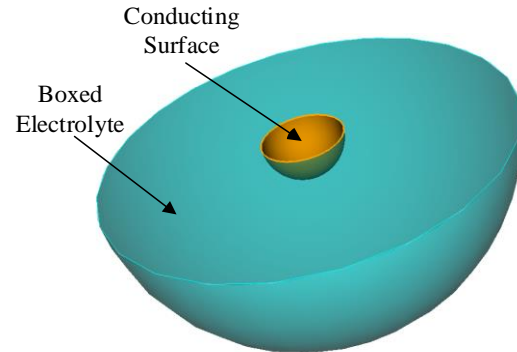
Fig. 2. Hemispherical conducting surface surrounded by a hemispherical-boxed electrolyte.
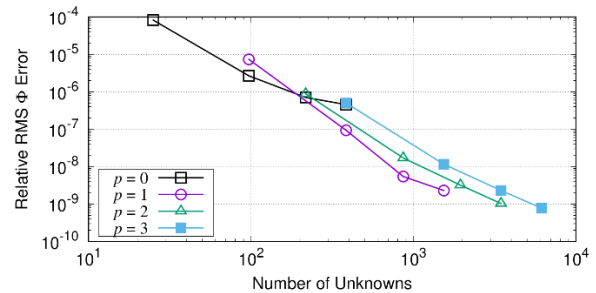
Fig. 3. Error convergence versus number of unknowns for various basis orders p for full sphere model of a hemisphere in an electrolytic half space.
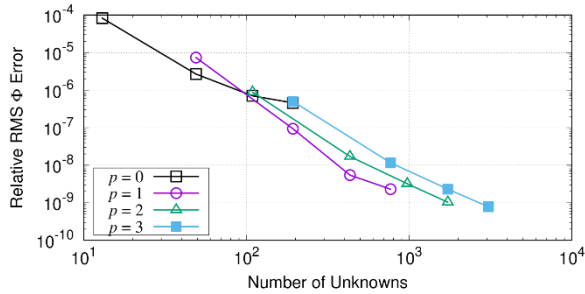
Fig. 4. Error convergence versus number of unknowns for various basis orders *p* for image plane Green's function model of a hemisphere in an electrolytic half space.
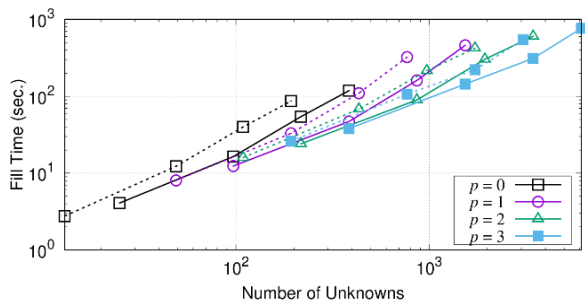
Fig. 5. Fill times versus number of degrees of freedom for full sphere model (solid lines) and half-sphere with image plane Green's function model (dashed lines).
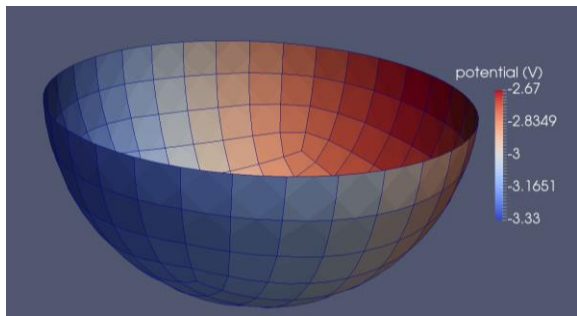
Fig. 6. Surface potential using image plane Green's function model for conducting hemisphere at surface of semi-infinite electrolyte.

The relative RMS error between the computed potential in the electrolyte and the analytic solution is plotted versus number of degrees of freedom in Fig. 3 for the fully imaged sphere and in Fig. 4 for the half-sphere with image plane Green's function. As can be seen from the data, the convergence is the same for both models, but the image plane model requires only half the number of degrees of freedom. Again for each basis order, meshes with an increasing number of elements were analyzed. The matrix fill times versus number of degrees

for these two models are plotted in Fig. 5. The use of the image Green's function is clearly more efficient in terms of both the number of degrees of freedom and the computation time. Finally, the surface potential over the hemisphere surface computed using the image plane Green's function model is depicted in Fig. 6 for a mesh of 384 cells and using 2nd order bases.
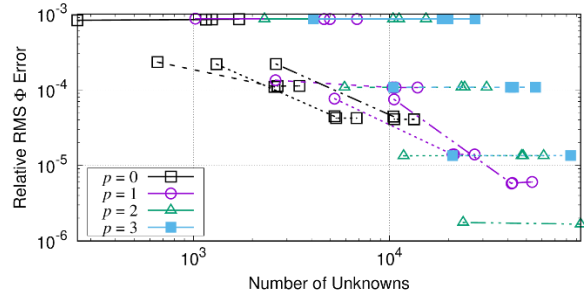
Fig. 7. Error convergence versus number of unknowns for various basis orders *p* for electrolyte boxed with outer hemispheres of radius $a = 8$ (solid line), $a = 16$ m (dashed line), $a = 32$ m (dotted line), and $a = 64$ m (dashed-dotted) line.
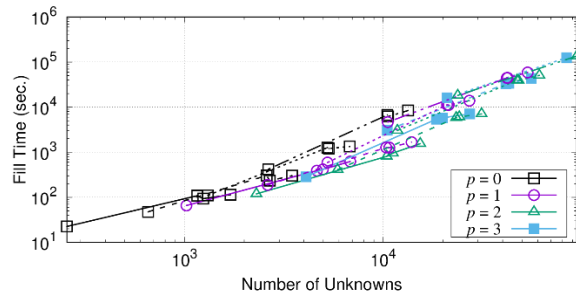
Fig. 8. Fill times versus number of unknowns for various basis orders *p* for electrolyte boxed with outer hemispheres of radius $a = 8$ (solid line), $a = 16$ m (dashed line), $a = 32$ m (dotted line), and $a = 64$ m (dashed-dotted) line.

For the last model where the electrolyte is boxed with a finite-radius hemisphere, the error convergence and fill times versus basis order are plotted in Fig. 7 and Fig. 8 respectively. Except for the original conducting hemisphere, the remaining surface mesh is assigned an insulating boundary condition. Hence, the Newton-Raphson iteration can be greatly accelerated using the Schur complement method outlined in II.C. However, in these cases, the matrix fill time dominates the computation time. One observes that the use of a truncated box around the electrolyte severely degrades the error convergence as well as drastically increases the number of unknowns and the computation time. The minimum error is limited by the radius of the outer hemisphere. Hence, the advantages of using image theory are readily apparent.

VI. CONCLUSION

A high-order electrostatic analysis of an impressed current cathodic protection systems was presented. Suitable boundary integral equation formulations were given for both interior and exterior domains, and appropriate constraints to remove any null spaces were discussed. The integral equations were discretized using the locally corrected Nyström method, and problems with nonlinear polarization curves were solved using the Newton-Raphson method. The methods were validated by comparison of computed solutions to analytic solutions for a sphere and hemisphere in an electrolytic half-space and higher-order solution convergence was observed.

ACKNOWLEDGMENT

REFERENCES

[1] J. M. Chuang, N. G. Zamani, and C. C. Hsuing, "Some computational aspects of BEM simulation of cathodic protection systems," *Applied Mathematical Modelling*, vol. 11, pp. 371-379, October 1987.

[2] N. G. Zamani, J. M. Chuang, and J. F. Porter, "BEM simulation of cathodic protection systems employed in infinite electrolytes," *International Journal for Numerical Methods in Engineering*, vol. 45, pp. 605-620, 1987.

[3] J. F. Yan, S. N. R. Pakalapati, T. V. Nguyen, R. E. White, and R. B. Griffin, "Mathematical modeling of cathodic protection using the boundary element method with a nonlinear polarization curve," *Journal of The Electrochemical Society*, vol. 139, pp. 1932-1936, July 1, 1992.

[4] W. Sun, G. Yuan, and Y. Ren, "Iterative algorithms for impressed cathodic protection systems," *International Journal for Numerical Methods in Engineering*, vol. 49, pp. 751-768, 2000.

[5] R. Pfeiffer, "High-order Integral Equation Methods for Quasi-Magnetostatic and Corrosion-Related Field Analysis with Maritime Applications," Ph.D., Electrical & Computer Engineering, University of Kentucky, Lexington, KY, 2018.

[6] J. C. Young, R. Pfeiffer, R. J. Adams, and S. D. Gedney, "Locally corrected Nyström discretization for impressed current cathodic protection systems," presented at the *2018 International Applied Computational Electromagnetics Society Symposium (ACES)*, Denver, CO, 2018.

[7] S. D. Gedney, "On deriving a locally corrected Nyström scheme from a quadrature sampled moment method," *IEEE Transactions on Antennas and Propagation*, vol. 51, pp. 2402-2412, September 2003.

[8] S. D. Gedney and J. C. Young, "The locally corrected Nystrom method for electromagnetics," in *Computational Electromagnetics: Recent Advances and Engineering Applications*, R. Mittra, Ed., New York: Springer, pp. 149-198, 2014.

[9] L. F. Canino, J. J. Ottusch, M. A. Stalzer, J. L. Visher, and S. M. Wandzura, "Numerical solution of the Helmholtz equation in 2D and 3D using a high-order Nyström discretization," *Journal of Computational Physics*, vol. 146, pp. 627-663, 1998.

[10] G. C. Hsiao and W. L. Wendland, *Boundary Integral Equations*. vol. 164, Berlin: Springer-Verlag, 2008.

[11] R. Pfeiffer, J. C. Young, and R. J. Adams, "Numerical characterization of divergence-conforming constrained basis functions for surface integral equations," *IEEE Transactions on Antennas and Propagation*, vol. 65, pp. 1867-1874, 2017.

John C. Young received the B.E.E. degree in Electrical Engineering from Auburn University in 1997, the M.S. degree in Electrical Engineering from Clemson University in 2000, and the Ph.D. degree in Electrical Engineering also from Clemson University in 2002. He received a National Science Foundation Graduate Fellowship in 1998 and served as a Graduate Research Assistant at Clemson University from 1997 to 2002. He is currently an Assistant Professor in the Department of Electrical and Computer Engineering at the University of Kentucky, Lexington, KY. He is a Senior Member of the IEEE and a Member of URSI Commission B, Tau Beta Pi, and Eta Kappa Nu.

Robert Pfeiffer received the B.A. degree in Liberal Arts from Thomas Aquinas College, Santa Paula, CA, USA, in 2012, and the M.S. and Ph.D. degrees in Electrical Engineering from the University of Kentucky, Lexington, KY, USA, in 2015 and 2018, respectively. He studied Electrical Engineering at the Milwaukee School of Engineering in Milwaukee, WI, USA, from 2012 to 2014, and was an Intern with Johnson Controls Inc., Milwaukee, from 2013 to 2014. Since 2014, he has been a Graduate Research Assistant with the University of Kentucky. He is currently with Sandia National Laboratories.

Robert J. Adams received the B.S. degree from Michigan Technological University, Houghton, MI, USA, in 1993, and the M.S. and Ph.D. degrees in Electrical Engineering from Virginia Tech, Blacksburg, VA, USA, in 1995 and 1998, respectively. From 1999 to 2000, he was a Research Assistant Professor with Virginia Tech. He is currently a Professor with the Department of Electrical and Computer Engineering, University of Kentucky, Lexington, KY, USA. His current research interests include applied and computational electromagnetics.

Stephen D. Gedney received the B.Eng.-Honors degree from McGill University, Montreal, P.Q., in 1985, and the M.S. and Ph.D. degrees in Electrical Engineering from the University of Illinois, Urbana-Champaign, IL, in 1987 and 1991, respectively. He is currently the Chair and the Don and Karen White Professor of the Department of Electrical Engineering at the University of Colorado Denver (UCD). Previously he was a Professor of Electrical Engineering at the University of Kentucky from 1991–2014. He worked for the U.S. Army Corps of Engineers, Champaign, IL ('85-'87). He was a visiting Professor at the Jet Propulsion Laboratory, (92',93'), HRL laboratories ('96-'97) and Alpha Omega Electromagnetics ('04-'05). He received the Tau Beta Pi Outstanding Teacher Award in 1995 and 2013. From 2002–2014, he was the Reese Terry Professor of Electrical and Computer Engineering at the University of Kentucky. He is a past Associate Editor of the IEEE Transactions on Antennas and Propagation (1997–2004), a Member of the IEEE Antennas and Propagation Society ADCOM (2000–2003), and served as the Chair of the IEEE Antennas and Propagation Society Membership Committee (1995–2002). He is a Fellow of the IEEE and Member of Tau Beta Pi.

"Faster" Could be "Slower": Uncovering the Salient Characteristics of Slow-light Guided Signals with the Finite-Difference-Time-Domain (FDTD) Method

Stavroula Foteinopoulou

Department of Electrical and Computer Engineering
University of New Mexico, Albuquerque, NM 87131, USA
sfoteino@unm.edu

Abstract ─ Slow-light mesophotonic waveguides have gained increasing interest in the recent years because of their catalyzing potential to transform applications relying on all-optical signal manipulation or enhanced light-matter interactions. The quests in this area have been targeting waveguide platforms with a giant group velocity index as determined by modal type of analyses in frequency domain. We show here that these efforts with frequency-domain methods have entirely missed on important mode features which are nevertheless crucial in practically effecting an ultra-slow guided pulsed signal with a large time delay. We utilize first-principle electromagnetic (EM) simulations in time-domain and show that contrary to conventional wisdom, the group-index by itself is not in general a good measure of the slow-down factor for a pulsed light signal propagating within the waveguide. We present a counterexample comparing two modes which demonstrates that the "faster" mode, the one with the lower group index, is the one that leads to larger effective time delays. The time-domain analysis in this counter-example uncovers a new figure of merit for practical slow-light platforms which indicates that along with a near-zero group velocity, a relatively low group-velocity dispersion value is simultaneously required.

Index Terms ─ Finite Difference Time Domain (FDTD) method, group index, group velocity, group velocity dispersion, left-handed materials, negative-index media, slow light, wave dispersion.

I. INTRODUCTION

Electromagnetic (EM) waveguiding platforms across the board have been predominantly studied in a frequency-domain framework for modal responses. In such framework, the modal behavior for the system is sought for a certain frequency, ω, and wavevector, $\mathbf{k}$. Such modal response can be calculated analytically for simple planar geometries, such as in dielectric slab [1], metallic [2-4], metal-slot [2,5], and negative-refractive-index waveguides [6] as well as for their heterostructures [7]. As the guiding structures however become more complicated, as for example in metallic periodically corrugated waveguides [8], metal/dielectric-strip waveguides [9] or all-dielectric designer surface plasmon waveguides [10-13], numerical approaches are needed to determine both the wave dispersion and spatial field profiles for the modes supported by the guiding system. One widely adopted example of such numerical approaches is the Finite-Difference-Frequency-Domain (FDFD) method [10,14-16].

While important information for a system's response to incoming EM waves can be obtained with these frequency-domain methods, a complete picture for the dynamic evolution of the propagating wave cannot actually be trivially deduced. Realistic source excitations are neither a perfect plane wave nor are they perfectly monochromatic even at continuous wave (CW) excitation. A framework for time-domain analysis is certainly highly desirable, especially for systems where the dynamic evolution of the guided wave is key to their operational principle. One such example is waveguides that support ultra-slow light waves [17] which have been realized in plasmonic-based systems [9, 18], in platforms based on negative-refractive-index metamaterials [7, 19-21], in photonic-crystal waveguides [22-24], as well as in certain atomically-thin materials with a phonon-polariton photonic response [25].

In this paper, we show that a time-dependent framework is key to obtaining understanding and uncovering design principles for slow-light platforms for practical applications. In principle, the system's time-domain response can be constructed from frequency-domain methods with the use of rigorous-modal matching analysis [26]. Actually, using this composite detailed analysis, He et al. [26] showed that a wave-packet in a tapered metamaterial waveguide gets back-reflected rather than attaining the "trapped rainbow" effect [21] which was hypothesized based on a purely frequency-domain analysis. However, the process followed by Ref. [26] can get quickly elaborate as structures or EM-wave launch geometries get more complicated and may require approximations that limit the range of validity. A brute-force, ab-initio method for

time-domain analysis is highly attractive. Free from any assumptions for simplifications, a highly popular widely used method for analysis in the time-domain is the Finite-Difference-Time-Domain (FDTD) method [27], which allows modeling of actual experimental set-ups.

In the following, we demonstrate why FDTD is highly suited for designing slow-light waveguides, uncovering salient mode characteristics that were missed with modal frequency-domain analyses. In particular, this paper is organized as follows. In Sec. II, we present the paradigm system that will be analyzed in two variations; these will serve as the counter-example showing that it is the system with the higher group velocity practically yielding the larger time delay for a guided pulsed signal. In Sec. III we analyze these designs in frequency-domain determining a prediction for their behavior as slow-light waveguides. In Sec. VI, we discuss the methodology to calculate appropriately the effective time delay and speed of a pulsed signal in the FDTD method. In Sec. V, we apply this methodology in the two paradigm system variations and extract an additional design principle that has been hitherto missed from standard modal dispersion analysis. Finally, we present our conclusions in Sec. VI.

II. THE SLOW-LIGHT BI-WAVEGUDE PARADIGM SYSTEM

We use the paradigm system of Ref. [7] as a counter-example to show that the frequency-domain predictions for a near-zero group velocity in two waveguide designs do not end-up yielding ultra-slow guided light in time-domain for both cases. This paradigm system is a bi-waveguide comprising a regular dielectric slab waveguide [1], i.e., a positive-index-medium (PIM) waveguide, and a slab waveguide made from a negative-index-medium (NIM) [see Fig. 1]. In the PIM waveguide, the guided mode has the Poynting vector $\mathbf{S}$, parallel to the direction of phase propagation, as given by the wavevector $\mathbf{k}$. Conversely, in the NIM waveguide the Poynting vector $\mathbf{S}$, is anti-parallel to the direction of phase propagation [6]. Outside the waveguide the EM energy decays exponentially (evanescent waves). The evanescent tails of the guided mode do carry some energy along the $+x$ direction, but this can be neglected in this case as the main waveguides have a width of about three times the free space wavelength.

As we also depict in Fig. 1, the phase (wave vector) direction is common in both constituent waveguides, as imposed by Maxwell's equations requiring continuity of the parallel component of the wave-vector across the waveguide interfaces. Then, it follows from the respective Poynting vector directions that the EM energy would have a disposition to propagate in opposite directions in each sub-waveguide if the waveguides were independent. Because of this competition in the direction of energy propagation in each of the sub-waveguides,

Ref. [19] envisioned the composite PIM-NIM bi-waveguide to possess nearly-frozen light modes. These manifest themselves in the waveguide dispersion relation, $\omega(k_x)$, with near-zero group velocity, i.e., $\partial\omega/\partial k_x=0$. Guided modes with near-zero group velocity can be found for a range of parameters in this system. An additional benefit of the PIM-NIM bi-waveguide is that it is also favorable for monomodal response [28].

(a) Bi-waveguide A, d_A=4.54 μm

(b) Bi-waveguide B, d_B=5.675 μm
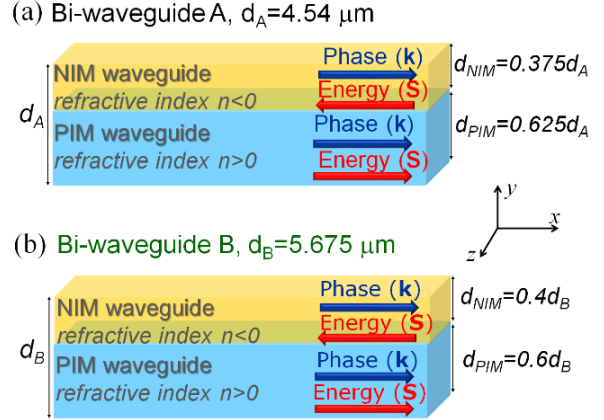
Fig. 1. The slow-light bi-waveguide paradigm system comprising a positive-index-medium (PIM) waveguide and a negative-index-medium (NIM) waveguide. Two cases, depicted in (a) and (b), have been chosen in order to showcase two near-zero group velocity examples but with distinctly different effective responses to an input EM signal. In each case, the widths for the individual PIM, NIM waveguides as well as the total width of the bi-waveguide are indicated.

We focus now our attention on two particular bi-waveguide designs A and B, in order to demonstrate how the FDTD method distinguishes the behavior between two modes which are both identified as slow-light modes with a modal analysis. Both bi-waveguide designs comprise the same materials: a permittivity of ε=4.0 for the PIM, and the Veselago dispersive material [29] for the NIM with a plasma frequency of ω_p=2π·308·10^{12} rad/s. The chosen waveguide widths however for each sub-waveguide, d_{NIM} and d_{PIM}, are different and result in a different total width for the bi-waveguide. In the following, we designate the total bi-waveguide width as d_A, and d_B, for design A and design B respectively (see Fig. 1 for their values). We note, the paradigm system is idealized, e.g., actual metamaterials do not follow the Veselago medium response. The purpose of using this idealized paradigm is to understand how features in the frequency-domain modal response effect behaviors in time-domain. This link is what has not been hitherto well understood. This understanding is however of utmost importance to design practical systems that guide ultra-slow EM pulses.

In the following section we present and compare the predictive response of the two paradigm designs based on a modal frequency-domain analysis.

III. BI-WAVEGUIDE DESIGNS A AND B: PROPERTIES IN FREQUENCY DOMAIN

The simple planar geometry of the bi-waveguide system allows calculating analytically the dispersion relation of the guided mode, $\omega(k_x)$, i.e., the relation between the frequency and the wave vector along the guide direction, This is done by considering a guided wave solution in the PIM, and NIM region, and evanescent tails outside the waveguide; the wave dispersion is then determined by applying the EM boundary conditions for the continuity of the tangential components of the electric and magnetic field (see Ref. [7] for details). This is depicted in Fig. 2 (a). Both frequency and wave vector are represented in dimensionless units [see caption of Fig. 2]. The dimensionless scaled wave vector along the guide direction, β, is also known as modal index [30]. We observe that a single guided-mode is present for each design in this frequency range. We recognize that for a range of modal index values the dispersion flattens for both waveguide designs. We designate this dispersion region with a yellow shading in Fig. 2 (a) and show it magnified in Fig. 2 (b) for both waveguide designs.

This nearly-flat dispersion region signifies a near-zero group velocity magnitude, v_g, and conversely a very large group index (absolute value), $|n_g|$, since:

$$v_g = \left| \frac{\partial \omega}{\partial k_x} \right| = \frac{c}{|n_g|}, \qquad (1)$$

where ω is the guided wave cyclic frequency, k_x, is the wavevector along the guiding direction and c is the speed of light. Equation (1) implies that a large group-index magnitude leads to a large light slow-down factor for the guided wave. For the case of design B, the dispersion band has a negative slope in a range of modal index values, and yields a negative group index, n_g. In Fig. 2 (c) the group index (absolute value) is plotted, but we use a dashed line, instead of a solid line, to designate the range for which the group index is negative (see also Ref. [31]).

We also mark in Fig. 2 (c) certain modes of interest for waveguide A and waveguide B. First, we make note of modes SLA and SLB, shown with a blue box and a red box, respectively. What is interesting about these two modes is that both have large group index (absolute values); so in principle both look like good candidate modes for slow-light guiding. Mode SLA has a group index of ~100 and mode SLB's group index is even higher, ~2000. So, if one was to think of a good slow-light waveguide design the obvious choice from such frequency domain analysis would be design B operating

at mode SLB. We will see however with the time-domain analysis in the following that this is not true; we will find that it is actually design A at mode SLA that makes a good slow-light waveguide. For this purpose, we need to analyze the signal propagation along the waveguide for both slow-light waveguide candidates in time-domain. Before doing so, we present in the following the details of the numerical determination of the signal propagation speed for a more general case of a moderate group index. We choose mode LB of design B, that we have designated with a brown square in Fig. 2 (c).
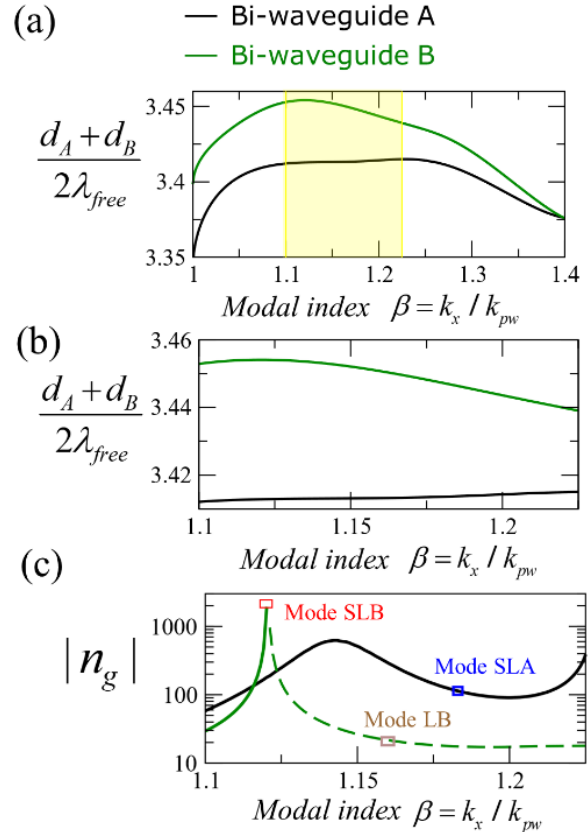
Fig. 2. (a) The wave dispersion for the two bi-waveguide designs, A and B of Fig. 1. Both the frequency and the wavevector along the guiding direction, x, are represented in dimensionless units; the former by multiplying the inverse of the free-space wavelength, λ_{free}, with the average width of the two waveguide designs and the latter by dividing with the free-space plane-wave wavevector, k_{pw}, to give β, which is known as the modal index [30]. The shaded area designates a region of nearly-flat dispersion for both designs. (b) Zoom of the shaded region of (a). (c) Magnitude of the group index, $|n_g|$, (logarithmic scale) versus the modal index, β, for the two waveguide cases [dashed lines indicate regions with $n_g<0$]. The three modes that are labeled (SLA, SLB and LB) will be analyzed further.

IV. SIGNAL PROPAGATION SPEED IN FDTD: CALCULATION METHOD

In the FDTD framework, a numerical experiment with an Otto set-up [7, 10-11, 32] can be implemented for the determination of the propagating signal's speed. The Otto set-up yields an evanescent wave that further excites the guided mode in the bi-waveguide system. The right-angle prism of the Otto configuration, lies above the bi-waveguide system of Fig. 1, with its hypotenuse along the x-direction; it so fixes the modal index to $\beta_0 = n_{prism} \cdot \sin(45^0)$ since EM boundary condition require the wavevector along the x-direction to be conserved. Therefore, an EM wave launched from the left-side of a prism with $\beta_0 = \beta_{LB}$ would couple to mode LB with a wavevector along the $+x$-direction. As mode LB has a negative group index as determined in Sec. III, the composite waveguide mode is expected to be a backward type of mode [10-11, 33]. This means the EM energy of the composite guided wave will propagate opposite to its wavevector, i.e., in the $-x$ direction. Indeed, we observe in the FDTD calculations that despite the different Poynting vector directions in the NIM and PIM sub-waveguide parts, in both of them the pulsed signal propagates in the direction predicted by the dispersion-band slope direction, i.e., in the $-x$ direction for mode LB (see also Refs. [7] and [31]).
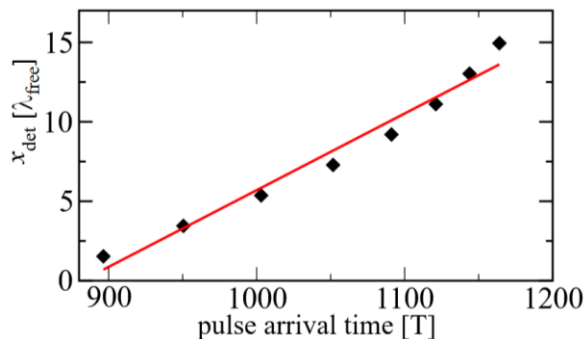
Fig. 3. FDTD results (filled diamonds) for the detector position, x_{det}, versus the arrival time of the pulsed signal at this detector for mode LB. The detector position is scaled with the free space wavelength, λ_{free}, while the pulse arrival time is scaled with the wave period T of the central frequency of the input EM pulse (filled diamonds). The red solid line represents a linear fit on the FDTD data.

To avoid any interference that would come from the reflected signal at the waveguide edges, the FDTD simulation set-up has the bi-waveguide terminated with suitable absorbers in both sides [see Ref. 7]. Different detectors are placed at various distances, x_{det}, from the left-side of the prism, to span different positions along the $-x$ direction. Each detector extends across the entire bi-waveguide width in the y-direction. For each of the detectors, each positioned at different x_{det}, the Poynting vector along the guide direction, S_x, is recorded at each time step for all spatial grid points in the y-extend of the detector. As the waveguide system is strongly dispersive it is not appropriate to monitor the peak of the pulse in order to determine its arrival time. To determine the EM signal's speed in the FDTD implementation of the bi-waveguide system, we follow a similar approach to that introduced by Peatross et al. in Ref. [34].

In particular, we calculate the arrival time, t_{arr}, at a detector at position x_{det} from:

$$t_{arr}(x_{det}) = \frac{\int_0^{t_{sim}} t \left(\int_0^{d_B} S_x(x_{det},y,t)dy \right) dt}{\int_0^{t_{sim}} \left(\int_0^{d_B} S_x(x_{det},y,t)dy \right) dt}, \qquad (2)$$

with d_B being the bi-waveguides B width across the y-direction (see schematics in Fig. 1). The FDTD simulation is terminated at t_{sim} at which time the signal strength should be at least three magnitudes lower than its peak value (the lower the more accurate the calculation). We show the results calculated from Eq. (2) with the FDTD method in Fig. 3. The numerical FDTD data can be fitted with a linear fit (red-solid line in the figure). From, the slope of the $x_{det}(t_{arr})$ fit line we determine $|n_g|$ for mode LB to be 20.7 which agrees excellently with the value determined from the frequency-domain analysis which is 21.7 [see Fig. 2 (c)]. So, we did not find any surprises for the case of mode LB and both frequency and time domain analysis agree on the propagating properties of the guided pulsed signal. Whether this holds to be true for the ultra-slow guided modes, namely modes SLA and SLB in Fig. 2 (c), we explore in the following section.

V. SIGNAL PROPAGATION SPEED OF MODES AT FLAT WAVE DISPERSION: FREQUENCY-DOMAIN VERSUS TIME-DOMAIN PREDICTIONS

Now we follow the process of Sec. IV in the FDTD simulations for mode SLA of waveguide design A and mode SLB of waveguide design B. Both correspond to regions of flat guided wave dispersion, $\omega(k_x)$. For design A, we obtain an effective slow down factor of ~300 which is actually quite higher than the frequency-domain prediction of ~100. The FDTD result for the SLB waveguide is even more cumbersome. We find that the effective slow down factor varies with the distance from the prism edge between the values ~10 and 40 which is about two orders of magnitude lower than the frequency-domain prediction of ~2000. We discuss below where this huge discrepancy between modal analysis and time-domain observations for mode SLB is coming from.

The input EM wave, has a Gaussian beam waist, which implies a spread $\Delta\beta$ around the β_0 value

corresponding to a certain mode. All observed guided waves, around LB, SLA and SLB modes are subject to the influence of the modal index spread, $\Delta\beta$, which introduces additional modes in the vicinity of the respective intended modes, e.g., LB, SLA or SLB. The case of mode SLB, is especially peculiar however when compared to the case of modes LB and SLA. The difference between mode SLB and modes LB and SLA is that the group index, n_g changes so much around mode SLB with modal index, β to the point that it goes from positive to negative.
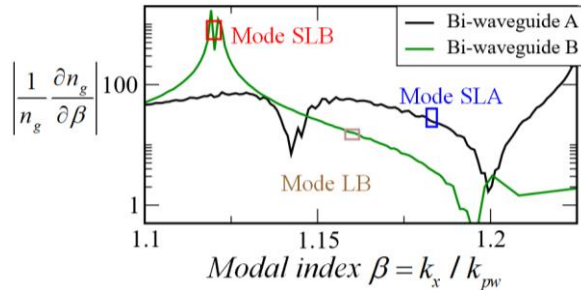
Fig. 4. Comparison of the relative group index variation with the modal index (absolute value), versus the modal index β for the different modes.

It appears there is a correlation between consistency of modal and time-domain analysis and the variation of the group index n_g with the modal index, β. We therefore plot in Fig. 4, the relative group index variation with the modal index (absolute value), i.e., $|\partial n_g/\partial\beta|/|n_g|$ versus the modal index β for both the bi-waveguide designs. This quantity is calculated from the dispersion relations of Fig. 2 (b). We also designate the modes LB, SLA and SLB that we have discussed above. Figure 4 confirms that the lower the value of this quantity the better the agreement between frequency-domain predictions and time-domain calculations for the effective guided-mode slow-down factor. In other words, the quantity $|\partial n_g/\partial\beta|/|n_g|$ can serve as a figure of merit (FOM) for slow-light waveguides, with lower values indicating a better performance. It can be shown that if $|n_g| \gg \beta$, which is typically the case for modes identified as slow modes in a modal analysis that:

$$FOM = \left|\frac{1}{n_g}\frac{\partial n_g}{\partial\beta}\right| \cong \left|GVD(\omega_0)\right| \cdot v_g^2 \cdot \frac{\omega_0}{c}, \qquad (3)$$

with ω_0 being the frequency of the corresponding mode and GVD the group velocity dispersion at that frequency. Equation (3) implies that along with a near-zero group velocity a relatively small GVD value is simultaneously required to practically achieve high effective slow-down factors.

VI. CONCLUSION

Our analysis here suggests that the Finite-Difference-Time Domain (FDTD) method gives a more complete picture for the system's response in a particular experimental set-up. Thus, the FDTD method is more suitable to characterize practical slow-light systems in comparison with modal methods in the frequency domain. The FDTD analysis on a paradigm system uncovered a figure of merit for design guidance of slow-light platforms. The latter stresses on the importance of an as low as possible GVD value along with a near-zero group velocity to practically achieve slow-light propagation.

REFERENCES

[1] D. Marcuse, *Theory of Dielectric Optical Wave-guides*. 2nd edition, Elsevier Inc., 1991.

[2] E. N. Economou, "Surface plasmons in thin films," *Phys. Rev.*, vol. 182, pp. 539-554, 1969.

[3] J. A. Dionne, et al., "Planar metal plasmon wave-guides: frequency-dependent dispersion, propagation, localization, and loss beyond the free electron model," *Phys. Rev. B.*, vol. 72, 075405-1-11, 2005.

[4] P. Berini, "Figures of merit for surface plasmon waveguides," *Opt. Express*, vol. 14, pp. 13030-13042, 2006.

[5] J. A. Dionne, et al., "Plasmon slot waveguides: Towards chip-scale propagation with subwavelength-scale localization," *Phys. Rev. B*, vol. 73, pp. 035407-1-9, 2006.

[6] I. V. Shadrivov, A. A. Sukhorukov, and Y. S. Kivshar, "Guided modes in negative-refractive-index waveguides," *Phys. Rev. E*, vol. 67, pp. 057602-1-4, 2003.

[7] S. Foteinopoulou and J.-P. Vigneron, "Extended slow-light field enhancement in positive-index/ negative-index heterostructures," *Phys. Rev. B*, vol. 88, pp. 195144-1-8, 2013.

[8] S. I. Bozhevolnyi, et al., "Photonic bandgap structures for long-range surface-plasmon polaritons," *Opt. Comm.*, vol. 250, pp. 328-333, 2005.

[9] A. Karalis, et al., "Surface-plasmon-assisted guiding of broadband slow and subwavelength light in air," *Phys. Rev. Lett.*, vol. 95, pp. 063901-1-4, 2005.

[10] S. Foteinopoulou, et al., "Backward surface waves at photonic crystals," *Phys. Rev. B*, vol. 75, pp. 245116-1-6, 2007.

[11] S. Foteinopoulou, et al., "Experimental verification of backward wave propagation at photonic crystal surfaces," *Appl. Phys. Lett.*, vol. 91, pp. 214102-1-3, 2007.

[12] S. Foteinopoulou, et al., "Tailoring the properties of designer surface plasmons for subdiffraction light

manipulation," in *FiO 2008/LS XXIV/Plasmonics and Metamaterials, OSA Technical Digest*, paper MThC6, 2008.

[13] A. I. Rahachou and I. V. Zozoulenko, "Waveguiding properties of surface states in photonic crystals," *J. Opt. Soc. Am. B*, vol. 23, pp. 1679-1683, 2006.

[14] E. I. Smirnova, et al., "Simulation of photonic band gaps in metal rod lattices for microwave applications," *J. Appl. Phys.*, vol. 91, pp. 960-968, 2002.

[15] G. Veronis, "Finite-difference-frequency-domain technique," *Encyclopedia of Nanotechnology*, Springer, pp. 843-852, 2012.

[16] W. Shin, "3D Finite-Difference-Frequency-Domain Method for Plasmonics and Nanophotonics," Ph.D. dissertation, Stanford U., 2013.

[17] K. L. Tsakmakidis, et al., "Ultraslow waves on the nanoscale," *Science*, vol. 358, pp. eaan5196-1-11, 2017.

[18] K. L. Tsakmakidis, et al., "Completely stopped and dispersionless light in plasmonic waveguides," *Phys. Rev. Lett.*, vol. 112, 167401-1-5, 2014.

[19] C. Vandenbem, et al., "Guided waves in a bilayer film made of right- and left-handed materials," presented at *Photonic Metamaterials: From Random to Periodic*, Grand Island, Bahamas, Paper WD5, 2006.

[20] S. Foteinopoulou, "Electromagnetic energy accumulation in mesophotonic slow-light waveguides," published in *19th International Conference on Transparent Optical Networks (ICTON), IEEE*, pp. 1-4, 2017.

[21] K. L. Tsakmakidis, A. D. Boardman, and O. Hess, "Trapped rainbow storage of light in metamaterials," *Nature*, vol. 450, pp. 397-401, 2007.

[22] T. F. Krauss, "Slow light in photonic crystal waveguides," *J. of Physics D-Appl. Phys.*, vol. 40, pp. 2666-2670, 2007.

[23] S. F. Mingaleev, A. E. Miroshnichenko, and Y. S. Kivshar, "Low-threshold bistability of slow light in photonic-crystal waveguides," *Opt. Express*, vol. 15, pp. 12380-12385, 2007.

[24] S. A. Schulz, et al., "Photonic crystal slow light waveguides in a kagome lattice," *Opt. Lett.*, vol. 42, pp. 3243-3246, 2017.

[25] A. Ambrosio, et al., "Selective excitation and imaging of ultraslow phonon polaritons in thin hexagonal boron nitride crystals," *Light Science and Appl.*, vol. 7, pp. 27-1-9, 2018.

[26] S. He, Y. He, and Y. Jin, "Revealing the truth about 'trapped rainbow' storage of light in metamaterials," *Scientific Reports*, vol. 2, pp. 583-1-9, 2012.

[27] A. Taflove, *Computational Electrodynamics: The Finite Difference Time-Domain Method*. Artech House, Boston, 1995.

[28] A. Alu and N. Engheta, "Guided modes in a waveguide filled with a pair of single-negative (SNG), double-negative (DNG), and/or double-positive (DPS) layers," *IEEE Trans. Microwave Theory Tech.*, vol. 52, pp. 199-210, 2004.

[29] V. G. Veselago, "The electrodynamics of substances with simultanesouly negative ε and μ," *Sov. Phys. Usp.*, 10, 509, 1968.

[30] J. C. Knight, "Photonic crystal fibers," *Nature*, vol. 424, pp. 847-851, 2003.

[31] S. Foteinopoulou, "Frequency-domain versus time-domain analysis of slow-light mesophotonic waveguides: Theoretical insights for practically realizable devices," *2018 International ACES Symposium*, Denver, CO, pp. 1-2, 2018.

[32] A. Otto, "Excitation of nonradiative surface plasma waves in silver by the method of frustrated total reflection," *Z. Phys.*, vol. 216, 398-410, Aug. 1968.

[33] S. Foteinopoulou and C. M. Soukoulis, "Negative refraction and left-handed behavior in two-dimensional photonic crystals," *Phys. Rev. B*, vol. 67, 235107-1-5, 2003.

[34] J. Peatross, S. A. Glasgow, and M. Ware, "Average energy flow of optical pulses in dispersive media," *Phys. Rev. Lett.*, vol. 84, pp. 2370-2373, 2000.

Stavroula Foteinopoulou is a Research Professor with the ECE Dept. of the U. of New Mexico. She received her Ph.D. in Condensed Matter Physics from Iowa State U. and has held post-doctoral positions in U. of Namur (Belgium) as well as the Institute of Electronic Structure and Laser (IESL) of FORTH (Greece). She was a Lecturer at the U. of Exeter (UK) until 2014 prior to joining the U. of New Mexico. Her research in theoretical/ computational photonics focuses on conceiving new photonic platforms for unconventional light control across the EM spectrum. She has authored more than 30 journal publications and conference papers, which have attracted to-date more than 2800 citations (source google scholar). She also holds one US patent. Stavroula is serving as an Associate Editor for the OSA Optical Materials Express (OMEX) Journal, as well as for the Journal of the European Optical Society: Rapid Publications (JEOS-RP). She is also a Chair of the annual SPIE Conference Active Photonic Platforms.

A Finite-Difference Frequency Domain Solver for Quasi-TEM Applications

J. Patrick Donohoe

Department of Electrical and Computer Engineering
Mississippi State University, Mississippi State, MS 39762, USA
donohoe@ece.msstate.edu

Abstract ─ A finite-difference frequency-domain (FDFD) solver applicable to quasi-TEM applications is defined. The FDFD solver is applicable to a wide variety of transmission line structures where the cross-sectional dimensions govern the frequency range over which the quasi-TEM approximation is valid. The quasi-TEM FDFD solver provides an efficient solution for conductor current distributions involving both skin effect and proximity effect. Simulation results obtained using the quasi-TEM FDFD solver are compared to measurements and other numerical methods.

Index Terms ─ Finite-difference frequency-domain, quasi-TEM approximation.

I. INTRODUCTION

Low-frequency electromagnetic simulation presents a variety of computational challenges, irrespective of the general solution technique employed. The accuracy of low-frequency solutions using the method of moments (MOM), the finite-element method (FEM) and the finite-difference time-domain (FDTD) technique all suffer due to ill-conditioned matrices for the frequency-domain schemes, and the exorbitant number of time-steps required for time-domain schemes.

A transmission line structure, operating under the quasi-TEM approximation, generates small longitudinal fields internal and external to the transmission line conductors. Under the quasi-TEM approximation, these longitudinal fields are assumed negligible in comparison to the transverse fields, such that the transverse fields are accurately approximated by the true TEM fields of the corresponding static problem. A low-frequency 2D FDFD scheme that exploits the quasi-TEM approximation and avoids the numerical pitfalls described above is defined in the next section.

II. QUASI-TEM FDFD SOLVER

A simple transmission line model is used to demonstrate the formulation of the quasi-TEM FDFD scheme. Non-ideal ($\sigma_c < \infty$) and nonmagnetic ($\mu_c = \mu_o$) transmission line conductors are assumed along with an ideal (μ_i, ϵ_i, $\sigma_i = 0$) insulating medium. Under quasi-TEM

operation, the displacement current is assumed to be negligible relative to the conduction current, and the fields are assumed to be invariant in the direction of wave propagation (the transmission line is assumed to be short relative to wavelength).

The transmission line structure carries a true TEM mode only if the conductors are assumed ideal. The transverse fields of the true TEM mode are identical to the static fields for the given conductor configuration. Low-level longitudinal fields are present throughout the system when realistic conductors are assumed, leading to a quasi-TEM mode (designated here as qTEM). According to the quasi-TEM approximation, the qTEM transverse fields are essentially identical to those of the corresponding static fields. Both electrostatic and magnetostatic solutions are not required to determine the complete qTEM transverse fields, however, since the transverse electric and magnetic fields of a TEM mode are related by a simple cross-product relationship. Thus, the electrostatic problem can be solved to determine the transverse electric field, and the resulting transverse magnetic field is found by implementing the TEM cross-product relationship. The qTEM transverse magnetic field on the surface of the non-ideal conductors is equated to the TEM transverse magnetic field on the surface of the ideal conductors, based on the quasi-TEM approximation [1]. One can then determine the surface qTEM magnetic field on the surface of the non-ideal conductors using Maxwell's equations, and solve the governing differential equation for the magnetic field internal to each non-ideal conductor. The basic steps of the FDFD scheme based on the quasi-TEM approximation are summarized as follows.

Step 1. Solve for the quasi-TEM electric field surrounding the conductors, which is approximated by the electrostatic solution, according to:

$$\nabla^2 \tilde{V}_{qTEM} = 0, \qquad (1)$$

and

$$\tilde{E}_{qTEM} = -\nabla \tilde{V}_{qTEM}, \qquad (2)$$

where $\tilde{V}_{qTEM}$ and $\tilde{E}_{qTEM}$ are the phasor potential and electric field, respectively, surrounding the conductors.

Step 2. Determine the quasi-TEM magnetic field surrounding the conductors ($\tilde{H}_{qTEM}$) according to [1]:

$$\tilde{H}_{qTEM} = \frac{1}{\eta_i} \hat{z} \times \tilde{E}_{qTEM} , \tag{3}$$

where η_i is the wave impedance of the insulating medium surrounding the conductors and $\hat{z}$ is the unit normal to the transverse plane.

Step 3. Use the quasi-TEM magnetic field surface boundary condition to solve the governing magnetic field PDE internal to each non-ideal conductor via FDFD as given by:

$$\nabla^2 \tilde{H}_{qTEM} - \gamma_c^2 \tilde{H}_{qTEM} = 0 , \tag{4}$$

$$\gamma_c^2 = j\omega\mu_o (\sigma_c + j\omega\varepsilon_c) \approx j\omega\mu_o\sigma_c , \tag{5}$$

where γ_c is the propagation constant of the respective conductor.

The aforementioned scheme accounts for both proximity effect and skin effects. The transverse components of the qTEM magnetic field in step 2 account for the proximity effects for the conductor configuration. These transverse qTEM fields are large in regions where the currents tend to crowd on the surface of the transmission line conductors. The governing PDE of the non-ideal conductor accounts for the skin effect within the conductor at the given frequency of operation, based on the proximity effect embedded in the surface field boundary conditions.

III. RESULTS

The qTEM FDFD technique is applied to an isolated square copper conductor of 2.54cm×2.54cm cross-section, in order to compare results with computed and measured values in a case where only skin effect is present. The ratio of the AC resistance (R_{ac}) to DC resistance (R_{dc}) is computed via qTEM FDFD and compared to the measured result. The AC resistance determined using qTEM FDFD is based on the conductor current distribution, and is given by:

$$R_{ac} = \frac{1}{\sigma_c} \frac{\iint |\tilde{J}_{qTEM}|^2 \, dxdy}{\left| \iint \tilde{J}_{qTEM} \, dxdy \right|^2} . \tag{6}$$

The value of R_{ac}/R_{dc}=1.72 computed using qTEM FDFD agrees favorably with the measured result of R_{ac}/R_{dc}=1.75 from [2]. The axial electric field distributions determined via qTEM FDFD and MOM [3] also agree well, as shown in Fig. 1. It should be noted that the qTEM FDFD results are obtained using a simulation model defined by the square conductor within a large enclosure (side length = 25.4 cm) as opposed to an isolated conductor.

The qTEM FDTD solver is applied to two diverse applications having similar skin effect and proximity effect characteristics, based on comparable quasi-TEM

properties. A bus conductor in proximity to its enclosure (low frequency) and a microstrip conductor in proximity to its ground plane (high frequency) are shown in Fig. 2. The bus frequency is chosen such that the bus conductor dimensions and skin depth scale by the same constant (3175) relative to the corresponding values for the microstrip. Given that the conductor shapes, aspect ratios and spacings exhibit the "principle of similitude" as defined in [2], the large low frequency bus and the small high frequency microstrip should result in identical values for the R_{ac}/R_{dc} ratio.
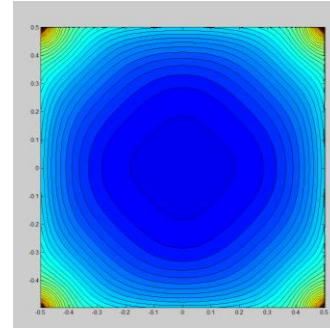
(a)
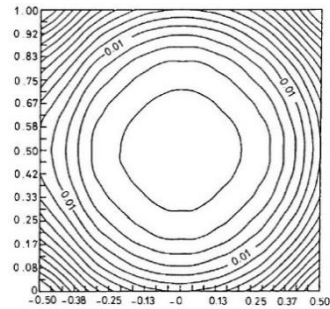
(b)

Fig. 1. Comparison of the axial electric field for a 2.54×2.54cm copper conductor using: (a) qTEM FDTD ($R_{ac}/R_{dc} = 1.72$), and (b) method of moments [3]. The measured value of $R_{ac}/R_{dc} = 1.75$ [2].
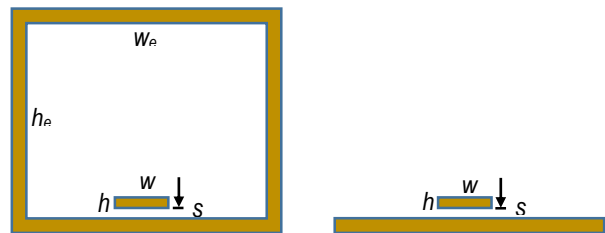
Fig. 2. (a) Bus conductor in proximity to the wall of a large enclosure (copper conductors, $h = 1.27$cm, $w/h = w/s = 5$, $f = 689$ Hz), (b) microstrip conductor in proximity to its ground plane (gold conductors, $h = 4\mu$m, $w/h = w/s = 5$, $f = 9.83$ GHz).

The bus configuration of Fig. 2 (a) was analyzed using the quasi-TEM FDFD scheme and compared with results for the microstrip configuration of Fig. 2 (b), which was analyzed in [4] using the method of moments. The current/field distributions and conductor resistance ratios R_{ac}/R_{dc} given in Fig. 3 are shown to agree well for the bus conductor at 689 Hz and the microstrip conductor at 9.83 GHz.
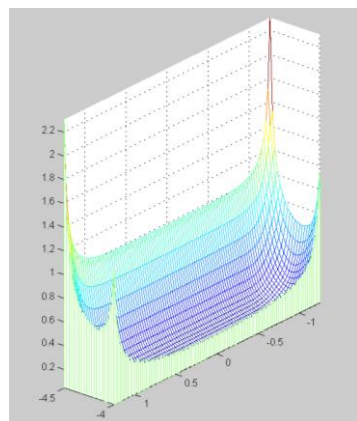
(a)
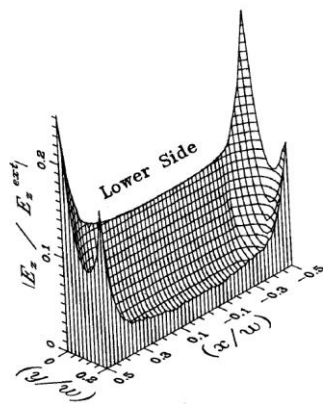
(b)

Fig. 3. Axial electric field for: (a) the bus conductor of Fig. 2 (a) (qTEM FDTD, $R_{ac}/R_{dc} = 3.05$), and (b) the microstrip conductor of Fig. 2 (b) (method of moments [4], $R_{ac}/R_{dc} = 2.95$).

VI. CONCLUSION

A two-dimensional quasi-TEM FDFD scheme has been formulated which is simple to implement for transmission line geometries and computationally efficient. The fundamental physics of proximity and skin effects in transmission lines have been demonstrated through comparisons with experimental measurements and results from other computational techniques.

REFERENCES

[1] R. E. Collin, *Field Theory of Guided Waves*. 2nd ed, IEEE Press, Piscataway, NJ, p. 253, 1991.

[2] S. J. Haefner, "Alternating current resistance of rectangular conductors," *Proc. IRE*, 25, pp. 434-447, 1937.

[3] R. Faraji-Dana and L. Chow, "Edge condition of the field and AC resistance of a rectangular strip," *IEE Proc.*, vol. 137, Pt. H, no. 2, pp. 133-140, Apr. 1990.

[4] R. Faraji-Dana and Y. L. Chow, "The current distribution and AC resistance of a microstrip structure," *IEEE Trans. MTT*, vol. 38, no. 9, pp. 1268-1277, Sept. 1990.

J. Patrick Donohoe received the B.S. and M.S. degrees in Electrical Engineering from Mississippi State University in 1980 and 1982, respectively. He received the Ph.D. degree in Electrical Engineering from the University of Mississippi in 1987. Donohoe joined the Department of Electrical and Computer Engineering at Mississippi State University in 1986 where he currently holds the title of Professor and Paul B. Jacob Chair. His primary research interests include computational electromagnetics, radar, electromagnetic compatibility, electromagnetic properties of composite materials, geomagnetic disturbances, and lightning protection. Donohoe is a Senior Member of IEEE, a registered Professional Engineer in the state of Mississippi, and a Member of Eta Kappa Nu.

DMD-Galerkin Model Order Reduction for Cardiac Propagation Modeling

Riasat Khan

Department of Electrical and Computer Engineering
New Mexico State University
Las Cruces, NM, USA
rkhan@nmsu.edu

Kwong T. Ng

Department of Electrical and Computer Engineering
New Mexico State University
Las Cruces, NM, USA
ngnsr@nmsu.edu

Abstract—Numerical simulation of cardiac propagation is a valuable tool for biomedical research. Due to the inhomogeneous, anisotropic conductive anatomy and complex nonlinear ionic current, numerical modeling of electrical activities in the heart is computationally demanding. Here, model order reduction is used to reduce the simulation time with a minimal effect on the accuracy. The semi-implicit finite difference method is used to discretize the governing equation of the monodomain (reaction-diffusion) model. The dynamic mode decomposition (DMD) is used in combination with the Galerkin projection to reduce the order of the original system. The reduced-order model is obtained by projecting the original system onto a subspace spanned by DMD basis vectors. Numerical results confirm the model order reduction decreases the simulation time by a factor of 5.96 while modifying the computed activation time, maximum time derivative and conduction velocity by 1.24%, 0.129%, and 0.639%, respectively.

Keywords—Dynamic Mode Decomposition, Finite Difference Method, Galerkin Projection, Model Order Reduction, Monodomain, Transmembrane Potential.

I. INTRODUCTION

Numerical modeling of cardiac electrical activities now plays a vital role in the search of effective treatments for arrhythmias. The action potential or transmembrane potential propagating in the heart generates an electric field that gives rise to the electrocardiogram recorded on the surface of a human body. This propagation is commonly simulated using the cardiac monodomain model that consists of a temporal derivative, a spatial Laplacian, and a nonlinear ionic current term [1]. A realistic three-dimensional cardiac tissue has a conductivity tensor (3×3 matrix) that varies continuously according to the fiber orientation in the tissue, so a numerical instead of an analytical solution is required. The numerical solution on appropriate spatial and temporal scales then requires finding multiple unknowns, including the transmembrane potential and ionic current components, at a large number of nodes that form a dense grid.

The transmembrane potentials at all the nodes form a high-dimensional or high-order state vector. As the computational complexity and solution time are proportional to the order of the state vector, researchers have developed order reduction techniques to improve computational efficiency through the definition of a new state vector with a lower order [2]. Among all such techniques, the dynamic mode decomposition (DMD) based approach has been chosen for its recent success in solving nonlinear problems in other scientific fields, e.g., fluid mechanics [3]. It involves only standard matrix computations and can capture frequency features of the dynamic systems [3–5]. DMD basis functions are constructed from the spatial distributions of the unknown of interest at specific time instants, known as the snapshots, which are obtained from an original full-order simulation. A truncated series of these basis functions encapsulate the characteristic dynamics of the original system. The reduced-order surrogate models are obtained by a Galerkin projection of the original system onto the vector space formed by DMD basis functions. DMD, in conjunction with the Galerkin projection, transforms the original full-order system, the discretized monodomain model in the present case, into a lower dimensional system, and subsequently reduces the computational cost. The root-mean-square (RMS) error of the transmembrane potential for the DMD-Galerkin order reduction will be examined together with its effect on solution time, activation time, maximum time derivative, and conduction velocity. To our knowledge, this is the first time computational performance results are presented for the application of model order reduction to finite difference modeling of cardiac propagation.

II. CARDIAC MONODOMAIN MODEL

The cardiac monodomain model derived from current continuity is described by a nonlinear reaction-diffusion partial differential equation,

$$\frac{\partial V_m}{\partial t} = \frac{1}{C_m}\left\{\frac{1}{\beta}\left[\nabla \cdot (\bar{\bar{\sigma}}\,\nabla V_m) + I_s\right] - \sum I_{ion}\right\}, \qquad (1)$$

where V_m is the transmembrane potential (the difference between the intracellular and interstitial potentials), C_m is the cell membrane capacitance per unit area, β is the membrane area per unit volume, and $\bar{\bar{\sigma}}$ denotes the inhomogeneous, anisotropic intracellular conductivity tensor. I_s is the source current that initiates the activation, and ΣI_{ion} represents the total ionic current through the membrane. The monodomain equation involves a temporal derivative and a Laplacian with spatial derivatives, $\nabla \cdot (\bar{\bar{\sigma}}\,\nabla V_m)$. The Laplacian is approximated with the second-order finite difference technique [6]. Temporal discretization is achieved with the semi-implicit or implicit-explicit scheme. Using an implicit method for the Laplacian and an explicit method for the ionic current, it avoids both the stability limit of the explicit technique and costly nonlinear

matrix inversion in a fully implicit method. The spatial and temporal discretization leads to a system of linear algebraic equations that can be put in a matrix form, $[A]\,\bar{x} = \bar{b}$, as:

$$\underbrace{\{[I] - \frac{\theta\Delta t}{c_m\beta}[D_o]\}}_{[A]}\underbrace{\bar{V}_m^{n+1}}_{\bar{x}} =$$

$$\underbrace{\bar{V}_m^n + \frac{(1-\theta)\Delta t}{c_m\beta}[D_o]\bar{V}_m^n + \Delta t[\frac{1}{c_m\beta}\bar{I}_s^{n+1} - \frac{1}{c_m}\sum\bar{I}_{ion}^n]}_{\bar{b}}, \quad (2)$$

where $[I]$ is the identity matrix, $0 \le \theta \le 1$ is a temporal discretization constant, Δt is the time step size, and the bar denotes a vector containing the corresponding quantity's values at all the nodes. $[D_o]\bar{V}_m$ is the finite difference approximation of the Laplacian, and n is the time step index. To obtain the value of $\bar{V}_m$ at time step $n+1$ from that at previous step n, Equation (2) is solved using an iterative conjugate gradient technique with Jacobi preconditioner. The operator splitting has also been implemented in which the time derivative is considered as the sum of several components, and the update of the Laplacian and ionic current term are performed in alternate steps with different time step sizes Δt and $\Delta t_i = \Delta t/5$, respectively [7]. A smaller time step is used for the ionic current to capture its faster temporal variation. The primary objective of this work is to reduce the size of $\bar{V}_m$, by projecting it onto a low-dimensional subspace.

III. DYNAMIC MODE DECOMPOSITION

The reduced-order DMD basis functions are constructed from the training sets or snapshot matrix, which is obtained from a simulation using the original full model. Each column in this matrix is a snapshot consisting of the solution of the state vector $\bar{V}_m$ at a given time instant. The trajectories of the original model at discrete time instants are represented by the rows of the snapshot matrix. The snapshots together capture all the desired spatial and temporal variations for the reduced-order model. For the DMD analysis, a set of M equidistant snapshots (i.e., a snapshot matrix of dimension $\mathbb{R}^{N\times M}$) is considered, where N is the number of state variables. Two zero-mean data matrices are obtained from the snapshot matrix, $\bar{x}(t_i), i = 1, M$:

$$X = [\bar{x}(t_1), \bar{x}(t_2), \dots\dots, \bar{x}(t_{M-1})];$$

$$Y = [\bar{x}(t_2), \bar{x}(t_3), \dots\dots, \bar{x}(t_M)]. \quad (3)$$

Next, a matrix A is constructed from the singular value decomposition (SVD) of X as:

$$A = u^T Y v S^{-1}, \quad (4)$$

where u and v are respectively the left and right singular vectors, and S is a diagonal matrix with the singular values of X. The reduced-order DMD basis functions are finally obtained from the eigen-decomposition of A,

$$\Psi = uW, \quad (5)$$

where Ψ consists of the DMD basis functions and W is made up of the eigenvectors of A. Despite the nonlinearity of the

monodomain model, the magnitudes of the complex eigenvalues decrease fast. The truncated series of the normalized eigenvectors corresponding to eigenvalues with the largest magnitudes give the reduced-order basis functions. By including the eigenvectors with the largest eigenvalues, the reduced-order basis functions preserve the most important dynamics of the original system. The normalization of the DMD basis functions was found to provide a better approximation of the original system [8]. It is interesting to note that the generations of the snapshot matrix and reduced-order basis functions are implemented in an offline stage.

IV. REDUCED-ORDER MODEL FROM GALERKIN PROJECTION METHOD

The full-order monodomain model is projected onto the subspace of DMD basis functions by performing the Galerkin projection technique in two steps. The state vector $\bar{V}_m$, consisting of the transmembrane potential values at all the nodes, is first approximated as a linear combination of the reduced-order DMD modes,

$$\bar{V}_m \approx (\bar{q} = \Psi \bar{z}), \quad (6)$$

where $\bar{z} \in \mathbb{R}^{d\times 1}$ represents the reduced-order state vector. Now, the number of unknowns or dimension is effectively reduced from N to d, with $d << N$, leading to a reduction in the number of equations.

With only spatial discretization, the monodomain equation, with $\bar{V}_m$ approximated by $\bar{q}$, turns into a system of nonlinear ordinary differential equations, $\frac{d\bar{q}}{dt} = \bar{f}(\bar{q}; t)$, where the unknown in each equation is the value of $\bar{q}$ at each node. In the second step, the Galerkin orthogonality condition is enforced such that the residual of the full-order model is orthogonal to the reduced-order DMD modal matrix Ψ,

$$\Psi^T \left(\bar{f}(\bar{q}; t) - \frac{d\bar{q}}{dt} \right) = 0. \quad (7)$$

The above two steps lead to the following DMD-Galerkin reduced-order model equation for the state vector $\bar{z}$,

$$\frac{d\bar{z}}{dt} = \Psi^T f(\Psi\bar{z}; t). \quad (8)$$

The semi-implicit method used for the original full-order model can also be used to perform the temporal discretization in (8).

V. RESULTS AND DISCUSSION

The three-dimensional cardiac tissue was 0.5 cm in x (horizontal) direction and 0.1667 cm in y and z (vertical) direction, as depicted in Fig. 1. Tissue fibers were assumed to lie in planes whose normal was at 20º to the z-axis, and the fiber angle with respect to the x-axis varied linearly in the normal direction with a rotation of 180º per centimeter. The conductivities longitudinal and transversal to the fiber are 0.174 S/m and 0.0193 S/m, respectively. The continuously inhomogeneous conductivity tensor (with respect to the x-y-z coordinate system) was assigned according to the fiber

orientation, and the derivatives of the conductivity tensor elements were evaluated analytically. The ionic current was computed as the sum of six different types of currents using the Luo-Rudy model. A 72×72×72 grid with 373,248 nodes (i.e., a dimension of 373,248) and a 1-ms point source with a constant magnitude and located at a vertex were used. A period of 12 ms was simulated with $\Delta t = 0.005$ ms. Equation (2) was implemented with $\theta = 0.5$. Results were obtained with and without operator splitting.
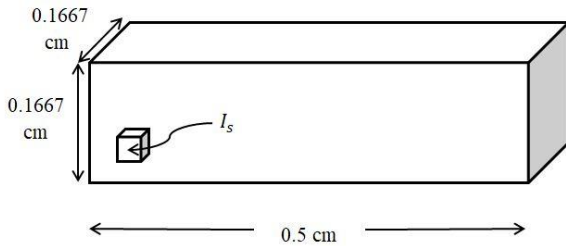
Fig. 1. Schematic representation of the three-dimensional cardiac tissue.

Equidistantly distributed snapshots in the interval $[0, T = 12$ ms] were constructed from a simulation of the original full-order monodomain solution. A specialized software library, Scalable Library for Eigenvalue Problem Computations [9], was utilized to generate the DMD basis functions in an offline stage. The default Krylov-Schur eigenvalue solver and thick-restart Lanczos SVD solver of SLEPc were used to obtain the DMD reduced-order subspace from the snapshot matrix. The largest 24,480 eigenvalues of the A matrix yielded 99.9% of the relative information content or energy, and the DMD subspace had a dimension of 24,480. The number of unknowns or state variables reduced by a factor of ~15 when the reduced-order model was used. Table I summarizes the RMS error (when compared the full-order and reduced-order solutions) and CPU time reduction for the DMD-Galerkin method. The order reduction decreases the CPU time by a factor of 5.96, while maintaining a small RMS error of 0.956 mV. For the operator split method, the RMS error improves to 0.762 mV, but the CPU time reduction factor decreases to 2.59. It is worth mentioning that the ionic current is updated in the operator split method with a smaller time step, which has an adverse effect on the solution time. Fig. 2 shows the close agreement between action potential waveforms obtained at node (36, 36, 36) with the full and reduced-order models using the operator split technique.

Table I. RMS error and CPU time reduction factor of the DMD-Galerkin reduced-order model with and without operator split.

Type of Solution	RMS Error (mV)	CPU Time Reduction Factor
Without operator split	0.956	5.96
Operator split	0.762	2.59

Activation time, maximum time derivative, and conduction velocity are parameters commonly used in electrophysiology studies. Table II gives their values computed using the full and reduced-order models. Specifically, maximum time derivative

is the highest value of the time derivative of the transmembrane potential at node (36, 36, 36). Activation time is the specific time at which the maximum time derivative occurs. Conduction velocity is the distance between any two points divided by the difference between the activation times at these two points. The velocity was calculated for the propagation from node (36, 36, 36) to node (37, 37, 37). As shown in Table II, using model order reduction modifies the activation time, maximum time derivative, and conduction velocity by +1.24%, +0.129%, and −0.639%, respectively. With the use of the operator split, the corresponding modifications are +0.640%, +0.0887%, and −0.321%.
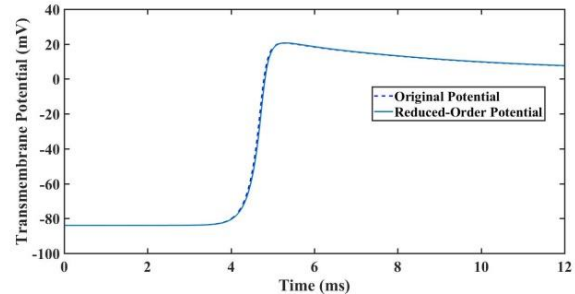
Fig. 2. Transmembrane potential for the full-order and reduced-order solutions with the operator split method.

Table II. Maximum time derivative, activation time, and conduction velocity of the full-order and DMD-Galerkin reduced-order models.

Parameters	Without Operator Split		Operator Split	
	Full-Order	Reduced-Order	Full-Order	Reduced-Order
Activation time (ms)	4.82	4.88	4.69	4.72
Maximum time derivative (V/s)	225.44	225.73	225.58	225.78
Conduction velocity (m/s)	0.313	0.311	0.312	0.311

VI. CONCLUSION

Model order reduction based on dynamic mode decomposition and Galerkin projection has been implemented for a finite difference monodomain model of cardiac tissue. Computational results demonstrate that the proposed approach improves computational efficiency. The dimension of the problem and required CPU time are reduced significantly while introducing less than 1 mV in RMS error and less than 1.3% error in the computed activation time, maximum time derivative, and conduction velocity. Operator splitting increases the accuracy but reduces the improvement in the required CPU time. Future studies may involve the implementation of more robust projection methods as well as techniques that capture the frequency features of cardiac propagation.

REFERENCES

[1] Z. Zhan and K. T. Ng, "Two-dimensional Chebyshev pseudospectral modelling of cardiac propagation," Medical and Biological Engineering and Computing, vol. 38, pp. 311-318, 2000.

[2] W. H. Schilders, v. d. Vorst, A. Henk, and J. Rommes, Model Order Reduction: Theory, Research Aspects, and Applications, 1st ed.,

Springer-Verlag, Heidelberg, Berlin, Germany, 2008.

[3] P. J. Schmid, "Dynamic mode decomposition of numerical and experimental data," *Journal of Fluid Mechanics*, vol. 656, pp. 5-28, 2010.

[4] P. J. Schmid, "Application of the dynamic mode decomposition to experimental data," *Experiments in Fluids*, vol. 50, pp. 1123-1130, 2011.

[5] B. W. Brunton, L. A. Johnson, J. G. Ojemann, and J. N. Kutz, "Extracting spatial-temporal coherent patterns in large-scale neural recordings using dynamic mode decomposition," *Journal of Neuroscience Methods*, vol. 258, pp. 1-15, 2016.

[6] R. Khan and K. T. Ng, "Higher order finite difference modeling of cardiac propagation," *Proceedings of the IEEE International Conference on Bioinformatics and Biomedicine*, pp. 1945-1951, 2017.

[7] S. Krishnamoorthi, M. Sarkar, and W. S. Klug, "Numerical quadrature and operator splitting in finite element methods for cardiac electrophysiology," *International Journal for Numerical Methods in Biomedical Engineering*, vol. 29, pp. 1243-1266, 2013.

[8] R. Khan and K. T. Ng, "Model order reduction for finite difference modeling of cardiac propagation using DMD modes," *Proceedings of the International Applied Computational Electromagnetics Society Symposium*, pp. 1-2, 2018.

[9] V. Hernandez, J. E. Roman, and V. Vidal, "SLEPc: A scalable and flexible toolkit for the solution of eigenvalue problems," *ACM Transactions on Mathematical Software*, vol. 31, pp. 351-362, 2005.

Riasat Khan is an Assistant Professor of the Electrical and Computer Engineering Department at North South University, Bangladesh. He obtained his M.S. and Ph.D. degrees in Electrical Engineering from New Mexico State University, Las Cruces, NM. His research interests include cardiac electrophysiology, bioelectromagnetics, computational electromagnetics, model order reduction, and power electronics.

Kwong T. Ng is a Professor of the Electrical and Computer Engineering Department at New Mexico State University, Las Cruces, NM. He received the M.S. and Ph.D. degrees from The Ohio State University, Columbus, in 1981 and 1985, respectively. His current research interests include bioelectromagnetics, computational electromagnetics, and biomedical instrumentation.

Efficient Adaptive Qualitative Methods for 3D Inverse Scattering Problems

Koung Hee Leem, Jun Liu, and George Pelekanos

Department of Mathematics and Statistics
Southern Illinois University Edwardsville, Edwardsville, IL 62026, USA
kleem@siue.edu, juliu@siue.edu, gpeleka@siue.edu

Abstract – In this paper we extend our recently developed 2D adaptive factorization method for efficiently solving 3D inverse acoustic and electromagnetic scattering problems. Different from the previously used Simpson rule, we propose to use Gaussian quadrature rule, which provides improved reconstruction quality. Several numerical examples are presented to illustrate the effectiveness of our proposed adaptive method. To achieve better efficiency and robustness, we have based our implementation on the existing adaptive quadrature codes.

Index Terms – adaptive Gaussian quadrature, factorization method, inverse scattering, linear sampling method.

I. INTRODUCTION

Inverse scattering problems [1] are of great importance in many fields of science and engineering, such as radar and sonar, medical imaging, and non-destructive testing. Efficient numerical algorithms for solving such nonlinear inverse problems have gained lots of recent attention, but the computational challenges remain for large-scale 3D applications. This paper is concerned with new efficient adaptive qualitative algorithms for solving 3D inverse scattering problems.

Depending on the amount of *a priori* knowledge of the physical properties of the underlying scatterer and the requirement of reconstruction quality in terms of resolution, current algorithms for inverse scattering problems can be roughly categorized into two groups: (i) *nonlinear optimization methods*, and (ii) *qualitative methods*. The nonlinear optimization methods [2–4] often involve an expensive iterative procedure, where a direct scattering problem needs to be (approximately) solved at each iteration. Although such optimization approaches require less number of incident fields, they do require *a priori* knowledge of the scatterer, such as boundary conditions (e.g, sound-soft or not) and its number of connected components, which may not be available in practice.

The established qualitative methods [5–7], including the linear sampling method [8] and the factorization method [9], have the key advantage of not requiring the aforementioned *a priori* information about the unknown scatterer. Moreover, qualitative methods were shown to be computationally parallelizable and faster than the nonlinear optimization methods. Nevertheless, the standard qualitative methods need to solve a large number of linear far-field equations over all sampling points of a possible very fine mesh over a large search domain, which can still be quite expensive in 3D applications involving large targets. Furthermore, qualitative methods often require a large amount of far-field measurements, although they can still deliver rough approximations with limited aperture data.

Within the framework of qualitative methods, many recent studies [10–12] have greatly improved the efficiency and applicability of the original linear sampling algorithm. In alignment with our proposed method, we point out that another adaptive scheme was proposed in [13], where only those coarse boundary cubes intersecting with a chosen cut-off plane is further subdivided into eight ($2 \times 2 \times 2$) sub-cubes. The multilevel linear sampling method (MLSM) [11] also demonstrates some local adaptive behavior by recursively labeling and removing non-boundary cells in different levels. However, the MLSM requires very careful numerical treatment on classifying all the square cells in order to avoid introducing breakage cells that should not be removed. We refer to [14] for a comparison between our adaptive factorization method and the MLSM in 2D cases. The more recently developed direct sampling methods [15, 16] have the benefit of using much less far-field data and avoiding directly solving ill-posed integral equations, which hence are more robust to data noise. Nevertheless, the mathematical foundation of such direct sampling methods is far less established.

We organize our paper as follows. In Section II, we briefly review the linear sampling and factorization methods. In Section III, based on adaptive Gaussian quadrature, we propose an adaptive factorization method that can automatically distribute more sampling points near the boundary of the scatterers. Section IV contains several numerical examples, which demonstrate the effectiveness of our proposed adaptive factorization method in comparison with the standard factorization method. Finally, some conclusions and remarks are given in Section V.

II. A REVIEW OF QUALITATIVE METHODS

In this section, following [1], we briefly describe the linear sampling and factorization methods for solving inverse acoustic obstacle scattering problems. For the purpose of exposition, we will only consider the scattering of a time harmonic acoustic wave by a bounded impenetrable sound-soft obstacle $D \subset \mathbb{R}^3$ and a C^2 boundary ∂D. Given an incident wave field u^i, its propagation against the obstacle D which is situated in a homogeneous medium will generate a scattered wave field u^s. Consider a time-harmonic plane wave $u^i(x) = e^{ikx \cdot \theta}$, where θ is the incident direction with $|\theta| = 1$ and $k > 0$ is the wave number. Let $u = u^i + u^s$ be the total field, which satisfies the following exterior Helmholtz equation:

$$\Delta u(x) + k^2 u(x) = 0, \quad x \in \mathbb{R}^3 \backslash \overline{D}, \quad (1)$$

subject to the Dirichlet boundary condition (sound-soft)

$$u = 0, \quad \text{on} \quad \partial D, \quad (2)$$

and the Sommerfeld radiation condition (with $r = |x|$)

$$\lim_{r \to \infty} r \left(\frac{\partial u^s}{\partial r} - i k u^s \right) = 0. \quad (3)$$

The above direct obstacle scattering problem (1-3) has a unique solution $u \in C^2(\mathbb{R}^3 \backslash \overline{D}) \bigcap C(\mathbb{R}^3 \backslash D)$. In addition, the scattered field u^s has an asymptotic behavior:

$$u^s(x) = \frac{e^{ikr}}{r} u_\infty(\hat{x}, \theta) + O(r^{-2}),$$

as $r = |x| \to \infty$ uniformly in all directions, where $\hat{x} = x/|x|$ is the observation direction and u_∞ is called the far-field pattern of u^s. In general, the far-field pattern u_∞ also depends on the scatterer D and the wave number k.

The inverse obstacle scattering problem is then to determine the shape of D from many noisy far-field measurements $u_\infty(\hat{x}, \theta)$ for all $\hat{x}, \theta \in \mathbb{S}$ and a fixed $k > 0$. In other words, we need to invert the following abstract operator equation:

$$\mathscr{G}(\partial D) = u_\infty(\hat{x}, \theta), \quad \hat{x}, \theta \in \mathbb{S},$$

where the abstract operator $\mathscr{G}$ maps the boundary of the obstacle D to the corresponding far-field pattern for all pair of directions $(\hat{x}, \theta)$. This operator equation turns out to be highly nonlinear and severely ill-posed, which has been solved by Newton's method [2, 3], with the Fréchet derivative of $\mathscr{G}$ being inverted using Tikhonov regularization at each iteration. It is well-known that such nonlinear iterative methods are costly in practical computations and their effectiveness often depends on the faithfulness of the initial guess (i.e., a priori information) of the scatterer ∂D. In a typical setting, however, it is assumed that we know no or very limited information about the physical properties (i.e., sound-soft or penetrable) of the obstacle. Hence, the above mentioned linear sampling method [17] and its variants are widely used in practice, although they indeed have certain limitations [18, 19].

A. The linear sampling method

The linear sampling method (LSM) suggests to solve the following linear integral equation:

$$(Fg)(\hat{x}) = \Phi_\infty(\hat{x}, z) := \frac{1}{4\pi} e^{-ik\hat{x} \cdot z}, \quad z \in \mathbb{R}^3, \quad (4)$$

where the far-field operator $F : L^2(\mathbb{S}) \to L^2(\mathbb{S})$ is defined by:

$$(Fg)(\hat{x}) := \int_\mathbb{S} u_\infty(\hat{x}, d) g(d) ds(d),$$

and $\Phi_\infty(\hat{x}, z)$ is the far field pattern of the fundamental solution $\Phi(\cdot, z)$ of the Helmholtz equation. It was shown [5] that for every $\epsilon > 0$, there exists a function $g_z := g(\cdot, z) \in L^2(\mathbb{S})$ such that $\|Fg - \Phi_\infty\| < \epsilon$ and $\|g_z\|$ becomes unbounded as z approaches the boundary ∂D. Here $\| \cdot \|$ denotes the standard L^2 norm.

Based on this fact, the basic idea of the linear sampling method is to solve the above far-field equation (4) for each sampling point z of a uniformly spaced mesh grid in $\mathbb{R}^3$ containing D, and then plot a profile with the computed values of the indicator function $\|g_z\|$. The obstacle boundary ∂D can then be identified as the locus of those points z where $\|g_z\|$ changes sharply. However, a mathematical justification of such a linear sample method turns out to be nontrivial, since we in general do not have an explicit characterization of the range of the far field operator F. Such a theoretical gap, however, does not prevent its popularity and success in practice.

B. The factorization method

The factorization method (FM) [20], mainly as a mathematical improvement of the linear sampling method, provides an explicit and theoretically well-justified characterization for the support of a scattering object. It is based on the similar idea that a point $z \in \mathbb{R}^3$ belongs to the scatter D if and only if the test function $\Phi_\infty(\hat{x}, z)$ belongs to the range of a 'factorized' far-field operator. In particular, the FM approximately solves the following 'factorized' far-field equation:

$$((F^*F)^{1/4} g_z)(\hat{x}) = r_z(\hat{x}) := \Phi_\infty(\hat{x}, z),$$

by computing the norm of a possible solution g_z using Pickard's criterion for all sampling points z. Plotting of the values of these norms $\|g_z\|$ yields a profile of the scattering object, which allows us to identify the obstacle shape. For this purpose, we define the following continuous indicator function:

$$W_c(z) = \frac{1}{\|g_z\|}.$$

Then the FM is based on the following equivalence:
$$z \in D \Leftrightarrow r_z \in \text{Range}((F^*F)^{1/4}) \Leftrightarrow W_c(z)^{-1} < \infty.$$

In practical computations, one has to work with a finite dimensional approximation of the far-field operator F. Let F_n be the discretized far-field operator of dimension n that constructed by Nyström method [1], and its singular system is given by $\{\sigma_j, u_j, v_j\}_{j=1}^n$, where σ_j, u_j, and

v_j is the j-th singular value, left and right singular vector of F_n, respectively. In numerical implementations, we compute the corresponding discrete indicator function:

$$W_c(z) \approx W(z) := \left(\sum_{j=1}^{n} \frac{|v_j^\mathsf{T} r_z|}{\sigma_j} \right)^{-1}.$$

The standard FM then determines the shape of the scatterer D as the location of those points z where $W(z)$ becomes significantly large, since the corresponding series defining $\|g_z\|$ fails to converge whenever $z \notin D$. In a standard implementation, one has to compute $W(z)$ over a possibly very fine uniformly spaced mesh that adequately covers the search domain Ω. More specifically, the factorization method consists of four steps: *(1) Measure the far-field patterns $u_\infty(\hat{x}_j, \theta_i)$ for a sufficient number of different directions $\hat{x}_j$ and θ_i; (2) Select an estimated large search domain Ω covering D and discretize it with a fine uniform mesh $\mathcal{T}_h$; (3) Compute the indicator functional $W(z)$ for all sampling points $z \in \mathcal{T}_h$; (4) Plot the profile of $W(z)$ and determine D with a heuristic cut-off value $c > 0$.*

This straightforward sampling procedure, however, can be computationally very expensive, especially for those 3D applications involving large obstacles. For example, given an $N \times N \times N$ uniform mesh, the standard implementation needs to compute $W(z)$ at N^3 different sampling points, which hence has a time complexity of $O(N^3)$ if we treat the computation of each $\|g_z\|$ as one operation. In fact, compute each $\|g_z\|$ requires a matrix-vector product with $O(n^2)$ operations, if assuming the singular-value decomposition (SVD) of F_n has been computed (only once).

III. ADAPTIVE QUALITATIVE METHODS

In this section, we introduce an adaptive factorization method based on adaptive quadrature methods. The concept of adaptive discretization or adaptive mesh refinement has been well studied in scientific computing, such as in numerical integration [21] and adaptive finite element methods [22]. Adaptive quadrature has a long and very rich history with many slightly different versions, where the commonly used error estimate techniques are reviewed in [23].

The key idea behind an adaptive method is to adaptively allocate more grid (sampling) points to those regions where it becomes necessarily. Compared with the already established MLSM, our proposed adaptive factorization method (AFM) [14], based on adaptive global integration, has the advantage of better accuracy and robustness in the reconstruction of multiple obstacles and easier generalization to 3D problems. Furthermore, our AFM doesn't require selection of any cut-off values as in MLSM. The similar idea of adaptive allocation of unknowns/grid points (e.g., multi-resolution inversion)

has also been widely discussed in microwave imaging [24–26].

Inspired by the fact that the indicator function $W_c(z)$ shows very sharp changes across the boundary of the obstacle domain, we propose to treat the indicator function $W_c : \mathbb{R}^3 \to \mathbb{R}_+$ as a function to be integrated over the global search domain Ω that contains the obstacle(s). To adaptively concentrate more sampling points near the unknown boundary ∂D of the obstacle D, we propose to utilize the efficient 3D adaptive Gaussian quadrature [27] to compute the 3D integration:

$$I(W_c) = \iiint_\Omega W_c(z) \, dV,$$

where $\Omega \subset \mathbb{R}^3$ is the estimated cube. The above integration is clearly well defined from the definition and boundedness of $W_c(z)$. It is important to mention here, that in our AFM, we are only interested in obtaining the adaptively generated quadrature points and use them as effective sampling points towards the reconstruction of the profile of the scatterer.

For simplicity, assume $\Omega = [-a, a]^3$. The standard m-point Gaussian(-Legendre) quadrature rule for approximating $I(W_c)$ reads:

$$I(W_c) \approx G_m(W) := \sum_{i=1}^{m} \sum_{j=1}^{m} \sum_{l=1}^{m} w_i w_j w_l W(x_i, y_j, z_l),$$

where $\{w_i, w_j, w_l\}$ are the Gaussian quadrature weights and $\{x_i, y_j, z_l\}$ are the Gaussian quadrature nodes. The above Gaussian quadrature rule is exact for multivariate polynomials of degree $2m - 1$ or less and is an accurate approximation when W_c can be well-approximated by multivariate polynomials.

Algorithm 1 AFM based on 3D Gaussian quadrature:
Initialization: $\Omega = [-a, a]^3, tol$
Output: A set of computed sampling points $\mathcal{A}$

1: **procedure** Q=AFM(Ω)
2:      $I_1 = G_5(W)$ over Ω
3:      $I_2 = G_8(W)$ over Ω
4:      Add new quadrature (sampling) points to $\mathcal{A}$
5:      **if** $|I_1 - I_2| < tol$ **then**   ▷ Exit Recursion
6:          $Q = I_2$
7:      **else**   ▷ Enter Recursion
8:          Divide Ω into eight subcubes $\{\Omega_j\}_{j=1}^8$
9:          For each Ω_j, compute Q_j =AFM(Ω_j)
10:         Add eight sub-integrals: $Q = \sum_{j=1}^8 Q_j$
11:      **end if**
12: **end procedure**

The 3D adaptive Gaussian quadrature is based on the principle of divide and conquer, where each cube is recursively divided into eight ($2 \times 2 \times 2$) subcubes until the difference between two different quadrature approximations (e.g., G_5 and G_8, other combinations can also be used) for the integral over the same cube becomes

less than a user-supplied tolerance tol. Following [28, p. 358], our AFM algorithm is summarized in Algorithm 1, where we usually choose tol to be between 10^{-3} and 10^{-5} based on the domain size and scatterer shape.

With the set $\mathcal{A}$ of sampling points and indicator values computed by Algorithm 1, we can obtain a full-mesh profile via standard scattered data interpolation (i.e., the `scatteredInterpolant` function in MAT-LAB). The total computational cost (or maximum level of recursion) of the algorithm depends on tol and the shape of the indicator function W [14]. Due to the dramatic changes of W around the obstacle boundary ∂D, one would expect that more quadrature points are automatically clustered near the boundary, which therefore achieves the purpose of qualitatively reconstructing the obstacle boundary efficiently with less sampling points.
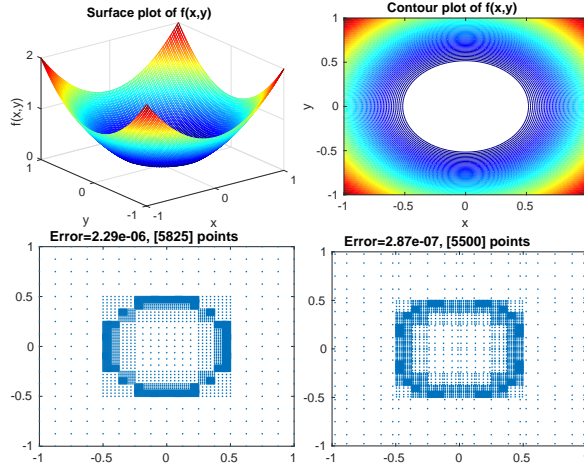
Fig. 1. Top: the surface (left) and contour (right) of a 2D indicator function $f(x,y) = (1/4 + (x^2 + y^2))/2 + \sqrt{(1/4 - (x^2 + y^2))^2}/2$. Bottom: sampling points used by the adaptive Simpson quadrature (left) and the adaptive Gaussian quadrature (right), respectively.

For the sake of easier visualization, we first illustrate in Fig. 1 the distribution of the adaptively generated quadrature (sampling) points with a bowl-shaped 2D test indicator function, where both the 2D adaptive Simpson quadrature and Gaussian quadrature are tested. As expected, the adaptive Gaussian quadrature is more accurate (compare error) than adaptive Simpson quadrature. It is clear that more quadrature points are clustered along the inner circle that indicating sharp changes in function values. Similarly, we also plot in Fig. 2 the isosurface (with isovalue 0.5) and generated quadrature (sampling) points with a 3D test indicator function, where the generated Gaussian quadrature points closely track the function shape. Our AFM implementation is based on the well-tested adaptive Gaussian quadrature MATLAB codes developed in [27], which was shown to be very effective in treating functions with sharp gradients and

cusps. Our main efforts lie in embedding the sampling procedure into this code to obtain an efficient implementation of AFM, without reinventing the wheels.
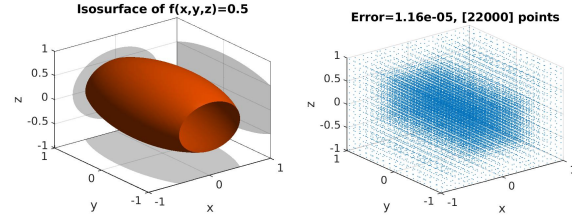
Fig. 2. The isosurface plot (left) of a 3D test indicator function $f(x,y,z) = (1/4 + (x^2 + y^2/4 + z^2))/2 + \sqrt{(1/4 - (x^2 + y^2/4 + z^2))^2}/2$. The generated sampling points by the adaptive Gaussian quadrature (right).

IV. NUMERICAL RESULTS

In this section, we provide some numerical examples to demonstrate the effectiveness of our proposed AFM. All simulations are performed using MAT-LAB R2017b on a Dell Desktop PC with i7-7700K CPU@4.2GHz and 32GB RAM. The CPU time (in seconds) is estimated by timing functions *tic/toc*. The used far-field data are provided by the authors of the cited references, where they take n equidistantly distributed incident and observation directions on the unit sphere. To simulate noisy data, the discrete far-field matrix $F_n \in \mathbb{C}^{n \times n}$ is perturbed into $F_n^\delta = F_n + \epsilon(E_1 + iE_2) \cdot * F_n$, where E_1 and E_2 are two random matrices with entries uniformly distributed in $[-1, 1]$. We choose $\epsilon = 10\%$ and denote $\delta := \|F_n - F_n^\delta\|_2$. For the standard FM, the Tikhonov regularization parameter is computed point-wisely using the `fzero` function at each sampling point via Morozonv's discrepancy principle [17], which costs about half of the total computation time. Inspired by the idea of one-shot regularization [29], in our AFM, we use a global regularization parameter that is estimated from the average of the 125 regularization parameters computed over a $5 \times 5 \times 5$ coarse mesh. The used isovalue γ for plotting isosurfaces is determined by the following global mean and standard deviation heuristic [30]:

$$\gamma = \text{mean}_{z \in \mathcal{T}_h}(W(z)) + 2 \text{ std}_{z \in \mathcal{T}_h}(W(z)).$$

A. Inverse acoustic scattering examples [31]

In Fig. 3, we plotted the reconstructed isosurfaces of four different shapes (acorn, cushion, and ellipsoid). Here we used a 258×258 far-field data with a $60 \times 60 \times 60$ sampling mesh points within a cube of size $[-1.5, 1.5]^3$, where our AFM (with $tol = 10^{-3}$) is about 50–100 times faster than the standard FM (this can also be inferred by comparing the number of total sampling points). As we can observe, the reconstructed iso-surfaces by our AFM are hardly distinguishable from the standard FM, although they do have slightly rougher surfaces due to the used scattered interpolation (not counted into CPU

time) based on much less number of adaptively generated quadrature points. Notice the disconnected peanut shape is due to the over-estimated isovalue from large variation in the indicator function. The reconstruction quality of our AFM can be further improved if more sampling points are used by choosing a smaller tol.
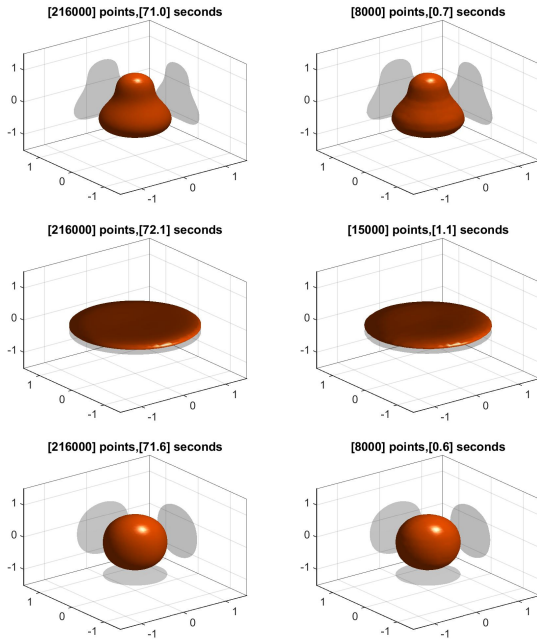
Fig. 3. Isosurfaces by the FM (left) and our AFM (right). From top to bottom: acorn, cushion, and ellipsoid shape.

B. Inverse electromagnetic scattering examples [5]

Due to limited space, we refer readers to [8] for the formulation of inverse electromagnetic scattering model and the corresponding linear sampling method. The application of our AFM to such problems is straightforward, but its overall computational cost becomes significantly higher due to expensive vector cross product operations. In Fig. 4 and Fig. 5, we plot the reconstructed isosurfaces of a teapot (with $k = 28, n = 252$ and a $50 \times 50 \times 50$ mesh within a cube of size $[-0.5, 0.5]^3$) and an aircraft (with $k = 4\pi, n = 252$ and a $80 \times 120 \times 160$ mesh within a box of size $[-1, 1] \times [-2, 2] \times [0, 4]$) by the standard FM and our AFM (with $tol = 10^{-4}$), respectively. Both scatterers have some very small detail feature that take more quadrature points to achieve a satisfactory resolution. In spite of some noticeable difference in detail feature, our AFM captures the major characteristics qualitatively and is significantly faster than the standard FM. The difference in size is due to slightly different regularization parameters and isovalues. The huge saving in computation time , or reduction in the total number of sampling points, makes our AFM very attractive to practical 3D applications.
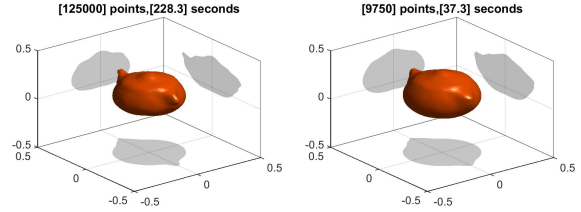
Fig. 4. Teapot by the FM (left) and our AFM (right).
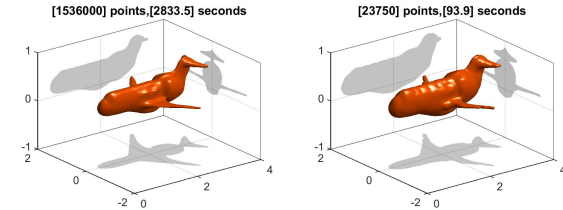
Fig. 5. Aircraft by the FM (left) and our AFM (right).

V. CONCLUSION

This paper presents an adaptive Gaussian quadrature based factorization method for solving 3D inverse obstacle scattering problems. It extends our previously developed 2D adaptive factorization method that was built upon 2D adaptive Simpson quadrature rule. With several benchmark inverse acoustic and electromagnetic scattering examples, the reported numerical results suggest our AFM achieves a dramatic improvement in the computational efficiency over the standard FM, while keeping a very satisfactory reconstruction quality.

One possible future work is to improve the computational efficiency of our AFM by using non-rectangular Gaussian quadrature rules to produce more irregular sampling points along a scatter of arbitrary shape.

REFERENCES

[1] D. Colton and R. Kress, *Inverse Acoustic and Electromagnetic Scattering Theory*, Springer New York, 2012.

[2] A. Roger, "Newton-Kantorovitch algorithm applied to an electromagnetic inverse problem," *IEEE Transactions on Antennas and Propagation*, vol. 29, no. 2, pp. 232–238, 1981.

[3] R. D. Murch, D. G. H. Tan, and D. J. N. Wall, "Newton-Kantorovich method applied to two-dimensional inverse scattering for an exterior Helmholtz problem," *Inverse Problems*, vol. 4, no. 4, pp. 1117–1128, 1988.

[4] G. Giorgi, M. Brignone, R. Aramini, and M. Piana, "Application of the inhomogeneous Lippmann–Schwinger equation to inverse scattering problems," *SIAM Journal on Applied Mathematics*, vol. 73, no. 1, pp. 212–231, 2013.

[5] D. Colton, H. Haddar, and M. Piana, "The linear sampling method in inverse electromagnetic scat-

tering theory," *Inverse Problems*, vol. 19, no. 6, pp. S105–S137, 2003.

[6] T. Arens and A. Lechleiter, "The linear sampling method revisited," *Journal of Integral Equations and Applications*, vol. 21, no. 2, pp. 179–202, 2009.

[7] F. Cakoni and D. Colton, *A Qualitative Approach to Inverse Scattering Theory*, Springer US, 2013.

[8] F. Cakoni, D. Colton, and P. Monk, *The Linear Sampling Method in Inverse Electromagnetic Scattering*, SIAM, Philadelphia, PA., 2011.

[9] A. Kirsch and N. Grinberg, *The Factorization Method for Inverse Problems*, Oxford University Press, Oxford, 2008.

[10] M. Brignone, G. Bozza, R. Aramini, M. Pastorino, and M. Piana, "A fully no-sampling formulation of the linear sampling method for three-dimensional inverse electromagnetic scattering problems," *Inverse Problems*, vol. 25, no. 1, p. 015014, 2008.

[11] J. Li, H. Liu, and J. Zou, "Multilevel linear sampling method for inverse scattering problems," *SIAM Journal on Scientific Computing*, vol. 30, no. 3, pp. 1228–1250, 2008.

[12] Y. Grisel, V. Mouysset, P. A. Mazet, and J. P. Raymond, "Adaptive refinement and selection process through defect localization for reconstructing an inhomogeneous refraction index," *Inverse Problems*, vol. 30, no. 7, p. 075003, 2014.

[13] D. Colton, K. Giebermann, and P. Monk, "A regularized sampling method for solving three-dimensional inverse scattering problems," *SIAM Journal on Scientific Computing*, vol. 21, no. 6, pp. 2316–2330, 2000.

[14] K. H. Leem, J. Liu, and G. Pelekanos, "An adaptive quadrature-based factorization method for inverse acoustic scattering problems," *Inverse Problems in Science and Engineering*, 2018, to appear. DOI:10.1080/17415977.2018.1459600.

[15] X. Liu, "A novel sampling method for multiple multiscale targets from scattering amplitudes at a fixed frequency," *Inverse Problems*, vol. 33, no. 8, p. 085011, 2017.

[16] K. H. Leem, J. Liu, and G. Pelekanos, "Two direct factorization methods for inverse scattering problems," *Inverse Problems*, vol. 34, no. 12, p. 125004, 2018.

[17] D. Colton, M. Piana, and R. Potthast, "A simple method using Morozov's discrepancy principle for solving inverse scattering problems," *Inverse Problems*, vol. 13, no. 6, pp. 1477–1493, 1997.

[18] A. G. Ramm and S. Gutman, "Analysis of a linear sampling method for identification of obstacles," *Acta Mathematicae Applicatae Sinica, English Series*, vol. 21, no. 3, pp. 399–404, 2005.

[19] A. Liseno and R. Pierri, "Shape reconstruction by the spectral data of the far-field operator: analysis and performances," *IEEE Transactions on Antennas and Propagation*, vol. 52, no. 3, pp. 899–903, 2004.

[20] A. Kirsch, "Characterization of the shape of a scattering obstacle using the spectral data of the far field operator," *Inverse Problems*, vol. 14, no. 6, pp. 1489–1512, 1998.

[21] W. Gander and W. Gautschi, "Adaptive quadrature—Revisited," *BIT Numerical Mathematics*, vol. 40, no. 1, pp. 84–101, Mar 2000.

[22] L. Beilina, M. V. Klibanov, and M. Y. Kokurin, "Adaptivity with relaxation for ill-posed problems and global convergence for a coefficient inverse problem," *Journal of Mathematical Sciences*, vol. 167, no. 3, pp. 279–325, 2010.

[23] P. Gonnet, "A review of error estimation in adaptive quadrature," *ACM Computing Surveys*, vol. 44, no. 4, pp. 1–36, 2012.

[24] S. Caorsi, M. Donelli, D. Franceschini, and A. Massa, "A new methodology based on an iterative multiscaling for microwave imaging," *IEEE Transactions on Microwave Theory and Techniques*, vol. 51, no. 4, pp. 1162–1173, 2003.

[25] X. Ye, L. Poli, G. Oliveri, Y. Zhong, K. Agarwal, A. Massa, and X. Chen, "Multi-resolution subspace-based optimization method for solving three-dimensional inverse scattering problems," *Journal of the Optical Society of America A*, vol. 32, no. 11, p. 2218, 2015.

[26] N. Anselmi, L. Poli, G. Oliveri, and A. Massa, "Iterative multiresolution bayesian CS for microwave imaging," *IEEE Transactions on Antennas and Propagation*, vol. 66, no. 7, pp. 3665–3677, 2018.

[27] S. Mousavi, J. Pask, and N. Sukumar, "Efficient adaptive integration of functions with sharp gradients and cusps in n-dimensional parallelepipeds," *International Journal for Numerical Methods in Engineering*, vol. 91, no. 4, pp. 343–357, 2012.

[28] M. Heath, *Scientific Computing: An Introductory Survey*, McGraw-Hill, 2002.

[29] R. Aramini, M. Brignone, and M. Piana, "The linear sampling method without sampling," *Inverse Problems*, vol. 22, no. 6, pp. 2237–2254, 2006.

[30] M. Fares, S. Gratton, and P. L. Toint, "SVD-tail: a new linear-sampling reconstruction method for inverse scattering problems," *Inverse Problems*, vol. 25, no. 9, p. 095013, 2009.

[31] K. A. Anagnostopoulos, A. Charalambopoulos, and A. Kleefeld, "The factorization method for the acoustic transmission problem," *Inverse Problems*, vol. 29, no. 11, p. 115015, 2013.

Enabling Batteryless Wearables and Implants

Wei-Chuan Chen, Brock DeLong, Ramandeep Vilkhu, and Asimina Kiourti

Department of Electrical and Computer Engineering
The Ohio State University, Columbus, OH, 43212, USA
{chen.5825, delong.178, vilkhu.2, kiourti.1}@osu.edu

Abstract ─ Powering of wearables and implants is a critical challenge. Conventional batteries are rigid and require frequent recharging and/or replacement, making their use cumbersome and obtrusive for body-area applications. Instead, this paper discusses three novel technologies that our group has recently explored toward batteryless wearables and implants, viz. a) DC power generation using fabric electrochemistry, b) Radio-Frequency (RF) power harvesting, and c) fully-passive RF backscattering. Notably, the proposed technologies bring forward transformational possibilities for batteryless sensing and/or stimulation.

Index Terms ─ Batteryless, implants, power harvesting, RF backscattering, wearables, wireless powering.

I. INTRODUCTION

Wearable and implanted electronics are recently gaining significant attention for a wide range of applications (medical, sports, tracking, consumer electronics, etc.) [1]-[5]. Such devices may operate as sensors of human vitals (temperature, glucose levels, brain signals, etc.), or as stimulators of the central or peripheral nervous system. In either case, powering of wearables and implants is a critical challenge. The conventional way of powering such devices entails use of batteries. Expectedly, batteries are typically bulky and rigid, and require frequent recharging and/or replacement. As such, they are cumbersome, obtrusive, and thus, undesirable for body-area applications

With these in mind, this paper discusses three novel technologies that our group has recently explored toward batteryless wearables and implants, viz. a) DC power generation using fabric electrochemistry, b) Radio-Frequency (RF) power harvesting, and c) fully-passive RF backscattering. Notably, the proposed technologies bring forward transformational possibilities for batteryless sensing and/or stimulation.

II. DC POWER GENERATION USING FABRIC ELECTROCHEMISTRY

We have recently introduced a new class of electrochemical fabrics which, when moistened by a conductive liquid, generate DC power capable of powering wearable electronics [6], [7]. Contrary to conventional rigid power generation techniques (batteries), the proposed electrochemical fabrics are fully-flexible, feel and behave like regular clothing, do not include any heavy or rigid components, and provide DC power via moistening by readily available conductive liquids. Generation of DC power is achieved via a redox reaction, which occurs between the Zinc to Silver Oxide-printed electrodes (anodes and cathodes), facilitated by a conductive liquid that enables electron movement. These anodes and cathodes are 'printed' onto the flexible fabrics with the use of polyvinyl binders, and can further be inter-connected via conductive E-threads to boost the generated voltage/current.

Figure 1 (a) shows the proposed concept of inter-connecting multiple 'printed' batteries on flexible fabrics, while Fig. 1 (b) shows a single 'printed' battery cell created as a proof-of-concept. Notably, the latter single cell has been demonstrated to generate voltage and current levels as high as 1.4 V and 100 µA, respectively. Higher voltage and current levels can be achieved in future via the inter-connections mentioned above.
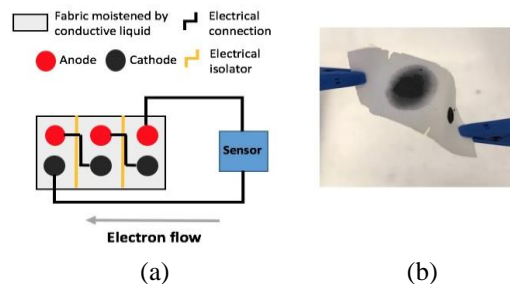
Fig. 1. (a) Proposed concept of 'printed' battery cells wired in series on a fabric connected to a sensor, and (b) a single 'printed' battery cell deposited on a fabric as a proof-of-concept [6], [7].

III. RF POWER HARVESTING

Wireless activation of implanted stimulators/ actuators can significantly improve their practicality and unobtrusiveness while dissolving critical concerns

associated with patient safety. As an example, Fig. 2 shows an implanted and wirelesss actuator placed right under the skin, and incorporating a miniaturized implanted antenna and a rectifier (rectenna). The first is responsible for capturing the Radio-Frequency (RF) waves transmitted by an exterior antenna placed in close proximity, and the latter converts the RF energy to DC. This DC power may then be either stored in a low-leakage capacitor as in [8], or used in real-time for medical device actuation. The external transmitter can be placed in very close proximity to the implant and fabricated on e-textiles for unobtrusive integration into shirts, wrap-around garments, etc.

A proof-of-concept implanted and batteryless actuator has already been demonstrated. At this stage, it occupies a 15 mm x 25 mm footprint, and can be encapsulated into polymers for biocompatibility and improved matching. We have also demonstrated low power rectifiers with conversion efficiency above 70% [9]. In this particular case, the RF device operated at 2.4 GHz.
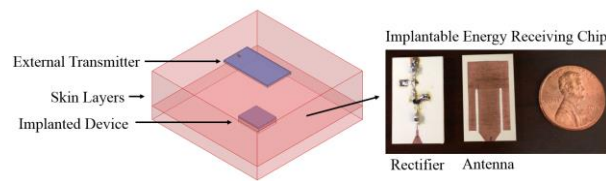
Fig. 2. RF power harvesting technology used to activate a batteryless device implanted inside the human body [9].
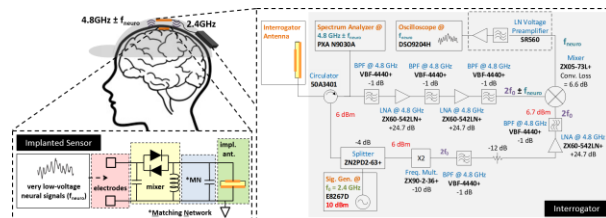
Fig. 3. Fully-passive RF backscattering technology used to collect deep-brain signals via a batteryless implant [11], [12].

IV. FULLY-PASSIVE RF BACKSCATTERING

Fully-passive RF backscattering is recently gaining significant attention in the area of batteryless brain implants. The conventional way of detecting deep brain signals relies on integrated circuits (IC) chips [10]. However, the latter consist of a multitude of power-hungry components (pre-amplifier, multiplexer, analog-digital converters etc.), that require batteries and generate excessive amounts of heat in the surrounding tissues. As an alternative, we recently proposed batteryless and wireless brain implants that rely on fully-passive RF

backscattering for signal acquisition [11], [12].

The block diagram of our proposed neuropotential monitoring system is depicted in Fig. 3. The system is comprised of two sub-systems: the brain implant and the exterior interrogator. The interrogator sends a carrier (2.4 GHz) to activate the implant. That, in return, detects the neural signals (f_{neuro}). To receive these signals at the interrogator, they are first mixed with the carrier at the implant prior to transmission. To do so, we employed an anti-parallel diode pair (APDP) mixer within the implant. The latter captures both positive and negative legs of the 2.4 GHz carrier, allowing for high-efficiency harmonic mixing at 4.8 GHz. We note that the latter is a unique aspect of our design. Subsequently, the mixed (4.8 GHz $\pm$ f_{neuro}) signal is transmitted to the exterior interrogator. The ~2X difference in frequency between the transmitted (2.4GHz) and received (4.8 GHz $\pm$ f_{neuro}) signals is used for isolation. For wireless communication, a dual-band (2.4 / 4.8 GHz) patch antenna is employed both in the implanted device and interrogator. The designated geometry of the patch antenna and the matching circuit between the APDP and antenna further reduce the transmission loss and mismatch loss respectively. The reduced system loss enhances the sensitivity to 20 μV_{pp}, implying detection of almost neural signal generated by human body. The received signal on the interrogator can eventually be viewed on a spectrum analyzer (frequency domain) or on an oscilloscope (after demodulating in time domain).

V. CONCLUSION

This paper discussed three novel technologies used for unobtrusively powering wearables and implants, viz. a) DC power generation via fabric electrochemistry, b) RF power harvesting, and c) fully-passive RF backscattering. At the conference, we showed experimental proof-of-concept results for each of these methods. Overall, the proposed technologies are expected to be of utmost significance for powering electronics in several military, healthcare (e.g., electroceutical), entertainment, arts, sports, and emergency applications, among others.

REFERENCES

[1] S. C. Mukhopadhyay, "Wearable sensors for human activity monitoring: A review," *IEEE Sensors J.*, vol. 15, no. 3, pp. 1321-1330, 2015.

[2] J. Li, et al., "Characterization of in-body radio channels for wireless implants," *IEEE Sensors J.*, vol. 17, no. 5, pp. 1528-1537, 2017.

[3] R. Bala, R. Singh, A. Marwaha, and S. Marwaha, "Wearable graphene-based curved patch antenna for medical telemetry applications," *ACES Journal*, vol. 31, no. 5, 2016.

[4] A. Sabban, "Small wearable metamaterials antennas

for medical systems," *ACES Journal*, vol. 31, no. 4, 2016.

[5] Y. Xu, Y. Lan, Y. Qiu, and R. Xu, "Compact implantable rectenna with light-emitting diode for implantable wireless optogenetics," *ACES Journal*, vol. 31, no. 6, 2016.

[6] R. Vilkhu, et al., "Power harvesting for wearable electronics using fabric electrochemistry," *2017 IEEE Int. Symp. Antennas Propog.*, San Diego, CA, 2017.

[7] R. Vilkhu, et al., "Power generation for wearable electronics: Designing electrochemical storage on fabrics," *IEEE Access*, 2018.

[8] B. DeLong, C. C. Chen, and J. L. Volakis, "Wireless energy harvesting for medical applications," *2015 IEEE Int. Symp. Antennas Propag.*, Vancouver, BC, 2015.

[9] B. DeLong, A. Kiourti, and J. L. Volakis, "A 2.4-GHz wireless sensor network using single diode rectennas," *2016 IEEE Int. Symp. Antennas Propag.*, Fajardo, Puerto Rico, 2016.

[10] R. R. Harrison, "The design of integrated circuits to observe brain activity," *Proc. IEEE*, vol. 96, no. 7, pp. 12031216, July 2008.

[11] A. Kiourti, C. W. L. Lee, J. Chae, and J. L. Volakis, "A wireless fully-passive neural recording device for unobtrusive neuropotential monitoring," *IEEE Trans. Biomed. Eng.*, vol. 63, no. 1, pp. 131-137, Jan. 2016.

[12] W. L. Lee, A. Kiourti, and J. L. Volakis, "Miniaturized fully-passive brain implant for wireless neuropotential acquisition," *IEEE Antennas and Wireless Propag. Lett*., vol. 16, pp. 645648, 2017.

Wei-Chuan Chen received the B.S. degree in Electrical Engineering from the National Taiwan University, Taipei, Taiwan in 2014. Since 2015, he is working toward the Ph.D. degree at The Ohio State University, Columbus, OH, USA. His research interests include antenna design, computational electromagnetic, RF/microwave circuits, and their applications in medicine.

Brock DeLong received the B.Sc. degree in Electrical and Computer Engineering (summa cum laude) in 2014, the M.Sc. in 2017, and the Ph.D. in 2018 from The Ohio State University, Columbus, OH, USA. His research interests include wireless power transmission, medical devices, and millimeter-wave antennas. He has previously worked as an Automation Engineer with Eaton Corporation, an Advanced High Frequency Engineer with NASA Glenn Research Center, and is currently an RF Engineer with Nikola Labs, Inc.

Ramandeep Vilkhu received the B.Sc. degree in Electrical and Computer Engineering in 2018 from the Ohio State University, and is currently pursuing the Ph.D. degree at Stanford University. In 2016 and 2017, he was a Software Engineering Intern with Cisco Systems Inc. and an Electrical Engineering Intern with Northrop Grumman Corporation, respectively. Vilkhu received the IEEE MTT-S Pre-Doctoral Student Fellowship, the IEEE AP-S Undergraduate Student Award, the Ohio State Undergraduate Honors Research Fellowship, and the 2017 TechHub Student Innovation Prize.

Asimina Kiourti received the Dip. degree in Electrical and Computer Engineering from the University of Patras, Patras, Greece, in 2008, the M.Sc. degree in Technologies for Broadband Communications from University College London, London, U.K., in 2009, and the Ph.D. degree in Electrical and Computer Engineering from the National Technical University of Athens, Athens, Greece, in 2013.

From 2013 to 2016, she served as a Post-Doctoral Researcher and then a Senior Research Associate with the ElectroScience Laboratory. She is currently an Assistant Professor of Electrical and Computer Engineering at The Ohio State University, Columbus, OH, USA. To date, she has authored over 40 journal papers, 85 conference papers, and 7 book chapters. Her research interests include wearable and implantable sensors, antennas and electromagnetics for body area applications, and flexible textile-based electronics.

Kiourti has received several awards and scholarships, including the URSI Young Scientist Award in 2018, the IEEE Engineering in Medicine and Biology Society Young Investigator Award for 2014, the IEEE Microwave Theory and Techniques Society Graduate Fellowship for Medical Applications for 2012, and the IEEE Antennas and Propagation Society Doctoral Research Award for 2011.

Circuitry Design and Magnetic Susceptibility Evaluation of 7T fMRI Implantable RF Coil

Rong Wang, Celia M. Dong, Ed X. Wu, Robert C. Roberts, and Li Jun Jiang

Department of Electrical and Electronic Engineering
The University of Hong Kong, City, Pokfulam Road, Hong Kong
wang1130@hku.hk

Abstract ─ Implantable coils have been widely utilized in functional magnetic resonance imaging (fMRI) owing to their superior signal to noise ratio. To effectively minimize the magnetic field distortion and image artifacts, the magnetic susceptibility of the implantable coil needs to be evaluated before practical use. In this work, we experimentally identify the magnetic susceptibility of each component of the implantable coil with the 7T Bruker NMR imaging scanner and provide useful guidelines for the following manufacturing. A 5×5 mm^2 implantable surface coil with a tunable frequency range is subsequently introduced for the 7T fMRI of the rat primary somatosensory cortex (S1FL). A detachable external tuning circuit for the implantable coil is employed to facilitate in-vivo measurements in the rat model.

Index Terms ─ fMRI, implantable coil, magnetic susceptibility.

I. INTRODUCTION

Radio frequency coils have become indispensable components for the magnetic resonance imaging (MRI) scanners owing to their ability to transmit RF pulse at the Larmor frequency and receive the free induction decay signal [1], [2]. The recent discovery that MRI could be utilized for sensing neural activity (also known as Functional MRI or fMRI) has greatly spurred the research and development of the miniaturized and implantable coils [3], [4]. In contrast with conventional T2-weighted MRI, fMRI sets stringent requirement of the magnetic susceptibility for the implantable coil since the fast image acquisition technique adopted such as echo planar imaging (EPI) is less tolerant of the magnetic field distortion induced by the implantable coil and tends to bring in susceptibility artifacts which diminish the quality of the retrieved image. Therefore, the magnetic susceptibility evaluation of each component of the implantable coil is crucial before system assembly and measurement. In this paper, a 5×5 mm^2 implantable planar coil is designed and manufactured for 7T fMRI of

the rat S1FL cortex region. As shown in the flowchart of Fig. 1 (a), after the circuitry design and simulation process, the magnetic susceptibility of all the components of the implantable coil are evaluated by capturing their EPI images within the cylindrical homogeneous saline phantom. The implantable coil is then carefully assembled following the guidelines offered by the magnetic susceptibility evaluation and finally connected with an external tuning circuit to experimentally function at 300 MHz, the Larmor frequency of 7T scanner.
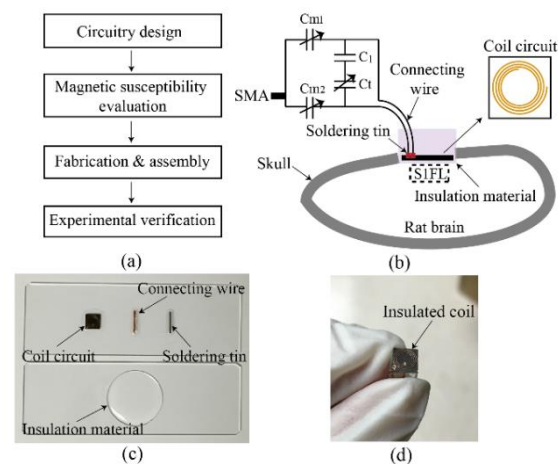
Fig. 1. (a) Flowchart of coil design, (b) schematic diagram of the proposed implantable coil, (c) samples of the coil components on glass slides, and (d) snapshot of the assembled coil.

II. CIRCUITRY DESIGN

The circuitry is mainly composed of an implantable coil and a tuning circuit. The proposed surface coil is constituted by four components, coil circuit, copper connecting wire, insulation material and soldering tin as shown in Fig. 1 (b). The substrate of the coil circuit is 0.254 mm thick Rogers 5880 laminate. The insulation material is Polydimethylsiloxane (PDMS) which is exhaustively used in implantable devices for electrical

sealing.

The simulated inductance and intrinsic resistance of the proposed 5×5 mm^2 four-turn planar coil (35 um thick copper trace, 0.127 mm trace width and spacing) are 67.2 nH and 0.38 Ω respectively, obtained from ANSYS Maxwell. Note that the Larmor frequency should be indicated in the simulation to obtain the additional resistance caused by the skin effect. The surface coil is then represented by an equivalent circuit in Agilent ADS simulator and the ranges of the variable matching and tuning capacitors C_m and C_t are further determined. In this design, the tuning circuit is constituted by a fixed capacitor C_1=2 pF and three identical trimmer capacitors C_{m1}, C_{m2} and C_t (tuning range: 1.8 to 4.5 pF, non-magnetic surface mount SGC3 series, manufactured by Sprague-Goodman).

III. MAGNETIC SUSCEPTIBILITY EVALUATION

Magnetic susceptibility χ_m is a measure indicating the magnetization extent of a material under external magnetic field. The magnetic induction **B** is related to χ_m by the relationship:

$$\mathbf{B} = \mu_0(1 + \chi_m)\mathbf{H},$$

where μ_0 is vacuum permeability and **H** is the magnetic field strength. For implantable coil, the extra magnetic induction **B** induced by its magnetic susceptibility χ_m will distort the base magnetic induction $\mathbf{B}_0$ and vary the base Larmor frequency f_0 which is proportional to $\mathbf{B}_0$. The frequency deviation, in turn, produces signal loss and brings in susceptibility artifacts to the retrieved image. Compared with the time-consuming T2-weighted MRI process, fMRI sacrifices the magnetic susceptibility tolerance to reduce the image acquisition time and capture the instant change of the neural activity.

Therefore, for fMRI application, the evaluation of the magnetic susceptibility of the elements and materials that constitute the implantable coil should be conducted before the manufacture and assembly process. In this work, we take a piece of every coil construction component and place it on glass slide as shown in Fig. 1 (c). Both T2 and EPI images of every piece immersed in a cylindrical homogeneous saline phantom are captured by the high-field 7T Bruker NMR imaging scanner. The induced susceptibility artifacts of each component could be easily identified by comparing its T2 and EPI images in Fig. 2. The susceptibility artifacts produced by the soldering tin is more significant over the other three, visually indicated by the distorted EPI image of the glass slide underneath soldering tin. Thus, particular attention should be paid to the amount of the soldering tin during fabrication. The image of the assembled implantable coil is shown in Fig. 1 (d). The whole implantable surface coil is totally wrapped with PDMS and electrically insulated from the rat brain.
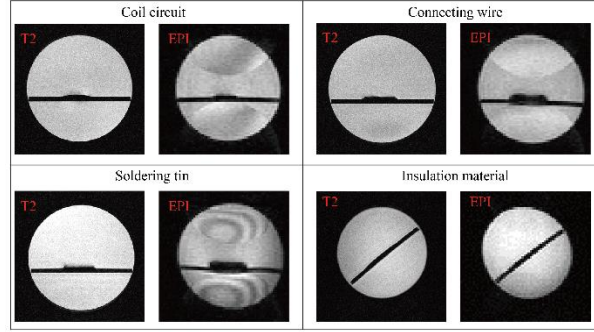
Fig. 2. T2 and EPI images of implantable coil components acquired by the high-field 7T Bruker NMR imaging scanner.

IV. MEASUREMENT

To facilitate the brain surgery for coil implantation, the implantable coil and the external tuning circuit are designed to be detachable with the aid of a plug-in detachable connector as shown in Fig. 3 (a). In Fig. 3 (b), the frequency tuning range is first measured in vacuum and the working frequency could be tuned to 300 MHz with S_{11} = -20.1 dB. A continuous range from 288 to 342 MHz is obtained ($S_{11} < -15$ dB) by tuning the variable capacitors. Furthermore, this tuning range is examined in an extreme case when the sealed coil is immersed in saline since the permittivity of saline (ε_r=78.4) is much larger than these of brain tissues, such as cerebral cortex and skull [5]. Here, the continuous tuning range shifts to 266 and 306 MHz and still covers the Larmor frequency of 300 MHz, validating the effectiveness of this surface coil for brain implantation.
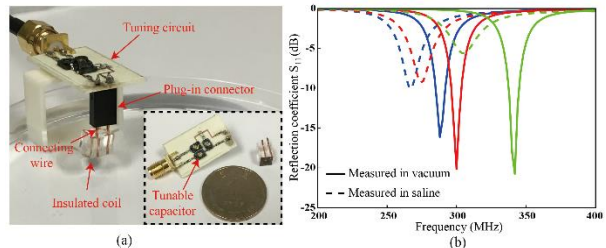
Fig. 3. (a) Photograph of the implantable surface coil immersed in saline. The inset shows the detachable tuning circuit and coil. (b) Measured reflection coefficient and tunable frequency range in vacuum and saline.

V. CONCLUSION

This paper carries out both circuitry design and magnetic susceptibility evaluation of an implantable, tunable and detachable surface coil for the 7T fMRI of the rat cortex region. The experimentally identified magnetic susceptibility of each component provides useful guidelines for the implantable fMRI coil design

and fabrication.

REFERENCES

[1] C. Massin, G. Boero, F. Vincent, J. Abenhaim, P-A. Besse, and R. S. Popovic, "High-Q factor RF planar microcoils for micro-scale NMR spectroscopy," *Sens. Actuators, A*, vol. 97, pp. 280-288, Apr. 2002.

[2] S. Eroglu, B.Gimi, B. Roman, G. Friedman, and R. L. Magin, "NMR spiral surface microcoils: Design, fabrication, and imaging," *Concepts in Magnetic Resonance Part B: Magnetic Resonance Engineering*, vol. 1, pp. 1-10, Apr. 2003.

[3] L. Renaud, M. Armenean, L. Berry, P. Kleimann, P. Morin, M. Pitaval, J. OBrien, M. Brunet, and H. Saint-Jalmes, "Implantable planar RF microcoils for NMR microspectroscopy," *Sens. Actuators, A*, vol. 99, pp. 244-248, June 2002.

[4] M. Bilgen, I. Elshafiey, and P. A. Narayana, "In vivo magnetic resonance microscopy of rat spinal cord at 7T using implantable RF coils," *Magn. Reson. Med.*, vol. 46, pp. 1250-1253, Nov. 2001.

[5] S. Wood and T. S. Ibrahim, "Design and fabrication of a realistic anthropomorphic heterogeneous head phantom for MR purposes," *PloS One*, vol. 12, pp. 0183168, Aug. 2017.

Theoretical Study of Different Access Points in coupled Wireless Power Transfer – Powerline Communication Systems

Sami Barmada and Mauro Tucci

Department of Energy, Systems, Territory and Constructions Engineering
University of Pisa, Pisa, Italy, 56122
sami.barmada@unipi.it, mauro.tucci@unipi.it

Abstract — In this contribution the authors investigate the possibility of improving the performances of a coupled Wireless Power Transfer (WPT) - Power Line Communications (PLC) system in case the WPT system is characterised by a four coils structure. The main idea is to use the so-called transmitting and receiving coil (the two "inner" coils) as access point for the PLC modems and use the drive and load loops (the two "outer" coils) as usual access point for power transfer. The simulations results show that a wider band for communication is achieved with respect the previously proposed system.

Index Terms — Communication channel characterization, four-coils WPT, powerline communications, wireless power transfer.

I. INTRODUCTION

Wireless Power Transfer (WPT) technology has lately gained increasing attention as an alternative way to transmit power with respect to a cabled connection, see for instance [1] – [3].

In the last decade, Power Line Communication (PLC) has been recognised as a viable option for broadband communications. PLC technology uses power cables (where power is typically delivered at 50/60 Hz) to transmit high speed data. PLC communication is now considered one of the main possibilities to transmit data in a smart grid environment (when, for instance, long distances do not allow wireless data transmission).

As an example, [4]-[6] shows how PLC can be used in the smart grid environment with special attention dedicated to home appliances and plug-in electric vehicles.

These two technologies are apparently colliding, since WPT transfers power wirelessly while PLC transmits data on a cabled connection originally designed for power.

This has led the authors to the idea that a full integration between WPT and PLC could be a solution allowing the use of WPT without the need of changes to the pre-existing PLC system. In [7] a feasibility study of such system is proposed, in which a preliminary logic outline of the whole system is shown, and the evaluation of the available channel capacity is performed based on a typical four-coils system.

In [8] an optimization procedure performed on the lumped equivalent circuit is presented, showing that such system can be properly designed taking into account both power and data transmission requirements. In addition, in [9] the full system (with coils and filters) was designed and built showing the actual feasibility of the proposal. In particular, [9] is specifically referring to a two-coils WPT system, while in this contribution the authors investigate the possibility of using the inner coils of a four-coils system as access points for data transmission retaining the usual access point for the power (i.e., the "outer coils").

II. EVALUATION OF THE THEORETICAL CHANNEL CAPACITY FOR FOUR COILS-SYSTEMS

Figure 1 shows the typical four-coils WPT system, consisting of the drive and load loops (where the source and the load are connected) and the transmitting and receiving coils. The outer loops are used in order to achieve maximum power transfer when the transmission distance increases, reducing the coupling coefficient k_{23} between the inner coils. The inner coils have normally no access point and are often mounted on the same equipment as the relative loop. Still, in Fig. 1, we consider that the PLC transmitter (V_T, R_T) and the PLC receiver (R_R), are connected in series to the inner coils.
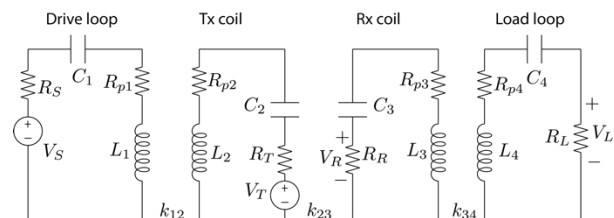
Fig. 1. Four-coils equivalent circuit.

Equations (1) and (2) show the transfer function between the power source (V_S) and the power load (R_L), with $R_R = R_T = V_T = 0$, (in the following we introduce filters to obtain this condition at the resonance frequency), i.e., the system is in its standard WPT state:

$$\frac{\dot{V}_L}{\dot{V}_S} = R_L \frac{j\omega^3 k_{12} k_{23} k_{34} L_2 L_3 \sqrt{L_1 L_4}}{A\omega^4 + B\omega^2 + C}, \qquad (1)$$

where

$$\begin{aligned}
A &= k_{12}^2 k_{34}^2 L_1 L_2 L_3 L_4 \\
B &= k_{12}^2 L_1 L_2 \bar{Z}_3 \bar{Z}_4 + k_{23}^2 L_2 L_3 \bar{Z}_1 \bar{Z}_4 \\
&\quad + k_{34}^2 L_3 L_4 \bar{Z}_1 \bar{Z}_2 \\
C &= \bar{Z}_1 \bar{Z}_2 \bar{Z}_3 \bar{Z}_4 \\
\bar{Z}_1 &= R_{p1} + R_S + j\omega L_1 - \frac{j}{\omega C_1} \\
\bar{Z}_2 &= R_{p2} + j\omega L_2 - \frac{j}{\omega C_2} \\
\bar{Z}_3 &= R_{p3} + j\omega L_3 - \frac{j}{\omega C_3} \\
\bar{Z}_4 &= R_{p4} + R_L + j\omega L_4 - \frac{j}{\omega C_4}.
\end{aligned} \qquad (2)$$

Equations (3) and (4) show the transfer function between the data receiver R_R and the data source V_T, in which the load and source resistances R_S and R_L are not excluded, since data and power transmission take place at the same time:

$$\frac{\dot{V}_R}{\dot{V}_T} = R_R \frac{j\omega k_{23} \bar{Z}_1 \bar{Z}_4 \sqrt{L_2 L_3}}{A\omega^4 + B\omega^2 + C}, \qquad (3)$$

where

$$\begin{aligned}
A &= k_{12}^2 k_{34}^2 L_1 L_2 L_3 L_4 \\
B &= k_{12}^2 L_1 L_2 \bar{Z}_{3b} \bar{Z}_4 + k_{23}^2 L_2 L_3 \bar{Z}_1 \bar{Z}_4 \\
&\quad + k_{34}^2 L_3 L_4 \bar{Z}_1 \bar{Z}_{2b} \\
C &= \bar{Z}_1 \bar{Z}_{2b} \bar{Z}_{3b} \bar{Z}_4 \\
\bar{Z}_1 &= R_{p1} + R_S + j\omega L_1 - \frac{j}{\omega C_1} \\
\bar{Z}_{2b} &= R_{p2} + R_T + j\omega L_2 - \frac{j}{\omega C_2} \\
\bar{Z}_{3b} &= R_{p3} + R_R + j\omega L_3 - \frac{j}{\omega C_3} \\
\bar{Z}_4 &= R_{p4} + R_L + j\omega L_4 - \frac{j}{\omega C_4}.
\end{aligned} \qquad (4)$$

The reason why R_R and R_T are, on the contrary, excluded from the circuit in the previous evaluation comes from the fact that a filter to be placed on the coil is needed, with the aim of excluding the power dissipation on the PLC transceivers at the resonant frequency of the power transfer.

The above equations have been evaluated for a circuit model whose parameters are reported in Table 1, that are taken from [10]. The evaluation of the transfer functions as a function of the coefficient k_{23} allows the comparison between the two possible configurations in terms of channel capacity.

Table 1: Circuit parameters

Element	Unit	Value
$R_S = R_L = R_R = R_T$	Ω	50
$L_1 = L_4$	μH	1.0
$L_2 = L_3$	μH	20.0
$C_1 = C_4$	pF	235.0
$C_2 = C_3$	pF	12.6
$R_{p1} = R_{p4}$	Ω	0.25
$R_{p2} = R_{p3}$	Ω	1.0
$k_{12} = k_{34}$		0.1
k_{23}		$10^{-4} < k_{23} < 0.8$
f_0	MHz	10

III. SIMULATION RESULTS FOR THE SYSTEM WITHOUT FILTERS

Figure 2 shows the transfer functions (TF) between the outer coils according to equations (1) and (2), that is the regular WPT operating situation. The frequency splitting phenomenon and the maximum value close to 1 of the TF appear as expected.
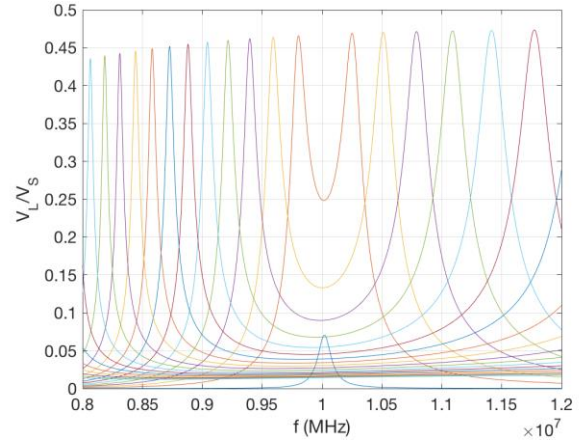
Fig. 2. Transfer functions between outer coils.

Figure 3 shows the transfer functions between the inner coils according to equations (3) and (4), i.e., when we suppose that data transfer happens between the inner coils. It is worth noticing that the maximum value of the TF is lower in this case, and this is consistent with the presence of the four resistances R_S, R_L, R_R, R_T; at the same time it is qualitatively evident that each single curve show a higher bandwidth if compared Fig. 2.

In order to better compare the performances of the two systems both the maximum value of each transfer function and the channel capacity (evaluated with a signal to noise ratio equal to 1) as a function of the coupling coefficient have been calculated.
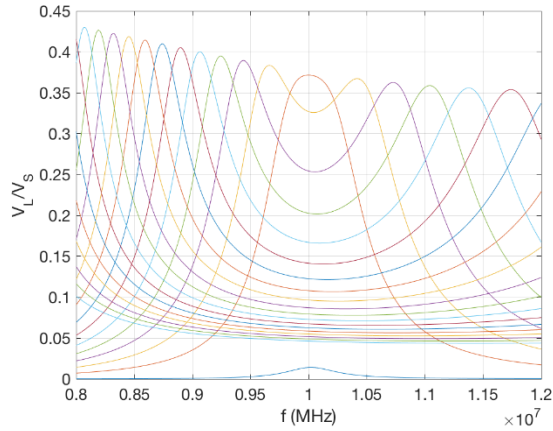
Fig. 3. Transfer functions between inner coils.

Figure 4 shows the maximum value of the TF (for inner and outer access point) as a function of the coupling coefficient: the maximum value is always higher in the first case, confirming that this is the best topology for power transfer (that should take place at the resonant frequency). On the contrary, Fig. 5 shows the channel capacity comparison: by looking at the figure it can be verified that for certain values of the coupling coefficient the achieved channel capacity (obviously proportional to the TF bandwidth) is higher: access from the inner coils guarantees better performances for a wide range of k_{23} values.

The results shown so far are relative to a basic system which does not take into account the need of filters which basically operate a separation between the power signal (characterized by a specific and designed frequency) and the data signal working on a (possibly) wide band.

In the following section the effect of the inclusion of basic filters has been added.
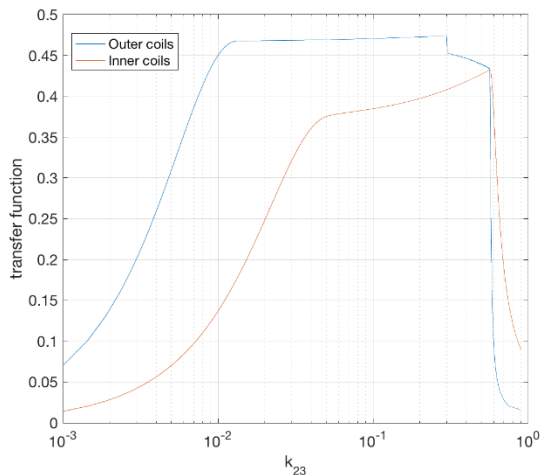
Fig. 4. Comparison between the maximum value of the transfer function.
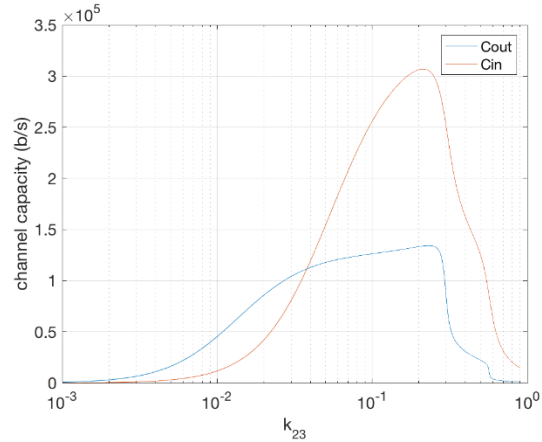
Fig. 5. Comparison between the channel capacity (S/N = 1).

IV. INCLUSION OF SECOND ORDER RESONANT FILTERS

The presence of additional filters is needed in the proposed combined system: they should prevent power to flow through the PLC modem (to avoid damages) and guarantee optimal coupling between the modem and the WPT system, possibly not affecting the power channel in terms of efficiency.

In this paper the authors have considered, for the sake of simplicity, second order parallel or series LC resonant circuits resonating at the power frequency f_0. Despite the simplicity of this approach, the results obtained clearly indicate that good performances can be achieved.
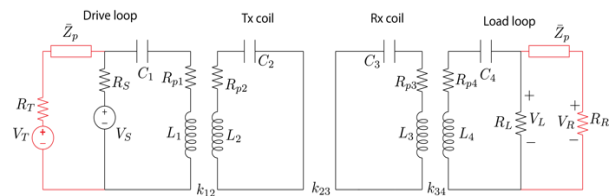
Fig. 6. Power and data from the outer coils, with the inclusion of the parallel filter.

The system in Fig. 6 is basically the one described in [7], with the parallel resonant circuit $\bar{Z}_p$ that resonates at the power frequency, hence operating as an open circuit. In this way the power signal (generated by $\dot{V}_S$ and received by R_L) does not flow into the PLC modem $\dot{V}_T$. On the contrary the wideband data signal generated by $\dot{V}_T$ and received by R_R is not affected by the higher magnitude power signal.

In Fig. 7 it is shown the new architecture proposed in this paper with the addition of the $\bar{Z}_s$ series resonant circuit (at the designed frequency). This series LC filter behaves as a short circuit at the power frequency,

basically eliminating from the inner loops the modem and the transmitting and receiving loads (respectively $\dot{V}_T, R_R, R_T$): in this way power does not flow through the PLC modem and it is not dissipated into the receiving and transmitting resistances.
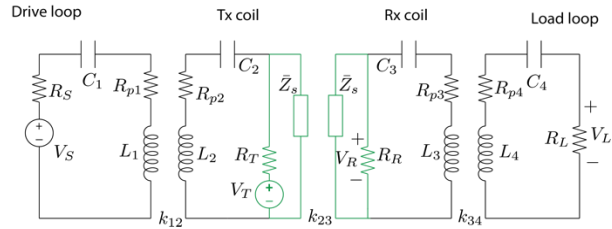
Fig. 7. Data from the inner coils, with the inclusion of the series filter.

At frequencies different from f_0, data signal can flow between the inner coils.

The TF of the two configurations have been analytically calculated with basic circuit theory, leading to expressions similar to equations (1) – (4) that are not reported here for the sake of simplicity. These expressions have been evaluated and the comparison between channel capacity was again calculated as before with a signal to noise ratio equal to 1.

V. SIMULATION RESULTS

Figures 8 and 9 show the TF of the circuit reported in Fig. 7, i.e., in the case data is transferred between inner coils and the corresponding LC series filers are added.

Analyzing Fig. 8 (relative to the power transfer), we can verify that far from the selected resonant frequency a performance decay (in terms of maximum value of TF, hence of transfer efficiency) is obtained. However, the resonant frequency of the system, which is the frequency at which power is transmitted, is chosen in the design phase and no drifting from this frequency should be allowed. For this reason, the results of Fig. 8 are acceptable from the WPT point of view.

Figure 9 shows the TF between the data points: because of the shunt filters, no data is received around the resonant frequency, but the TF is not negligible above and below f_0, resulting in the possibility of transferring data.

Figure 10 shows a comparison between the channel capacities calculated for the systems represented in Figs. 6 and 7. It can be easily seen that the configuration in which power and data are sent through different access points outperforms the one in which data and power share the same access point. At the same time, the use of the shunt filters in the inner coils to protect the PLC modem allows efficient power transfer if the working frequency is well defined and the filters are properly designed.
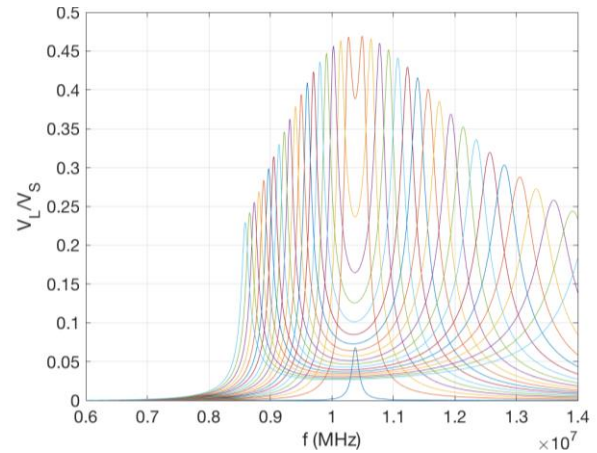
Fig. 8. TF between power terminals for the circuit with inner coils data access.
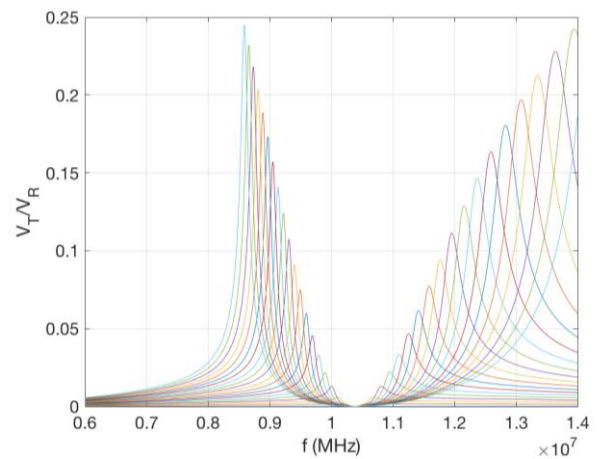
Fig. 9. TF between data terminals for the circuit with inner coils data access.
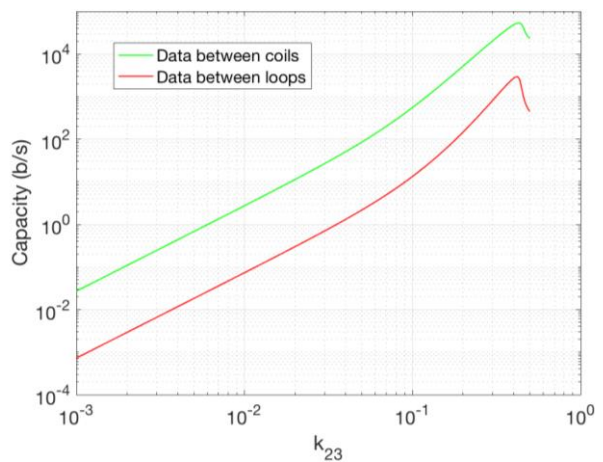
Fig. 10. Channel capacity comparison between different data access points in presence of filters.

VI. CONCLUSION

This preliminary study shows that in the case a four-coil WPT system is used (usually to increase transmission distance with respect to a two-coil system), the two inner coils could be used as access point to PLC data transfer. The numerical example shown here demonstrates that differentiating the access point (of power and data) leads to the achievement of a 30db higher channel capacity with respect to the case of using the outer access points (for a fixed value of k_{23}). As a general conclusion, the possibility of using different access points leads to new criteria in the design of WPT systems with data transmission capabilities.

The systems analyzed for comparison are characterized by second order L-C circuits, and the results of this study will be the object of future investigation and experimental validation.

REFERENCES

[1] A. Kurs, A. Karalis, R. Moffatt, J. Joannopoulos, P. Fisher, and M. Soljacic, "Wireless power transfer via strongly coupled magnetic resonances," *Science*, vol. 317, no. 5834, pp. 83-86, July 2007.

[2] S. H. Lee and R. D. Lorenz, "Development and validation of model for 95%-efficiency 220-W wireless power transfer over a 30-cm air gap," *IEEE Trans. Ind. Appl.*, vol. 47 no. 6, pp. 2495-2504, Nov.-Dec. 2011.

[3] U. K. Madawala and D. J. Thrimawithana, "A bidirectional inductive power interface for electric vehicles in V2G systems," *IEEE Trans. Ind. Electron.*, vol. 56, no. 10, pp. 4789-4796, Oct. 2011.

[4] S. Barmada, M. Tucci, M. Raugi, Y. Maryanka, and O. Amrani, "PLC systems for electric vehicles and smart grid applications," *Proceedings of IEEE International Symposium of Powerline Communications and its Applications (ISPLC)*, Johannesburg, South Africa, pp. 23-28, 2013.

[5] M. Lienard, M. Carrion, V. Degardin, and P. Degauque, "Modeling and analysis of in-vehicle power line communication channels," *IEEE Trans. Veh. Technol.*, vol. 57 no. 2, pp. 670-679. Mar. 2008.

[6] M. Mohammadi, L. Lampe, M. Lok, S. Mirabbasi, M. Mirvakili, R. Rosales, and P. van Veen, "Measurement study and transmission for in-vehicle power line communication," *Proceedings of IEEE International Symposium of Powerline Communications and its Applications (ISPLC)*, Dresden, Germany, pp. 73-78. 2009.

[7] S. Barmada, M. Raugi, and M. Tucci, "Power line communication integrated in a wireless power transfer system: A feasibility study," *Proceedings of IEEE International Symposium of Powerline Communications and its Applications (ISPLC)*, Glasgow, UK, pp. 116-120, 2014.

[8] S. Barmada and M. Tucci, "Optimization of a magnetically coupled resonators system for power line communication integration," *Proceedings of the IEEE Wireless Power Transfer Conference (WPTC)*, Boulder, CO, USA, pp. 1-4, 2015.

[9] S. Barmada, M. Dionigi, P. Mezzanotte, and M. Tucci, "Design and experimental characterization of a combined WPT - PLC system," *Wireless Power Transfer*, Cambridge, vol. 4, no. 2, pp. 160-170, 2017.

[10] A. P. Sample, D. A. Meyer, and J. R. Smith, "Analysis, experimental results and range adaptation of magnetically coupled resonators for wireless power transfer," *IEEE Transactions on Industrial Electronics*, vol. 58, no. 2, pp. 544-554 Feb. 2011.

Sami Barmada received the M.S. and Ph.D. degrees in Electrical Engineering from the University of Pisa, Italy, in 1995 and 2001, respectively. He currently is Full Professor with the Department of Energy and System Engineering (DESTEC), University of Pisa. His teaching activity is related to circuit theory and electromagnetics. His research activity is mainly dedicated to applied electromagnetics, power line communications, non destructive testing and signal processing. He is author and coauthor of approximately 100 papers in international journals and refereed conferences. Barmada was the recipient of the 2003 J. F. Alcock Memorial Prize, presented by the Institution of Mechanical Engineering, Railway Division, for the Best Paper in Technical Innovation, he is IEEE Senior Member and ACES Fellow. He served as ACES President from 2015 to 2017 and now he is a Member of the International Steering Committee of the CEFC Conference.

Mauro Tucci received the Ph.D. degree in Applied Electromagnetism from the University of Pisa, Italy, in 2008. Currently, he is an Associate Professor with the Department of Energy, Systems, Territory and Constructions Engineering, University of Pisa. His research interests include computational intelligence and big data analysis, with applications in electromagnetism, non destructive testing, powerline communications, forecasting and smart grids. He is author and coauthor of approximately 80 papers in international journals and refereed conferences, he is IEEE Senior Member and he served as Technical Program Chair of ACES 2017 conference.

A Six-Elements Circularly Polarized Sequential Array for Dedicated Short Range Communications in C-band

Lisa Berretti, Stefano Maddio, Giuseppe Pelosi, Monica Righini, and Stefano Selleri

Department of Information Engineering
University of Florence, Via di S. Marta 3, Florence, Italy
lisa.berretti@stud.unifi.it, [stefano.maddio,giuseppe.pelosi,monica.righini,stefano.selleri]@unifi.it

Abstract — In this paper an antenna array operating in circular polarization in the C-band is presented. The array is based on the sequential rotation architecture, applied to six elements, and arranged in hexagonal shape. Thanks to its geometry, the array is suitable for tiling of surfaces as well as for regular solid arrangement. Satisfying experimental validation of a prototype based on the proposed design is observed, with a peak gain of 10.4 dB at 5.8 GHz maintained within 3 dB over a 500 MHz band, a 10 dB return loss bandwidth of 500 MHz, and a 3dB axial ratio bandwidth of almost 400 MHz, meaning 6.5% of fractional bandwidth.

Index Terms — Antennas, Network and circuits, Circular Polarization, Dedicated Short Range Communications, C-band.

I. INTRODUCTION

Printed antennas are the preferred choice in almost every modern application. Their advantages in terms of low profile, light weight, manufacturing easiness and conformability are well-known in science and industry.

In applications where the polarization of the source or target is arbitrary or unknown, such as indoor positioning or short-range communications, antennas operating in circular polarization (CP) are preferred [1]. This also holds for applications in complex scenarios, where the CP is a strong aid in contrasting multipath [2,3]. Furthermore, compact CP antenna with moderate to high gain are also necessary in Intelligent Transportation System applications, operating in the band centered at 5.8 GHz [4].

While it is relatively easy to design a printed antenna for CP operation, solutions based on a single antenna typically do not match adequate performance in terms of gain and polarization purity for actual applications.

One of the best and most known solution to increase the number of radiating elements is the use of the sequential rotation architecture (SRA) [5,6,7], which serves as beamforming network for the array configuration as well as an enhancer of polarization purity. This architecture is based on a sequential rotation network (SRN) which serves as the building block of the array.

SRNs are found in open literature with a number of outputs usually equal to 4, or higher powers of 4. The reason is the availability of a simple analytical approach to cope with the design of the network. Being requested with providing 90° of phase delay in each sequential step, the network can be indeed realized with quarter wavelength lines, which easily provide also impedance matching acting as quarter wavelength transformers. Networks with outputs exceeding 4 based on the SPN, however, are seldom proposed for the lack of an analytical solution. Indeed, a 5-elements SRA was proposed by the authors in [8], demonstrating the possibility of a generalized design based on $N > 4$.

We push even further the idea, presenting an array based on six elements, arranged as a hexagon. The hexagonal shape is suitable for 2D tiling, making the device suitable to be the subarray for even larger planar array. Furthermore, combining this shape with the pentagon, it is possible to build a truncated icosahedron, suitable for the problem of a sampling the sphere [9]. As far as the authors know, no such design is present in literature.

Here, the synthesis of the 6-elements SPN is addressed via numeric optimization on a custom vector-based cost-function, permitting the optimal balance of both the magnitude and the phase at each port. The SPN is then assembled with disc-based patch elements, leading to the design of a complete array. Thus, a prototype based on the proposed network has been built, arranged in a single-layer via-less hexagonal board, and experimentally validated.

II. SEQUENTIAL ARCHITECTURE

The SPN, which serves as the feeding network of the array, is a type of structure that guarantees equal power division between the N outputs of the device with a regular progression of the signal phase. The equivalent circuit of the proposed SPN is depicted in Fig. 1. This design is an evolution of the one proposed in [8], and it is treated with a similar approach, briefly summarized

here.

The core of the network is the cascade of five transmission lines in series with characteristic impedances Z_i and electrical lengths θ_i, $i = 1, 2, \ldots, 5$. Along this cascade, six shunt output lines are considered, characterized by impedances Z_i^o and electrical length Impedances θ_i^o, $i = 1, 2, \ldots, 6$. Furthermore, six stubs are placed in correspondence of the six junctions (characterized by impedances Z_i^s and electrical length θ_i^s, $i = 1, 2, \ldots, 6$).
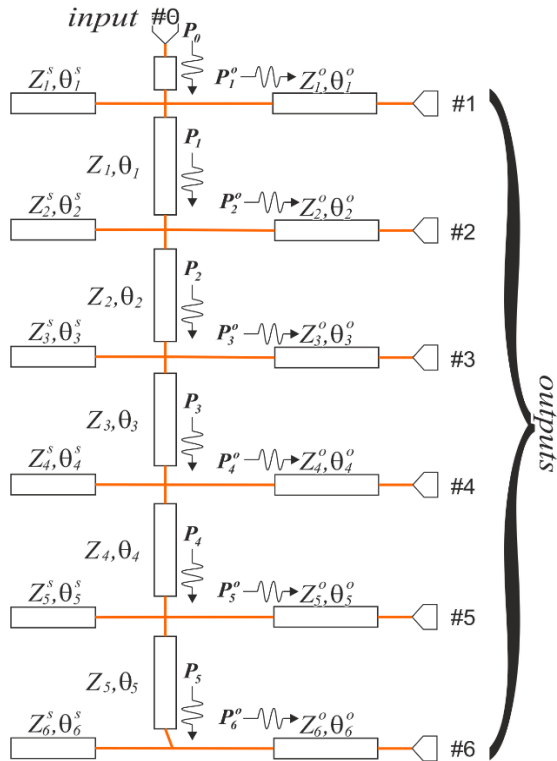
Fig. 1. Representation of the sequential rotation network with $N = 6$ outputs.

In the ideal case, the six output transmission parameters $\hat{S}_n$ exhibit identical module $\left| \hat{S}_n \right| = \sqrt{1/6}$ as well as identical phase sequential increment equal to $\angle \hat{S}_n - \angle \hat{S}_{n-1} = \frac{2\pi}{6}$. Therefore, it is assumed a relative error metric which measures the distance between such an ideal value and the numerically computed one, S_n, at the ith step:

$$E_n = \frac{|S_n - \widehat{S_n}|}{|S_n|}. \tag{1}$$

The large number of geometrical parameters (17 transmission line sections, hence 34 parameters among widths and lengths) and the natural multi-objective nature of the problem (one goal per output parameter), makes the design process suitable for the Taguchi multi-objective optimization method [10,11].

Figure 2 shows the conditions on the amplitudes and phases of the parameters of transmission realized for 6 outputs at central frequency after a full-wave simulation carried out with a commercial CAD. Since the final optimization has to be carried including the antenna elements, hence the unavoidable mutual coupling, the shown results are adequate as a starting point for the final optimization.
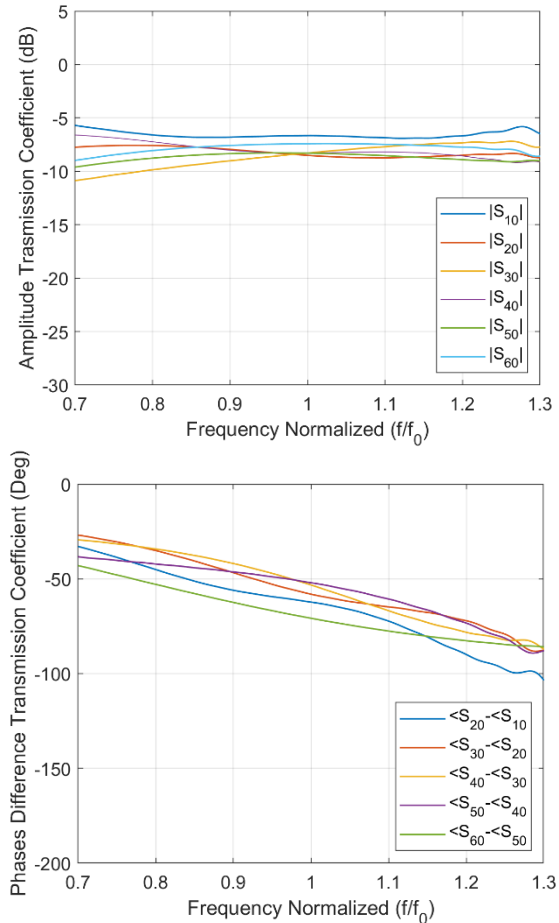
Fig. 2. Amplitudes and differences of phase of transmission coefficients for $N = 6$ outputs. Center frequency is 5.8 GHz.

III. ANTENNA ELEMENT

The radiating element of the proposed antenna is, in view of integrating pentagonal and exagonal subarrays on a bucky-ball structure, the same implemented in [8]. The element consists of a circular patch centrally slitted by an elliptical cut, splitting the fundamental TM_{11} mode into two detuned modes, TM_x and TM_y, Figure 3 shows the geometry of the circular patch antennas and Fig. 4 shows the real and imaginary part of the element input impedance simulated tuning the angle of rotation θ of the central split ellipses with respect to the feeding line.
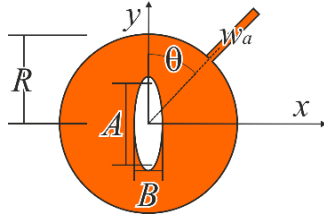
Fig. 3. Element antenna geometry.

With the aid of a parametric simulation. the optimal angle of rotation is found as θ = 48°, measured with respect to the central axis of the central ellipse. In the second analysis, the complete array with sequential feeding and patches was assembled, as it follows in the next Section.
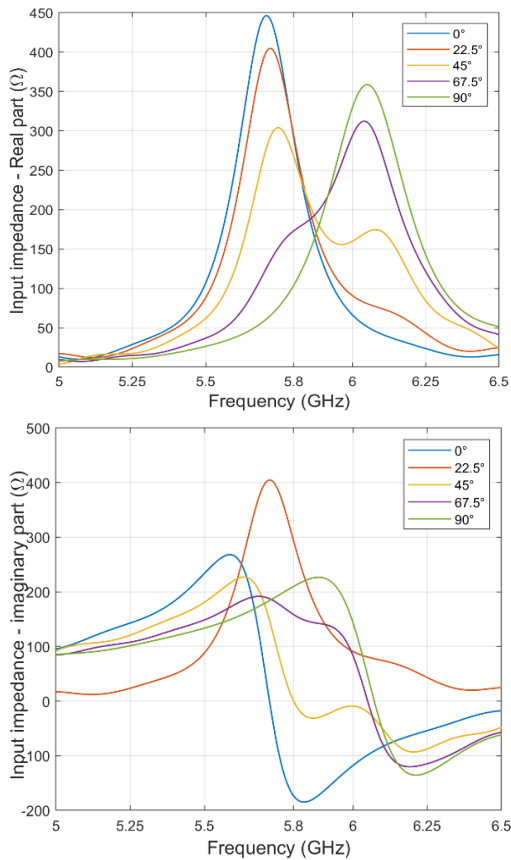
Fig. 4. Real and imaginary part of the input impedance of the circular patch antenna with elliptical split.

IV. IMPLEMENTATION AND EXPERIMENTAL VALIDATION

With the feeding design procedure previously discussed and the tuning of the circular patches, this section describes the implementation and the experimental validation of the sequential array based on 6 microstrip patches. With the aid of the full-wave suite

by Computer Simulation Technologies, the assembly comprising the SPN and the six rotated patch is analyzed.

Figure 5 shows the hexagonal printed prototype measured with the N5242 VNA from Keysight inside an anechoic structure. The realized prototype is a hexagon of side equal to *39* mm, (hence inscribed in a circle of radius *39* mm) and thickness equal to *1.6* mm, fabricated with a photo-etching process on commercial substrate (Isola FR-408 ϵ_r = 3.75, tanδ = 0.001). The actual dimensions of the prototype are reported in Table 1, with reference to the parameters defined in Fig. 3 and Fig. 5. For the sake of clarity, only the branch #5 is graphically quoted, being identical the definition for each of them.
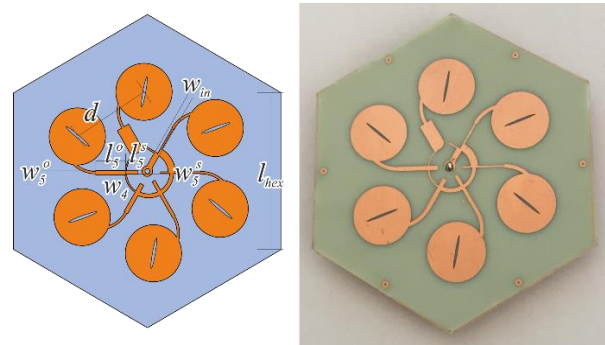
Fig. 5. Printed hexagonal array realized with sequential architecture (SRA).

Table 1: Parameters of the proposed antenna (lengths in millimeters, angles in degrees)

R	A	B	θ	w_a	w_{in}
7.05	8	0.6	48	0.9	1.4
w_1	w_2	w_3	w_4	w_5	d
1.781	0.861	0.993	0.397	0.270	3.170
l_1^o	l_2^o	l_3^o	l_4^o	l_5^o	l_6^o
7.537	5.94	7.8	5.0	7.217	7.183
w_1^o	w_2^o	w_3^o	w_4^o	w_5^o	w_6^o
0.39	0.4	0.82	1.06	1.50	3.29
l_1^s	l_2^s	l_3^s	l_4^s	l_5^s	l_6^s
3.167	*4.214*	*2.357*	*3.10*	*2.583*	*0.015*
w_1^s	w_2^s	w_3^s	w_4^0	w_5^s	w_6^s
3.17	4.214	4.214	4.214	4.214	4.214

Figure 6 shows the reflection coefficient of the proposed prototype. Despite a small shift in value and frequency, attributed to the process of fabrication, and to the tolerances in permittivity value, a good matching between simulations and measurements is observed. A return loss exceeding 15 dB is measured at the center design frequency f = 5.8 GHz, as well as a performance exceeding 10 dB from 5.6 GHz to 6.25 GHz.
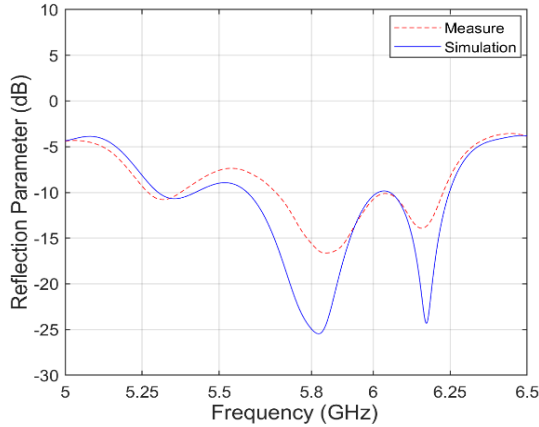
Fig. 6. Comparison between measurement and simulation of the reflection parameter (S_{11}).

Figure 7 presents the *LH (co-polar)* and *RH (cross-polar)* realized gain versus frequency in *broadside* direction. A maximum level of cross-polarization ratio of 23 dB is observed at 5.8 GHz frequency, and very high levels of polarization purity are observed within the C-band, kept over 10 dB from 5.3 GHz to 6.2 GHz. The level of cross-polarization observed is a proof of to the effectiveness of the proposed feeding network.
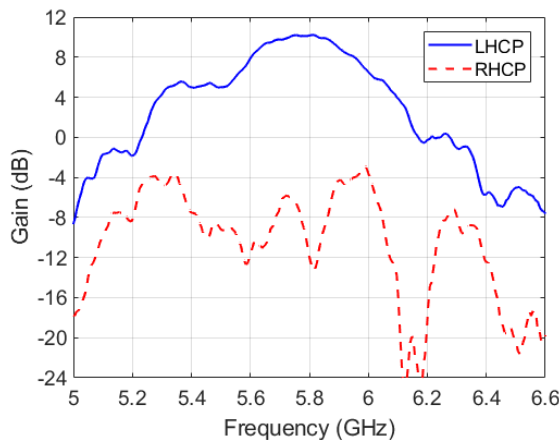
Fig. 7. Co-polar (LHCP) and cross-polar (RHCP) measured realized gain vs frequency.

The *LH* gain has a peak of 10.4 dB at 5.8 GHz and remains above 7 dB over an 18.4% bandwidth. The *RH* gain has a value of −13 dB at 5.8 GHz. With reference to Fig. 8, the high level of cross polarization is also revealed by the axial ratio (AR), depicted against the angle theta at center frequency.

In Figs. 9, 10 and 11, the measured and simulated pattern are compared at center frequency. Three cuts are

considered, corresponding to the cuts $\phi = 0°$, 120°, 240°, measured in anechoic chamber with a Keysight N5242 Vector Network Analyzer. The lobe is quite symmetric and invariant for each considered cut, maintaining a HPBW of about 45° in the main lobe of radiation. The lobe in broadside is the result of the sequential feeding of the patches perfectly phased.
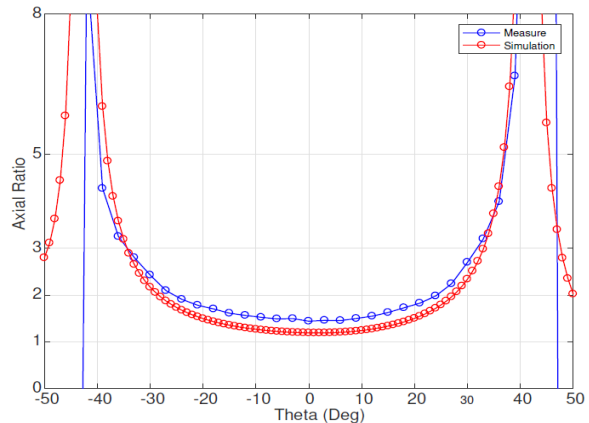
Fig. 8. Comparison between measurement and simulation of Axial Ratio (AR).

Figure 12 presents the antenna gain, measured for the cut to $\phi = 0°$, as a contour plot. The plot presents frequency on the abscissa's axis, and the theta angle in the ordinate. This plot demonstrates the symmetry and the good frequency behavior, with the peak performance at 5.8 GHz and θ = 0, i.e., the *broadside* direction at the center frequency.
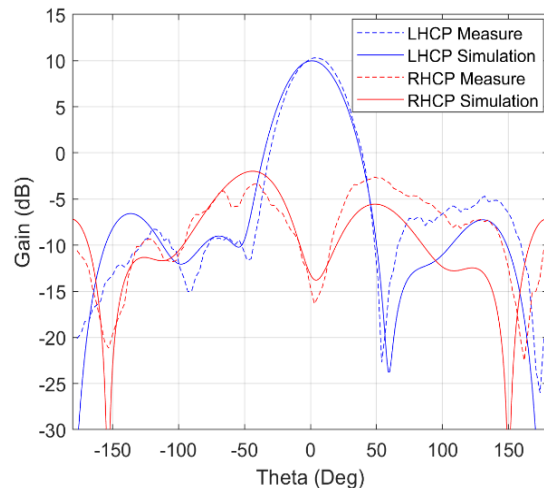
Fig. 9. Comparison between simulation and measure of radiation pattern $\phi = 0°$ at 5.8 *GHz.*
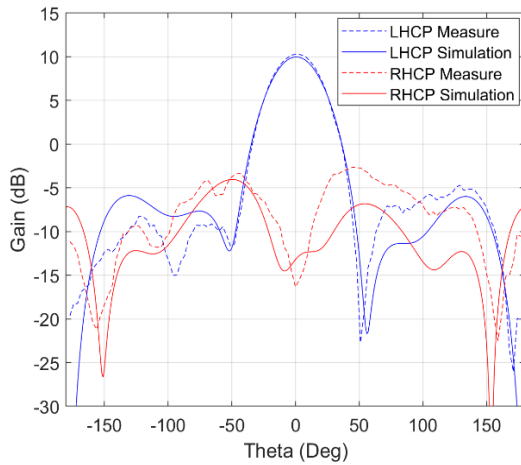
Fig. 10. Comparison between simulation and measure of radiation pattern $\phi = 120°$ at 5.8 *GHz.*
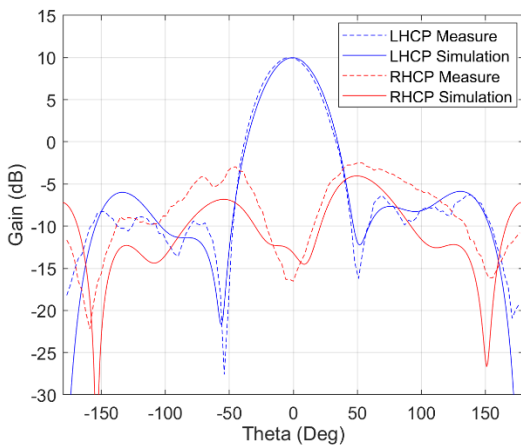
Fig. 11. Comparison between simulation and measure of radiation pattern $\phi = 240°$ at 5.8 *GHz.*
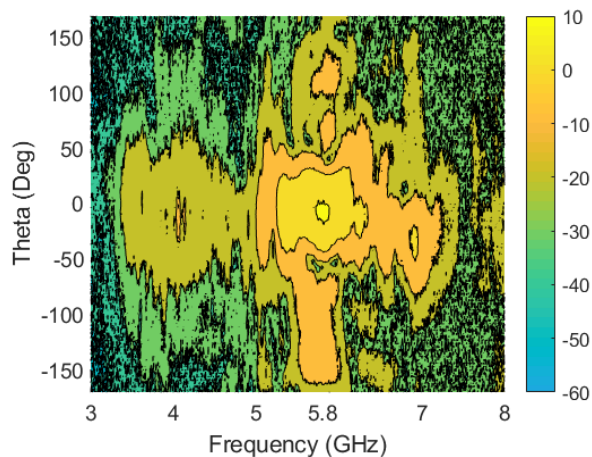
Fig. 12. Co-polar gain versus frequency and pointing angle θ.

V. CONCLUSION

A compact circularly polarized array for C-Band application was designed, simulated, and fabricated. The antenna is arranged in a hexagon of side 39 mm, hence a surface of $2\lambda_0{}^2$ at the center frequency of 5.80 GHz. The fabricated device exhibits a peak gain of 10.4 dB at 5.8 GHz, maintained within 3 dB within the range 5.5–6.0 GHz. The axial ratio is 0.1 dB at the central frequency, and below 3 dB from 5.6 GHz to 6.0 GHz. A cross polarization ratio exceeding 15 dB is observed between 5.75 GHz and 5.85 GHz, the central band of DSRC communications. The latter performance, the moderately high gain, and the single-layer via-less design makes the proposed antenna suitable for integration with compact commercial tag.

REFERENCES

[1]   S. Maddio, M. Passafiume, A. Cidronali, and G. Manes, "A distributed positioning system based on a predictive fingerprinting method enabling sub-metric precision in IEEE 802.11 networks," *IEEE Trans. Microwave Theory Tech.*, vol. 63, no. 12, pp. 1-14, 2015.

[2]   R. Szumny, K. Kurek, and J. Modelski, "Atten-uation of multipath components using directional antennas and circular polarization for indoor wireless positioning systems," *2007 European Microwave Conference*, Munich (Germany), pp. 1680-1683, 9-12 Oct. 2007.

[3]   A. Cidronali, G. Collodi, S. Maddio, M. Passafiume, G. Pelosi, and S. Selleri, "Improving phaseless DoA estimation in multipath-impaired scenarios by exploiting dual-band operations," *2016 IEEE MTT-S International Microwave Symposium*, San Francisco (California, USA), pp. 1-4, 22-27 May 2016.

[4]   A. Cidronali, S. Maddio, M. Passafiume, and G. Manes, "Car talk: technologies for vehicle-to-roadside communications," *IEEE Microwave Magazine*, vol. 17, no, 11, pp. 40-60, 2016.

[5]   T. Teshirogi, M. Tanaka, and H. Chuju, "Wideband circularly polarized array antenna with sequential rotations and phase shift of elements," in D. Pozar (Ed.) *Microstrip Antennas: The Analysis and Design of Microstrip Antennas and Arrays*, IEEE-Wiley Interscience, Hoboken (NJ), pp. 136-140, 1995.

[6]   J. Huang, "A technique for an array to generate circular polarization with linearly polarized elements," *IEEE Trans. Antennas Propagat*, vol. 34, no. 9, pp. 1113-1124, 1986.

[7]   V. Rafii, J. Nourinia, C. Ghobadi, J. Pourahmadazar and B. S. Virdee, "Broadband circularly polarized slot antenna array using sequentially rotated technique for C-band applications," *IEEE Antennas*

Wireless Propagat. Lett., vol. 12, pp. 128-131, 2013.

[8] S. Maddio, G. Pelosi, M. Righini, and S. Selleri, "A five elements sequential rotation array arranged in a single-layer pentagonal substrate," *Microwave Optical Techn. Lett.*, vol. 59, no. 5, pp. 1077-1081, 2017.

[9] T. A. Lam, D. C. Vier, J. A. Nielsen, C. G. Parazzoli, and M. H. Tanielian, "Steering phased array antenna beams to the horizon using a buckyball NIM lens," *Procdings of the IEEE*, vol. 99, no. 10, pp. 1755-1767, 2011.

[10] E. Agastra, G. Pelosi, S. Selleri, and R. Taddei, "Taguchi's method for multi-objective optimization problems," *Int. J. RF Microwave CAE*, vol. 23, no. 3, pp. 357-366, 2013.

[11] G. Pelosi, S. Selleri, and R. Taddei, "A novel multiobjective Taguchi's optimization technique for multibeam array synthesis," *Microwave Optical Techn. Lett.*, vol. 55, no. 8, pp. 1836-1840, 2013.

Lisa Berretti was born in Grosseto, Italy in 1995. She received the Laurea (BS) degree in Electronic and Tele-communication Engineering from the University of Florence in 2018. She is currently enrolled on Master in Electronic Engineering at the Uni-versity in Florence. Her particular interests are mainly in electromagnetic fields, antenna design and simulations.

Stefano Maddio was born in Florence, Italy in 1978. He received the Electronic Engineering degree in 2005 and the Ph.D. degree in 2009 from University of Florence. He is currently a Research Fellow at the University of Florence. His current research interests include analysis and design of radiative systems for microelectronics in the field of smart antenna technology for wireless applications with a particular emphasis on the issues of wireless localization and special-purpose antenna systems for dedicated short range communications, as well modeling of microwave, devices and circuits.

Giuseppe Pelosi was born in Pisa, Italy, in 1952. He received the Laurea (Doctor) degree in Physics (summa cum laude) from the University of Florence in 1976. He is currently with the Department of Information Engineering of the same university, where he is currently Full Professor of Electromagnetic Fields. His research activity is mainly focused on numerical techniques for applied electromagnetics (antennas, circuits, microwave and millimeter-wave devices, scattering problems). He was coauthor of several scientific publications on the aforementioned topics, appeared in international refereed journals. He is also coauthor of three books and several book chapters.

Pelosi was elected a Fellow of the IEEE for contributions to computational electromagnetics.

Monica Righini was born in Prato (Italy) in 1984. She received the degree (cum laude) in Telecom-munications Engineering in 2011 and her Ph.D in 2016 from the University of Florence (Italy). Her recent research interests are mainly in multilayer planar technology radiating boards for space and radar applications and in ultra-wideband electrically small antennas for direction finding.

Stefano Selleri was born in Viareggio, Italy, on December 9th, 1968. He obtained his degree (Laurea), cum laude, in Electronic Engineering and the Ph.D. in Com-puter Science and Telecommunica-tions from the University of Florence in 1992 and 1997, respectively. He is author of over 100 papers on international referred journals and eight books or books chapters. He is currently an Assistant Professor at the University of Florence, where he conducts research on numerical modeling of microwave, devices and circuits with particular attention to numerical optimization.

A Quad-Band Antenna with AMC Reflector for WLAN and WiMAX Applications

Ernst W. Coetzee, Johann W. Odendaal, and Johan Joubert

Department of Electrical, Electronic & Computer Engineering
University of Pretoria, Gauteng, 0028, South Africa
u13014422@tuks.co.za

Abstract ─ This letter presents a quad-band antenna with high gain for wireless local area network (WLAN) and Worldwide Interoperability for Microwave Access (WiMAX) communication covering the IEEE 802.11a/b and IEEE802.16d/e standards. The antenna consists of a microstrip feed line with a complementary microstrip-slot pair and a secondary slot element on a single dielectric medium. A single-band artificial magnetic conductor (AMC) surface was used as a reflector to achieve a unidirectional radiation pattern with an average gain of 9.3 dBi. The antenna was optimized to achieve a radiation efficiency of more than 90% in the WLAN and WiMAX frequency bands. The size of the antenna with the AMC reflector is $80\times80\times10$ mm^3. The radiation properties of the antenna were measured in a compact antenna range and simulated and measured results are presented.

Index Terms ─ AMC, directional antennas, multi-band antenna, wireless local area network (WLAN), Worldwide Interoperability for Microwave Access (WiMAX).

I. INTRODUCTION

The design of a multi-band, high-gain, low-profile and directional antenna for wireless local area network (WLAN) applications have become more desirable in communication solutions [1]. The WLAN frequency bands include $2.4 - 2.483$, $5.15 - 5.25$ and $5.725 - 5.825$ GHz for the IEEE802.11a/b standards.

The application of artificial magnetic conductor (AMC) surfaces have become more popular in antenna applications, due to improved antenna performance and low-profile designs [2]. Various antennas with AMC reflectors suitable for WLAN applications were proposed and include a dual-band C-slotted, a wideband circularly polarized antenna, a circular disc monopole, and a V-shaped slot antenna. These antennas all have an average gain of less than 8.0 dBi in the WLAN frequency bands or are larger than $80\times80\times11$ mm^3.

A dual-band C-slotted antenna with a single-band diamond shaped AMC reflector is presented in [3]. The antenna had an overall size of $90\times90\times6.5$ mm^3, which was larger than $80\times80\times11$ mm^3. The antenna operated in the 2.4 and 5.8 GHz WLAN frequency bands with gains of about 5.3 and 10.7 dBi.

A wideband circularly polarized antenna with a single-band patch AMC reflector was proposed in [4]. The antenna consisted of two barbed-shape dipoles and two bowtie dipoles printed on the same substrate. The AMC reflector, 80×80 mm^2, was positioned at 17 mm from the antenna substrate and had peak gains of 6.6 and 7.4 dBi in the 2.4 and 5 GHz WLAN frequency bands.

A wideband circular disc monopole antenna was combined with a dual-band AMC reflector, as proposed in [5]. The combination of the wideband monopole antenna with a dual-band AMC resulted in a dual-band response which covered the 2.4 and 5 GHz WLAN bands. The antenna had a size of $88\times88\times7.8$ mm^3 and gains of 3.9 and 6 dBi in the 2.4 and 5 GHz bands.

The combination of a dual-band V-shaped slot etched monopole antenna with a dual-band AMC surface was proposed in [6]. The antenna had a size of $57\times57\times12.68$ mm^3 and due to the monopole antenna, the peak gains were 6.6 and 7.8 dBi at 2.4 and 5.5 GHz.

The proposed quad-band antenna is based on an ultra-wideband slot radiating element presented in [7]. The ultra-wideband characteristics of the strip-slot pair were implemented in [8], where the feedline was terminated with a short circuit termination. The antenna was combined with a perfect electric conductor (PEC) reflector, which resulted in a high-gain directional antenna for WLAN and WiMAX applications.

In this letter, a new high-gain antenna that operates in the IEEE802.11a/b WLAN frequency bands is presented. The PEC reflector is replaced with an AMC reflector and an additional slot element is included. The antenna is combined with a single-band AMC reflector and has an overall size of $80\times80\times10$ mm^3 with measured gains of 9.6, 8.6 and 10.3 dBi in the three WLAN frequency bands. The antenna is also suitable for Worldwide Interoperability for Microwave Access (WiMAX) applications in the frequency band $3.4 - 3.6$ GHz [9].

II. ANTENNA DESIGN

The geometry of the proposed quad-band antenna is shown in Fig. 1.
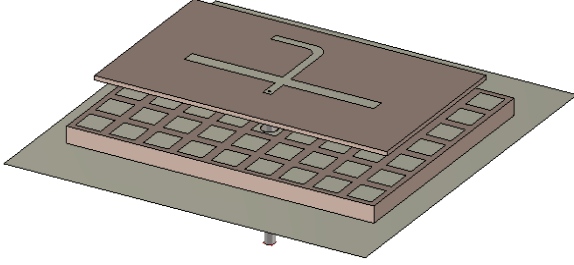
Fig. 1. 3D view of the proposed quad-band antenna.

The slot radiating element structure consists of a microstrip line with a microstrip stub and a complementary slot in the ground plane, which is approximately the same size as the microstrip stub. The combination of the microstrip-slot pair results in an even- and odd-mode and the analysis of it was performed in [7]. he modes are referred to as quasi-strip and quasi-slot modes and the even- and odd-modes can be approximated by [7]

$$Z_{0e} \approx 2Z_M, \quad \epsilon_{eff,e} \approx \epsilon_{eff,M}, \tag{1}$$

$$Z_{0o} \approx \frac{Z_S}{2}, \quad \epsilon_{eff,o} \approx \epsilon_{eff,S}, \tag{2}$$

where Z_{0e} and Z_{0o} signify the characteristic impedances for the even- and odd-modes of the substructure. The characteristic impedances of the microstrip line and the slot are presented by Z_M and Z_S, respectively. The effective dielectric constant for the even-mode, $\epsilon_{eff,e}$, is equal to the effective dielectric constant of the microstrip line, $\epsilon_{eff,M}$. The effective dielectric constant for the odd-mode, $\epsilon_{eff,o}$, is also equal to the effective dielectric constant for the slot, $\epsilon_{eff,S}$. The image impedance of the microstrip-slot pair is then determined by [7]:

$$Z_{im} = \sqrt{Z_{0e}.Z_{0o}.\cot\theta_e.\tan\theta_o}, \tag{3}$$

where θ_e and θ_o are the electrical lengths of the even- and odd-modes, respectively. When the effect of losses is ignored, the electrical lengths can be approximated in terms of transmission line parameters as [7]:

$$\theta_e = \sqrt{\epsilon_{eff,M}} \times L_M, \tag{4}$$

$$\theta_o = \sqrt{\epsilon_{eff,S}} \times L_{S1}, \tag{5}$$

where L_M is the length of the microstrip line, when measured from the microstrip feed line and L_{S1} is the length of the slot when measured from the centre of the slot. When the electrical lengths of both modes are made equal to each other ($\theta_e = \theta_o$), the characteristic impedance of the microstrip feedline can be calculated as [7]:

$$Z_0 = \frac{1}{2}\sqrt{Z_{0e}.Z_{0o}}, \tag{6}$$

which is also used as a design condition to achieve impedance matching. The microstrip-slot pair structure can be described by four parameters W_M, W_{S1}, L_M and L_{S1}, which are the widths and lengths of the microstrip line stub and the slot.

An additional slot element was also incorporated to increase the bandwidth. The size of the secondary slot element is almost half the size of the initial slot and was placed close to the initial slot. This resulted in an additional resonance close to the resonance created by the strip-slot pair and improved the impedance bandwidth of the antenna.

The feedline of the proposed antenna was terminated with an open circuit, which improved the radiation efficiency to above 90% in the frequency bands of operation. The dimensions of the antenna structure are shown in Fig. 2 and summarized in Table 1. The antenna was designed on 0.81 mm thick Rogers RO4003C with a dielectric constant of 3.38 and a loss tangent of 0.0027. The antenna is fed with a 50Ω coaxial transmission line through the back of the AMC reflector.

The AMC reflector has a size of 80×80×3.2 mm³. The spacing between the antenna and AMC was 6 mm and optimized for improved impedance bandwidth. The AMC reflector is printed on 3.2 mm thick FR4 substrate with a dielectric constant of 4.4 and a loss tangent of 0.02. The AMC consists of an array of rectangular patches, where the size of a unit cell is 7.5 mm and the size of the patch is 5.5 mm. The AMC reflector has a 0° reflection phase at 5.6 GHz, with a ±45° reflection phase bandwidth of 4.8 − 6.1 GHz (23.9%), which covers the 5.2 and 5.8 GHZ WLAN bands.

The near electric fields close to the antenna are shown in Fig. 3 at the respective resonances. The lower operating resonance at 2.4 GHz is primarily controlled by the length of the antenna substrate/ground (L). The AMC surface and the ground plane of the antenna support a radiating patch mode, as can be seen by the high value fields in Fig. 3 (a) at the two vertical edges of the antenna ground plane. Design equations of a patch antenna can be implemented to determine the size of the antenna substrate/ground. Figure 3 (b) shows that the resonance at 3.5 GHz is achieved by the unique coupling between the strip-slot pair and the secondary slot element.
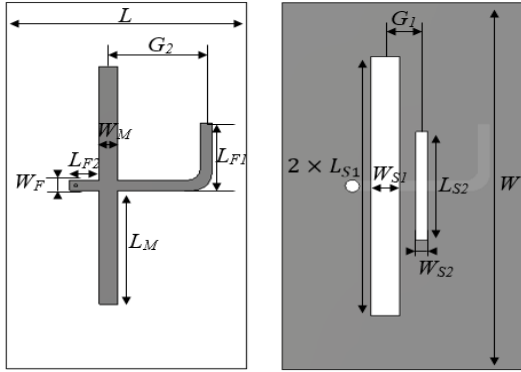
Fig. 2. Layout and dimensions of the quad-band antenna: (a) top and (b) bottom.

Table 1: Dimensions of quad-band antenna

Dimension	Length (mm)	Parameter
L	37.50	Substrate length
W	64.74	Substrate width
$2 \times L_{S1}$	45.72	Slot length
W_{S1}	4.43	Slot width
L_{S2}	19.11	Secondary slot length
W_{S2}	1.79	Secondary slot width
G_1	5.59	Gap between slots
L_M	20.08	Strip length
W_M	2.82	Strip width
G_2	15.19	Gap length
L_{F1}	11.90	Curve Length
L_{F2}	4.62	Feed line length
W_F	1.80	Feed line width

The antenna achieves two resonances in the upper operating WLAN band, which allows for the 5.2 and 5.8 GHz WLAN bands to be covered. The upper operating frequency band is controlled by the length of the strip-slot pair (dimension L_M and L_{S1}) as well as the length of the secondary slot element (dimension L_{S2}). Figure 3 (d) shows that 5.8 GHz resonance is controlled by the length of the strip-slot pair and can be determined by implementing equation (1) to (6). Figure 3 (c) shows that the 5.2 GHz resonance is controlled by the length of the secondary slot element. The length of the secondary slot element, L_{S2}, can be determined by first calculating the effective dielectric constant of the slot, ϵ_a, from equation (7). Thereafter the length of the secondary slot element, L_{S2}, is determined from equation (8). This slot is half a wavelength long which indicates that the secondary slot element operates at a half wavelength in the slot:

$$\epsilon_a = \frac{\epsilon_r + 1}{2}, \tag{7}$$

$$L_{S2} = \frac{c}{2f_c\sqrt{\epsilon_a}}. \tag{8}$$
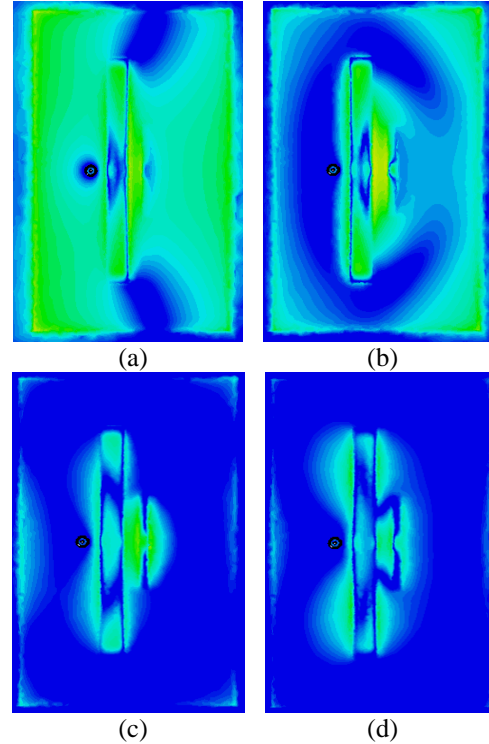
Fig. 3. Electromagnetic field intensity close to the antenna: (a) 2.4 GHz, (b) 3.5 GHz, (c) 5.2 GHz, and (d) 5.8 GHz

The antenna is designed on Rogers RO4003C, which has a dielectric constant of 3.38. From equation (7) the effective dielectric constant for the slot, ϵ_a, is calculated to be 2.19. The length of the secondary slot element, L_{S2}, is then calculated to operate at $f_c = 5.2$ GHz and from equation (8) found to be 19.49 mm.

To ensure that functionality is maintained in one frequency band, the dimension for the other frequency bands can only be adjusted by 10%. The ground plane of the antenna and the AMC reflector acts as a patch antenna and produces the 2.4 GHz resonance, while the AMC was designed to operate at a fixed spacing of 6 mm for the 5.2 and 5.8 GHz resonances. Increasing the spacing between the antenna and the AMC reflector improves the bandwidth of the 2.4 GHz resonance, due to the patch mode, but decreases the bandwidth in the 5.2 and 5.8 GHz resonance as the AMC was designed to operate at 6 mm. The overall size of the AMC reflector has to be larger than the antenna substrate, but the antenna performance is more dependent on the length of the reflector than the width.

III. NUMERICAL MODEL

CST Microwave Studio was used to analyse and design the antenna [10]. The simulation tool allows for two different solvers to be used. The Finite Integration Technique (FIT) based Time Domain Solver (TDS) and the Finite-Element Method (FEM) based Frequency

Domain Solver (FDS). The AMC reflector was simulated with the FDS using a tetrahedral mesh. The design for the AMC reflector, followed the procedure described in [2]. The performance of an infinite repetition of the basic unit cell was simulated, by applying the proper boundary conditions. The boundaries normal the polarization of the incident field was chosen as perfect electric boundaries, while the planes parallel to the polarization of the incident field was chosen as perfect magnetic boundaries. The AMC unit cell with the proper boundary conditions is shown in Fig. 4. The AMC reflector was designed to operate 6 mm away from the antenna. The unit cell was excited with a waveguide port, 6 mm from the top of the unit cell. The AMC reflector consists of a conductor backed dielectric substrate with an array of square conducting patches.

The AMC reflector was combined with the antenna and was also solved with the FDS with a tetrahedral mesh. The antenna was excited with a coaxial transmission line, through the AMC and connected to the microstrip feedline on the top of the antenna. The coaxial feed line was excited with a waveguide port. The antenna was simulated from 2 – 7 GHz with local mesh refinement, while adaptive meshing was applied at the centre frequency of the simulation, at 4.5 GHz. A total of 113234 tetrahedrons were used to provide a sufficient representation of the antenna geometry. The mesh view of the antenna with the tetrahedral meshing is shown in Fig. 5.
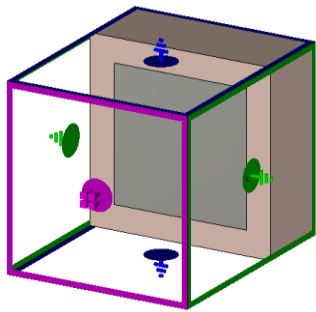
Fig. 4. 3D view of AMC unit cell with boundary conditions.
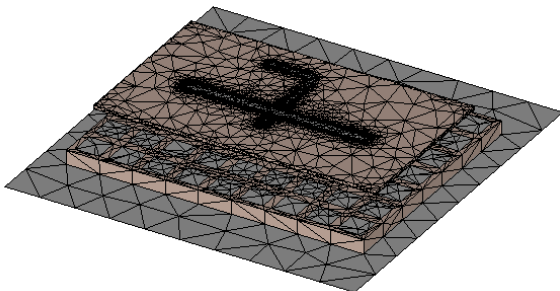
Fig. 5. 3D view of antenna with tetrahedral meshing.

IV. SIMULATIONS AND MEASUREMENTS

The antenna was designed and simulated with CST Microwave Studio. The reflection coefficient of the manufactured antenna was measured with an HP8510 Vector Network Analyzer and the simulated and measured reflection coefficients are shown in Fig. 6. The antenna has a reflection coefficient below -10 dB in all three WLAN frequency bands, as well as the WiMAX bands.

The gain and radiation patterns of the manufactured quad-band antenna were measured in the compact antenna range at the University of Pretoria, as shown in Fig. 7. The simulated realized gain of the antenna is compared to the measured gain in Fig. 8, and the largest difference was found to be 1.7 dBi. The measured average gain was 9.5, 8.6 and 10.2 dBi in the three WLAN bands respectively, and 8.9 dBi in the WiMAX frequency band. The difference between the simulated and measured gain values are likely due to the measurement setup in the compact range. The simulated and measured radiation patterns in the *E*- and *H*-planes at 2.4, 3.5, 5.2 and 5.775 GHz are compared to each other and shown in Fig. 9.
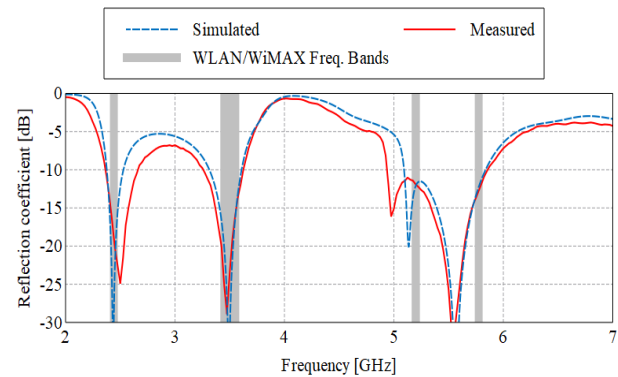
Fig. 6. Simulated and measured reflection coefficient of the antenna.
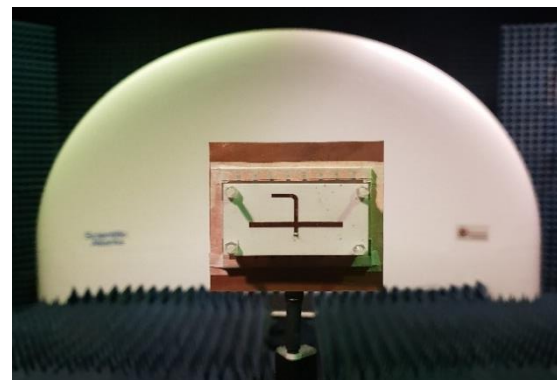
Fig. 7. Manufactured quad-band antenna in the compact antenna range.
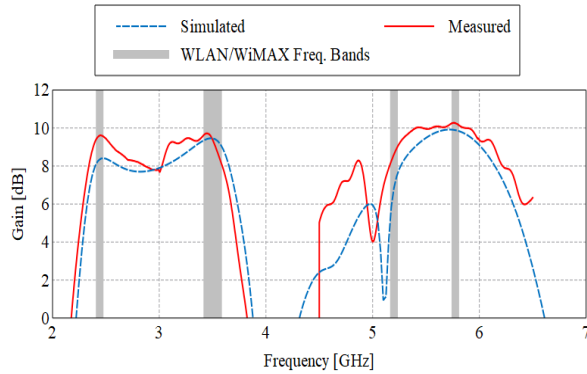
Fig. 8. Simulated and measured gain of the antenna.

(a)   (b)
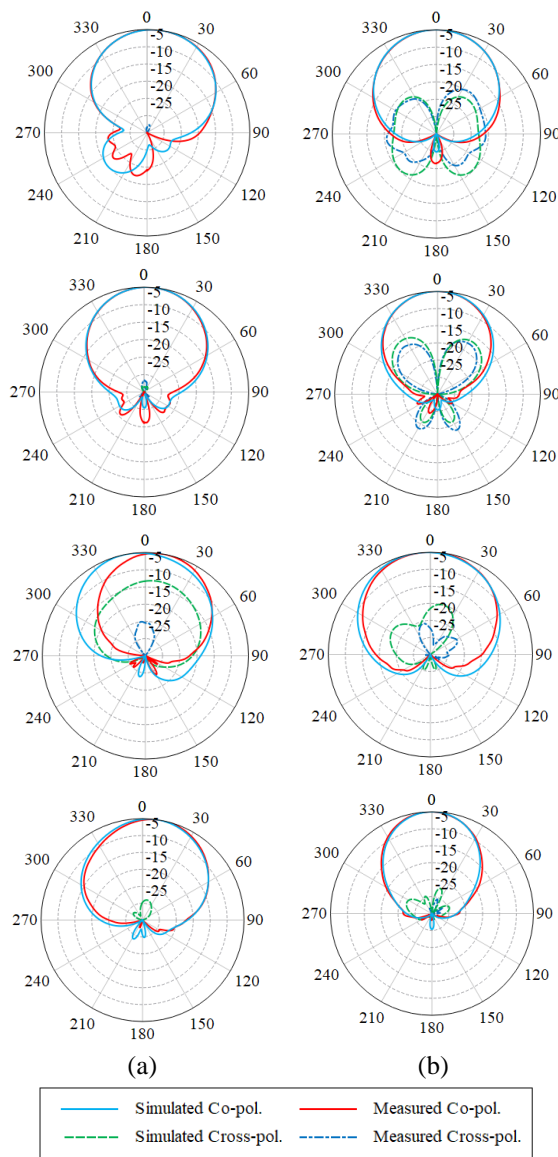
Fig. 9. Simulated and measured radiation patterns in the E- and H-planes of the antenna at the four frequencies 2.4, 3.5, 5.2 and 5.775 GHz: (a) E-plane and (b) H-plane.

The simulated E-plane radiation pattern at 5.2 GHz is slightly wider than the measured pattern. This is the cause for the noticeable difference in gain at 5.2 GHz. The beamwidth at 5.2 GHz is also wider than the beamwidth at 5.775 GHz, which is due to radiation from the secondary slot element. The simulated and measured radiation patterns show good correlation. The measured maximum cross-polarization is less than -20 dB in the E-plane. The front-to-back ratio is also better than -22 dB in the respective WLAN and WiMAX frequency bands.

V. CONCLUSION

The design of a quad-band, high-gain and directional antenna with a low-profile suitable for WLAN and WiMAX applications was presented. The proposed antenna consists of a microstrip-slot pair with a parasitic slot element, to ensure a wide impedance bandwidth. A high radiation efficiency was achieved by terminating the feed line with an optimized open circuit termination. A low-profile design was realized by including an AMC reflector to achieve a directional radiation pattern and high gain. The proposed antenna has a higher gain and smaller size when compared to other directional WLAN antennas found in the literature. The simulated and measured results were compared and have a good correlation.

ACKNOWLEDGMENT

REFERENCES

[1] B. Kelothu, K. R. Subhashini, and G. L. Manohar, "A compact high-gain microstrip patch antenna for dual band WLAN applications," *2012 Students Conference on Engineering and Systems*, Allahabad, Uttar Pradesh, pp. 1-5, 2012.

[2] J. Joubert, J. C. Vardaxoglou, W. G. Whittow, and J. W. Odendaal, "CPW-fed cavity-backed slot radiator loaded with an AMC reflector," in *IEEE Transactions on Antennas and Propagation*, vol. 60, no. 2, pp. 735-742, Feb. 2012.

[3] P. J. Soh, F. N. Giman, M. F. Jamlos, H. Lago, and A. A. Al-Hadi, "A C-slotted dual band textile antenna for WBAN applications," *2016 URSI Asia-Pacific Radio Science Conference (URSI AP-RASC)*, Seoul, pp. 1621-1624, 2016.

[4] H. H. Tran and I. Park, "A dual-wideband circularly polarized antenna using an artificial magnetic conductor," in *IEEE Antennas and Wireless Propagation Letters*, vol. 15, pp. 950-953, 2016.

[5] N. A. Abbasi and R. J. Langley, "Multiband-integrated antenna/artificial magnetic conductor," in *IET Microwaves, Antennas & Propagation*, vol.

5, no. 6, pp. 711-717, 26 Apr. 2011.

[6] V. K. Pandit and A. R. Harish, "Design of dual-band CPW-fed monopole antenna with dual-band AMC surface for WLAN," *2016 IEEE Annual India Conference (INDICON)*, Bangalore, pp. 1-4, 2016.

[7] F. Rashid, M. M. Mustafiz, M. K. Ghosh, and S. Hossain, "Design and performance analysis of ultra-wideband inverted-F antenna for Wi-Fi, WiMAX, WLAN and military applications," *2012 15th International Conference on Computer and Information Technology (ICCIT)*, Chittagong, pp. 610-614, 2012.

[8] E. Abdo-Sanchez, J. E. Page, T. M. Martin-Guerrero, J. Esteban, and C. Camacho-Penalosa, "Planar broadband slot radiating element based on microstrip-slot coupling for series-fed arrays," in *IEEE Transactions on Antennas and Propagation*, vol. 60, no. 12, pp. 6037-6042, Dec. 2012.

[9] M. van Rooyen, J. W. Odendaal, and J. Joubert, "High-gain directional antenna for WLAN and WiMAX applications," in *IEEE Antennas and Wireless Propagation Letters*, vol. 16, pp. 286-289, 2017.

[10] CST STUDIO SUITE® 2018, CST AG, Germany, www.cst.com

Ernst W. Coetzee received the B.Eng. and B.Eng.Hons. in Electronic Engineering from the University of Pretoria, Pretoria, South Africa in 2016 and 2017, respectively. He is currently employed as an Assistant Lecturer at the University of Pretoria and also busy with his M.Eng. in Electronic Engineering in the field of electromagnetism.

Johann W. Odendaal (M'90–SM'00) received the B.Eng., M.Eng., and Ph.D. degrees in Electronic Engineering from the University of Pretoria, Pretoria, South Africa, in 1988, 1990, and 1993, respectively. From September 1993 to April 1994, he was a Visiting Scientist with the ElectroScience Laboratory at the Ohio State University.

From August to December 2002, he was a Visiting Scientist with CSIRO Telecommunications and Industrial Physics in Australia. Since May 1994, he has been with the University of Pretoria, where he is currently a Full Professor. His research interests include electromagnetic scattering and radiation, compact range measurements, and signal processing. He is also Director of the Centre for Electromagnetism at the University of Pretoria. Odendaal is a Member of the Antenna Measurement Techniques Association (AMTA) and is registered as a Professional Engineer in South Africa

Johan Joubert (M'86–SM'05) received the B.Eng, M.Eng and Ph.D degrees in Electronic Engineering from the University of Pretoria, Pretoria, South Africa, in 1983, 1987 and 1991 respectively. From 1984 to 1988 he was employed as a Research Engineer at the Council for Scientific and Industrial Research, Pretoria. In 1988 he joined the Department of Electrical and Electronic Engineering at the University of Pretoria, where he is currently a Professor of Electromagnetism. From July to December 1995 he was Visiting Scholar with the Department of Electrical and Computer Engineering, California State University, Northridge, USA. From July to December 2001 he was Visiting Scientist at Industrial Research Laboratories in Wellington, New Zealand. From July to December 2006 he was Visiting Scholar at the Institut für Höchstfrequenztechnik und Elektronik, Universität Karlsruhe (TH), Germany, and from July to September 2010 he visited Loughborough University in the UK for a collaborative research project on meta-materials. His research interests include antenna array design and computational electromagnetism. Joubert is a registered Professional Engineer in South Africa.

A Wideband Antenna for Biotelemetry Applications: Design and Transmission Link Evaluation

Ala Alemaryeen and Sima Noghanian

Department of Electrical Engineering, University of North Dakota
Grand Forks, ND, USA
ala.alemaryeen@und.edu, sima.noghanian@und.edu

Abstract—In this paper, the design of a miniature wideband antenna for biotelemetry applications is presented. We propose a biocompatible antenna to be printed on the outer surface of a capsule. The size of the antenna in planar form is 2.52 mm^3. The antenna shows a wide impedance bandwidth of 7.31 GHz (0.78 GHz – 8 GHz, for -10dB reflection coefficient) when implanted inside a simple three layer body model. The antenna gain values at 915 MHz and 2.45 GHz are -25.23 dBi and -27.51 dBi, respectively. The antenna resonance frequency is shown to be robust when implanted in a realistic anatomical body model. The performance of the communication link between the implanted antenna and an external half-wavelength dipole at 915 MHz and 2.45 GHz is also presented.

Keywords—bandwidth enhancement, implantable antenna.

I. INTRODUCTION

Implantable medical devices (IMDs) have gained substantial attention due to their advantage in improving patient's quality of life. In biotelemetry, wireless links are needed for the communication between an implanted system and an external receiver unit. Antennas are the most important components to ensure robust wireless link performance. It is a great challenge to design an implantable antenna due to the complexity and variation of human tissues, which have an effect on the antenna propagation characteristics, i.e., frequency detuning may happen due to the loading effects of tissue covering the antennas. This necessitates the design of implantable antenna of a wide bandwidth characteristic to withstand the frequency shift when implanted inside tissues with different dielectric properties. Furthermore, biocompatibility and small implant size are another critical constraints that should be considered [1-3]. In this paper, we propose a wideband biocompatible small capsule antenna for biotelemetry applications. Numerical investigations were carried out using CST Microwave Studio software [4].

II. IMPLANTABLE ANTENNA DESIGN

The configuration of the proposed implantable antenna is shown in Fig. 1 (a). It consists of a conformal meandered antenna, to achieve miniaturization, designed on the outer wall surface of a capsule, with a diameter of 11 *mm* and length of 24 *mm*. It is assumed that the capsule inner volume will be utilized for the necessary electronic circuits and sensors. A flexible biocompatible material, ultem of 0.5 *mm* thickness with a relative permittivity (ε_r) and loss tangent (tanδ) of 3.15 and 0.0013 S/m, respectively, is used as the capsule substrate.
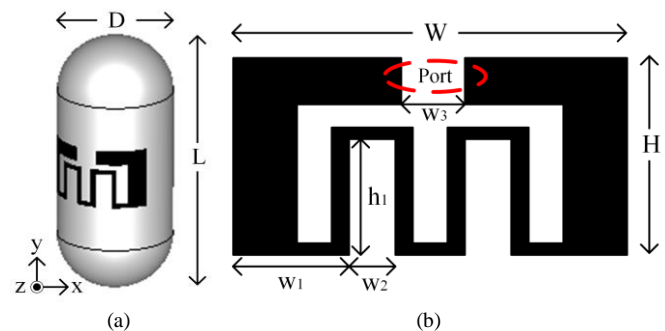
Fig. 1. Configuration of the proposed capsule antenna in: (a) conformal form and (b) planar form. Dimensions in *mm* are: L = 24, D = 11, W = 12, H = 6, h_1 = 3.5, w_1 = 3.5, w_2 = 1.5, and w_3 = 2.

This material is chosen because it has stable properties not affected by the variations of different parameters, such as temperature and frequency. For easy optimization of the antenna, the antenna is first embedded in a three-layer body model (named as Layered Model) that consisted of skin, fat and muscle body tissues of 2 *mm*, 8 *mm*, and 80 *mm* thicknesses, respectively. The dimensions of the body model are $100 \times 100 \times 90$ mm^3, and the depth of embedding the capsule is 40 mm. Properties of dispersive tissue layers are obtained from the material library in CST Microwave Studio software. The antenna in planar form measures $12 \times 6 \times 0.035$ mm^3 and the geometrical parameters of the antenna are shown in Fig. 1 (b).

When considering the influence of the electrical components of the implantable system on the antennas, the batteries are expected to have the most significant effects because of their size. Batteries are simply represented as a perfect electric conductor (PEC) cylinder with a length of 8 *mm* and diameter of 10 *mm* inside the capsule. This model is named as Layered_battery. Moreover, the proposed capsule antenna is analyzed in the anatomical Ella voxel model (without the battery) in two different locations: chest and shoulder, named as Ella_shoulder and Ella_chest, respectively. For the chest implanting the proposed antenna is envisioned as a pacemaker antenna, and for the shoulder implanting the application is for the patients suffering from osteoarthritis [1]. The Ella voxel model consists of various organs and represents a 26-year-old female with a height of 1.36 *m* and weight of 57.3 kg. In order to reduce the simulation time, we only imported the upper part of the human body torso, excluding the head, into our simulation model.
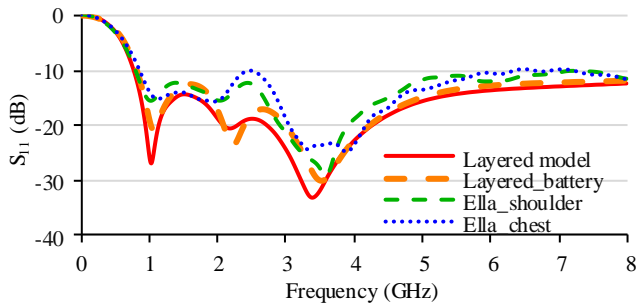
Fig. 2. Comparison of simulated reflection coefficients (S_{11}) of conformal capsule antenna for different simulations setups.

TABLE I. SUMMARY OF THE REALIZED GAIN OF CAPSULE ANTENNA

Scenario	915 MHz	2.45 GHz
Layered model	-25.23 dBi	-27.51 dBi
Layered_battery	-23.31 dBi	-25.32 dBi
Ella_shoulder	-21.77 dBi	-22.20 dBi
Ella_chest	-25.86 dBi	-28.78 dBi

III. RESULTS AND DISCUSSION

In order to test the robustness of the proposed antenna, reflection coefficients (S_{11}) for the aforementioned simulation setups are compared in Fig. 2. The antenna bandwidth ($S_{11} <$ -10 dB) of the layered model implantation case is about 7.31 GHz (0.78 GHz – 8 GHz). Integrating the battery causes a slight shift in the resonance frequencies. The implanted antennas in Ella's shoulder or chest also show a reduction in the S_{11} level and a detuning effect. The most noticeable reduction in the obtained bandwidth, which is about 800 MHz, is observed in the case of implanting antenna in Ella's chest. However, since the antenna is a wideband, these detuning effects do not cause a significant effect on the bandwidth variation. The antenna gain at the center frequencies of the 902.8 MHz – 928.0 MHz, and 2.40 GHz – 2.50 GHz ISM bands are summarized in Table I. These frequency bands are selected as they are commonly used for biotelemetry applications [1], [5]. From Table I, it is clear that the antenna gain is higher within ISM–915 MHz for all the studied cases.

For accurate assessment of the antenna performance for near/far-field communication in biotelemetry applications, where the near-field boundary is approximated at $\lambda/2\pi$ [6], the coupling strength (S_{12}) between an external half-wavelength dipole and the proposed capsule antenna implanted in the layered body model is evaluated for two scenarios. First, the free-space distance (s) of the external dipole is changed in the range of 10 mm – 70 mm, while the implanting depth (d) is 40 mm. Second, distance d is changed in a range of 10 mm – 70 mm, while s is 10 mm. The simulation setup is shown in Fig. 3 (a). For each of the studied frequency bands, a different dipole is adopted. As shown in Fig. 3 (b), the coupling strength at 915 MHz is higher than that at 2.45 GHz for both studied cases due to the larger obtained gain values at 915 MHz with changing d and s distances (results are not shown here due to space limitations and will be discussed during the presentation).
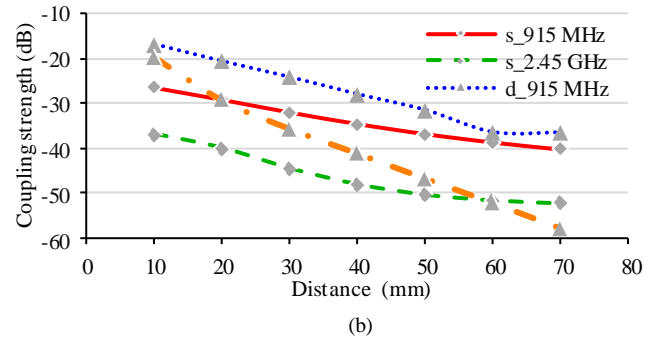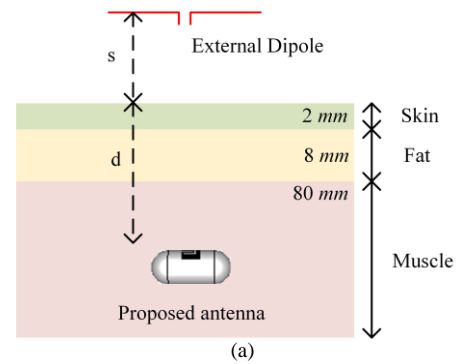
Fig. 3. Coupling strength for external half wavelength dipole: (a) simulation setup, and (b) results for different free space distances (s) and implant depths (d).

IV. CONCLUSION

The design and performance evaluation of a miniaturized wideband implantable capsule antenna is presented. The advantage of the wideband property of the proposed antenna is demonstrated through the performance evaluation of this antenna when it is implanted in a simplified layered body model and an anatomical realistic body model, as well as when it is integrated with a battery. Also, the near/far-field communication analysis is carried out at 915 MHz and 2.45 GHz for different free space distances of the receiver and different implant depths. Findings of this study suggest that the proposed capsule antenna support the functionality of wireless data transmission and wake-up receiver signal within 902.8 MHz–928.0 MHz and 2.40 GHz–2.50 GHz ISM bands, respectively. The wake-up receiver signal is necessary to save power by transmitting data only when is needed.

REFERENCES

[1] Z. Duan, Y. X. Guo, M. Je, and D. L. Kwong, "Design and in vitro test of a differentially fed dual-band implantable antenna operating at MICS and ISM Bands," IEEE Trans. Antennas Propag., vol. 62, no. 5, pp. 2430–2439, 2014.
[2] L. J. Xu, Y. X. Guo, and W. Wu, "Bandwidth enhancement of an implantable antenna," IEEE Antennas Wirel. Propag. Lett., vol. 14, pp. 1510–1513, 2015.
[3] A. Kiourti and K. S. Nikita, "Miniature scalp-implantable antennas for telemetry in the MICS and ISM bands: Design, safety considerations and link budget analysis," IEEE Trans. Antennas Propag., vol. 60, no. 8, pp. 3568–3575, 2012.
[4] CST Microwave Studio [Online]. Available: http/www.cst.com
[5] R. Das and H. Yoo, "A wideband circularly polarized conformal endoscopic antenna system for high-speed data transfer," IEEE Trans. Antennas Propag., vol. 65, no. 6, pp. 2816–2826, 2017.
[6] J. D. Kraus, Antenna Measurements, in Antennas for All Applications, 3rd ed., New York, NY, USA: McGraw-Hill, 2002.

Design and Implementation of a Quad Element Patch Antenna at 5.8 GHz

Mohammad R. Sobhani [1], Negar Majidi [2], and Şehabeddin T. Imeci [3]

[1] Department of Electrical and Computer Engineering
University of Alberta, Edmonton, AB T6G 2W3, Canada
rahimsob@ualberta.ca

[2] Department of Electrical and Electronics Engineering
Özyeğin University, Istanbul, Çekmeköy 34794, Turkey
negar.majidi@ozu.edu.tr

[3] Department of Electrical and Electronics Engineering
International University of Sarajevo, Sarajevo 71210, Bosnia and Herzegovina
simeci@ius.edu.ba

Abstract ─ This paper presents simulation and experimental verification of a quad microstrip patch antenna that operates at 5.8 GHz. Sonnet antenna design software was used to simulate the performance of the antenna. To reduce the design's complexity and the computational load, the antenna and the feeding lines were simulated separately. An optimization was done for each subpart to get the optimum desired results. Finally, all the subparts were merged and the final structure was simulated to check the performance. A prototype of the antenna was fabricated on a double-sided PCB substrate (relative permittivity=10.2, thickness=1.28 mm) using a PCB milling machine. The S11 of -14 dB and -18.8 dB and maximum gain of 6.2 dB and 4.2 dB were obtained, from the simulation and experimental measurements, respectively.

Index Terms ─ 2x2 Microstrip Patch Antenna, 5.8 GHz Antenna, Quad Microstrip Patch Antenna.

I. INTRODUCTION

An antenna is a transducer that converts voltage and current on a transmission line into an electromagnetic wave and to transmit and receive data wirelessly. Antennas are a crucial component of all types of wireless devices and technologies that we use everyday and almost everywhere.

Nowadays, microstrip patch antennas are frequently used in telecommunication products like Wireless Local Area Networks (WLAN), cellphones, Global Positioning Systems (GPS), and in many other technologies due to their low cost, low profile, light weight, and easiness of fabrication and integration [1-3]. Because the size of the microstrip antennas are directly related to wavelength of resonance frequencies they are typically used at

microwave band frequencies. The small features of these devices and feasibility of fabrication on the same electrical board, increases the demand of patch antennas for of grid sensor and energy harvesting applications too, as providing the energy to a sensor operating in harsh environment is important [4-7].

Literately, when the microstrip patch antenna is excited, the electrical charges are accumulated at the edges of the patches. These electrical charges make curved fringing fields and therefore these fields at the edges of the microstrip antenna generate electromagnetic radiation [8, 9]. Therefore, the parameters such as frequency, input impedance and gain of the antenna depend on the geometrical shape and the feeding type as well as the physical properties of the substrate [10].

The frequency band of 5.8 GHz is especially important for high speed Wi-Fi routers, FPV (First Person View) applications like remote controlling and online streaming where the transmitter could be placed in a remotely controlled device where antennas with smaller dimensions and profile are desirable.

This paper represents a designed and fabricated antenna to operate at 5.8 GHz, optimizing all the geometrical shape and feeding lines of a 2x2 array. For the antenna, the architecture presented in [11, 12] was used where a 2x2 array of microstrip patch antennas were simulated. The shape and feeding lines were changed and redesigned to operate the antenna at 5.8 GHz. An inset-fed feeding method was chosen which provides an effortless way of impedance control [13-15].

II. DESIGN CONSEDIRATION

The design of the antenna array was started by choosing the suitable patch shape of the antenna. The rectangular patch shape antenna was chosen because it

simplifies the analysis and numerical calculations. The single path antenna was designed with input impedance of 100 Ohm on a substrate with high ε_r of 10.2 and thickness of 1.28 mm (ROGERS, RO3010) to operate at 5.8 GHz. The single patch antenna was simulated in SONNET and the inset feed's parameters were adjusted to obtain lowest input reflection coefficient as much as possible.

As a start point, the patches were simulated with inset feeds. The simulations were started with known theoretical equations for the rectangular single patch antenna. The dimensions and the feed lines were optimized using Sonnet Suite. Then 4 of these single patch antennas were combined through feed lines and the central input via. A 100 mm thick of air layer was added during the Sonnet simulations such that the whole antenna was placed in a 100 x 400 x 300 mm insulation box.

Separately, the feed line for an array of 2 by 2 antennas was simulated where 100 Ohm resistors were connected to end of the lines. Finally, all the components were merged and connected to each other and the parameters were swept to get the lowest S11. Figure 1 shows the geometry of the 2x2 microstrip patch antenna that was designed in this paper.
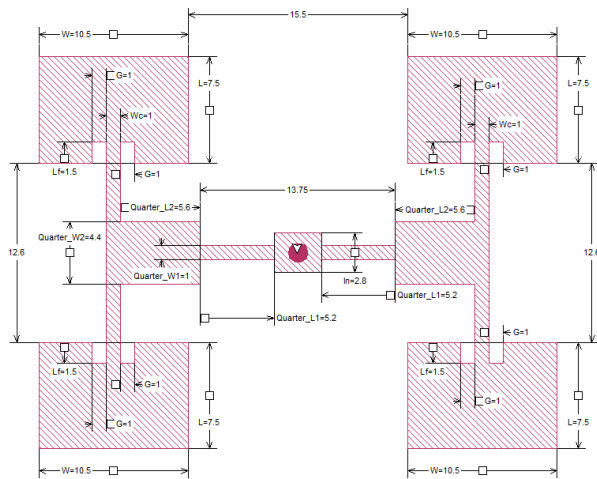
Fig. 1. Proposed 2x2 microstrip patch antenna with via feeding. The antenna was put inside a box with multiple times of the antenna's exact size (box size of 400 x 300 mm and air height of 100 mm on top of it).

The input port of the antenna was a via placed at the center as shown in the Fig. 1. The input was coupled to the antenna patches through a 2 stage Binomial feeding line to achieve good impedance matching. Dimensions of the patch antennas were calculated using analytical equations and then few optimizations were done to get the optimum dimensions. In order to reduce the proposed antenna size, a substrate with high ε_r of 10.2 with thickness of 1.28 (ROGERS, RO3010) was used for the simulations and the prototype.

The last optimization was done to adjust the dimensions of the whole antenna to reach the lowest reflection coefficient as much as possible. The final dimensions of the antenna are shown in Table 1. Figure 2 shows the fabricated antenna using drilling machine.

(a)

(b)
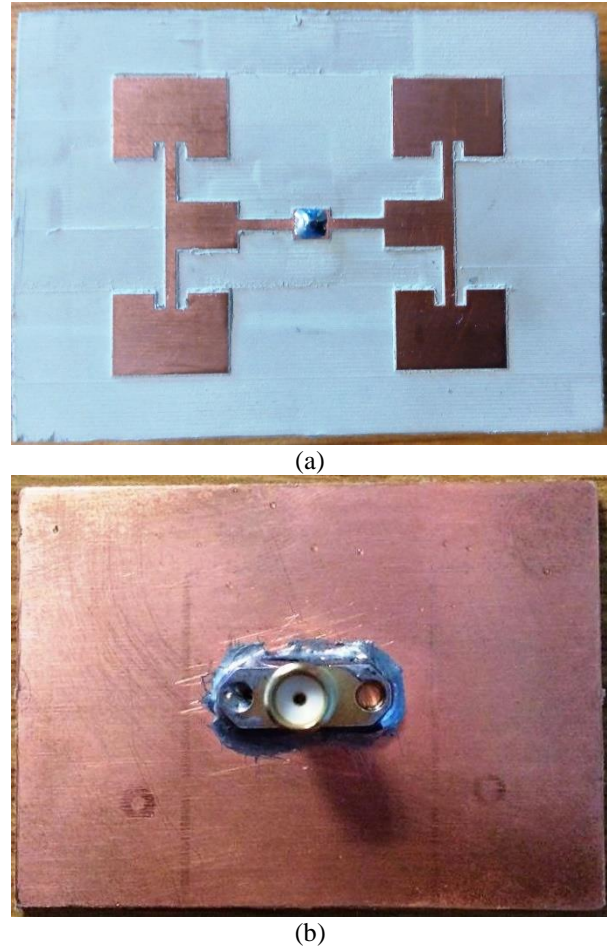
Fig. 2. Prototype of the designed antenna on the RO3010 substrate using drilling machine: (a) front view and (b) back view.

Table 1: Dimensions of the proposed antenna

Uppercase	Dimensions (mm)
Rectangular patch	W = 10.5 L = 7.5
Inset feed	G = 1 Lf = 1.5 Wc = 1
Microstrip feed line	Quarter_L1 = 5.2 Quarter_W1 = 1 Quarter_L2 = 5.6 Quarter_W2 = 4.4 In = 2.8
Other parameters	Vertic. gap = 12.6 Horiz. gap = 15.5

III. RESULTS

Based on the results obtained from simulations by SONNET, the maximum gain of 6.2 dB on the side lobes, and the input reflection coefficient of -14 dB were achieved at the operation frequency of 5.8 GHz. Obtaining these satisfying results from the simulations made the fabrication to start for prototype antenna.

The antenna was fabricated on the specified substrate (ROGERS, RO3010) as shown in Fig. 2. A 50 Ohm female socket was soldered from back side of the antenna. The antenna was sent to another facility to perform the practical measurements by an expert. The measurements for the prototype antenna and the simulation results are shown in Fig. 3. There is a good agreement between the measurements and the simulations. However, the slightly differences can be attributed to the inaccuracies during the fabrication and measurement process. The used substrate has a soft dielectric layer and it is not good to be fabricated by drilling machine.

(a)

(b)
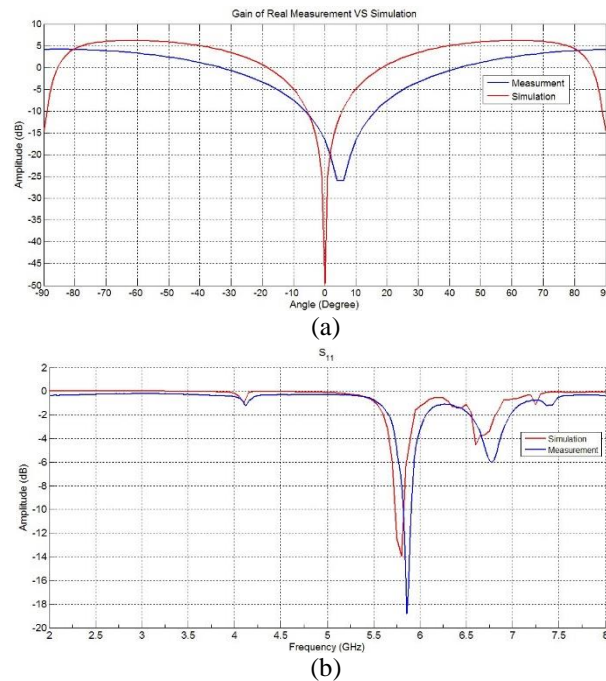
Fig. 3. Comparison of measurement and simulation results: (a) directivity gain of the antenna and (b) input reflection coefficients.

A simulation for the current density over the antenna patches also was done as illustrated in Fig. 4. The microstrip patch antennas emit electromagnetic waves at the outer edges of the antennas; therefore, the current density along the perimeter of the patch antenna should be higher compared to the other parts at resonance frequencies. Figure 4 illustrates the JXY Magnitude for the current density in Amps/Meter unit.
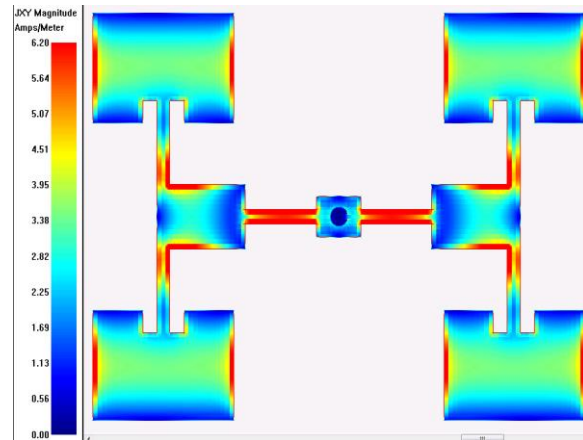
Fig. 4. Current density of the antenna operating at 5.8 GHz in JXY Magnitude (Amps/Meter).

IV. CONCLUSION

In this work, a 2x2 microstrip patch antenna was designed and fabricated at 5.8 GHz that only occupies 2.7 cm by 3.6 cm. The design was done somehow to obtain the low S11 as much as possible. The measured gain of 4.2 dB and S11 of -18.8 dB were obtained for the antenna. There is a good agreement between results obtained by measurements and simulations. However, the slight differences between the simulation and measurements are due to the inaccuracy of the drilling machine that was used to build the antenna. Inaccuracy in the directivity gain may come from slightly shifted mounting of the antenna on the chunk. Also, from fabricated errors which introduces nonsymmetric shapes to the array.

To keep the computational load as low as possible, only a few parameters were contributed in the parameters sweep. However, the results can be further optimized by using high performance workstations to execute the sequential optimization algorithms and manipulation of all possible parameters to obtain the optimum dimensions.

Also, a precise antenna can be fabricated using laser-based fabrication methods. This will further reduce the error of fabrication and prevent of dielectric layers peeling off.

REFERENCES

[1] J. R. James and P. S. Hall, *Handbook of Microstrip Antennas*. Peter Peregrinus, London, UK, 1989.
[2] J. Q. Howell, "Microstrip antennas," *IEEE Trans. Antennas Propagation Magazine*, vol. AP-23, pp.

90-93, 1975.

[3] R. Garg, P. Bhartia, I. Bahl, and A. Ittipiboon, *Microstrip Antenna Design Handbook*, London, Artech House, 2001.

[4] X. Li, J. Wang, X. Wu, and H. Zaho, "A dual-band integrated wireless energy harvesting system," *International Applied Computational Electromagnetics Society Symposium (ACES)*, Sept. 2017.

[5] M. Aboualalaa, A. B. Abdel-Rahman, A. Allam, H. Elsadek, and R. K. Pokharel, "Design of a dualband microstrip antenna with enhanced gain for energy harvesting applications," *IEEE Antennas and Wireless Propagation Letters*, vol. 16, pp. 1622-1626, Jan. 2017.

[6] M. Palandoken, "Microstrip antenna with compact anti-spiral slot resonator for 2.4 GHz energy harvesting applications," *Microwave and Optical Letters*, vol. 58, no. 6, Mar. 2016.

[7] O. Amjad, S. W. Munir, S. T. Imeci, and A. O. Ercan, "Design and implementation of dual band microstrip patch antenna for WLAN energy harvesting system," *ACES Journal*, vol. 33, no. 7, July 2018.

[8] P. S. Nakar, "Design of a Compact Microstrip Patch Antenna for use in Wireless/Cellular Devices," *Thesis*, Florida State University, pp. 20-45, 2004.

[9] A. F. Alsager, "Design and Analysis of Microstrip Patch Antenna Arrays," *Thesis*, University College of Boras, 2011.

[10] J. R. Ojha and M. Peters, "Patch Antennas and Microstrip Lines," *Microwave and Millimeter Wave Technologies Modern UWB Antennas and Equipment*, I. Mini (Ed.), ISBN: 978-953-7619-67-1.

[11] C. K. Ghosh and S. K. Parui, "Design and study of a 2x2 microstrip patch antenna array for WLAN/MIMO application," *2009 International Conference on Emerging Trends in Electronic and Photonic Devices & Systems (ELECTRO-2009)*, 2009.

[12] C. Ninan, C. H. Shekhar, and M. Radhakrishna, "Design and optimization of a 2x2 directional microstrip patch antenna," *Communications in Computer and Information Science*, July 2013.

[13] S. Rajan, "Design and analysis of rectangular microstrip patch antenna using inset feed technique for wireless application," *IJIRSET*, vol. 4, spec. iss. 4, Apr. 2015.

[14] M. S. R. Mohd Shah, M. Z. A. Abdul Aziz, M. K. Suaidi, and M. K. A Rahim, "Dual linearly polarized microstrip array antenna, *Trends in Telecommunications Technologies*, C. J. Bouras (Ed.), ISBN: 978-953-307-072-8.

[15] M. A. Matin and A. I. Sayeed, "A design rule for inset-fed rectangular microstrip patch antenna," *WSEAS Transactions on Communications*, vol. 9, iss. 1, Jan. 2010, ISDN: 1109-2742.

Mohammad Rahim Sobhani received the B.Sc. degree in Biomedical Engineering (Bio-electric) from Sahand University of Technology, Tabriz, Iran, in 2012, and the M.Sc. in Electrical and Electronics Engineering from Özyeğin University, Istanbul, Turkey, in 2015.

He was a Research and Teaching Assistant at Özyeğin University, from 2013 to 2016. Currently he is a Ph.D. Student and a Graduate Assistant in Electrical and Computer Engineering Department, University of Alberta, AB, Canada since January 2017. His current research interests include Ultrasound Imaging and Transducers, micro fabrication, and Bio-Sensors.

Negar Majidi received the B.Sc. degree in Biomedical Engineering (Bioelectric) from Sahand University of Technology, Tabriz, Iran, in 2014, and the M.Sc. in Electrical and Electronics Engineering from Özyeğin University, Istanbul, Turkey, in 2018.

She was a Research and Teaching Assistant at Özyeğin University, from 2014 to 2016. Her current research interests include MEMS, Optic and Laser, and Bio-Sensors.

Şehabeddin Taha İmeci received the B.Sc. degree in Electronics and Communications Engineering from Yildiz Technical University, Istanbul, Turkey in 1993, and the M.S.E.E. and Ph.D. Degrees from Syracuse University, Syracuse, NY in 2001 and 2007, and Associate Professorship degree from Istanbul Commerce University, Istanbul Turkey in 2014, respectively. Imeci was appointed as Full Professor in Int. Univ. of Sarajevo in Nov. 2017. He is working as the Dean of FENS (Faculty of Engineering and Natural Sciences) in Sarajevo. He was with Anaren Microwave Inc., East Syracuse, NY from 2000 to 2002, and Herley Farmingdale, New York from 2002 to 2003, and PPC, Syracuse, NY from 2003 to 2005, and Sonnet Software Inc., Liverpool, NY from 2006 to 2007. He was a Teaching Assistant in the Department of Electrical Engineering and Computer Science at Syracuse University from 2005 to 2006. His current research areas are microwave antennas and electromagnetic theory.

Design and Comparison of 4 Types of Dual Resonance Proximity Coupled Microstrip Patch Antennas

Negar Majidi [1], Mohammad R. Sobhani [2], Bahadır Kılıç [3], Mustafa Imeci [4], Oğuzhan S. Güngör [5], and Şehabeddin T. Imeci [6]

[1] Department of Electrical and Electronics Engineering
Özyeğin University, Istanbul, Çekmeköy 34794, Turkey

[2] Department of Electrical and Computer Engineering
University of Alberta, Edmonton, AB T6G 2W3, Canada

[3] Department of Electrical and Electronics Engineering
Halic University, Istanbul Turkey

[4] Department of Electrical and Electronics Engineering
Ankara Yildirim Beyazit University, Ankara, Turkey

[5] Department of Electrical and Electronics Engineering
Selcuk University, Konya, Turkey

[6] Department of Electrical and Electronics Engineering
International University of Sarajevo, Sarajevo 71210, Bosnia and Herzegovina

Abstract ─ In this paper there are four different shapes of proximity patch antennas (straight, trimmed, trapezoid and ribbon). The minimum input match achieved with the straight proximity patch antenna as -39.68 dB. The maximum gain is achieved with the ribbon proximity patch antenna as 12.1 dB. Simulation and measurement results are presented. There is a perfect match with simulated and measured gain. The antenna is first demonstrated example of working with four different geometries, having satisfactory gain and input match.

Index Terms ─ bandwidth, gain, patch antenna, proximity, return loss, ribbon, trapezoid.

I. INTRODUCTION

The four antennas that will be explained in this article have a midband between 3.15 and 3.56 GHz and bandwidth of 0.19 and 0.23 GHz, which are typically used in various applications like military, satellite communications or wireless. This work explains the design and test of a proximity coupled patch antennas constructed from relatively high-quality dielectric material. Two dielectric substrates are used such that the feed line is between the two substrates and the radiating patch is on top of the other substrate [1]. The purpose of this work is to make a comparative study on the technique that helps to overcome the bandwidth constraint of microstrip patch antennas and to propose the better technique by taking different consideration such as the antenna gain, bandwidth and related issues [2]. Basic ideas about microstrip patch antenna, its working principle and important parameters have been discussed. The paper explained the analysis and designs a typical patch antenna that helps describing its narrow bandwidth problem as well. A paper shows improving the bandwidth of proximity coupled stacked microstrip patch antennas [3]. The results obtained clearly indicate the main factors that affect the bandwidth of a particular microstrip antenna are thickness of the dielectric substrate, the size of the metallic patch, the dielectric constant of the dielectric substrate, the feed type to be used (as seen in the non-contacting feed techniques) and the coupling level to some extent [4]. Aperture coupling is also used in [5] for this purpose. Most efficient part of the gain enhancement is maintained by changing the geometries of the slots [5].

II. DESIGN DETAILS

The work is done by using a high frequency electromagnetic simulator called Sonnet Suites [6]. The same software was used to simulate different types of microstrip patch antennas operating at 2.4 and 5.8 GHZ

[7, 8].

In order to meet the required design specifications, important parameters need to be optimized. Better results could be obtained after several iteration steps. All antennas are placed on 290 x 290 mm box. The material used for the substrates is Rogers RT5880 (εr = 2.2). The thickness of the dielectric layers is used as 0.8 mm. Feeding line dimensions are 145.9 x 2.6 mm. Edge feeding is used.

A. The straight proximity patch antenna

The dimension of antenna is 27 x 39 mm. The minimum return loss was achieved with this antenna among all four antennas. The minimum return loss achieved is -39,68 dB and the maximum gain of 8.05 dB is achieved at 3.56 GHz. Table 1 has different proximity patch antenna geometries which are discussed below.

B. The trimmed proximity patch antenna

The trimmed antenna is a different form of the straight proximity patch antenna. Short sides are angled as 3° with both ways. 41.52 x 27.03 mm and 1,315 mm sliding are dimensions of this antenna. The minimum return loss achieved is -29,07 dB and the maximum gain of 8.25 dB is achieved at 3.52 GHz.

C. The trapezoid proximity patch antenna

The height of the antenna is 27 mm. Opposite sides of the antenna measures are 45 x 30 mm. The shape of the antenna is isosceles trapezoid. Isosceles zones both have 15° contraction. The minimum return loss achieved is -14.63 dB and the maximum gain of 7.98 dB is achieved at 3.448 GHz.

D. The ribbon proximity patch antenna

The maximum gain was achieved with this antenna among all four antennas. The maximum gain is 12,10 dB at 10.2 GHz. The minimum return loss achieved is -17.55 dB at 3.15 GHz. The height of the antenna is 27 mm and opposite edges of the antenna measures are 40 x 40 mm.

Table 1: Different geometries of proximity patch antennas
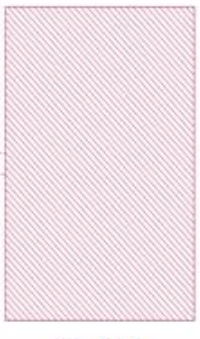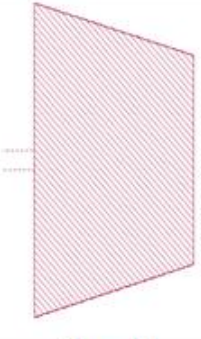
Type	Straight	Trimmed	Trapezoid
S-11	-39.68 dB	-14.63 dB	-29.07 dB
Gain	8.05 dBi	7.29 dBi	8.25 dBi
Frequency	3.56 GHz	3.52 GHz	3.309 GHz

The most important result about the ribbon proximity patch antenna is dual resonance. The ribbon proximity patch antenna has dual resonance with high gain. As it is seen in the literature, this kind of antenna has better solutions in communication. As seen in Fig. 1, input match of the ribbon antenna at 3.15 GHz is 17.55 dB and at 10.2 GHz is 14.96 dB. Figure 2 shows the current distribution of the ribbon antenna at 3.15 GHz. Figure 3 shows the current distribution of the ribbon antenna at 10.2 GHz. Figure 4 shows The ribbon proximity coupled patch antenna has a gain of 7.21 dB at 3.15 GHz at θ = 0° and it has also a gain of 12.10 dB at 10.2 GHz with θ = 0°. Figure 5 shows far field radiation pattern of the ribbon proximity coupled patch antenna which has a gain of 12.10 dB at 10.2 GHz with θ 0°.
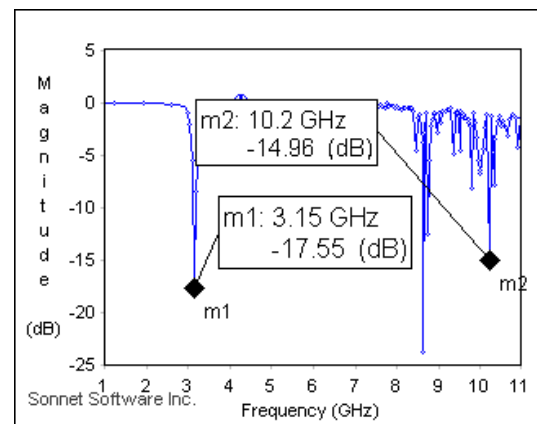
Fig. 1. Input match of the Ribbon Antenna.
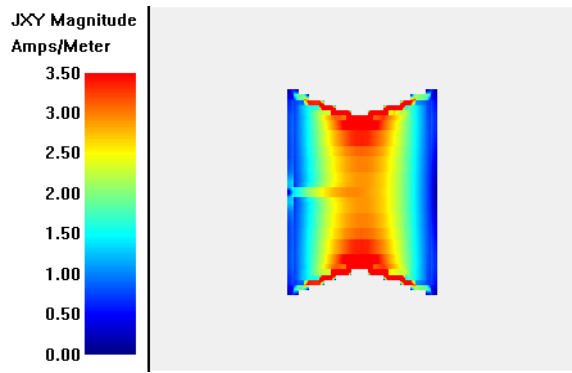
Fig. 2. Current dist. of the ribbon antenna at 3.15 GHz.
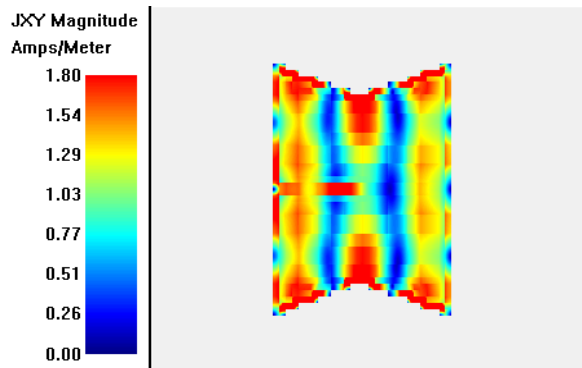
Fig. 3. Current dist. of the Ribbon Antenna at 10.2 GHz.
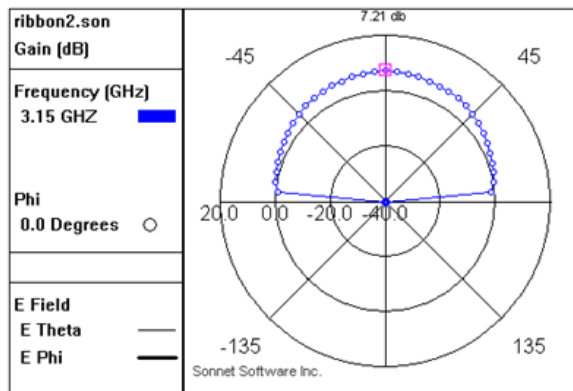
Fig. 4. Far field view of the Ribbon Proximity Coupled Patch Antenna, which has a gain of 7.21 dB at 3.15 GHz with θ = 0°.
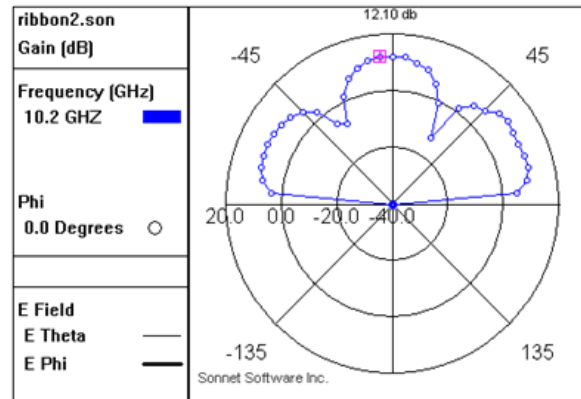
Fig. 5. Far field view of the Ribbon Proximity Coupled Patch Antenna, which has a gain of 12.10 dB at 10.2 GHz with θ=0°.

III. RESULTS AND FABRICATION

The straight antenna was fabricated due to its easiest structure among others. Top view is in Fig. 6. Figure 7 shows the input match of the simulated and measured antenna. 3D view of straight antenna is in Fig. 8 and Fig. 9 shows the radiation pattern comparison of the simulated and measured antenna. There is only a small frequency shift between the simulated and measured input match. Furthermore, the gain has perfect match at Θ = 0°.

Fig. 6. Top view of the fabricated antenna.
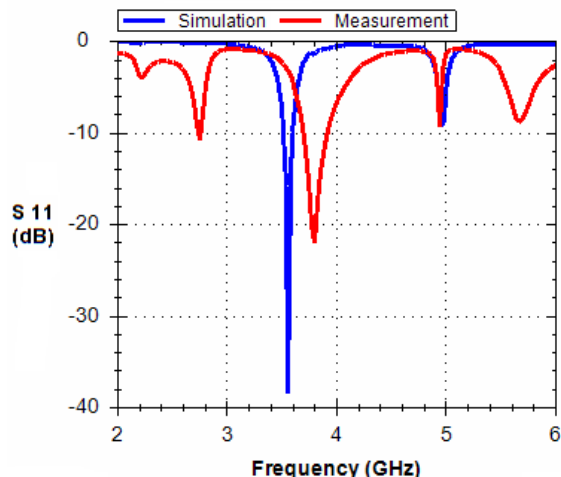
Fig. 7. Input reflection coefficient comparison of the antenna.
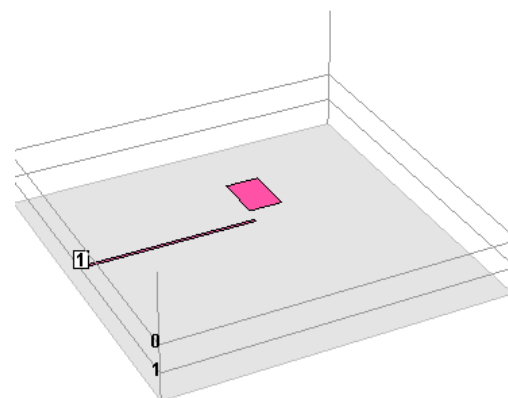
Fig. 8. 3D view of the Straight Proximity Patch Antenna simulated in SONNET.

Table 2 has a parametric study with variations of dielectric thicknesses.

Table 2: Thickness response of the ribbon patch antenna

DIELECTRIC THICKNESS mm.	FREQUENCY GHz	S-11 dB	GAIN dB
1.5	3.025	-21.67	7.70
	10.125	-9.94	10.18
0.9	3.125	-16.74	7.20
	10.275	-10.95	11.86
0.85	3.15	-14.003	7.48
	10.3	-10.39	11.54
0.74	3.15	-15.86	7.22
	10.225	-14.28	12.19
0.7	3.175	-15.19	6.42
	10.35	-11.09	12.006
0.6	3.175	-18.23	6.57
	10.275	-13.27	12.04
0.3	3.25	-26.09	6.33
	10.3	-12.71	12.52
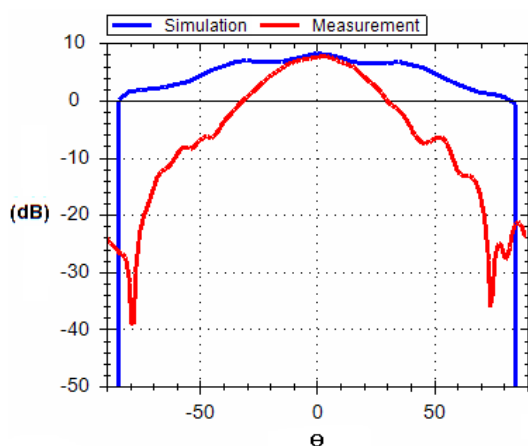
Fig. 9. Directivity gain of the proposed antenna.

IV. CONCLUSION

In this work, four different geometries of proximity coupled patch antenna were designed, simulated, fabricated and tested. Dual resonance has been achieved with the ribbon shaped proximity patch antenna.

The minimum return loss achieved is -39,68 dB with the straight proximity patch antenna at 3.56 GHz. The maximum gain is achieved 12.10 dB at 10.2 GHz with ribbon proximity patch antenna. Measurement result of straight patch antenna as follows: S11 = -21 dB at 3.79 GHz and Gain = 7.3 dB.

REFERENCES

[1] Z. Hailu, "Comparative Study on Bandwidth Enhancement Techniques of Microstrip Patch Antenna," *Thesis*, pp. 1-86, Jan. 2008.

[2] K. Wong, Compact and Broad Band Microstrip Antennas. *John Wiley & Sons Inc.*, 2002.

[3] W. S. T. Rowe and R. B. Waterhouse, "Investigation into the performance of proximity coupled stacked patches," *IEEE Antennas and Propagation*, vol. 54 pp. 1693-1698, June 2006.

[4] R. Sastry and K. J. Sankar, "Proximity coupled rectangular microstrip antenna with X-slot for WLAN application," *Global Journal of Researches in Engineering: Electrical and Electronics Engineering*, vol. 14, no. 1, pp. 1360-1370, Jan. 2014.

[5] M. Ali, A. Kachouri, and M. Samet, "Novel design of a compact proximity coupled feed antenna," *International Journal of Computer Science Issues*, vol. 9, no. 3, pp. 419-426, Jan. 2012.

[6] Sonnet Suites, version: 13.56, www.sonnetsoftware.com, 2014.

[7] O. Amjad, S. W. Munir, S. T. Imeci, and A. O. Ercan, "Design and implementation of dual band microstrip patch antenna for WLAN energy harvesting system," *ACES Journal*, vol. 33, no. 7, July 2018.

[8] N. Majidi, G. Goksenin Yaralioglu, M. Rahim Sobhani, and S. T. Imeci, "Design of a quad element patch antenna at 5.8 GHz," 2018 *ACES Conference*, 2018.

Negar Majidi received the B.Sc. degree in Biomedical Engineering (Bioelectric) from Sahand University of Technology, Tabriz, Iran, in 2014, and the M.Sc. in Electrical and Electronics Engineering from Özyeğin University, Istanbul, Turkey, in 2018.

She was a Research and Teaching Assistant at Özyeğin University, from 2014 to 2016. Her current research interests include MEMS, Optic and Laser, and Bio-Sensors.

Mohammad Rahim Sobhani received the B.Sc. degree in Biomedical Engineering (Bio-electric) from Sahand University of Technology, Tabriz, Iran, in 2012, and the M.Sc. in Electrical and Electronics Engineering from Özyeğin University, Istanbul, Turkey, in 2015.

He was a Research and Teaching Assistant at Özyeğin University, from 2013 to 2016. Currently he is a Ph.D. Student and a Graduate Assistant in Electrical and Computer Engineering Department, University of Alberta, AB, Canada since January 2017. His current research interests include Ultrasound Imaging and Transducers, micro fabrication, and Bio-Sensors.

Mustafa Imeci received the B.Sc. degree in Electronics and Communications Engineering from Yildirim Bayezid University, Ankara in 2018. His main research area is Digital Signal Processing and Microwave Antennas.

Oguzhan Salih Gungor is pursuing his B.Sc. in Electronics and Communications Engineering in Selcuk University, Konya, Turkey. He published three IEEE conference papers.

Bahadir Kilic received the B.Sc. degree in Electronics and Communications Engineering from Halic University, Istanbul in 2017. He is working in medical electronics area.

Şehabeddin Taha İmeci received the B.Sc. degree in Electronics and Communications Engineering from Yildiz Technical University, Istanbul, Turkey in 1993, and the M.S.E.E. and Ph.D. Degrees from Syracuse University, Syracuse, NY in 2001 and 2007, and Associate Professorship degree from Istanbul Commerce University, Istanbul Turkey in 2014, respectively. Imeci was appointed as Full Professor in Int. Univ. of Sarajevo in Nov. 2017. He is working as the Dean of FENS (Faculty of Engineering and Natural Sciences) in Sarajevo. He was with Anaren Microwave Inc., East Syracuse, NY from 2000 to 2002, and Herley Farmingdale, New York from 2002 to 2003, and PPC, Syracuse, NY from 2003 to 2005, and Sonnet Software Inc., Liverpool, NY from 2006 to 2007. He was a Teaching Assistant in the Department of Electrical Engineering and Computer Science at Syracuse University from 2005 to 2006. His current research areas are microwave antennas and electromagnetic theory.

Supercapacitor Implementation for PV Power Generation System and Integration

Abdullah Eroglu[1], Tunir Dey[2], Kowshik Dey[2], and Greg Whelan[2]

[1] Department of Electrical and Computer Engineering
North Carolina A&T State University, Greensboro, NC, 27411, USA
aeroglu@ncat.edu

[2] Department of Electrical and Computer Engineering
Purdue University Fort Wayne, Fort Wayne, IN, 46805, USA

Abstract—**Novel hybrid energy storage system configuration is introduced by interleaving the supercapacitor between the electrostatically sensitive devices (ESDs) and DC-link capacitors that can handle all power demands in transient or steady state conditions, and perform the ESD functions. The new system integrates an adaptive sliding-mode DC-DC control method to address the voltage permutations and ensure the required output voltage. Bi-directional power flow, important to the continuous hybrid energy storage system operation is also fulfilled. The continuous successful operation is provided with supplemental protection controls. The operation of the proposed system is verified through simulation with Matlab/Simulink. The hybrid energy system developed in this paper can be used in several applications including electrical vehicles and grid integration of Photovoltaic (PV) systems.**

Index Terms—**adaptive sliding-mode control, electric vehicles, grid, Hybrid energy storage, PV, supercapacitor.**

I. INTRODUCTION

Energy storage systems are becoming of greater importance due to the rising need for reliable back-up power to ensure power continuity and renewable energy power integration with potential intermittent power output. The conventional energy storage is in the form of a battery. However, an additional element is needed to provide instantaneous power for transient loads. The hybrid energy storage system has been developed to provide power for transient loads by integrating another energy storage element, supercapacitor, to overcome this challenge. Hybrid energy storage utilizes this combination of the supercapacitor and a battery to provide continuous and instantaneous demand response such as the one shown in Fig. 1 with additional PV power generation system. Hence, the hybrid energy storage system is designed to be capable of nearly all the required load responses since it has the near instantaneous response due to supercapacitor and the energy density contained within a charged battery for non-transient responses.

Hybrid energy storage has been well researched including various energy storage element combinations and configurations with several critical quantities [1-3]. It has been shown that an electrostatically sensitive devices (ESDs) and supercapacitor connected in parallel to a common dc bus is the widely used configuration for the energy storage elements [4-5]. The two energy storage elements cover the entire operational spectrum, the supercapacitor providing instantaneous response and the ESD provides steady state response [6]. Fundamentally, different demand responses are a result of the nature and design of each energy storage element type so determination of the demands nature, and differentiation thereof, expresses the required response [1-3]. Hence, the procedures and processes to achieve such a task complicates the control structure and requires additional resources.
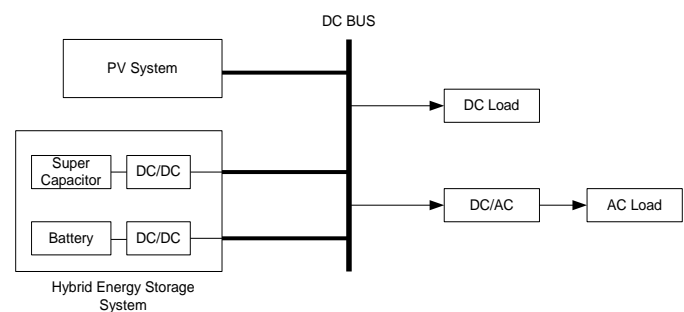
Fig. 1. Typical hybrid energy storage system.

In this paper, novel hybrid storage system configuration according to author's knowledge has been developed by interleaving the supercapacitor between the ESD and DC-link capacitor. This enables the supercapacitor to directly handle all power demands in transient or steady state conditions, and perform the ESD functions to maintain the supercapacitor charged. Furthermore, the configuration proposed eliminates the differentiation regarding the nature of the power demand and thus reduces the system's control complexity. The adaptive sliding-mode DC-DC control method [7] is integrated to the configuration to address the voltage permutations to ensure the desired output voltage. The new hybrid storage system provides bi-directional power flow which is important to the continuous hybrid energy storage system operation as well. The continuous successful operation is fulfilled with supplemental protection controls to prevent component failure. The operation of the proposed configuration is simulated and verified with Matlab/Simulink using Power Systems toolkit.

II. FORMULATION

In the proposed hybrid energy system, the bi-directional DC-DC converter is based on the cascaded buck-boost converter topology which has an intermediate stage to store energy at a higher voltage and allows the overlap between battery voltage

and DC bus voltage in the whole operating range [8] as shown in Fig. 2.
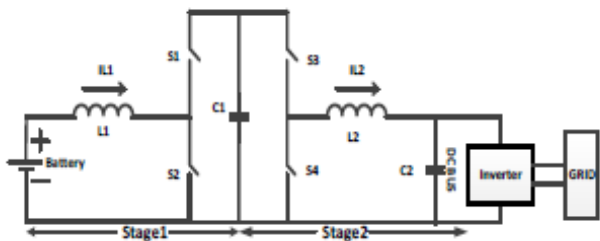
Fig. 2. Cascaded buck-boost converter topology [8].

The new hybrid system that is developed in this paper places the supercapacitor as the intermediate capacitor in this topology. It operates at a high reference voltage as the supercapacitor voltage and hence it reduces the complexity in the control scheme. This is due to fact that supercapacitor's charge is used to track its reference as power must flow through the interleaved stage throughout operation. The equivalent circuit of the supercapacitor [9] used in the system is given in Fig. 3.
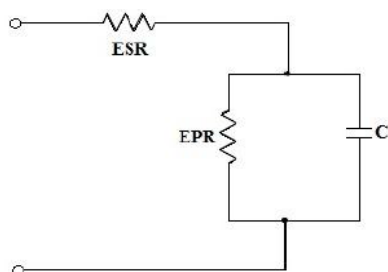
Fig. 3. The equivalent circuit of the supercapacitor.

In the equivalent circuit shown in Fig. 3, an equivalent series resistance (ESR) is used to represent charging and discharging, capacitance (C) and parallel capacitor (EPR) represent the losses during discharging [10]. The total supercapacitance and supercapacitance resistance are all described in [11].

The computational burden in regards to the nature of the power demand with the parallel energy storage configuration makes the control scheme's cumbersome. The proposed interleaved configuration with supercapacitor eliminates several challenges such as filtering to categorize the nature of the load presented and need for processing resources [1] or prior knowledge of the required load for processing [4]. The proactive adaptive sliding mode controller is integrated to the proposed design to achieve the correct response to a maximum transient load and all other transient loads of lesser magnitude. This control method also eliminates the potential need for additional computation. Proper DC-DC converter control providing bi-directional power flow allows the system to be recharged during periods of low or null demand for continuous operation. The adaptive sliding-mode controller achieves this through the use of the direction of current flow. The capability of the control to track the reference voltage ensures that the system output

requirements are fulfilled. The adaptive sliding mode control for DC-DC converter used in the proposed design [7] is shown in Fig. 4.
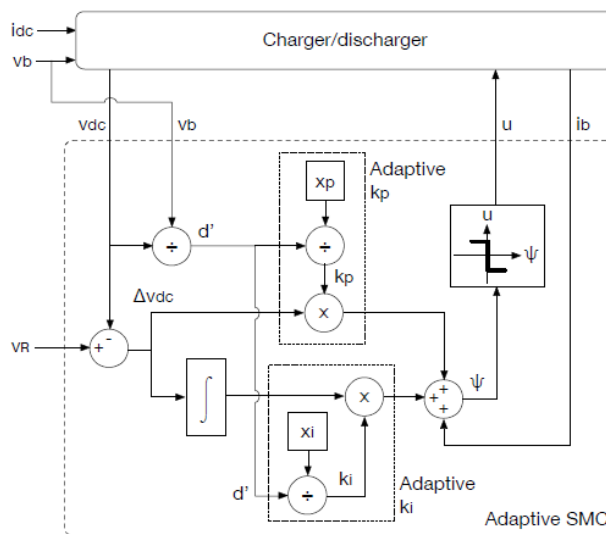
Fig. 4. The adaptive sliding mode control for dc-dc converter.

The fundamental theory governing sliding mode control defines a sliding surface, a defined value so the controlled quantity value slides around that target value. The controller in Fig. 4 triggers an opposite output once a determined threshold is away from the control variable surface of reference value. Two complementary signals, one to each switch, result which influences the DC-DC converter operation to bring the output value towards its reference. The switching function is a combination of the system state vectors and dictates a change in a control vector. The optimal condition for control vector occurs when the control function resides at the reference value. When less than or greater than the reference quantity for the control function is characterized, the switching function will reach a deviation threshold and the control will operate to reverse the systems motion.

The proposed hybrid energy system interleaving the supercapacitor is illustrated in Fig. 5. The interleaved supercapacitor in Fig. 5 operates at a voltage greater than both the ESD and output and hence provides greater available energy suitable for the transient load responses. Two DC-DC conversion stages are used to achieve this task: one to boost the voltage flowing into the capacitor from the ESD and another to buck the voltage required by the output. Maintaining the supercapacitor as the target for the boosted voltage provided by both stages allows for the fundamental control to be mirrored in regards to the boosted voltage target. With mirrored bidirectional DC-DC converters, the directions for power flow characterized by the battery current oppose each other. The second stage control only requires a scaled input and the application of a DC-DC converter duty cycle characteristic to ensure the proper power flow direction and the buck output voltage from the supercapacitor.
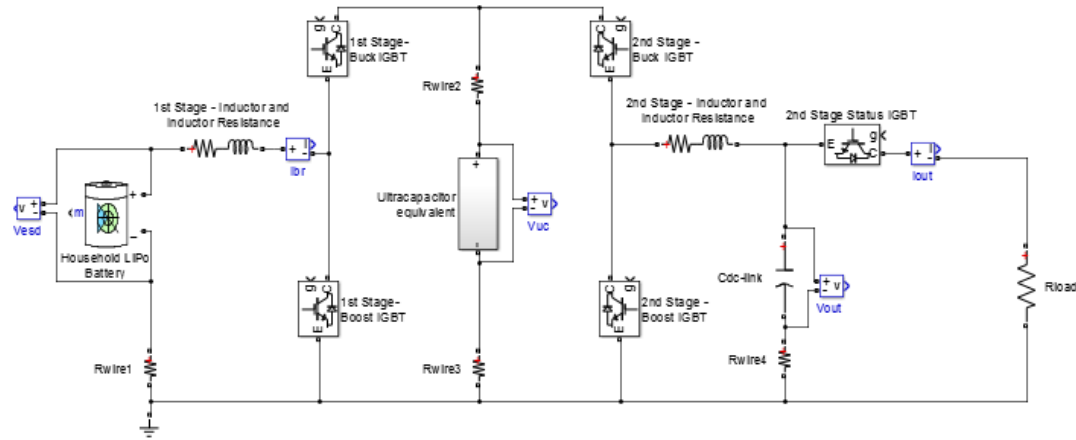
Fig. 5. The proposed new hybrid energy system.

An important property of the DC-DC converter duty cycle simplifies implementation of the adaptive sliding-mode control: the buck and boost duty cycles are complements of each other. Operation further qualifies this property: the voltage at one terminal must be greater than the other, expressing both a bucked and boosted conversion in one of the directions. The utilization of the property expressed prior with the adaptive sliding-mode control dictates that the boosted voltage for this system must be directed at the interleaved supercapacitor. The adaptive sliding mode control functions, their equations, related constraints that are used in the design are shown in Table 1 following the design process outlined in [7]. In Table 1,

Ψ: switching function
i_b: battery current
i_{DC}: measured load current
Vr: output target voltage
V_{DC}: measured output voltage
u: control variable/Boolean switch signal
kp: proportional coefficient
ki: integral coefficient.

The proportional and integral coefficients kp and ki are calculated using the equations given in Table 2 [7]. The controller stability is also addressed by analyzing closed-loop behavior presented in Table 2. Due to the discrete nature of DC-DC converter, the behavior needs to be averaged in regards to the normalized duty cycle complement, d'. The quadratic denominator clearly must not have any negative poles, verifying the range of the coefficients presented in the sections on the conditions. Furthermore, the relation between k_p and k_i can be defined. The critical values required to define the controller are the following: V_{bat}, V_{out}, element parameters, Δi_{DC}, safe response time, safe operating range. To constrain the operating frequency, a threshold value, H, must be calculated for the comparison to Ψ, resulting in the discrete control signal, u,

operation which is generated using a Flip-Flop S-R and two classical comparators.

Table 1: Adaptive sliding mode control functions

	Function
Switching Function	$\Psi = i_b + k_p*(V_R-V_{DC}) + k_i*\int(V_R-V_{DC})\,dt$ ^ $\Phi = \{\ \Psi = 0\}$ (1)
Switching Function Derivative	$d\Psi = di_b/dt - k_p*V_{DC} + k_i*(V_R-V_{DC})$ (2) $d\Psi = [(V_b - V_{DC}*(1-u))/L] - k_p*[(i_b*(1-u)$ $- i_{DC})/C] + k_i*(V_R-V_{DC})$ (3)
Power Balance	$I_b * V_B = i_{DC} * V_{DC}$ (4) $V_B = (1-d)*V_{DC}$ (5) $I_b * (1-d) = i_{DC}$ (6)
Transversality	Requirement: $V_{DC}/L > 0$
Condition: presence of control variable in switching function derivative	$d/du(d\Psi/dt) \neq 0$ (7) therefore $V_{DC}/L + k_p*i_b/c \neq 0$ (8) $-k_p < V_{DC}/i_b *C/L$ (9)
Reachability	
Control Variable Motion	$d/du(d\Psi/dt) > 0$ for u = 1 (10)
	Below Surface: Lim $(d\Psi/dt)\|_{u=1} > 0$ (11) $\Psi \to 0^-$ $V_b/L + k_p*i_{DC}/C + k_i*(V_r - V_{DC}) > 0$ (12)
	Power Balance Substitutions: $(V_b/V_{DC})*[V_{DC}/L + kp*i_b/C] + k_i*(V_r - V_{DC}) > 0$ (13)
	Above Surface: Lim $(d\Psi/dt)\|_{u=0} < 0$ (14) $\Psi \to 0^+$ $(V_b - V_{DC})/L - k_p*(I_b - i_{DC})/C < 0$ (15)
	Power Balance Substitutions: $-((V_{DC} - V_b)/V_{DC})*[V_{DC}/L + kp*i_b/C] + k_i*(V_r - V_{DC}) < 0$ (16)
Equivalent Control	$(d\Psi/dt)\|_{u=ueq.} = 0$ (17)
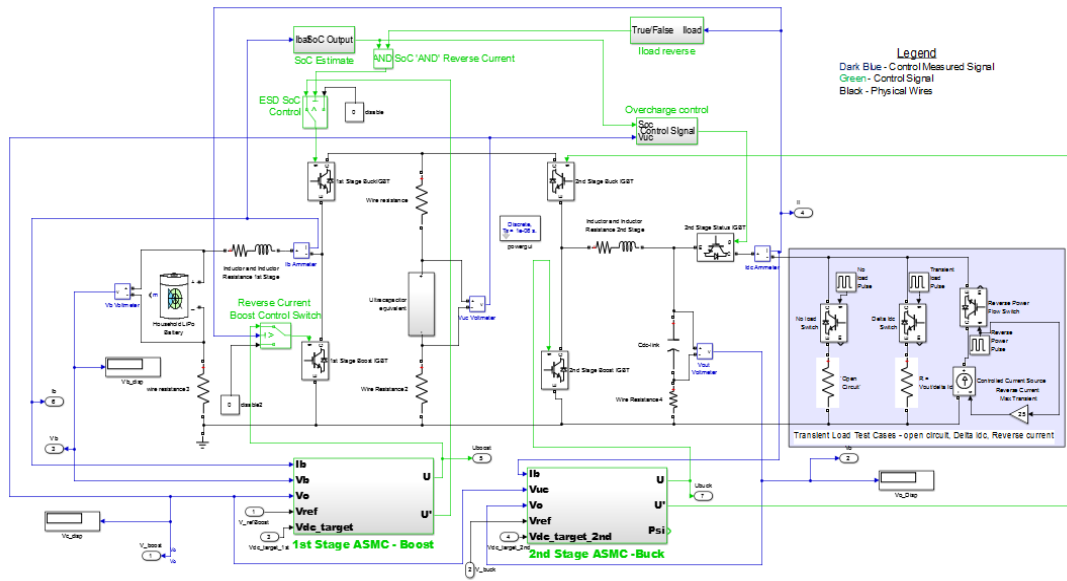
Fig. 6. The complete simulation of the proposed hybrid storage system with interleaved supercapacitor.

Table 2: Closed loop control parameters

	Equation
Closed-Loop Behavior (s-domain)	$V_{DC}(s) = [-s/(-s^2-k_p*d'*s-k_i*d'*i_{dc}(s))] + [(-k_p*s-k_i)*d']/(-s^2-k_p*d'*s-k_i*d'*V_r(s))]$ $\Rightarrow V_{DC}(s)/i_{dc}(s) = -s/(C*s^2-k_p*d'*s-k_i*d')$ (18)
Maximum Deviation	$t_{MO} = (-2*C)/(k_p*d')$ (19) $MO = [(2*\Delta i_{DC})/(k_p*d')]*exp(-1)$ (20)
k_p	$k_p = [(2*\Delta i_{DC})/(MO*d')]*exp(-1)$ (21) adaptive: $k_p = x_p/d'$ (22)
	$x_p = [(2*\Delta i_{DC})/MO]*exp(-1)$ (23)
k_i	$k_i = (-k_p^2*d')/(4*C)$ (24) adaptive: $k_i = x_i/d'$ (25)
	$x_i = -x_p^2/(4*c)$ (26)
$t_{Delta} < t_{safe}$	$\delta_{safe} = [(-\Delta i_{DC}/C)*t_{Delta}]*exp([(k_p*d')/(2*C)]*t_{Delta})$ (27)
Hysteresis/Sw Control	$H = (1/f_{sw})*(1-(V_b/L - i_{DC}/C)$ (28)
Thresholds	Lower - -H/2; Upper – H/2 (29)

In Table 2, the parameters are defined as:

i_{DC}: measured load current
Δi_{DC}: transient load current change
V_r: output target voltage
V_{DC}: measured output voltage
d': duty cycle complement
MO: maximum overshoot
t_{MO}: maximum overshoot time
t_{delta}: time until voltage falls within MO
u: control variable/Boolean switch signal
x_p: k_p parameter unscaled by d'
x_i: k_i parameter unscaled by d'
f_{sw}: maximum switching frequency
H: hysteresis threshold

III. SIMULATION RESULTS

The simulation of the proposed hybrid energy system with interleaving supercapacitor shown in Fig. 5 has been performed by Matlab Simulink using Power Systems toolkit. The verification for the operation of proposed design has been done for a household energy backup system. The AC-DC conversion is achieved using a commercially available inverter. Since the ESD and output voltage can be selected to be identical, the mirrored controller approach is implemented to a greater degree. 50 Vnom ESD was selected to have the same voltage requirements. Therefore, the adaptive sliding-mode controller parameters for both DC-DC converter stages are kept identical. The simulation design parameters are given in Table 3.

The complete system that is simulated using household energy backup system is shown in Fig. 6. The power quality requirements that are used as standards to measure the performance of the designed system are illustrated in Table 4 [12], whereas test load parameters used in the simulation are given in Table 5.

Table 3: Simulation Design Parameters

Simulated Hybrid Energy Storage Parameters	
Vb (v) and Vdc (v)	50
Vsc (v)	100
ΔIdc (A)	25
F (Hz)	95000
MO (v)	4.8
Csc (F)	5.8
Vcmax (v)	160
L (H)	.001
Cdc-link (F)	.0014
Adaptive Sliding Mode Parameters	
Xp	-3.83208
Xi	-0.63297
H	0.263135

Table 4: Power quality requirements

Nominal Voltage	± 10%		Cycles
Voltage Sag	Below 90%		.5 – 30 cycles
Voltage Swell	Above 110%		.5 – 30 cycles

Table 5: Test load parameters for simulation of household energy backup system

	Load	Period (s)	% Active	Time (H)	Delay (s)
Open Cir	1.0E+06	.1	40	.4	.8
Δidc	2Ω (50v/25A)	2	30	.6	0.2
Reverse current	25A	2	30	.6	1.2

The voltage at one terminal must be greater than the other, expressing both a bucked and boosted conversion in one of the directions. The utilization of the property expressed prior with the adaptive sliding-mode control dictates that the boosted voltage for this system must be directed at the interleaved supercapacitor.

In the simulation, adaptive sliding mode controller is implemented as boost controller and buck controller at two stages. The controllers at the first and second stages are modeled and simulated as shown in Fig. 7 and Fig. 8, respectively. The adaptive nature of the control utilizes the difference between actual and reference voltages to maintain the sliding-mode.
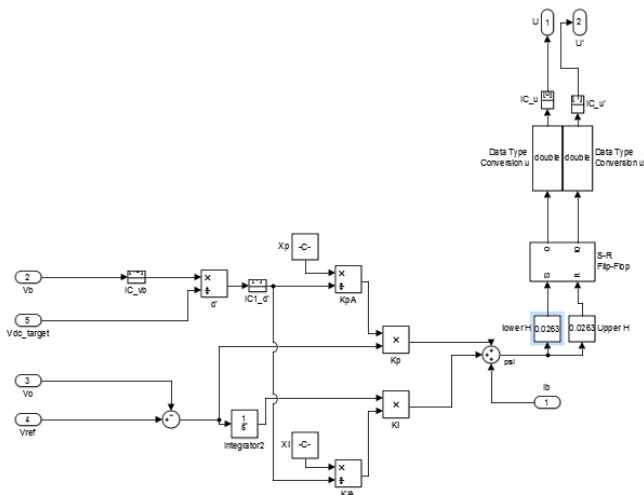
Fig. 7. 1st Stage Boost Controller Model.
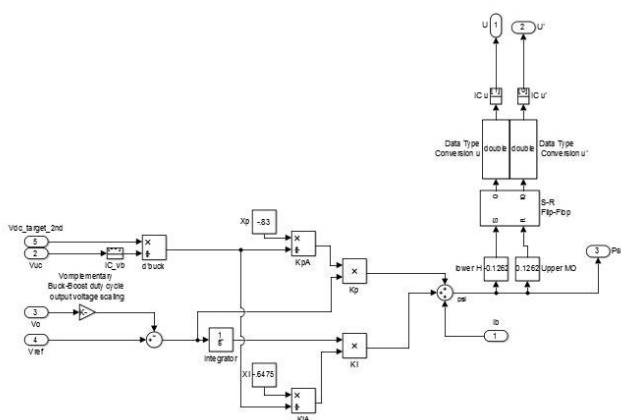
Fig. 8. 2nd Stage Buck Controller Model.

The simulation results are given in Fig. 9 and Fig. 10 for the test load parameters given in Table 5. From the system parameters provided, the output voltage, Vout in Fig. 9 (a), and output current in Fig. 10 (a) achieve the power quality definition given in Table 4. At the point of transient loading, the voltage only deviates from the nominal voltage by less than ±10% and for a period less than 0.5 cycles. The power quality requirements for household energy backup system are successfully fulfilled. Successful system operation has been achieved by providing the correct output voltage within the power quality requirements and displaying reverse power flow capabilities.
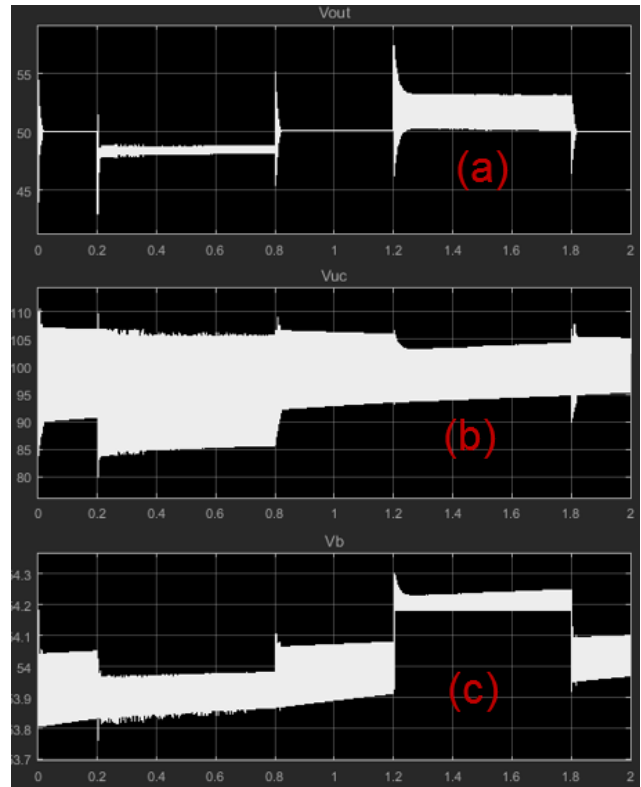
Fig. 9. Simulation results: (a) Vout, (b) Vuc, and (c) Vb.
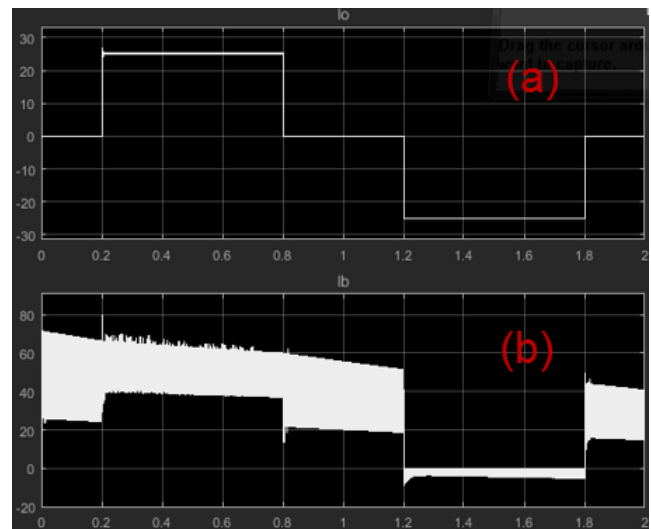
Fig. 10. Simulation results: (a) Io and (b) Ib.

It should be noted that the simulation results were attained with the initial voltage present across the supercapacitor. A large current far exceeding the ESD maximum output current and the inductor current limit threshold results without soft-start mechanism.

In summary, it has been shown that the simulation results verified the operation of the proposed interleaved hybrid energy storage system configuration using adaptive sliding-mode DC-DC converter control per the power quality requirements of the household energy backup scenario.

IV. CONCLUSION

In this paper, novel hybrid energy system to author's knowledge has been presented by interleaving the supercapacitor between the electrostatically sensitive devices (ESDs) and DC-link capacitors. An adaptive sliding-mode DC-DC converter control method has been adapted to have the desired bi-directional power flow and ensure the required output voltage. The simulation has been performed with Matlab/Simulink to verify the operation of the proposed design by considering the household energy backup system as the test case. Several parameters including output voltage, current and battery voltage for various load conditions has been tested. It has been shown that the proposed design with the new interleaved supercapacitor configuration met the power quality requirements as expected by minimizing the power fluctuations. The proposed design can be used in several applications including electrical vehicles (EVs) and grid integration of Photovoltaic (PV) systems.

REFERENCES

[1] W. Hhuijian and Z. Jiancheng, "Research on charging/discharging control strategy of battery-super capacitor hybrid energy storage system in photovoltaic system," in IEEE 8th International Power Electronics and Motion Control Conference (IPEMC-ECCE Asia), pp. 2694-2698, 2016.

[2] F. S. Garcia, A. A. Ferreira, and J. A. Pomilio, "Control strategy for battery-ultracapacitor hybrid energy storage system," in Twenty-Fourth Annual IEEE Applied Power Electronics Conference and Exposition, pp. 826-832, 2009.

[3] D. Pavković, M. Lobrović, M. Hrgetić, and A. Komljenović, "A design of DC bus control system for EVs based on battery/ultracapacitor hybrid energy storage," in IEEE International Electric Vehicle Conference (IEVC), pp. 1-8, 2014.

[4] D. Jianmin, X. Min, "Simulation research on hybrid energy storage system of hybrid electric vehicle," in IEEE International Conference on Automation and Logistics, pp. 197-201, 2010.

[5] J. J. Awerbuch and C. R. Sullivan, "Control of ultracapacitor-battery hybrid power source for vehicular applications," in IEEE Energy 2030 Conference, pp. 1-7, 2008.

[6] P. J. Grbovic, Ultra Capacitors in Power Systems. United Kingdom: Wiley, Chap. 1 and 2, 2013.m

[7] S. I. Serna-Garces, D. G. Montoya, and C. A. Ramos-Paja, "Sliding-mode control of a charger/discharger DC/DC converter for DC-bus regulation in renewable power systems," in MDPI Energies, 9, 245, 2016.

[8] M. Khan, I. Husain, Y. Sozer " A bidirectional DC-DC converter with input and output voltage ranges and vehicle to grid energy transfer capability," IEEE Journal of Emerging and Selected Topics in Power Electronics, vol. 2, no. 3, pp.507-516, Sept. 2014.

[9] N. S. Jayalakshmi, D. N. Gaonkar, J. V. Kumar, and R. P. Karthik, "Battery-ultracapacitor storage devices to mitigate power fluctuations for grid connected PV system," 2015 Annual IEEE India Conference (INDICON), pp. 1-6, 2015.

[10] F. M. Gonzlez-Longatt, "Model of photovoltaic module in Matlab," CIBELEC, pp. 1-5, 2005.

[11] V. S. Menon and A. Sukesh, "Solar energy conversion using isolated soft switching buck boost converter for domestic applications," International Conferences on Advances in Electrical Energy, Vellore, pp. l-6, 2014.

[12] R. C. Dugan, M. F. McGranaghan, S. Santoso, and H. Wayne, Electrical Power Systems Quality. McGraw Hill, ISBN: 0-07-138622-X, 528 pages, 2003.

Design and Study of a Small Implantable Antenna Design for Blood Glucose Monitoring

Ayesha Ahmed [1], Tahera Kalsoom [2], Masood Ur-Rehman [3], Naeem Ramzan [2], Sajjad Karim [4], and Qammer H. Abbasi [5]

[1] School of Computer Science and Technology
University of Bedfordshire, Luton, UK
ayeshanazahmed@hotmail.com

[2] School of Engineering and Computing
University of West of Scotland, Paisley, UK
tahera.kalssom@uws.ac.uk, naeem.ramzan@uws.ac.uk

[3] School of Computer Science and Electronic Engineering
University of Essex, Colchester, UK
masood.urrehman@essex.ac.uk

[4] Department of Electrical Engineering
Foundation University Islamabad, Pakistan
sajjad.karim@fui.edu.pk

[5] School of Engineering
University of Glasgow, Glasgow, UK
Qammer.abbasi@glasgow.ac.uk

Abstract ─ In this paper, a miniaturized implantable antenna with the dimensions of $8\times8\times1$ mm^3 has been studied for continuous monitoring of Blood Glucose Levels (BGL). The antenna performance is analyzed numerically for both the free space and implanted operation. The results show that the works excellently in both the scenarios. The antenna has the lowest resonant frequency of 3.58 GHz in free space with a gain 1.18 GHz while it operates at 2.58 GHz with a gain of 4.18 dBi. Good performance, small size and resilience to the human body effects make the antenna to have a good potential use in future implantable glucose monitoring devices.

Index Terms ─ Implantable, glucose monitoring, small antennas, tele-health systems.

I. INTRODUCTION

Diabetes, the most worried threat to the modern people, has brought about substantial economic loss not only to people with them but also to the public health system and national economy system [1]. According to [2], effective diabetes management could reduce the risk of the complications associated with the disease; therefore, real time monitoring techniques are indispensable. Among these techniques, implanted glucose sensors attract a lot of interest [3], [4] and various implanted antenna are designed [5]–[8], where the miniaturization of the antenna with high performances is still a great challenge. To realize such antennas, several methods like high-permittivity substrates, fractal structures, shorting pins loading and *etc.* have been studied [9]. The high permittivity method and split-ring resonator (SRR) are more commonly used techniques. In [6], the miniaturization was completed realizing an antenna size of $8.5\times8.5\times1.27$ *mm*^{3} by loading C-shaped slots and Complimentary Split-Ring Resonator (CSRR) on the radiation patch. However, there is a need to further decrease the size of the antenna to meet the requirements of continually miniaturizing implantable devices.

In this paper, following the work in [6], efforts are made to further reduce the antenna size. A smaller implantable antenna size is realized for glucose monitoring located in subcutaneous layer of the human tissues with the techniques of the Complimentary Split-Ring Resonator (CSRR) and high permittivity substrates. The antenna performance is studied for the free space and implanted in-body operation through numerical modeling and analysis.

The paper is organized as follows: Section II

presents the configuration of the proposed implantable antenna and the numerical model of the human body phantom with antenna injected in the subcutaneous layers. Section III gives the analysis of the antenna performance in terms of numerical results. Conclusions are drawn in Section IV.

II. ANTENNA DESIGN AND DISCUSSION

A. Antenna design

The structure of the proposed antenna is shown in Fig. 1, while the corresponding geometrical parameters are given in Table 1. The antenna is modeled and simulated using Computer Simulation Technology (CST) Microwave Studio package. The substrate and superstate used are the lossy Rogers TMM 13i (ε_r = 12.85, $tan\delta$=0.0019) with a height of 0.5 mm. The patch and ground are all considered as Perfect Electric Conductors (PEC) for simplification having the length and width of same size as the substrate and thickness of 35 μm.

(a) Front view
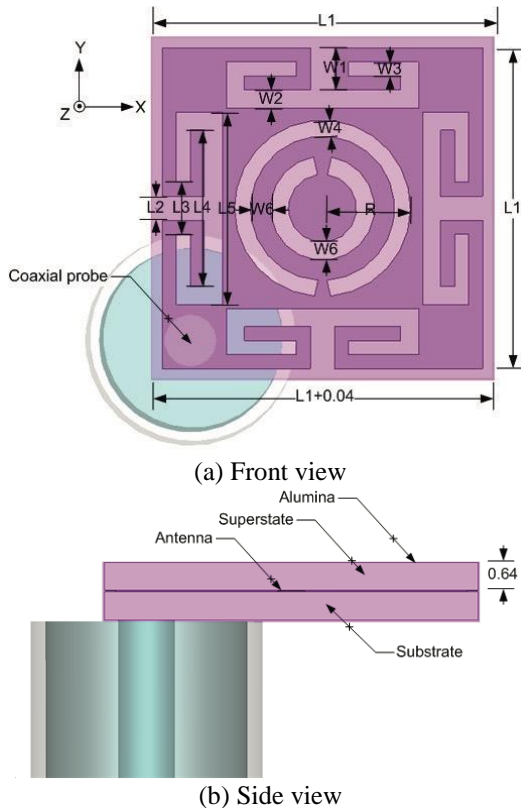
(b) Side view

Fig. 1. Top and side view of the geometrical structure of the proposed implantable antenna.

The antenna is fed through a 50 ohm coaxial probe. The SMA connector is also modeled as shown in Fig. 1 (b). The inner and outer conductors of the SMA connector are modeled as PEC while the coaxial conductor has a

ε_r = 2.1 and μ = 1. To alleviate the effects of the human tissues, the antenna is covered in a film made of Alumina with ε_r = 9.2, $tan\delta$ = 0.008 and a thickness of 0.02 mm, as shown in the Fig. 1.

Table 1: Structural parameters of the proposed antenna

Antenna Parameter	Value (mm)
W_1	1.05
W_2	0.45
W_3	0.35
W_4	0.4
W_5	0.5
W_6	0.45
L_1	8.0
L_2	0.6
L_3	1.3
L_4	3.9
L_5	4.8
R	2.2

B. Numerical phantom model

To test the antenna in implantable conditions, a three-layer numerical phantom of the human body is modeled and used in the CST Microwave Studio. The phantom has an overall size of 80×80×38 mm^3 as depicted in Fig. 2. The phantom consists of three layers, i.e., skin, fat, and muscle. The electrical parameters (the relative permittivity and the conductivity) in the Industrial, Scientific and Medical (ISM) band (which is our targeted operation region) are given in Table 2. The proposed antenna is implanted in the human body skin at a depth of 2 mm from the body surface.
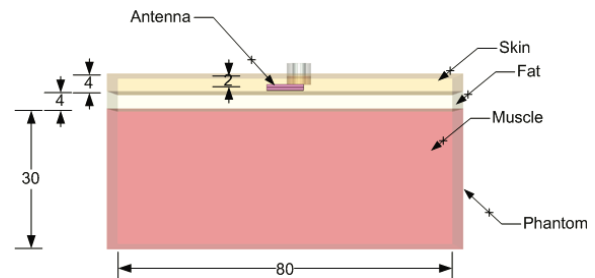
Fig. 2. Schematics of three-layer phantom with antenna implanted at a depth of 2 mm in the skin layer.

Table 2: Electrical properties of the three-layer human body phantom used to test the antenna performance in implantable conditions [10], [11]

Tissue Layer	ε_r	σ (S/m)
Skin	38	1.44
Fat	5.28	0.1
Muscle	52.7	1.74

0   100   180   350   580   1100

A/m

(a) 3.75 GHz   (b) 11 GHz   (c) 14 GHz   (d) 2.58 GHz (implanted)
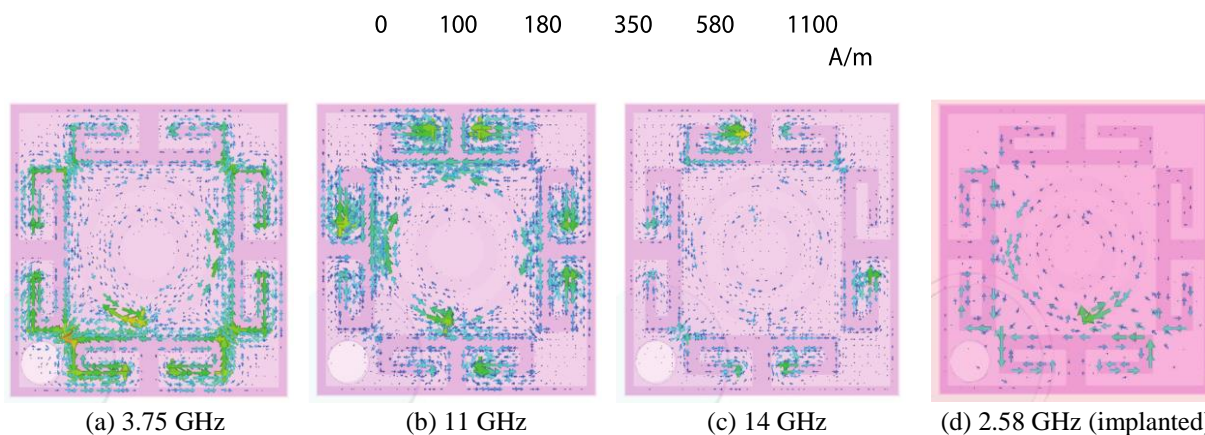
Fig. 3. Surface current distribution for proposed antenna's operation in free space at 3.75 GHz, 11 GHz and 14 GHz and in implantable condition at 2.58 GHz.

III. NUMERICAL RESULTS AND ANALYSIS

The antenna performance is analyzed in terms of surface current distribution, reflection coefficient, radiation pattern and gain in free space and implanted configurations. Figure 3 shows the current distribution on the antenna surface for the two operational conditions at free space frequencies of 3.75 GHz, 11 GHz and 14 GHz and implanted frequency of 2.58 GHz. It shows that the current path has increased with the introduction of the slots and CSRR in the patch thus lowering the resonant frequency.

The reflection coefficient (S_{11}) response of the proposed antenna in free space and in the phantom are shown in Fig. 4. It can be seen that the resonance frequency changes from 3.75 GHz in free space to 2.58 GHz with excellent impedance matching for the antenna in implanted condition. For the free space case, the antenna has various parasitic resonances in the higher frequency band but it has limited effect on the antenna performance when the antenna is implanted in human body.

The radiation patterns are observed at 3.75 GHz, 11 GHz and 14 GHz for the free space operation while at 2.58 GHz for the implanted scenario as illustrated in Fig. 5. These results indicate that the antenna has good radiation coverage in both *Phi (ϕ) = 0°* and *Phi(ϕ) = 90°* planes with nearly omni-directional far-field at all the observed frequencies. More tellingly, the antenna successfully maintains the pattern shape and coverage in both the planes when implanted into the skin tissues as evident from Fig. 5 (d). The near-omnidirectionallty helps the antenna to send and receive the signal/ information in all directions, hence mitigating possible body posture and shape implications.

(a) *f* = 3.75 GHz

(b) *f* = 11 GHz

Fig. 4. Reflection coefficient response of the antenna with phantom and without phantom.

(c) f = 14 GHz

(d) f = 2.8 GHz (implanted)
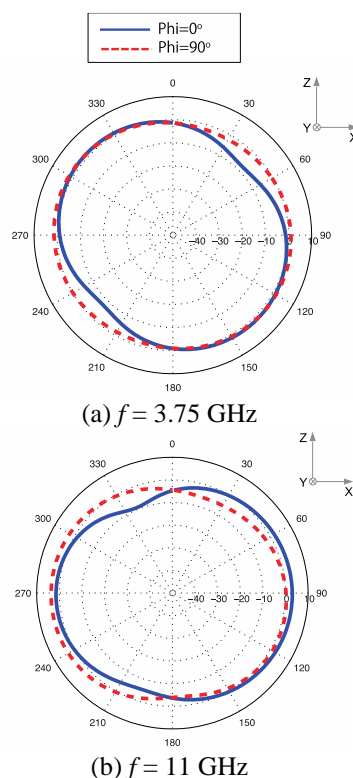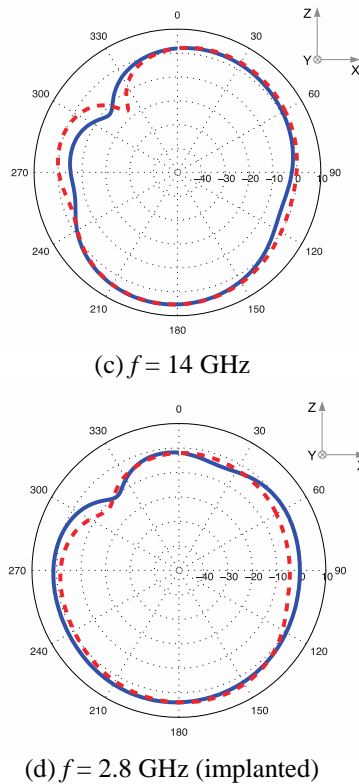
Fig. 5. Radiation patterns of the proposed antenna at different frequencies for free space and implanted operation.

Figure 6 illustrates the simulated peak gain of the proposed antenna in free space and implanted scenarios. It is evident that the proposed antenna offers a good gain performance in all working conditions. The antenna achieves the highest gain of 5.48 dBi at 14 GHz in free space while a very good gain of 4.18 dBi in the implanted configuration.
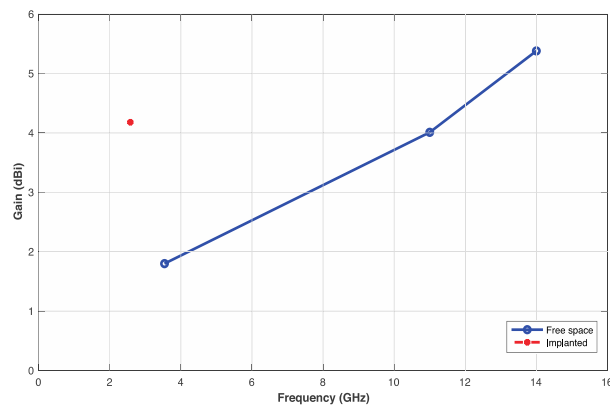
Fig. 6. Peak gain of the proposed antenna in free space and implanted conditions.

VI. CONCLUSION

A miniaturized implantable antenna with the dimension 8×8×1 mm^3 has been studied for the free space and implanted in the skin working conditions in this paper for continuous blood sugar monitoring. The antenna performance is analyzed numerically using a three-layer human body phantom consisting of skin, fat and muscle tissues. The results have shown that a peak gain of 4.18 dBi could be obtained despite the small size of the antenna at the frequency of 2.58 GHz when implanted in body. The antenna also offers good near-omnidirectionality in the radiation pattern. Low profile, small size, good gain and resilience to the human body effects make this antenna a good candidate for tele-health monitoring systems.

REFERENCES

[1] World Health Organization, *Global report on diabetes*, World Health Organization, 2016.

[2] Horizon Scanning Research and Intelligence Centre, *New and emerging non-invasive glucose monitoring*, Horizon Scanning Research and Intelligence Centre, 2016.

[3] P. S. Hall and Y. Hao, *Antennas and Propagation for Body-Centric Wireless Communications*. Artech House, 2012.

[4] Q. H. Abbasi, M. Ur-Rehman, K. Qaraqe, and A. Alomainy, "Advances in body-centric wireless communication: Applications and state-of-the-art," *The IET, (UK)*, 2016.

[5] Y Cho and H Yoo, "Miniaturised dual-band implantable antenna for wireless biotelemetry," *Electronics Letters*, 52(12):1005-1007, 2016.

[6] X. Y. Liu, Z. T. Wu, Y. Fan, and E. M. Tentzeris, "A miniaturized CSRR loaded wide-beamwidth circularly polarized implantable antenna for subcutaneous real-time glucose monitoring," *IEEE Antennas and Wireless Propagation Letters*, 16:577-580, 2017.

[7] T. Yilmaz, R. Foster, and Y. Hao, "Broadband tissue mimicking phantoms and a patch resonator for evaluating noninvasive monitoring of blood glucose levels," *IEEE Transactions on Antennas and Propagation*, 62(6):3064-3075, 2014.

[8] M. Ur-Rehman, N. A. Malik, X. Yang, Q. H. Abbasi, Z. Zhang, and N. Zhao, "A low profile antenna for millimeter-wave body-centric applications," *IEEE Transactions on Antennas and Propagation*, 65(12):6329-6337, Dec. 2017.

[9] H. Li, Y.-X. Guo, C. Liu, S. Xiao, and L. Li, "A miniature-implantable antenna for medradio-band biomedical telemetry," *IEEE Antennas and Wireless Propagation Letters*, 14:1176-1179, 2015.

[10] S. Gabriel, R. W. Lau, and C. Gabriel, "The dielectric properties of biological tissues: II.

Measurements in the frequency range 10 Hz to 20 GHz," *Physics in Medicine and Biology*, 41(11):2251-2269, 1996.

[11] Dielectric properties. ITIS website. http://www.itis. ethz.ch/virtual-population/tissue-properties/database/ dielectric-properties)

Ayesha Ahmed received the degree in M.Sc. Electronic Engineering from University of Bedfordshire, Luton, UK in 2017. She is currently working in the industry as a Design Engineer. Her research interests include antenna design for implantable devices and IoT applications.

Tahera Kalsoom received the BBA degree in Hospitality Management from Stenden University, Doha, Qatar in 2010. She received the degree in M.Sc. Financial Management from Middlesex University, London, UK in 2015. She is currently pursuing her Ph.D. in Engineering and Computing at University of West of Scotland, Scotland, UK. Her research interests include use of IoT at personal and industrial level, economic challenges in adoption of the IoT, and societal and behavioural impact of the IoT.

Masood Ur Rehman received the B.Sc. degree in Electronics and Telecommunication Engineering from University of Engineering and Technology, Lahore, Pakistan in 2004 and the M.Sc. and Ph.D. degrees in Electronic Engineering from Queen Mary University of London, London, UK, in 2006 and 2010, respectively. He is working as an Assistant Professor at the University of Essex, Colchester, UK. His research interests include compact antenna design, radiowave propagation and channel characterization, satellite navigation system antennas in cluttered environment, electromagnetic wave interaction with human body, body-centric wireless networks and sensors, remote health care technology, mmWave and nano communications for body-centric networks and D2D/H2H communications.

He has worked on a number of projects supported by industrial partners and research councils. He has contributed to a patent and authored/co-authored 4 books, 7 book chapters and more than 85 technical articles in leading journals and peer reviewed conferences. Ur Rehman is a Fellow of the Higher Education Academy (UK), a Senior Member of IEEE, a Member of the IET and part of technical program committees and organizing committees of several international conferences, workshops and special sessions. He is acting as an Associate Editor of the IEEE Access and IET Electronics Letters and Lead Guest Editor of numerous special issues of renowned journals. He also serves as a Reviewer for book publishers, IEEE conferences and leading journals.

Naeem Ramzan received the M.Sc. degree in Telecommunication from University of Brest, France, in 2004 and the Ph.D. degree in Electronics Engineering from Queen Mary University of London, London, U.K, in 2008. Currently, he is a full Professor at the School of Engineering and Computing, University of the West of Scotland.

He has authored or co-authored over 150 research publications, including journals, book chapters, and standardisation contributions. He is the recipient of the Best paper award 2017 IEEE Transaction of circuit and systems for video technology. He is a Fellow of the Higher Education Academy and a Senior Member of IEEE. He served as a Guest Editor for a number of special issues in technical journals. He has organized and co-chaired three ACM Multimedia Workshops, and served as the Session Chair/Co-Chair for a number of conferences. He is the Co- Chair of the Ultra HD Group of the Video Quality Experts Group (VQEG) and the Co-Editor-in-Chief of VQEG E-Letter. He has led/ participated in more than 20 projects funded by European and U.K. research councils.

Sajjad Karim received his B.S Electrical Engineering degree in 2003 from MUST, AJK and M.S. Electrical Engineering degree in 2007 from BTH University, Sweden. Currently he is a Ph.D. scholar at Capital University of Science and Technology (CUST), Islamabad, Pakistan. He has been working as an Assistant Professor at Foundation University Islamabad, Pakistan since 2008. His research interests include wireless fading channels and power quality disturbances.

Qammer Hussain Abbasi received his B.Sc. and M.Sc. degrees in Electronics and Telecommunication Engineering from University of Engineering and Technology, Lahore, Pakistan (with distinction). He received his Ph.D. degree in Electronic and Electrical Engineering from Queen Mary University of London, UK, in January

2012. From February 2012 to June 2012, he was Post-Doctoral Research Assistant in Antenna and Electromagnetics group at Queen Mary University of London, UK. From 2012 to 2013, he was International Young Scientist under National Science Foundation China (NSFC), and Assistant Professor in University of Engineering and Technology, KSK, Lahore. From August, 2013 to April 2017 he was with the Centre for Remote Healthcare Technology and Wireless Research Group, Department of Electrical and Computer Engineering, Texas A & M University (TAMUQ) initially as an Assistant Research Scientist and later was promoted to an Associate Research Scientist and Visiting Lecturer, where he was leading multiple Qatar national research foundation grants (worth $3 million). Currently, Abbasi is a Lecturer (Assistant Professor) in University of Glasgow in the School of Engineering in addition to Visiting Research Fellow with Queen Mary, University of London and Visiting Associate Research Scientist with Texas A & M University. He has been mentoring several undergraduate, graduate students and postdocs.

Abbasi has contributed to a patent, more than 100 leading international technical journal and peer reviewed conference papers and 5 books and received several recognitions for his research. His research interests include compact antenna design, RF design and radio propagation, nano communication, Biomedical applications of Terahertz communication, Antenna interaction with human body, Implants, body centric wireless communication issues, wireless body sensor networks, non-invasive health care solutions, cognitive and cooperative network and multiple-input-multiple-output systems. He is an Associate Editor for IEEE Access journal and acted as a guest editor for numerous special issues in top notch journals. Abbasi has been a Member of the technical program committees of several IEEE flagship conferences and Technical Reviewer for several IEEE and top notch journals. He contributed in organizing several IEEE conferences, workshop and special sessions in addition to European school of antenna course.

A Cost-Effective Far-Field Antenna Pattern Measurement System

Kyle Patel
Department of Electrical Engineering
Colorado School of Mines
Golden, CO 80401 USA
kypatel@mines.edu

Robert Jones
Department of Electrical Engineering
Colorado School of Mines
Golden, CO 80401 USA
rojones@mines.edu

Atef Elsherbeni
Department of Electrical Engineering
Colorado School of Mines
Golden, CO 80401 USA
aelsherb@mines.edu

Abstract—A low-cost far-field antenna measurement solution is developed and presented. In an increasingly wireless society, it is important to be able to characterize antennas. Unfortunately, determining antenna radiation pattern characteristics is an involved and often expensive process. The presented system provides a complete combination of hardware and software that can be used for far-field pattern measurements of an antenna operating in the 700 MHz to 18 GHz range. This would allow institutions and groups with few resources to be able to characterize the radiation pattern of antennas for many emerging applications.

Keywords—Anechoic chamber, antenna pattern measurement, far-field measurement, low cost.

I. INTRODUCTION

Antennas are typically characterized by their impedance bandwidth and their radiation qualities. The impedance bandwidth is easily determined through a one-port measurement with a VNA, however, the radiation qualities of an antenna require specialized ranges to ascertain [1-2]. These ranges typically consist of a standard antenna that is used to determine the radiation parameters of an unknown antenna. The distance between the two antenna must meet the far-field criteria for accurate measurements [3].

There are many types of such far-field ranges, however, the one this paper focuses on is an implementation of a system that works within an anechoic chamber.

The proposed system consists of electrical hardware, mechanical fixtures, and in-house software as explained in the following sections. The far-field measurement is conducted by analyzing S21 data taken using a Keysight VNA connected to a source fixture and an antenna-under-test (AUT) fixture spaced approximately three meters apart. There is one rotary table for the source antenna, typically a horn, and two rotary tables for the AUT. These rotary tables allow the system to perform S21 measurements as a function of multiple angles and frequencies. An example dipole antenna pattern measurement with this system can be seen in Fig. 1. The pattern is asymmetrical because the measurement was conducted without calibration or absorbers lining the anechoic chamber at the time of this writing.
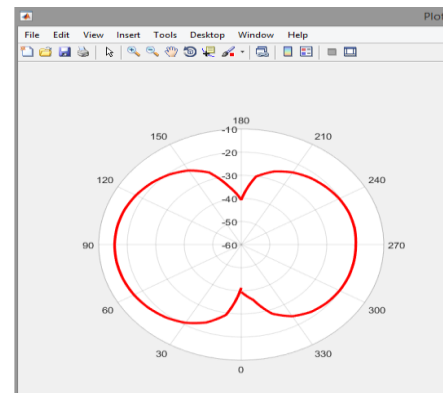
Fig. 1. The measured y-z plane pattern cut of a z-directed half-wavelength dipole antenna [4].

II. ELECTRONIC HARDWARE

Several pieces of equipment facilitate the measurement process. The system components are shown in Fig. 2. There are two LNAs, one at the output of port 1 and one at the input of port 2. The software automatically powers the LNAs through a programmable BK-Precision power supply. Three Velmex rotary tables are used, one on the source side, and two on the AUT side. These rotary tables allow for two axes of rotations at the AUT and one axis of rotation at the source antenna. There are also two Pololu linear actuators that allow for horizontal and vertical alignment of the source antenna with the AUT.
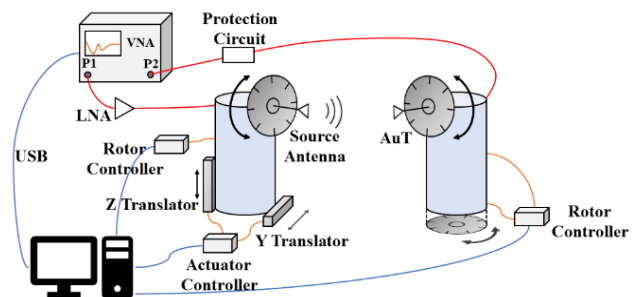
Fig. 2. Schematic for the designed antenna pattern measurement system [4].

In this design, there is a novel protection mechanism that is optional to the base functionality of the system but adds to the robustness of the overall system. This protection circuit was added to protect the VNA receiver from damage due to high power levels which may occur with novice users. This circuit essentially consists of a limiter and detector diode. The detector diode serves to notify the software and operator that a hazardous condition has been reached and halts the measurement until it is reviewed. This equipment can be seen on the control table in Fig. 3.

Fig. 3. Control table featuring all necessary electronic hardware.

III. MECHANICAL FIXTURES

The fixtures shown in Fig. 4 that hold the source and AUT were designed using MDF plywood, which was chosen for its low cost, relative strength, and machining ease. Furthermore, MDF plywood would not reflect electromagnetic waves as much as metal materials such as aluminum, which would disturb the measurement results. The AUT fixture allows for different antenna to be easily mounted. The fixtures are also designed to be easily taken apart so that maintenance and inspection can be done in a short amount of time.
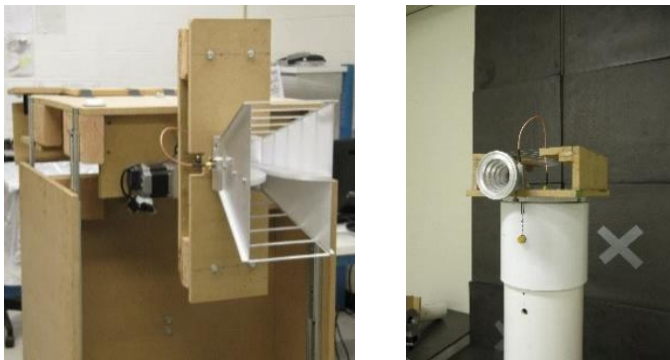
Fig. 4. Source fixture with source horn (left) and AUT fixture with mounted dipole antenna (right).

IV. SOFTWARE

The developed software consists of a main GUI written in MATLAB and custom C# drivers that communicate with SCPI-enabled programmable power supplies and Keysight ENA/ Fieldfox series VNAs [4]. This software allows for complete setup and control of the measurement. The software was designed to be modular so it could be easily upgraded and adapted to different equipment.

V. FUTURE ENHANCEMENT

Currently, the alignment of the source antenna with the AUT is done manually. An automated system for alignment utilizing lasers is in progress. Furthermore, the fixtures can be greatly improved by moving away from the MDF that was used and instead utilizing 3D printed plastics and belts to make them more compact, lightweight, and robust. Lastly, the linear actuators are to be replaced with geared stepper motors for better positional accuracy of the source fixture.

VI. PRECAUTIONS

Most groups who try to make their first antenna pattern measurement system will underestimate how important it is to have a defined and consistent antenna mounting scheme. There are many kinds of antennas which may potentially require measuring different planes, so it is important to always define measurement sweeps in a consistent manner for clarity of measurement results across operators and antennas. This is directly related to how each group decides to mount their rotary tables, as no single combination of rotary table placements is necessarily more correct over another especially when one is measuring many different types of antennas. Depending on where one chooses to locate their rotary tables, they may or may not get pure ϕ or θ plane cuts of their antenna, which is important to take into consideration when defining measurements and analyzing data.

VII. COST

The presented system provides antenna far-field measurement capability at low cost. The total costs is less than $10,000. A majority of this cost can be further reduced by utilizing less precise rotary tables for which the software and fixtures can easily be adapted to. This of course does not include the costs for a two port VNA and absorbers for the chamber, which are a significant cost of any antenna pattern measurement system. However, one may not need to buy an expensive VNA like the ones used in this system. Depending on the user's needs, one could opt for one of the growing consumer and affordable VNAs on the market, which would reduce entry costs significantly. These other VNAs can easily be adapted to the controller software due to its modularity.

VIII. CONCLUSION

Cost effective antenna measurement system is developed. Components, associated cost, and precautions in developing the system are presented.

REFERENCES

[1] R. C. Johnson, Antenna Engineering Handbook. New York: McGraw-Hill, Inc., 1993.

[2] J. S. Hollis, T. J. Lyon, and L. Clayton Jr., Microwave Antenna Measurements. Atlanta, GA: Scientific-Atlanta, Inc., 1970.

[3] C. A. Balanis, Antenna Theory Analysis and Design. New York: John Wiley & Sons, Inc., 1997.

[4] K. Patel, "Design of an Antenna Measurement System," M.S. Thesis, Elect. Eng. Dept., Colorado School of Mines, Golden, CO, 2017.

Reduction of Coupling between Flush-Mounted Antennas

Prathap Valale Prasannakumar, Mohamed A. Elmansouri, Maxim Ignatenko, and Dejan Filipovic

Department of Electrical, Computer, and Energy Engineering
University of Colorado, Boulder
Boulder, Colorado, USA, 80309
{Prathap.Valaleprasannakumar, Mohamed.Elmansouri, Maxim.Ignatenko, and Dejan.Filipovic}@colorado.edu

Abstract—**This paper discusses some numerical aspects of the coupling study between two flush-mounted antennas. It is shown that a bed of nails embedded between flush-mounted quad-ridge horns separated by 20 cm ($4\lambda_{6\ GHz}$) edge-to-edge greatly reduces coupling by about 17 dB at lower frequency end, where the electrical distance between antennas is the shortest. The considered antenna system operates from 6-19 GHz and has $|S_{11}| < -10$ dB, and coupling < -60 dB. The numerical modelling is carried out using MoM and FEM solvers. The computed results are in good agreement with measurements.**

Keywords—Bed of nails, coupling, method of moments.

I. INTRODUCTION

Coupling between antennas sharing common platform is a critical parameter in the design of in-band full duplex systems. Often, coupling < -60 dB (or isolation > 60 dB) is desired from the antenna layer itself to achieve total system isolation in the order of 110-140 dB [1]. Minimizing the coupling for an electrically-short separation between transmitter (TX) and receiver (RX) is a challenging task. Various techniques to improve the antenna layer isolation are considered in open literature including recessing the RX antenna in absorber, the use of band-gap structures, and the implementation of high impedance surfaces (HIS) [2,3]. High impedance surfaces (capacitive or inductive) can be implemented over an octave bandwidth by means of a bed of nails [4,5]. The practical realization and fabrication of these structures are relatively easy and cost effective. However, numerical modelling and solving of the bed of nails (312 nails/unit cells in this paper) requires intricate meshing and thereby, considerable computational resources. Moreover, computation of the expected low level of coupling can be challenging because of high required accuracy. Further, the reflections from absorbing/radiation boundaries could influence the calculation of low level of coupling, when finite element method (FEM) solvers are used. In this work, coupling between two quad-ridge horns operating in 6-19 GHz is considered using commercially available method of moment (MoM) solver – Altair FEKO. In spite of numerical challenges, good agreement between measurements and simulated results is achieved. It is demonstrated that 17 dB reduction in coupling can be obtained by embedding bed of nails between the antennas separated 20 cm edge-to-edge.

II. ANTENNAS COUPLING MECHANISM

Radiation is the main path of coupling between two co-located antennas in free space. Hence, the coupling is proportional to the gain in the direction between the antennas. When the antennas are flush mounted on a metallic ground plane, surface currents provide an additional path for coupling. Specifically, when two WR90 (X-band) open-ended waveguides (OWG) oriented in **E**-plane are flush mounted on a metallic ground plane, the coupling due to surface currents alone is approximately 10% of the total coupling at 8 GHz, as shown in the Fig. 1. This coupling is calculated in FEKO using currents on the ground plane as a source of the received power at the RX aperture. Suppressing these currents will reduce coupling. It should be noted that manipulating the surface currents will also affect the electromagnetic waves above the surface, and thus much stronger than 10% impact on coupling is expected.

The predominant E_z amplitude at the surface in the E-plane of the antennas (x-axis in Fig. 2) is in accordance with the study in [3] that TM waves are supported over a metal with finite conductivity. TM surface waves have capacitive wave impedance, and hence a capacitive surface will inhibit its propagation. Desired capacitive impedance is realized by using $\lambda/4$ (at 8 GHz) grounded metallic nails arranged in double-periodic structure [4]. To reduce computational requirements, pins are modeled as wire segments of radius 1 mm in FEKO. As seen in Fig. 2 (d), the bed of nails reduces E_z at the RX aperture by 18 dB. This clearly demonstrates that the bed of nails can be effectively used to reduce coupling between flush-mounted antennas, as further discussed in Section III. The CAD model of the bed of nails consisting of 0.93cm ($\lambda_{8\ GHz}/4$) long metallic pins is shown in Fig. 2 (b).
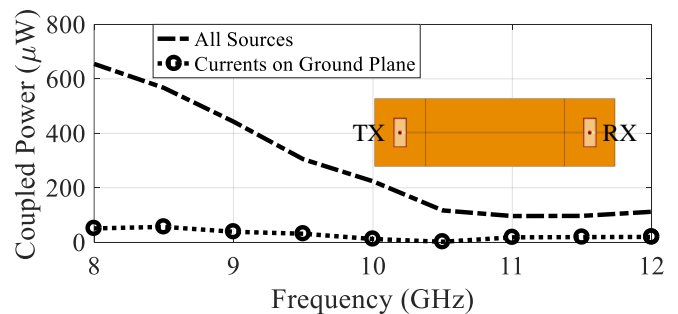
Fig. 1. Power coupled through the RX aperture when 1 W power is fed at the input of TX antenna. Antennas are mounted on a metallic ground plane with 14 cm separation from edge-to-edge.
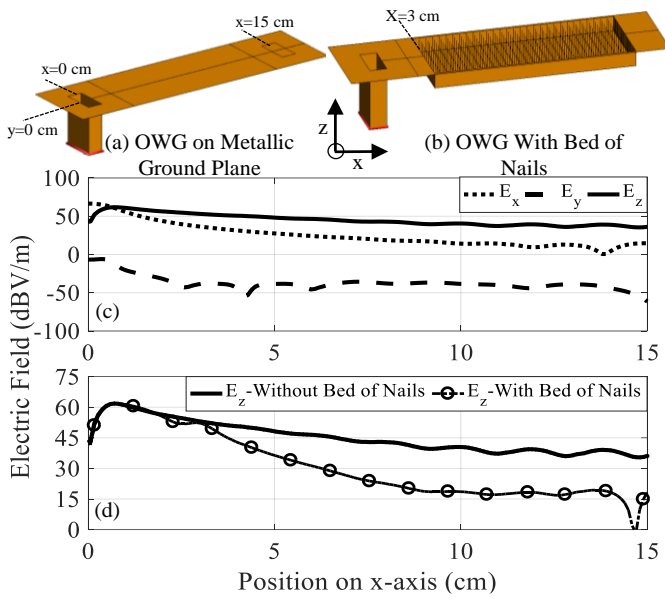
Fig. 2. CAD model of open ended waveguide flush mounted on: (a) metallic ground plane, and (b) with bed of nails. Magnitude of electric field components over the ground plane: (c) without, and (d) with bed of nails at 8 GHz.

III. FLUSH-MOUNTED QUAD-RIDGE HORNS

The considered quad-ridge horn (QRH) antenna supports dual-polarization operation, and can handle high power [5]. Impedance match of the antenna is a crucial parameter for high power applications. Therefore, to reduce the reflections from the aperture, the ridges of the horn are shaped as a Klopfenstein taper. Moreover, the edges of the horn aperture and the ridges are rolled into semielliptical shape to reduce the reflections resulting from the edge diffraction. The designed horn is 8cm long and has an aperture of 3 cm × 3 cm. FEM and MoM hybridization supported by FEKO is used in order to excite quad-ridge waveguide cross-section. Adaptive mesh shown by green bubbles in the inset of Fig. 3 was found to be critical for achieving good accuracy. The antenna has reflection coefficient ($|S_{11}|$) < -10 dB (< -20 dB for 94% of the bandwidth) when fed at the quad ridge section (see Fig. 3 (a)). The designed quad-ridge to double-ridge transition used in measurements has $|S_{11}|$ < -10 dB over 98% of bandwidth. Good agreement between simulation and measurement is observed.

The QRHs are flush mounted on a metallic ground plane of size 13 cm × 38 cm (Fig. 4 (a)), which corresponds to 8 λ_{19GHz} × 24 λ_{19GHz}. Also, QRH with the transition is about 10λ_{19GHz} in z-axis which results in a computationally-large problem. The system has coupling < -40 dB at 6 GHz over a metallic ground plane and < -60 dB when the proposed bed of nails is embedded between the antennas oriented 45° to each other, as seen from Figs. 4 (b) and (c). Good agreement between the measured and simulated results highlights the ability and accuracy of numerical solvers in handling complex and electrically-large problems. The model solved using MoM in FEKO, meshed at 19 GHz, has 51,616 triangles, 758 FEM surface triangles, 624 metallic segments, and 28,658 tetrahedral.
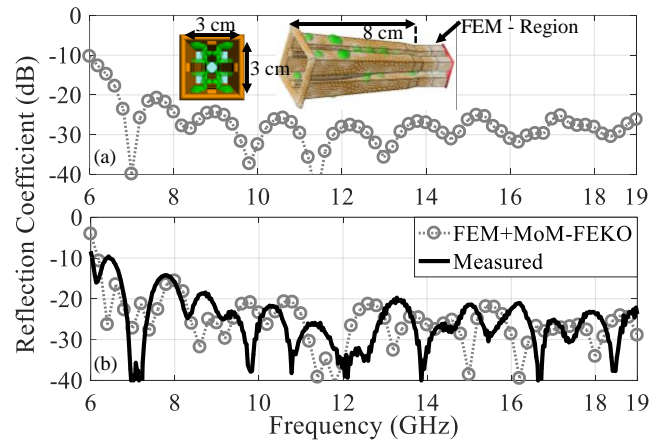
Fig. 3. Reflection coefficient of quad-ridge horn: (a) fed at the input of quad-ridge section (simulated results), and (b) fed using quad ridge to double ridge section (FEKO, and measured results).
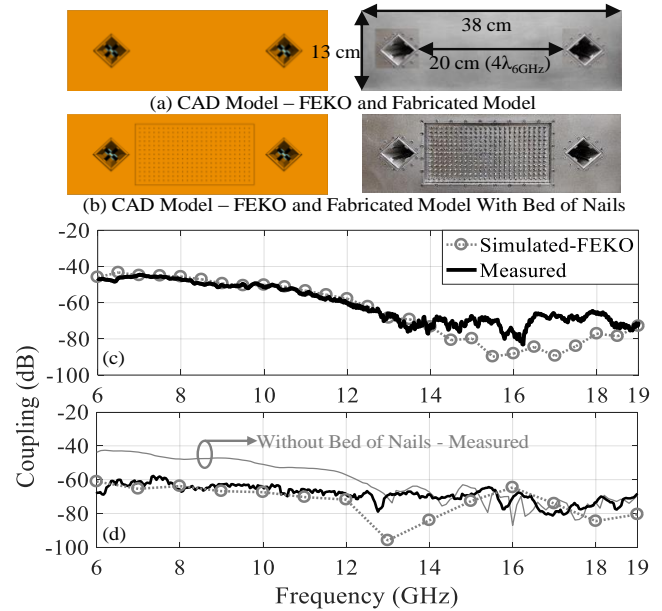
Fig. 4. CAD and fabricated models of QRH over metallic ground plane: (a) without and (b) with bed of nails. Simulated and measured coupling: (c) without and (d) with bed of nails.

REFERENCES

[1] D. Bharadia, E. McMilin, and S. Katti, "Full duplex radios," Proc. SIGCOMM'13 Conf., China, pp. 375-386, 2013.

[2] J. A. M. Lyon, C. J. Digenis, W. W. Parker, and M. A. H. Ibrahim, "Electromagnetic coupling reduction techniques," The University of Michigan, Ann Arbor, MI, USA, AFAL-TR-68-132, June 1968. Available: https://deepblue.lib.umich.edu/handle/2027.42/6402

[3] D. Sievenpiper, "High-Impedance Electromagnetic Surfaces," Ph.D. dissertation, Dept. Elect. Eng., Uni. California, Los Angeles, CA, 1999.

[4] R. J. King and K. S. Park, "Synthesis of surface reactances using grounded pin bed structure," in Electronics Letters, vol. 17, no. 1, pp. 52-53, Jan. 1981.

[5] P. Valale Prasannakumar, M. A. Elmansouri, and D. S. Filipovic, "Wideband decoupling techniques for dual-polarized bi-static simultaneous transmit and receive antenna subsystem," in IEEE Trans. Antennas and Propag., vol. 65, no. 10, pp. 4991-5001, Oct. 2017.

Full-Wave Modeling of RF Exciters Using WIPL-D: Road to Real-Time Simulation and Optimization

Pranav S. Athalye [1], Milan M. Ilić [1,2], and Branislav M. Notaroš [1]

[1] Electrical & Computer Engineering Department, Colorado State University, Fort Collins, CO
athalye@rams.colostate.edu, notaros@colostate.edu

[2] School of Electrical Engineering, University of Belgrade, Serbia
milanilic@etf.bg.ac.rs

Abstract — Computational tools for full-wave three-dimensional (3-D) simulations of linear passive electromagnetic (EM) components have reached a point where they became both practical and necessary in computer aided design (CAD) of RF devices. Although circuit-based solvers still offer unprecedented speed and true real-time tuning, full-wave software tools, which take into account almost all physical EM phenomena, rapidly approach similar efficiency and applicability. This, however, is not possible by just using modern hardware environment, but it also requires the numerical method of choice, encapsulated within a software tool, to be extremely precise and conservative in consumption of computer resources, i.e., CPU and memory. We here report a case study which demonstrates highly efficient utilization of higher order large-domain method of moments (MoM) modeling and optimization using WIPL-D. The example includes an RF exciter, based on axial-mode helical antennas mounted on a dielectric support, designed for utilization in the state-of-the-art pre-clinical magnetic resonance imaging (MRI) scanners.

Index Terms — 7-T, antennas, bioelectromagnetics, computational electromagnetics, FDTD, helical antenna, high-frequency, imaging, microwave, resonance imaging, RF coil.

I. INTRODUCTION

Magnetic resonance imaging (MRI) is an important non-invasive diagnostic technique that is still being explored to its full potential. The radio frequency (RF) coil is a crucial element in any MRI system that is used to excite the water molecules inside the sample being imaged. This paper addresses application of computational electromagnetics (CEM) to the modeling and full-wave analysis of MRI RF coils for ultra-high field magnetic resonance imaging. Modeling of RF coil is generally performed using the finite difference-time domain (FD-TD) methods [1]. In this study we explore the possibility of using the method of moments (MoM)

in the frequency domain to perform the same analysis.

We here compare the results obtained from the rigorous full-wave near field computational analysis in the frequency domain based on the MoM using the commercially available software WIPL-D [2] and the finite element method (FEM) using the commercially available software ANSYS HFSS, in the ANSYS Electronics Desktop [3].

II. FEM AND MOM MODELING

For our simulation models we consider a 7-T MRI system. The MRI bore contains a quadrifilar helical antenna RF coil [4] as the RF exciter with a phantom, as shown in Fig. 1.
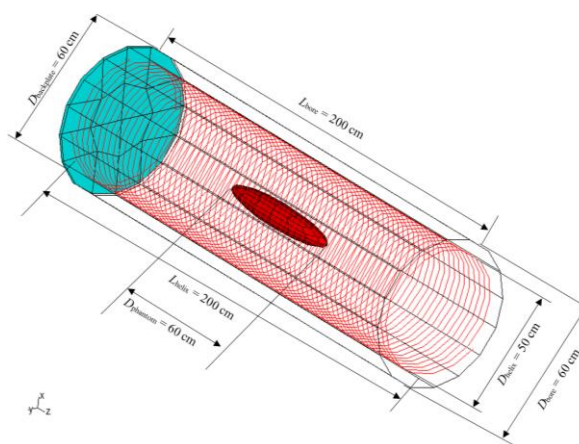
Fig. 1. WIPL-D model of the quadrifilar helical antenna RF coil with an ellipsoid phantom inside it.

The Larmor frequency for 7-T is 300 MHz. The diameter of the bore considered here is 60 cm and length is 200 cm. A helical antenna is a metallic wire antenna wound periodically with N wire turns and a pitch P about an imaginary (or dielectric) cylinder of diameter D_{helix} and length $L_{\text{helix}} = NP$ [5]. The pitch P relates to the pitch angle, α, as $P = C_{\text{helix}} \tan α$, where

$C_{helix} = \pi D_{helix}$ is the helix circumference. The antenna is fed at one wire end against a circular back plate, acting as a ground plane, i.e., the input power is supplied at a lumped excitation port between the wire end and the plate. A quadrifilar helical antenna is an array of four helical antennas connected to the same circular backplate and fed separately. The four helices (channels) are fed in proper phases in order to generate right handed circularly polarized magnetic field along the axis of the helices inside the coil.

The phantom used is a saline-water ($\varepsilon_r = 81$, $\sigma = 0.6$ S/m) filled ellipsoid. Ellipsoid longer axis is 60 cm long and aligned along the axis of the helix and the bore. It is rotationally symmetric and its shorter axis is 10 cm long.

In order to reduce complexity, the four "wire" helices were modeled in ANSYS-HFSS as a thin strips. The width of the strip is chosen as $a = 4r$, where $r = 1$ mm is the radius of the wire in the WIPL-D thin-wire model.

III. RESULTS AND DISCUSSION

In the results we plot and compare H_{rcp}, i.e., the right handed circularly polarized magnetic field and H_{lcp}, i.e., the left handed circularly polarized magnetic field inside the phantom. The aim of the RF coil is to maximize the right handed circularly polarized component of the magnetic field and to minimize the left handed circularly polarized component. Therefore H_{rcp} should be as high as possible and relatively uniform throughout the phantom, whereas H_{lcp} should be minimized and almost 0 on the longer axis of the phantom.

In order to equalize the feed powers in both models the excitation voltage of delta-type generators in the WIPL-D model is scaled to match that of the lumped excitation ports in the ANSYS-HFSS model such that:

$$V_x = \sqrt{\frac{P_{incx}\left(1 - |S_{xx}|^2\right)}{\text{Re}\{Y_{xx}\}}}, \quad (1)$$

where Y_{xx} is input admittance and S_{xx} is the corresponding S-parameter for each of the individual helices.
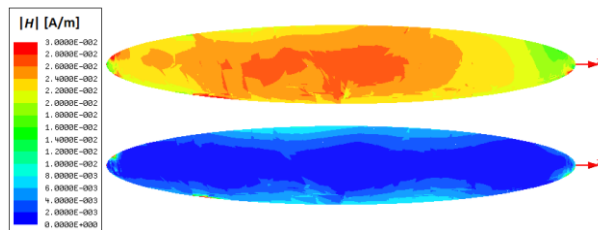
Fig. 2. H_{rcp} and H_{lcp} in xz-plane (sagittal/coronal) inside the phantom from ANSYS-HFSS.

The HFSS model run through 7 adaptive passes. Its final mesh comprised 299,584 tetrahedra and the matrix size was 5,394,535 unknowns. Total simulation time was 3 h : 20 m : 38 s. Simulated near field results are shown in Fig. 2.

The WIPL-D model had 11,736 unknowns. The order of polynomial expansion on the wires was 2 and on the plates it was a combination of 3 and 4. Total simulation time was 4 m : 24 s. Simulated near field results are shown in Fig. 3.

A comparison of H_{rcp} and H_{lcp} on the longer axis of the phantom, i.e., along the z-axis computed by ANSYS-HFSS and WIPL-D is shown in Fig. 4. We can conclude from Figs. 2-4 that the results are in a very good agreement.
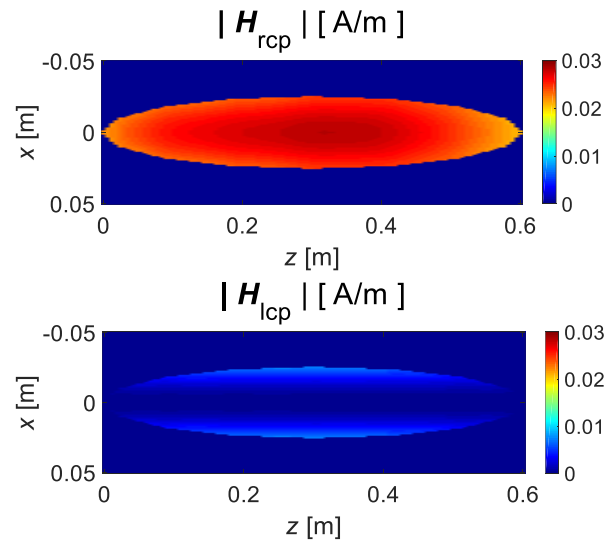
Fig. 3. H_{rcp} and H_{lcp} in xz-plane (sagittal/coronal) inside the phantom from WIPL-D. (Plotted using MATLAB).
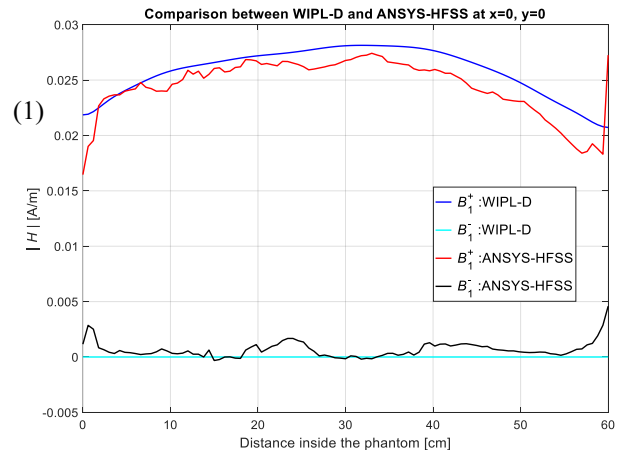
Fig. 4. Comparison of WIPL-D and ANSYS-HFSS results for H_{rcp} and H_{lcp} along the z-axis inside the phantom.

REFERENCES

[1] H. Yoo, A. Gopinath, and J. T. Vaughan, "A method to localize RF B_1 field in high-field magnetic resonance imaging systems," *IEEE Trans. on Biomedical Engineering*, vol. 59, pp. 3365-3371, Dec. 2012.

[2] WIPL-D Pro v11. WIPL-D d.o.o. ed2014.

[3] HFSS, ANSYS®. Electromagnetics Suite 17.1.0, ed: ANSYS, Inc.

[4] B. M. Notaros, M. M. Ilic, A. A. Tonyushkin, N. J. Sekeljic, and P. Athalye, "Quadrifilar helical antenna as a whole-body traveling-wave RF coil for 3T and 7T MRI," *Proceedings of the 23th Scientific Meeting of the International Society for Magnetic Resonance in Medicine*, *ISMRM 2015*, Toronto, Ontario, Canada, pp. 1825, 30 May–5 June, 2015.

[5] A. R. Djordjevic, A. G. Zajic, M. M. Ilic, and G. L. Stuber, "Optimization of helical antennas," *IEEE Antennas and Propagation Magazine*, vol. 48, no. 6, pp. 107-115, 2006.

Nonlinear Neural Network Equalizer for Metro Optical Fiber Communication Systems

Mahmoud M. T. Maghrabi, Shiva Kumar, and Mohamed H. Bakr

Department of Electrical and Computer Engineering
McMaster University, Hamilton, Ontario, L8S 4K1, Canada
maghrabm@mcmaster.ca, kumars@mcmaster.ca, mbakr@mcmaster.ca

Abstract — We present a neural network-based nonlinear electronic feed-forward equalizer. It compensates for the chromatic dispersion (CD) distortions in fiber optic communication systems with direct photo-detection. The proposed equalizer achieves bit error rate (BER) performance comparable to the maximum-likelihood sequence estimator (MLSE), with significantly lower computational cost. The complexity of the introduced equalizer scales linearly with the length of the inter-symbol interference (ISI) as opposed to exponential growth the MLSE complexity.

I. INTRODUCTION

Direct detected fiber-optic communication systems operating at 10 *Gbps* and beyond suffer from severe ISI caused by CD [1]. Electronic dispersion compensation (EDC) techniques have been identified as cost-effective solutions to combat ISI and to guarantee speed, robustness, stability and adaptability [1]. Feed-forward equalizer (FFE) [1], decision feedback equalizer (DFE) [2] and MLSE [3] are most common amongst EDC techniques. Although the CD causes linear distortions to the received optical signal, they turn into nonlinear impairments in the electrical domain, due to the square law detection. As a result, linear equalizers, e.g., FFEs and DFEs, fail to compensate for these nonlinear distortions. Only nonlinear equalizers, e.g., MLSEs, can effectively mitigate these nonlinear impairments [4]. However, the MLSE suffers from its intensive computational cost that grows exponentially with the length of ISI span.

In this paper, we introduce a nonlinear FFE that is capable of compensating for the nonlinear distortions, with computational cost growing linearly with the ISI span. The proposed equalizer consists of single artificial neural network (NN) layer [5]. At first, the parameters of the NN are optimized using extensive training process considering all possible data combinations that will be transmitted through the optical channel. Then, this trained NN acts as a nonlinear filter whose impulse response inverts the nonlinear response of the optical communication channel.

II. CHANNEL AND EQUALIZER MODELS

The received optical field $r(t)$ of a metro fiber-optic communication channel is related to the transmitted optical modulated signal $x(t)$ as [1]:

$$r(t) = \left(x(t) * h_f(t) \right) * h_o(t), \qquad (1)$$

where the operation $*$ denotes convolution and $h_f(t)$ and $h_o(t)$ are the impulse responses of the fiber and the optical filter, respectively. $x(t)$ is the input optical field consisting of binary sequence $\{a_k\}$. The received optical field $r(t)$ is passed through a photo-detector, electrical low pass filter (LPF) and analog-to-digital converter with $1/T_s$ oversampling rate. The output electrical current at each sampled time $y_k = y(kT_s)$ is then given by:

$$y(kT_s) = \left(\left| r(kT_s) \right|^2 + n_e(kT_s) \right) * h_e(kT_s), \qquad (2)$$

where $h_e(t)$ is the impulse response of the electrical LPF and $n_e(t)$ denotes to the receiver noise. Due to linear distortions imposed by the channel $h_f(t)$ and the square-law detection, nonlinear ISI is introduced at the output signal $y(t)$. Therefore, a nonlinear equalizer is necessary to compensate for these nonlinear impairments and to recover the transmitted data effectively.

The model of the introduced nonlinear NN equalizer is shown in Fig. 1. Given an input kth vector $\boldsymbol{y}_k$ that contains n-samples corresponding to the current symbol and its interfering neighbors, kth output $\hat{X}_k$ of the equalizer is given as:

$$\hat{X}_k = \sum_{j=1}^{m} w_j^o f_h \left(\sum_{l=1}^{n} w_{jl}^h y_l \right), \qquad (3)$$

where n and m are the numbers of equalizer taps and hidden neural layer nodes, respectively. $f_h(\cdot)$ is the nonlinear activation function, w_{jl}^h is the weight assigned to the connection between lth input and jth node of the hidden layer, and w_j^o is the weight assigned to the connection between jth node of the hidden layer and the output layer node. These NN weights are optimized in the training process in order to minimize the difference between the equalizer output $\hat{X}_k$ and the transmitted data X_k.
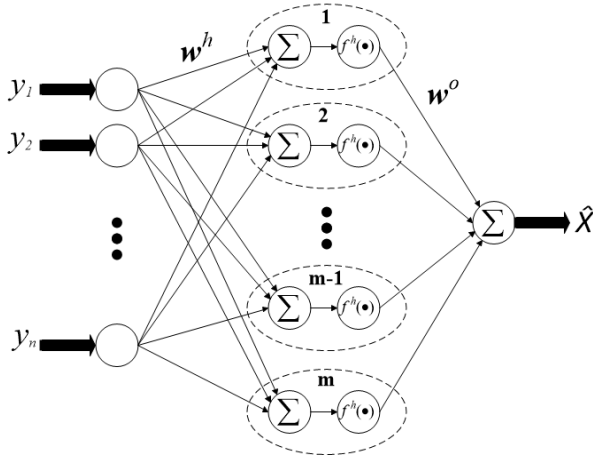
Fig. 1. The model of nonlinear neural network equalizer.
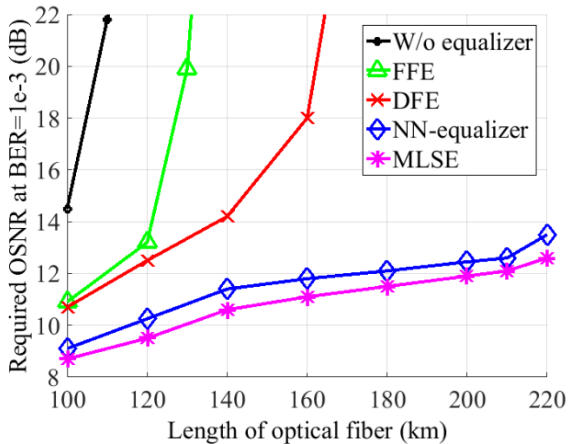
Fig. 2. The required OSNR at received $BER = 1 \times 10^{-3}$ versus fiber optic length. The performance without equalization is compared to the performance obtained using NN-equalizer with $n = 7$ and $m = 6$, FFE with 7-taps, DFE with 4-forward-taps and 3-backward-taps, and MLSE with 7-memory-size.

III. RESULTS

To evaluate the performance of the introduced equalizer, we consider a metro fiber-optic communication systems operating at $10\ Gbps$. The optical carrier is modulated by raised-cosine non-return to zero (NRZ) on-off keying (OOK). A single-mode fiber with dispersion coefficient of $17\ ps/nm/km$ is used in the system. The bandwidth of the optical and electrical filters are set as $50\ GHz$ and $7\ GHz$, respectively. In the Monte-Carlo simulation, pseudorandom binary sequence (PRBS) of length $2^{10} - 1$ is used to estimate BER. Total number of bits simulated $= 2^{14}$ bits. The parameters of equalizers are set as: $n = 7$, $m = 6$, and $f_h(\cdot) = \tanh(\cdot)$. Figure 2 shows the optical signal to noise ratio (OSNR) required to achieve a BER of 10^{-3} (sufficient for error-free operation with an advanced forward error correction)

versus swept fiber-optic lengths. As can be seen, without equalization the maximum feasible transmission distance is limited to about $100\ km$. However, using the NN-equalizer this feasible distance is extended up to $200\ km$. Furthermore, in Fig. 2, we compare the performance of our NN-equalizer to the performance obtained using FFE, DFE and MLSE. It is clear that the linear equalizers (FFE and DFE) do not provide performance benefit since the channel (fiber channel + detection) is nonlinear. Although the MLSE slightly outperforms the NN-equalizer, it requires $128\ -$multiplication operations per bit. In contrast, our NN-equalizer needs only $42\ -$multiplication operations per bit. Hence, the NN-equalizer provides a better trade-off between performance and computational complexity.

IV. CONCLUSION

A nonlinear feed forward equalizer exploiting neural networks has been proposed to mitigate chromatic dispersion impairments of fiber-optic communication systems with direct detection. We show that the introduced equalizer extends the feasible transmission distance up to 200 km, whereas the distance is limited to about $100\ km$ in the case of no equalizer used. The introduced equalizer is shown to have performance comparable to performance achieved by MLSE, with much lower computational cost.

REFERENCES

[1] S. Kumar and M. J. Deen, *Fiber Optic Communications: Fundamentals and Applications*. John Wiley & Sons, 2014.

[2] G. Katz and D. Sadot, "A nonlinear electrical equalizer with decision feedback for OOK optical communication systems," *IEEE Trans. Commun.*, vol. 56, no. 12, pp. 2002-2006, 2008.

[3] M. Bohn and C. Xia, "Electrical and optical equalization strategies in direct detected high speed transmission systems," *AEU-Int. J. Electron. Commun.*, vol. 63, no. 7, pp. 526-532, 2009.

[4] T. Foggi, E. Forestieri, G. Colavolpe, and G. Prati, "Maximum-likelihood sequence detection with closed-form metrics in OOK optical systems impaired by GVD and PMD," *J. Lightwave Technol.*, vol. 24, no. 8, pp. 3073-3087, 2006.

[5] M. Bakr, *Nonlinear Optimization in Electrical Engineering with Applications in Matlab*. The Institution of Engineering and Technology, London, 2013.

Synthesis of NFC Antenna Structure under Multi-Card Condition

Paul Baumgartner [1], Thomas Bauernfeind [1], Oszkar Biro [1], Christian Magele [1], Werner Renhart [1], and Riccardo Torchio [2]

[1] Institute of Fundamentals and Theory in Electrical Engineering
Graz University of Technology, Graz, Austria
paul.baumgartner@tugraz.at, t.bauernfeind@tugraz.at, biro@tugraz.at, christian.magele@tugraz.at,
werner.renhart@tugraz.at

[2] Dipartimento di Ingegneria Industriale
Università degli Studi di Padova, Padova, Italy
riccardo.torchio@studenti.unipd.it

Abstract ─ Wireless communication technologies such as Near Field Communication (NFC) found its way into our everyday life. The antenna structures used in such systems have to comply with several standards to achieve all requirements defined for the specific application. However, in practice there are scenarios for such antennas which are not considered in standards or design guides, but mainly influence the antenna behavior. In the present paper the synthesis of an antenna used for NFC-cards in a contactless payment system under multi-card condition is presented. The optimization relies on the differential evolution (DE) strategy. The computation of the forward problem is based on the partial element equivalent circuit (PEEC) method.

Index Terms ─ Near field communication, numerical optimization, partial element equivalent circuit method.

I. INTRODUCTION

NFC applications, which belong to the contactless communication technologies, have become popular within the last decade. Especially for the usage of contactless payment systems a big increase is recognized. Although there are design guides and standards which describe the requirements and limits of the antennas used in such systems, there are applications and use cases which are not covered by the standards but have significant impact on the overall system behavior.

One of those use cases for contactless payment is a wallet loaded with credit cards or cash cards of different providers, which should operate under those conditions. The standard for contactless payment EMVCo [1] only defines parameters for a system consisting of a Proximity Coupling Device (PCD), which provides the power to one Proximity IC Card (PICC). There are specific tests for the power and data transfer defined in a given three dimensional operating volume, as shown in Fig. 1. The

antenna design under these standardized tests have been done by [2], but without considering, e.g., multi-card condition.
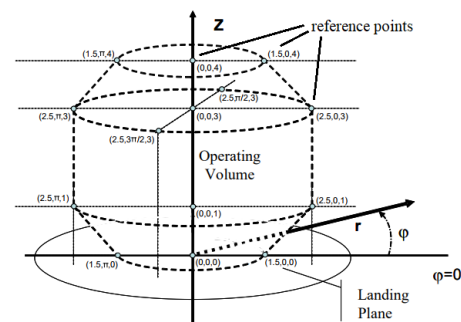
Fig. 1. The Operating Volume defined by EMVCo [1]. Tests have to be carried out in different defined points of this volume.

The communication of a NFC device is established at an operating frequency of 13.56 MHz in the near field surrounding the antennas, consequently loop antennas are utilized. For achieving optimal power transfer, the system consisting of the PCD and the PICC should result in a resonance frequency at 13.56 MHz.

In this paper the synthesis of a PICC-antenna with its corresponding matching network under the effect of multiple stacked PICC-cards is proposed. Aspects for conformance to the ISO/IEC14443 [3] as well as the EMVCo standard are considered.

II. NFC REQUIREMENTS

The tests for designing a PICC-antenna, with respect to the power transfer (defined in the EMVCo standard), forces to place the defined Poller-0 antenna [1] in the landing plane of the operating volume, as shown in Fig.

1. The PCD should be matched to an input impedance of $Z = 50 \, \Omega$ at the operating frequency. To fulfill the resonance requirements, the PICC antenna is connected to a matching circuit, as shown in Fig. 2. To model the behavior of the card-IC, an input impedance is connected, which values were taken from [4]. The standardization test demands to place the PICC at given reference points in the operating volume as shown in Fig. 1. The measured voltage at R_{IC} have to exceed a voltage level higher than 100mV to guarantee the power supply of the reader-IC [4].
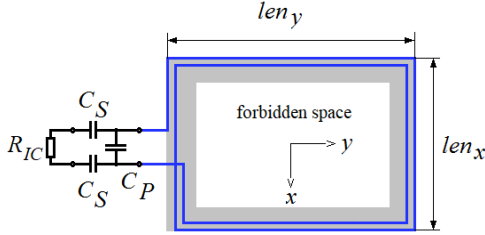
Fig. 2. Typical PICC-antenna design enclosed in an ID card.

III. ANTENNA OPTIMIZATION

Figure 2 shows the geometry and matching circuit of the antenna design to be optimized. The antenna have to be placed in an area defined for ID1 cards [3], considering a forbidden space. The parameter vector x to be optimized consists of the lengths len_x and len_y for the antenna size and the capacitors C_s and C_p of the matching circuit. The whole problem has been computed in the presence of one to five PICCs. The optimization of the antenna design is done by a standard DE [5]. For solving the forward problem a one dimensional type of the PEEC method [6] is used. Due to the fact, that within this method the antenna structure is described in terms of lumped elements the matching circuit can easily be added to the system. Consequently, the combined system, consisting of the antenna structure and the matching circuit can be solved within one step.

In this work the power requirements for the PICC, in this case the voltage conditions U_{IC} defined in chapter II, in all fourteen positions and in the presence of one to five antennas were used for the quality function. Additionally, the area A_{ant} of the antenna was minimized.

Introducing sigmoidal membership functions μ for these parameters, a scalar quality function can be defined:

$$q = \sum_{N_{card}=1}^{5} \sum_{pos=1}^{14} \mu(U_{IC}) + \mu(A_{ant}). \qquad (1)$$

In Fig. 3 the input impedances of the PCD antenna with the optimized antenna design and different numbers of PICC antennas are shown. The detuning effect of

the additional antennas can clearly be seen. This effect results in a deterioration of the power transfer to the card system.
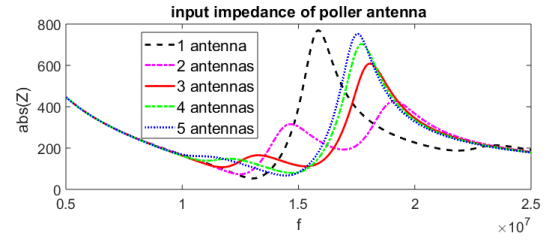
Fig. 3. Input impedance at the matching circuit of the PCD antenna for different numbers of PICC-antennas.

In Table 1 the voltages at the reader-IC's input resistance R_{IC} of the optimized and of the reference antenna design [1] are compared. As can be seen for a one antenna system the reference design delivers a higher voltage, which results in a better power transfer to the PICC. In contrast, for the three and five antenna system, the optimized design outperforms the reference design. Especially for the system consisting of five PICC's, the voltages of the reference design does not comply with the voltage level defined in the datasheet of the supplier [4]. It can also be observed, that the optimized design has a higher voltage with the three card system than with the single card system. This effect can be described with a better tuning of this system.

Table 1: Voltage at IC-terminal of card

	U_{IC} of	Position (0,0,0)	Position (2.5,0,3)	Position (1.5,π,3)
1 Card	Reference design	12.29 V	5.82 V	5.32 V
	Optimized design	7.18 V	1.32 V	1.18 V
3 Cards	Reference design	1.84 V	0.42 V	0.38 V
	Optimized design	14.87 V	3.52 V	3.15 V
5 Cards	Reference design	1.60 V	0.07 V	0.08 V
	Optimized design	5.12 V	1.07 V	0.95 V

Voltages at IC-terminal for different antenna designs and with different numbers of cards at specific positions as shown in Fig. 1.

IV. CONCLUSION

In this paper an approach for a design optimization of an antenna system, compliable to the EMVCo-standard and considering multi-card conditions has been presented. Since the PEEC method offers the possibility to directly connect lumped circuit elements, the integration of the matching circuit within the optimization process is enabled. Since a typical use case with several cards in the wallet was considered, a more robust antenna design could be achieved.

REFERENCES

[1] EMV Contactless Specifications for Payment Systems, Version 2.6, March 2016. (www.emvco.com/specifications.aspx?id=21)

[2] M. Gebhart, R. Neubauer, M. Stark, and D. Warnez, "Design of 13.56 MHz smartcard stickers with ferrite for payment and authentication," in *Proc. 3rd International Workshop on Near Field Communication*, February 2011.

[3] ISO/IEC 14443-1, Identification cards – Contactless integrated circuit cards – Proximity cards – Part 1: Physical characteristics.

[4] NXP, "NFC controller with integrated firmware, supporting all NFC Forum modes," PN7120 Datasheet, October 2017.

[5] P. Alotto, "A hybrid multiobjective differential evolution method for electromagnetic device optimization," *COMPEL, Int. J. Comput. Math. Electr. Electron. Eng.*, vol. 30, no. 6, pp. 1815-1828, 2011.

[6] T. Bauernfeind, P. Baumgartner, O. Bíró, C. A. Magele, K. Preis, and R. Torchio, "PEEC-based multi-objective synthesis of non-uniformly spaced linear antenna arrays," in *IEEE Transactions on Magnetics*, vol. 53, no. 6, pp. 1-4, June 2017.

A Low Complexity GNSS Array Signal Angle of Arrival (AoA) Estimation Algorithm and Validation

Boyi Wang[1,2], Yafeng Li[1,3], Nagaraj Channarayapatna Shivaramaiah[1], and Dennis M. Akos[1]

[1]Dept. of Aerospace Engineering Sciences, University of Colorado at Boulder, Boulder, CO 80309, USA
[2]School of EIC, Huazhong University of Science and Technology, Wuhan, 430074, China
[3]School of Automation, Beijing Institute of Technology, Beijing, 100081, China

Abstract—**Adaptive antenna array techniques are widely utilized to reject multipath and interference errors in Global Navigation Satellite System receivers (GNSS). Several methods have been proposed to tackle this issue. However, one severe problem for existing methods is the implementation complexity as GNSS receivers usually work under a high-dynamic receiving environment, thus may have the requirement of rapid angle estimates. In this paper, we propose a low complexity GNSS array signal estimation algorithm. Live data validation shows that the estimated AoA values can be used to improve the Carrier-to-Noise-Ratio by 1~4 dB-Hz.**

Keywords—**AoA, GNSS, GPS, Matlab, SDR, Array Signal.**

I. INTRODUCTION

With the development of Global Navigation Satellite Systems (GNSS), both high-accuracy and robust receivers are in high demand. To address the accuracy and reliability issue, sophisticated multipath rejection and high-sensitivity signal processing techniques are being incorporated into the receivers. The angle of arrival (AoA) estimation is a fundamental problem of GNSS antenna array signal processing in the same way that it is a critical task of radar, sonar and navigation systems.

Several non-adaptive AoA estimation methods have been proposed to tackle this issue. Delay-and-Sum [1] and Minimum Variance Distortion-less response Method (MVDR) [2] are two typical approaches. The basic idea behind the non-adaptive methods is to scan a beam through the signal reception space and measure the power received from each direction. Therefore the non-adaptive methods have low resolution as well as high implementation complexity. To improve the angle resolution of AoA estimation, AoA estimators that make use of the signal subspace have been proposed. Multiple Signal classification Algorithm (MUSIC) [3], root-MUSIC [4], Estimation of Signal Parameters via Rotational Invariance Techniques (ESPRIT) [5] are three representative algorithms. These subspace-based algorithms have high-resolution estimation capabilities. The basic idea of subspace-based algorithms is estimating the covariance of a signal plus noise model and then use it to form a matrix whose eigenstructure gives rise to the signal and noise subspaces. However, when considering the high-speed mobility of receiver and satellites for GNSS application, high complexity of subspace calculations and searches are not acceptable.

In this paper, we propose a low complexity GNSS array

signal AoA estimation algorithm. The live data validation of the proposed algorithm shows that it can successfully estimate AoA of array signal. Rough analyses in terms of receiver complexity shows that the proposed algorithm has a lower implementation complexity compared to the subspace-based algorithm.

II. ANTENNA ARRAY AND GNSS SIGNAL MODEL

A. Antenna Array Signal Model

In order to model an antenna array for GNSS signal, we make the following assumptions [6]:

1. We assume that several wavefronts are impinging on an antenna array with M isotropic sensor elements.
2. The transmission medium between the transmitter, receiver and possible scatterers is assumed linear, non-dispersive, and isotropic.
3. Radiation impinging on an array of sensor elements can be modeled as a superposition of wavefronts generated by each point source.
4. The point sources are located far from the array such that the direction of propagation is nearly equal at each sensor and the wavefronts are approximately planar (far-field assumption).
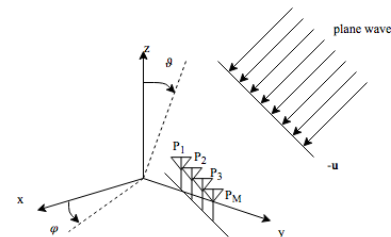
Fig. 1. Schematic of plane wave and antenna array.

As shown in Fig. 1, the array consists of isotropic sensors located at positions $\mathbf{p}_m, m = 1, \ldots, M$ which spatially sample the signal filed. The array receives wave propagating in the direction **-u**. This yields a set of signals:

$$\mathbf{s}(t, \mathbf{p}) = \begin{bmatrix} S(t - \tau_1)e^{-j2\pi f_c \tau_1} \\ S(t - \tau_1)e^{-j2\pi f_c \tau_2} \\ \ldots \\ S(t - \tau_1)e^{-j2\pi f_c \tau_M} \end{bmatrix}. \quad (1)$$

Here, τ_m denotes the time delays corresponding to the time of arrival at the various sensors at locations $\mathbf{p}_m$ where,

$$\tau_m = -\frac{\mathbf{u}^T \mathbf{p}_m}{c}. \qquad (2)$$

And c is the speed of the light. The vector $\mathbf{u}$ is a unit vector with:

$$\mathbf{u} = \begin{bmatrix} \sin(\vartheta)\cos(\varphi) \\ \sin(\vartheta)\sin(\varphi) \\ \cos(\varphi) \end{bmatrix} = \begin{bmatrix} u_x \\ u_y \\ u_z \end{bmatrix}. \qquad (3)$$

Where φ is the elevation angle, and ϑ is the azimuth angle.

Thus, $\tau_m = -\frac{1}{c}(u_x p_{x,m}, u_y p_{y,m}, u_z p_{z,m})$, with $\mathbf{p}_m = \begin{bmatrix} p_{x,m} \\ p_{y,m} \\ p_{z,m} \end{bmatrix}$.

For narrowband signals with $B\Delta T_{max} \ll 1$, where B is the signal bandwidth, $\Delta T_{max} \ll \tau_m$ is the maximum travel time between any two sensor elements in the array we can write:

$$s(t - \tau_m)e^{-j2\pi f_c \tau_m} \approx s(t)e^{-j2\pi f_c \tau_m}. \qquad (4)$$

Thus, in the narrowband case the time delays τ_m can be approximated by only a phase shift and we can write:

$$\mathbf{s}(t, \boldsymbol{p}) = \begin{bmatrix} S(t - \tau_1)e^{-j2\pi f_c \tau_1} \\ S(t - \tau_1)e^{-j2\pi f_c \tau_2} \\ ... \\ S(t - \tau_1)e^{-j2\pi f_c \tau_M} \end{bmatrix} = \boldsymbol{\alpha}(\varphi, \vartheta)s(t). \qquad (5)$$

Where $\boldsymbol{\alpha}(\varphi, \vartheta) \in \mathbb{C}^{M \times 1}$ is called steering vector with:

$$\boldsymbol{\alpha}(\varphi, \vartheta) = \begin{bmatrix} e^{\frac{j2\pi}{\lambda}(U_x P_{x,1} + U_y P_{y,1} + U_z P_{z,1})} \\ e^{\frac{j2\pi}{\lambda}(U_x P_{x,2} + U_y P_{y,2} + U_z P_{z,2})} \\ ... \\ e^{\frac{j2\pi}{\lambda}(U_x P_{x,M} + U_y P_{y,M} + U_z P_{z,M})} \end{bmatrix}. \qquad (6)$$

Where λ is the wavelength.

B. GNSS Signal Model

The single channel GNSS RF signal can be modeled as:

$$S(t) = \sqrt{2P}\left(s_I(t)\cos(2\pi f_c t) - s_Q(t)\sin(2\pi f_c t)\right)$$
$$= \sqrt{2P}\Re(s(t)e^{j2\pi f_c t}). \qquad (7)$$

Where P is the power of the RF signal; $\Re(\cdot)$ represents real operator; f_c is the center frequency; S_I and S_Q are baseband I and Q signals that can be denoted as:

$$s_I(t) = \sum_{k=-\infty}^{+\infty} D_I(n)\mu_{T_c}(t - T_c)$$
$$s_Q(t) = \sum_{k=-\infty}^{+\infty} D_Q(n)\mu_{T_c}(t - T_c). \qquad (8)$$

Fig. 2 shows the traditional GNSS receiver architecture.

The incoming RF signal, $S_{IF}(t)$, is multiplied and down converted to a baseband signal by locally the generated carrier signal. Then the baseband signal, $i(t)$ and $q(t)$ are correlated by locally generated early-, late-, and prompt-code signals. The correlated signals of prompt branches can be denoted as:

$$i_P(n) = aD(n)R(\tau_P)\cos(\omega_e(n)t(n) + \theta_e)$$
$$q_P(n) = aD(n)R(\tau_P)\sin(\omega_e(n)t(n) + \theta_e). \qquad (9)$$

Where $D(n)$ is the navigation data bit; τ_p is the phase difference between locally generated prompt code and received PRN code; $R(\cdot)$ represents the normalized auto-correlation function (ACF) of PRN code; ω_e is the frequency difference

between the generated carrier and the received carrier signal in rad; θ_e is the initial phase difference.
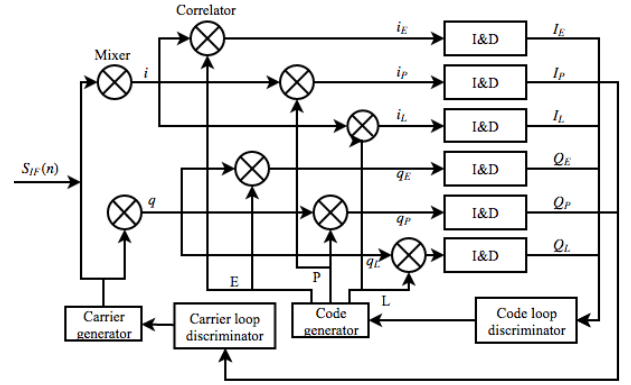
Fig. 2. Traditional GNSS receiver architecture.

The correlated signals of prompt branches are sent into integration and dumping (I&D) processor and can be denoted as:

$$I_P(n) = aD(n)R(\tau_P)sinc(f_e T_{coh})\cos\phi_e \qquad (10)$$
$$Q_P(n) = aD(n)R(\tau_P)sinc(f_e T_{coh})\sin\phi_e .$$

Where ϕ_e is the carrier phase difference; T_{coh} is the coherent integration time; f_e is the frequency difference in Hz. The integrator outputs of early and late branches can be denoted in a similar way. The only difference is value of the ACF of $R(\tau_E)$ and $R(\tau_L)$.

As it can be seen that the integrator outputs are determined by not only the code phase differences between local and received signals, but also by the carrier phase differences. In order to work independent from the carrier tracking loop, the code tracking loop usually uses the non-coherent discriminator to detect the correlation values between early and late branches. The traditional NELP discriminator can be denoted as:

$$V(n) = \frac{1}{2}\left(E(n) - L(n)\right). \qquad (11)$$

Where,

$$E(n) = \sqrt{I_E^2(n) + Q_E^2(n)} = aR(\tau_E)|sinc(f_e T_{coh})|$$
$$P(n) = \sqrt{I_P^2(n) + Q_P^2(n)} = aR(\tau_P)|sinc(f_e T_{coh})| . \qquad (12)$$
$$L(n) = \sqrt{I_L^2(n) + Q_L^2(n)} = aR(\tau_L)|sinc(f_e T_{coh})|$$

III. PROPOSED ARCHITECTURE FOR GNSS ARRAY SIGNAL AOA ESTIMATION AND BEAM-STEERING

A. Post-Correlation AoA Estimation Architecture

According to Eq. (4), we ignore the time delay between elements. Then the GNSS array signal from one satellite can be denoted as:

$$S(t, \mathbf{p}) = \begin{bmatrix} \sqrt{2P}\left(s_I(t)\cos(2\pi f_c t) - s_Q(t)\sin(2\pi f_c t)\right)e^{-j2\pi f_c \tau_1} \\ \sqrt{2P}\left(s_I(t)\cos(2\pi f_c t) - s_Q(t)\sin(2\pi f_c t)\right)e^{-j2\pi f_c \tau_2} \\ ... \\ \sqrt{2P}\left(s_I(t)\cos(2\pi f_c t) - s_Q(t)\sin(2\pi f_c t)\right)e^{-j2\pi f_c \tau_M} \end{bmatrix}. \qquad (13)$$

Compared to the single element GNSS signal, the difference of GNSS array signal is that the received signal for every element has a corresponding phase shift $e^{-j2\pi f_c \tau_m}$. There are two approaches to estimate the corresponding phase shift angles between different elements: (1) pre-correlation estimation, and (2) post-correlation estimation. The pre-correlation estimation approach, as its name implies, is estimating AoA before the correlation operation. However, the pre-correlation GNSS signal is buried in the white noise environment, which is extremely weak for further signal processing. In this manner, it is hard to extract spatial information in weak GNSS array signal. Therefore, post-correlation processing is used to enhance the strength of the received GNSS array signal.

In Fig. 2 we can see that the correlators and I&D processors are used to enhance the signal strength. However, the carrier- and the code-phase difference between elements will be changed due to tracking loop adjustment. Therefore, to obtain correlated GNSS array signals, while maintaining the phase differences between elements, we propose the AoA estimation architecture in Fig. 3.
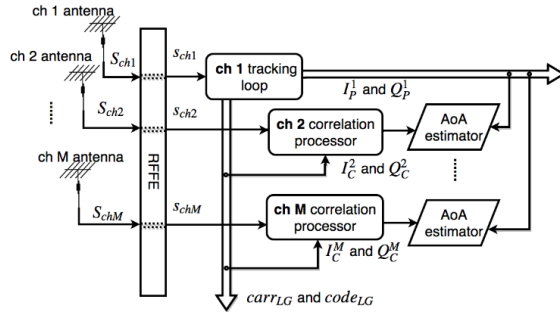
Fig. 3. Schematic diagram of the proposed AoA estimation architecture.

It can be seen that the GNSS array signals are received from antenna array for channel 1 to channel M. The received array signals are down-converted to base-band signals by the radio frequency front end (RFFE). Then the down-converted channel 1 signal is sent into a typical carrier- and code-tracking loop (described in Fig. 2) for correlation and integration processing. According to Eq. (10), the outputs of I&D for channel 1 can be denoted as:

$$I_P^1(n) = aD(n)R(\tau)sinc(f_e T_{coh}) \cos\phi_e$$
$$Q_P^1(n) = aD(n)R(\tau)sinc(f_e T_{coh}) \sin\phi_e \qquad (14)$$

The superscript of $I(n)$ and $Q(n)$ stands for the element numbers m, where $m = 1,2,...,M$.

Instead of being processed in the tracking loop, the rest of the $M-1$ channels (channel 2 to channel M) are sent into corresponding correlation processors respectively. The difference between a tracking loop and a correlation processor is: for a tracking loop the local carrier and code signals are generated based on the feedback loop adjustment. In this way, the tracking loop is able to maintain alignment of the received and generated signals. In order to adjust the loop adaptively, the early, late, and prompt branches are used.

The correlation processor, however, does not have the

adaptive adjustment process. The input signals are correlated and integrated in the correlation processor. As can be seen from Fig. 3, two inputs of the m_{th} correlation processor are the locally generated carrier signal ($carr_{LG}$) and code signal ($code_{LG}$) from channel 1, while another input, s_{chm}, is the corresponding base-band signal down-converted from the m_{th} element. In this paper we assume that the tracking loop of channel 1 is in the lock condition. In this manner, both $carr_{LG}$ and $code_{LG}$ are aligned with the received $S_{ch1}(t)$. Therefore, the outputs of I&D for $m = 1,2,...,M$ can be denoted as:

$$I_C^m(n) = aD(n)R(\tau)sinc(f_e T_{coh}) \cos(\phi_e + 2\pi f_c \tau_m)$$
$$Q_C^m(n) = aD(n)R(\tau)sinc(f_e T_{coh}) \sin(\phi_e + 2\pi f_c \tau_m) \qquad (15)$$

In order to distinguish between the I&D outputs obtained from the prompt branch of channel 1 tracking loop, we use the subscript C for the I&D outputs obtained from correlation processor of the rest $M-1$ channels. As it can be seen, by correlating to $carr_{LG}$ and $code_{LG}$, the phase differences between different elements are remained. At the same time, the signal strength is improved significantly due to the correlator gain.

Hence, we can consider the correlated signals, χ_m, as an array signal that has the same spatial characteristics as the signals that arrive at the GNSS antenna array. Where χ_m can be denoted as:

$$\chi_m(n) = \begin{cases} I_P^m(n) + jQ_P^m(n), & \text{where } m = 1 \\ I_C^m(n) + jQ_C^m(n), & \text{where } m = 2,...,M \end{cases} \qquad (16)$$

From Eq. (16) we can see that the post-correlated array signal, χ_m, is composed of the real and imaginary parts of I&D outputs.

B. Carrier Phase Difference Extraction Method

Without loss of generality, we consider the carrier phase of χ_1 as the reference phase, i.e., $\tau_1 = 0$. Therefore, τ_m is the phase difference between m_{th} element (m ≥ 2) and channel 1. Then the relationship between χ_m and τ_m can be denoted as:

$$\chi_m(n) = aD(n)R(\tau)sinc(f_e T_{coh})e^{j(\phi_e + 2\pi f_c \tau_m)}. \qquad (17)$$

In order to extract τ_m, we propose the Carrier Phase Difference Extraction (CPDE) method. The implementation of CPDE can be expressed as:

$$\tau_m(n) = -\text{angle}\{\chi_1 \times \chi_m^*\}. \qquad (18)$$

Where χ_m^* is the complex conjugate of χ_m. CPDE uses the angle information of the product between χ_1 and χ_m^* to extract τ_m. The detailed derivation of Eq. (18) can be written as:
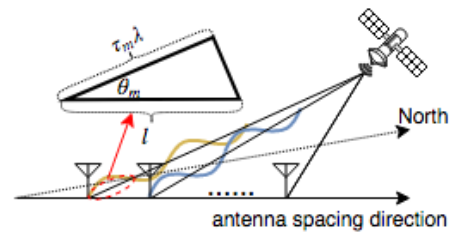
Fig. 4. Schematic of the geometrical relationship of Satellite and GNSS array signal.

$$\chi_1 \times \chi_m^* = \left(aD(n)R(\tau)sinc(f_e T_{coh})\right)^2 \times [\cos(\phi_e + 2\pi f_c\tau_m) - j\sin(\phi_e + 2\pi f_c\tau_m)] \times [\cos(\phi_e) + j\sin(\phi_e)]$$

$$= \left(aD(n)R(\tau)sinc(f_e T_{coh})\right)^2 \times [\cos(\phi_e + 2\pi f_c\tau_m)\cos(\phi_e) + j\cos(\phi_e + 2\pi f_c\tau_m)\sin(\phi_e) - j\sin(\phi_e + 2\pi f_c\tau_m)\cos(\phi_e) + \sin(\phi_e + 2\pi f_c\tau_m)\sin(\phi_e)]$$

$$= \frac{1}{2}\{\cos(2\phi_e + \tau_m) + \cos(\tau_m) + j[\sin(2\phi_e + 2\pi f_c\tau_m) - \sin(\tau_m)] - j[\sin(2\phi_e + 2\pi f_c\tau_m) + \sin(\tau_m)] - [\cos(2\phi_e + 2\pi f_c\tau_m) - \cos(\tau_m)]\}$$

$$= \left(aD(n)R(\tau)sinc(f_e T_{coh})\right)^2 \times e^{-j2\pi f_c\tau_m}.$$

(19)

Fig. 4 illustrates the geometrical relationship of Satellite and GNSS array signal. The carrier phase difference between channel 1 and channel 2 is taken as an example of how to calculate the AoA from τ_m. The AoA of m_{th} element, θ_m, can be denoted as:

$$\theta_m = \arccos(\frac{\tau_m \lambda}{l}).$$

Where λ is the wavelength of the received GNSS signal, and l is the distance between the two antennas.

IV. LIVE DATA VALIDATION AND PERFORMANCE ANALYSES

In this section, we use live GPS L1 data to validate the proposed AoA estimation technique. Then we provide qualitative analyses in terms of receiver implementation complexity.

A. Live Data Validation

1) GPS L1 Data Collection

The actual experiment setup and the schematic are shown in Fig. 5. In the data collection configurations, two Tallysman TW7872 antennas [7] are used to collect RF data. The Amungo board [8] is used as a front-end to down-convert GPS RF signal to IF data. A Rubidium clock is used to provide a stable reference clock input for front-end sampling.
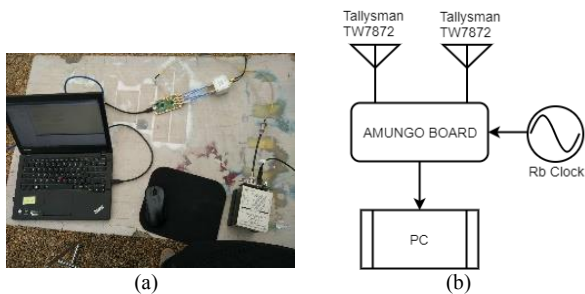
Fig. 5. (a) Actual setup, and (b) data collection schematic.

Two Tallysman TW7872 dual-band GNSS antennas were used to collection GPS RF signal. The TW7872 is a dual-band, antenna for reception of GPS L1/L2, GLONASS G1/G2, BeiDou B1, Galileo E1 and is specially designed for precision dual frequency positioning. Two TW7872 antennas that used in this paper can be found in Fig. 6. In this paper, two antennas were placed with 9.5 cm spacing, which is the half-wavelength for GPS L1 carrier at 1575.42 MHz.

The Amungo board, as shown in Fig. 7 is a Multi-band RF transceivers for the L-band, that equipped with NT1065 "Nomada" as shown in Fig. 8.

Fig. 6. Tallysman TW7872 antennas.

Fig. 7. Amungo board.

NT1065 [9] is a four-channel radio frequency (RF) front-end for simultaneous reception of GPS, GLONASS, Galileo, Beidou, IRNSS, QZSS and SBAS signals of various frequency bands L1, L2, L3, L5, E1, E5a, E5b, E6, B1, B2, B3.
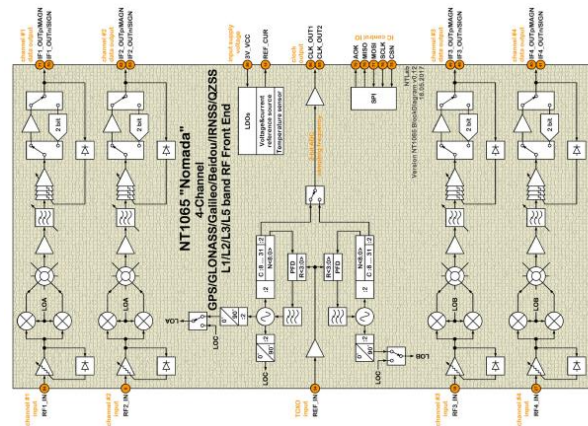
Fig. 8 NT1065 block diagram.

The GPS L1 data were collected on September 29th, 2017, at the Rooftop of the University of Colorado Boulder Discovery Learning Center. The selected data scenario is shown in Fig. 9.
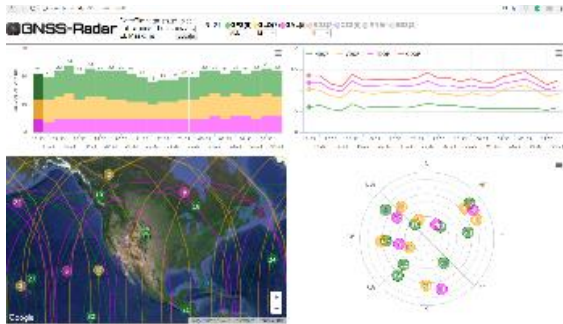
Fig. 9. Data collection scenario on September 29th, 2017, at the Rooftop of CU Boulder DLC.

2) Post-processing for AoA Estimations

Post-processing is a common and flexible approach for GPS data processing. In addition, the Software Defined Receiver (SDR) technique is frequently used for GPS data processing. In this paper, an open source Matlab-based SDR was used [10] to implement the proposed architecture shown in Fig. 3.

Table I is typical settings for the SDR implemented in this paper. The definations of those settings are detailed in [10], so they will not be described herein. Note that except for integration time T_{coh}, the remaining parameters are for the channel 1 tracking loop. As mentioned above, instead of generating a local carrier and code replica, the correlation processor uses the local replica from channel 1 tracking loop. Thus, it does not need to be configured with DLL and PLL settings.

TABLE I.　　SDR SETTINGS

Parameters	Value
DLL damping ratio	0.7
DLL damping ratio	1.5
DLL Correlator spacing	0.5
PLL damping ratio	0.7
PLL noise BW	20
Coherent integration time T_{coh}	1 ms

The correlator outputs of the prompt branch of the channel 1 tracking loop of PRN 18 is shown in Fig. 10. From Fig. 10 we can see that the magnitude of I_P is significantly higher than Q_P, which means the carrier tracking loop successfully tracked the received signal.
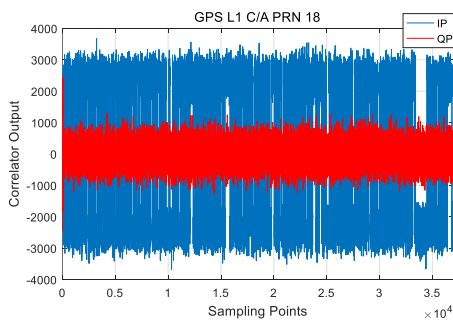
Fig. 10. Correlator output.

Positioning solutions obtained from SDR (channel 1 processing) and actual location obtained from Google Maps are shown in Fig. 11 and Fig. 12 respectively. From Fig. 11 and Fig. 12 we can conclude that the GPS L1 C/A signal has been successfully processed.
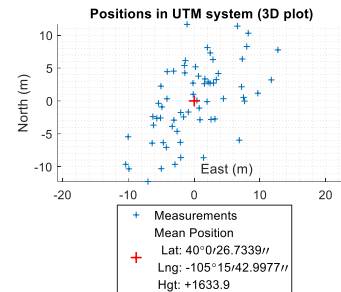
Fig. 11. Positioning solutions of SDR.

Fig. 12. Screen shot from Google Maps.

To further enhance the signal strength, we should use a longer non-coherent integration time T_{ncoh}. However, in order to estimate AoA more precisely in dynamic environment, T_{ncoh} cannot be too long. Thus, we choose a intermediate value of $T_{ncoh} = 20$ ms. The process of non-coherent integration of m_{th} channel can be expressed as:

$$\chi_m|_{N_{nc}} = \frac{1}{N_{nc}} \sum_{n=1}^{N_{nc}} \chi_m(n).$$

Where N_{nc} is the non-coherent number where $N_{nc} = \frac{T_{ncoh}}{T_{coh}}$. Note that this process should be done after navigation data bit synchronization. Fig. 13 shows the CPDE AoA estimations of GPS L1 C/A signals from PRN 18, PRN 21, PRN 10, and PRN 8.

The mean elevation/azimuth angles in 37 ms for four satellites obtained from SDR processing are listed in Table II. Note that since the orientation of the two antennas is not pointing to the north, the estimated AoA angles do not match the elevation angles shown in Table II.
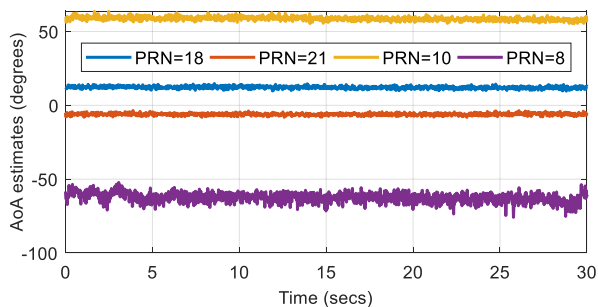
Fig. 13. AoA estimations of GPS L1 C/A using CPDE.

TABLE II.   MEAN EL./AZ. ANGLES

PRN	Az.	El.
18	7.9801°	72.7560°
21	133.2669°	66.7735°
10	293.7491°	54.9897°
8	318.4287°	15.4279°

To further validate the correctness of CPDE, we plot the comparisons between CPDE and MUSIC in Fig. 14. In a MUSIC implementation, the angle resolution is set to be 0.5° and 2°. In this scenario, two settings result in 720 times and 180 times of MUSIC processing for every estimated value, respectively. Every MUSIC processing includes a 360° angle space searching, as well as MUSIC spectrum calculations.

As it can be seen that the results of CPDE and MUSIC (reso=0.5) estimates are consistent. However, for MUSIC with resolution of 2°, there is a bias of ~0.5° compared to CPDE and MUSIC (reso=0.5) for part of the estimated values.
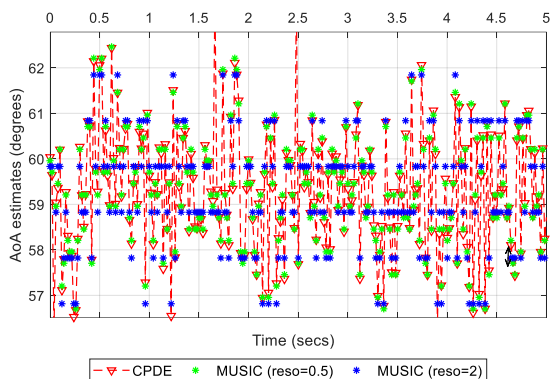
Fig. 14. AoA estimates comparisons between CPDE and MUSIC (reso = 1°) for PRN 10.

3) Beam-steering Architecture and Validation

A beam-steering technique is used to further validate the proposed CPDE algorithm. The pre-correlation beam-steering architecture is shown in Fig. 15. As shown, the beam-steering and combination process is done before correlator. For every estimated value, the AoA estimates stream is sent into the phase shifter. Then the phase shifter is used to steer the 2nd channel to the direction of the 1st channel. The steered 2nd channel signal and the 1st channel signal are combined together and then sent into the GNSS signal tracking loop.
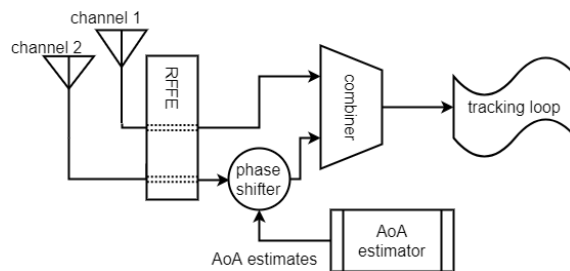
Fig. 15. Pre-correlation beam-steering architecture.

The comparison of CNo of the single channel signal and the beam-steered & combined dual-channel signal for PRN 21 is shown in Fig. 16. The averaged CNo improvement is 3.8439 dB-Hz.
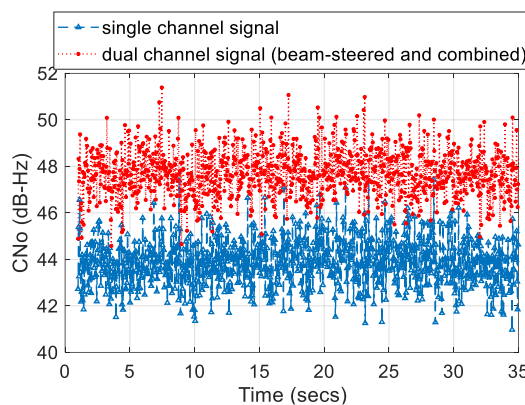
Fig. 16. CNo comparison of single and dual channel signal for PRN 21.

Fig. 17 shows the CNo improvement for PRN 18, PRN 21, and PRN 10. Note that for different elevation angles. Table III shows the Averaged CN_0 improvements vs. PRNs and AoA estimates. As it can be seen that the averaged improvements of beam-steering various from 1.34~3.84 dB-Hz. We can also see the nearer the AoA to 0°, the better its signal strength improvement is.
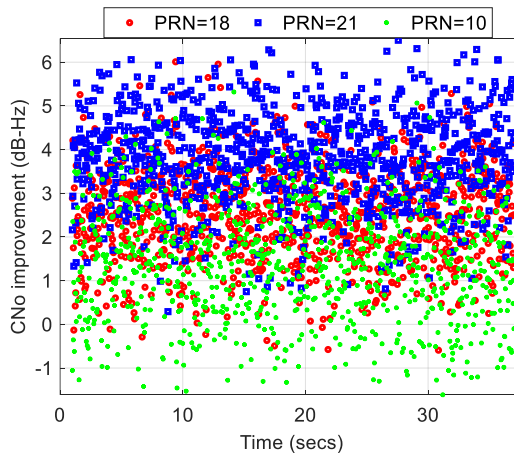
Fig. 17. CNo improvement for three satellites.

TABLE III.   AVERAGED CN_0 IMPROVEMENT VS. PRNS AND AOA ESTIMATES

PRN	Averaged CN_0 Improvement (dB-Hz)	Averaged AoA Estimate (°)
18	2.4907	12.1370
21	3.8439	-6.0692
10	1.3460	58.6869

B. Analyses of Receiver Implementation Complexity

The proposed CPDE is based on extracting the phase difference between elements. Therefore, compared to a subspace-based AoA estimation algorithms that focus on searching in the signal subspace and noise subspace, CPDE has a significant lower implementation complexity. The following are two simple demonstrations of the implementation of CPDE and MUSIC for post-correlated signals. Since the detailed information and definitions of MUSIC has been documented in [3], they will not be illustrated herein.

CPDE Algorithm

Vector Multiplication: $\chi_1 \times \chi_m^*$

Obtaining angle: $\tau_m(n) = -\text{angle}\{\chi_1 \times \chi_m^*\}$

Converting τ_m to θ_m: $\theta_m = \arccos(\frac{\tau_m \lambda}{l})$

MUSIC Algorithm

Matrix Multiplication: $Q_n = \frac{\begin{bmatrix} \chi_1 \\ \chi_m \end{bmatrix} \times \begin{bmatrix} \chi_1 \\ \chi_m \end{bmatrix}^T}{n}$

Calculating eigenvalues of Q_n

Searching for $\theta \in (0°, 360°)$ *that maximums:*

$$P_{MUSIC}(\theta) = \frac{1}{\alpha^H(\theta) Q_n Q_n^H \alpha(\theta)}$$

From the above analyses, we can see that for every estimated value, CPDE only needs $1 \times$ simple vectors multiplication, $1 \times$ angle calculation, and $1 \times$ arccos operation. However, for MUSIC, it has to do $1 \times$ complicated matrix multiplication, $1 \times$ eigenvalues calculation, and searches in the whole angle space (360°) for the maximum value of MUSIC spectrum. As mentioned above, for every AoA estimate, MUSIC needs to search 720 or 180 times for angle resolution of 0.5° and 2°, respectively. The rough analyses show that CPDE has a lower implementation complexity than MUSIC.

V. CONCLUSIONS

In this paper, we proposed a low complexity GNSS array signal processing algorithm. The live data validation results show that the proposed algorithm can successfully estimate the AoA of array signal. More importantly, the proposed architecture is easy to implement and has a low receiver complexity.

REFERENCES

[1] L. C. Godara, "Application of antenna arrays to mobile communications. II. Beam-forming and direction-of-arrival considerations," Proc. IEEE, 85(8): pp. 1195-1245, 1997.

[2] A. Alexiou and M. Haardt, "Smart antenna technologies for future wireless systems: Trends and challenges," Communications Magazine IEEE, 42(9): pp. 90-97, 2004.

[3] R. Schmidt, "Multiple emitter location and signal parameter estimation," IEEE Transactions on Antennas & Propagation, 34(3): pp. 276-280, 1986.

[4] B. D. Rao and K. V. S. Hari, "Performance analysis of root-MUSIC," IEEE Transactions on Acoustics Speech & Signal Processing, 37(12): pp. 1939-1949, 1989.

[5] R. Roy and T. Kailath, "ESPRIT-estimation of signal parameters via rotational invariance techniques," IEEE Transactions on Acoustics Speech & Signal Processing, 37(7): pp. 984-995, 2002.

[6] Signals and Array Signal Processing for Global Navigation Satellite Systems. Available from: https://www.msv.ei.tum.de/en/courses/master-lectures/signals-and-array-signal-processing-for-global-navigation-satellite-systems/

[7] Tallysman Home Page. Available from: http://www.tallysman.com/index.php/gnss/products/antennas-l1l2-g1g2/tw7872/

[8] Amungo Navigation. Available from: https://www.Amungo-navigation.com/nut4nt

[9] NT1065_USB3_description_v1.03.pdf. Available from: http://www.ntlab.com/IP/NT1065/NT1065_USB3_description_v1.03.pdf

[10] B. Kai, et al., A Software-Defined GPS and Galileo Receiver. Birkhäuser Boston, pp. 1632-1637, 2007.

Power Transfer Efficiency for Distance-Adaptive Wireless Power Transfer System

Dong-Geun Seo [1], Seong-Hyeop Ahn [1], Ji-Hong Kim [1], Seung-Tae Khang [2], Soo-Chang Chae [2], Jong-Won Yu [2], and Wang-Sang Lee [1*]

[1] Department of Electronic Engineering/Engineering Research Institute
Gyeongsang National University, 501 Jinju-daero, Jinju, Gyeongnam, 52828, Republic of Korea
*wsang@gnu.ac.kr

[2] School of Electrical Engineering, Korea Advanced Institute of Science and Technology (KAIST)
291, Daehak-ro, Yuseong-gu, Daejeon, 34141, Republic of Korea

Abstract — In this paper, a highly efficient distance-adaptive wireless power transfer system with automatic impedance tuning control at variable distances is proposed, and we compare the power transfer efficiency of wireless power transfer system at different operating conditions using the method of moments (MoM) technique. By sensing a reflected power and controlling impedance tuning networks, the proposed wireless power transfer system achieves the high and stable efficiency with regard to the variable operating distances. According to adaptive impedance matching algorithms under the minimum reflected power conditions, the proposed system achieves an improved power transfer efficiency of approximately maximum 160% within the operating distance.

Index Terms — Distance-adaptive, Power Transfer Efficiency (PTE), variable distances, Wireless Power Transfer (WPT).

I. INTRODUCTION

Wireless power transfer (WPT) technology transfers electrical energy using electromagnetic waves without electrical wires in various industries related to remote energy transfer, µ-sensors, digital IT consumer devices, and electric vehicles (EV) [1]. Due to the impedance matching characteristic of WPT systems that use coupled resonant antennas, WPT systems with different operating distances, variable impedance loads, and lateral misalignment between the transmitting and receiving antennas result in a significant degradation in power transfer efficiency (PTE) [2]–[4]. To achieve a highly efficient WPT, it is necessary for the system to be able to detect the location of the receiving device. In addition, in order to improve PTE for any transfer distance, adaptive frequency tracking was proposed, but it is not practical due to frequency regulation [5]. In this paper, a highly efficient WPT system with automatic

impedance tuning control at variable operating distances is presented and by comparing the impedance matching algorithms under different conditions, its optimal performance is verified.
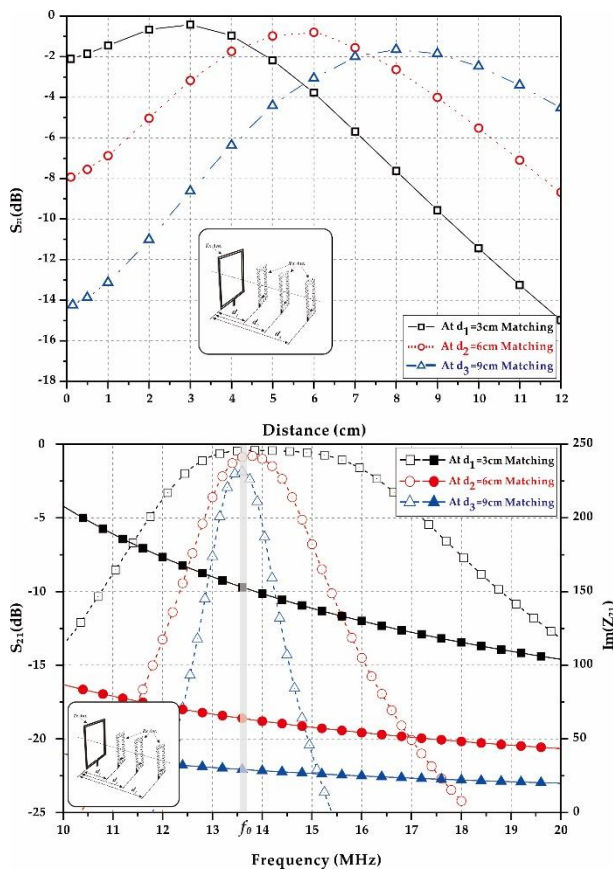
Fig. 1. The simulated transmission coefficient (S_{21}, related to the PTE) between the transmitting and receiving antennas with regard to the operating distance (a), and the operating frequency (b).

II. PROPOSED WPT SYSTEM CONFIGURATIONS

The practical applications for the WPT with regard to the different mutual couplings between the transmitting and receiving antennas (i.e., variable operating distance and misalignments) are near-field communication (NFC), wireless charging pad, wireless electric vehicle charging, and medical implant. Using a method of moments (MoM) technique, the simulated transmission coefficient (S_{21}, related to the PTE) between the transmitting and receiving antenna with regard to the operating distance and the operating frequency in Fig. 1, respectively. The maximum PTE is obtained at the matching distance, and at other distances due to the impedance mismatching, the PTE is drastically degraded at operating distance. For a highly efficient WPT system, it is necessary to have a distance-adaptive impedance variation characteristic. By controlling an impedance tuning network, an impedance matching characteristic is obtained, and the PTE can be improved.

To improve the WPT efficiency with variable distances, the distance-adaptive WPT system with automatic impedance tuning control is proposed in Fig. 2. The proposed system consists of resonant antennas for magnetic field generation, an impedance tuner (lumped network), a reflectometer to measure the reflection coefficient by detecting the reflected power, a matching

algorithm for maximum PTE, and a signal source of 13.56 MHz (ISM band) with a Class-E power amplifier in Fig. 2.
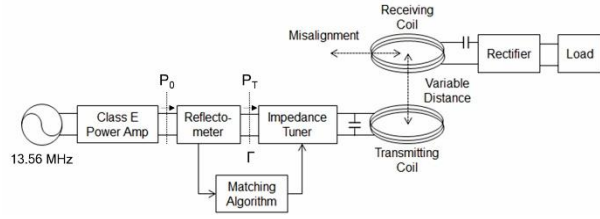
Fig. 2. The overall system block diagram for the proposed WPT system.

III. RESULTS AND DISCUSSION

To verify the PTE of the proposed WPT system with regard to the operating distances, we designed and implemented the proposed distance-adaptive WPT system with automatic impedance matching networks in Fig. 3. The simplified receiving device has a receiving antenna and a rectifying circuit with load. To investigate the power transfer link efficiency between the transmitting and receiving antennas, the coil antennas are designed and fabricated on an FR4 printed circuit board (PCB) substrate with a dielectric constant of 4.4 and thickness of 0.8 mm.

Table 1: The PTE comparison with regard to the operating conditions

Conditions (Dist: 3cm)	Γ	Voltage (V)	P_{in} (mW)	P_{out} (mW)	Efficiency (%)
Initial (Ref.)	0.691	10.5	163	110	68
Γ_{min}	0.541	11.6	149	135	90
$P_{0, max}$	–	10.2	1556	104	7
$P_{T, max}$	0.594	15.4	391	237	61

Conditions (Dist: 6cm)	Γ	Voltage (V)	P_{in} (mW)	P_{out} (mW)	Efficiency (%)
Initial (Ref.)	0.832	5.55	133	31	23
Γ_{min}	0.499	9.95	204	99	48
$P_{0, max}$	–	7.25	1409	53	4
$P_{T, max}$	0.574	9.95	201	99	49

Conditions (Dist: 6cm)	Γ	Voltage (V)	P_{in} (mW)	P_{out} (mW)	Efficiency (%)
Initial (Ref.)	0.832	5.55	133	31	23
Γ_{min}	0.499	9.95	204	99	48
$P_{0, max}$	–	7.25	1409	53	4
$P_{T, max}$	0.574	9.95	201	99	49
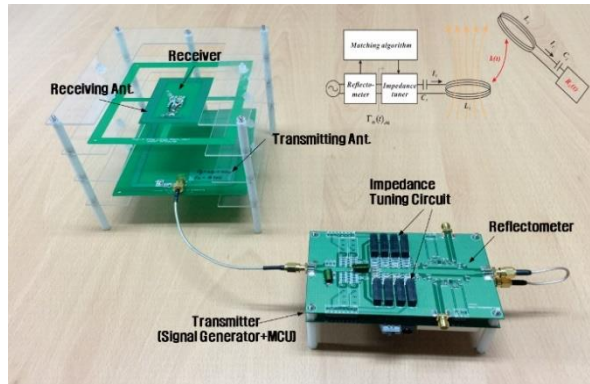
Fig. 3. The prototype of the proposed distance-adaptive WPT system.

Table 1 shows the received DC voltage and overall PTEs with regard to the fixed matching and proposed adaptive tuning conditions for the operating distance. The adaptive tuning conditions represent the maximum output power ($P_{0,max}$) at the output of the power amplifier, the maximum transmitting power ($P_{T,max}$), and the minimum reflection coefficient (minimum reflected power, min). If the WPT transmitting system has the maximum transmitting power condition ($P_{T,max}$), it can increase the received DC in the receiving device, but the overall PTE is less than the fixed matching condition of the impedance tuner. Within an operating distance of 3 cm to 9 cm, the minimum reflection coefficient condition displays an improved PTE of maximum approximately 160%.

IV. CONCLUSION

We propose a highly efficient wireless power transfer system with automatic impedance tuning control for practical applications with variable operating distances. Under misalignment between the transmitting and receiving antenna or any operating distance, the proposed distance-adaptive WPT system achieves an improved PTE of maximum 160% by minimizing the reflection coefficient in the transmitting system. It can be useful in wireless charging without the response of the portable receiving device.

ACKNOWLEDGMENT

REFERENCES

[1] J.-M. Kim, M. Han, and H. Sohn, "Magnetic resonance-based wireless power transmission through concrete structures," *J. of Electrom. Eng. and Sci.*, vol. 15, no. 2, pp. 104-110, Apr. 2015.

[2] K. Na, H. Jang, H. Ma, and F. Bien, "Tracking optimal efficiency of magnetic resonance wireless power transfer system for biomedical capsule endoscopy," *IEEE Trans. on Microw. Theo. and Tech.*, vol. 63, no. 1, pp. 295-303, Jan. 2015.

[3] J. Lee, Y.-S. Lim, W.-J. Yang, and S.-O. Lim, "Wireless power transfer system adaptive to change in coil separation," *IEEE Trans. on Ant. and Prop.*, vol. 62, no. 2, pp. 889-897, Feb. 2014.

[4] J. Kim and J. Jeong, "Range-adaptive wireless power transfer using multiloop and tunable matching techniques," *IEEE Trans. on Ind. Elect.*, vol. 62, no. 10, pp. 6233-6241, Oct. 2015.

[5] N. Y. Kim, K. Y. Kim, J. Choi, and C.-W. Kim, "Adaptive frequency with power-level tracking system for efficient magnetic resonance wireless power transfer," *Electr. Lett.*, vol. 48, no. 8, pp. 452-454, Apr. 2012.

Dong-Geun Seo received the B.S. degree in Electronic Engineering from Gyeongsang National University (GNU), Jinju, South Korea, in 2016, where he is currently pursuing the M.S. degree. His current research interests include near-field wireless power transfer and communication systems, beamforming antenna array and its feeding network for UAV communications, and RFID/IoT sensors.

Seong-Hyeop Ahn received the B.S. degree in Electronic Engineering from Gyeongsang National University (GNU), Jinju, South Korea, in 2018, where he is currently pursuing the M.S. degree. His research interests include near-field wireless power transfer and communications systems, RFID/IoT sensors, and RF/microwave circuit and antenna designs.

Ji-Hong Kim received the B.S. and M.S. degrees in Electronic Engineering from Gyeongsang National University (GNU), Jinju, South Korea, in 2016 and 2019, respectively, where he is currently pursuing the Ph.D. degree. His current research interests include RF system interference analysis, small antenna miniaturization, RFID/IoT sensors, and RF/microwave circuit and antenna designs.

Seung-Tae Khang received the B.S. degree in Electronic Engineering from Chung-Ang University, Seoul, South Korea, in 2012, and the M.S. degree in Electrical Engineering from the Korea Advanced Institute of Science and Technology, Daejeon, South Korea, in 2014, where he is currently pursuing the Ph.D. degree in Electrical Engineering. His current research interests include frequency-modulated continuous-wave (FMCW) radar system, millimeter-Wave transceiver design, and wireless power transfer system.

Soo-Chang Chae received the B.S. and M.S. degrees in Electrical Engineering from the Korea Advanced Institute of Science and Technology, Daejeon, South Korea, in 2014 and 2016, respectively, where he is currently pursuing the Ph.D. degree in Electrical Engineering. His current research interests include near-field wireless charging system and coil design, active array antenna, and RF/microwave circuit design.

Jong-Won Yu received the B.S., M.S., and Ph.D. degrees in Electrical Engineering from the Korea Advanced Institute of Science and Technology (KAIST), Daejeon, South Korea, in 1992, 1994, and 1998, respectively. From 2000 to 2001 and 2001 to 2004, he was also with Wide Telcom Head and Telson, South Korea. From 2004 to 2013, he was with KAIST, initially as an Assistant Professor of Electrical Engineering and as an Associate Professor. He is currently a Professor in KAIST. His research interests emphasize microwave/millimeter-wave circuits (monolithic microwave integrated circuits (MMICs), hybrid), wireless communication systems, and RFID/ubiquitous sensor network.

Wang-Sang Lee received the B.S. degree from Soongsil University, Seoul, South Korea, in 2004, and the M.S. and Ph.D. degrees in Electrical Engineering from the Korea Advanced Institute of Science and Technology (KAIST), Daejeon, South Korea, in 2006 and 2013, respectively. From 2006 to 2010, he was with the Electromagnetic Compatibility Technology Center, Digital Industry Division, Korea Testing Laboratory (KTL), Ansan, South Korea, where he was involved in the international standarization for RFID and Photovoltaic Systems as well as EMI/EMC analysis, modeling, and measurements for IT devices. In 2013, he joined the Korea Railroad Research Institute (KRRI), Uiwang, South Korea, as a Senior Researcher in the position detection for high-speed railroad systems and microwave heating for low-vibration rapid tunnel excavation system. He is currently an Associate Professor with the Department of Electronic Engineering, Gyeongsang National University (GNU), Jinju, South Korea. His current research interests include the nearfield communication and power systems, RF/microwave circuit and antenna design, RFID/IoT sensors, and EMI/EMC. Lee was a recipient of the Best Paper Award at the 7th Annual IEEE International Conference on RFID in 2013.

Printed Cross-Slot Wideband Conformal Antenna for GPS Application

Ratikanta Sahoo, Damera Vakula, and NVSN Sarma

Department of Electronics and Communication Engineering
National Institute of Technology, Warangal, 506004, India
ratikanta.sahoo15@gmail.com, vakula@nitw.ac.in, sarma@nitw.ac.in

Abstract ─ A novel cross-slot printed wideband conformal antenna is proposed for GPS application. Initially a planar antenna with cross-slot is designed at a slightly higher frequency and then the planar antenna is transformed to the corresponding cylindrical conformal antenna with the desired radius of curvature. The combination of partial ground plane and cross-slot on patch are used for bandwidth enhancement. The proposed conformal antenna exhibits a fractional bandwidth (for the definition of -10dB) of 79.28% operating from 1091 to 2524 MHz, which is suitable for all GPS bands, GLONASS and GALILEO applications. The radiation pattern exhibits an omnidirectional pattern and gain of proposed conformal antenna is 2.37 to 5.33dBi within operating frequency range.

Index Terms ─ Conformal antenna, GPS application, printed antenna, wideband antenna.

I. INTRODUCTION

Global Positioning System (GPS) requires wideband antenna for receivers installed on moving vehicles, missiles and hand held devices. These antennas play a vital role in the GPS receiver as they have to receive weak signals from satellites and as well work in remote areas. GPS antennas are to be placed on convenient location on the platform where omnidirectional coverage is assured without any obstruction of the signal transmitted from satellites. The platform for mounting the antenna is not always flat. Some cases, it is recommended to make the antenna conformal to the device to reduce aerodynamic drag, less visible to human eye and omnidirectional coverage for example on missile or aircraft [1-4]. So, there is a requirement to develop conformal antennas with omnidirectional coverage for GPS receivers.

For bandwidth improvement of patch antenna, a few methodologies have been proposed [5-14]. A three-dimensional microstrip feed line is reported in which an additional plastic supporting post is required in between ground plane and radiating patch to obtain a bandwidth of 31% in [5]. Combined utilization of both L-probe feeding and patch loaded with U-slot are used, where an extra foam substrate is required between ground and patch for the bandwidth of 42.7% in [6]. A similar foam layer is used in L-probe feed antenna designed by Guo, et al. in [7]. A capacitively probe-fed structure has been implemented in the microstrip antenna design to enhance the bandwidth up to 35% by using hard foam material which can be considered as a shortcoming [8].

A microstrip antenna loaded with chip resistor is proposed in [9]. These antennas are designed using lossy material which is a drawback and bandwidth obtained is only 9.8%. A patch antenna is designed with U-shaped slot for reactive loading and the presence of air or foam medium in between ground plane and patch is difficult to implement in [10]. The bandwidth obtained in this design is 12.4%.

An antenna with two gap coupled parasitic patches and a directly coupled patch is proposed to obtain broadband characteristics with 12.7% of bandwidth in [11]. But in the design, stacking of four patches are used. Various resonators and thick substrates with low dielectric constant have been utilized to design the patch antenna on a planar surface for obtaining bandwidth up to 20 to 32.3% [12-13]. Pues et al. have designed an impedance matching system to enhance bandwidth up to 12% [14].

Applications are developed for Global Positioning System in L_1 (1.57 GHz), L_2 (1.22 GHz), L_3 (1.38 GHz), L_4 (1.37 GHz) and L_5 (1.17 GHz) bands. The L_1 band is required for C/A procurement, and the L_2 is necessary for military and P(Y) codes. The L_5 band is used for safety life of civilian and the L_3 band is used for atomic explosion identification. The L_4 band is under development for climatic analysis. Along these lines, it can be viewed that use of GPS bands reach out from L_5 to L_1 bands.

Few circularly polarized antenna designs have been reported [15-17] for GPS application on planar surfaces. But according to [18], in the multi path environment, the linearly polarized signal is less vulnerable to distortions compared to circularly polarized signal. So, the omnidirectional linearly polarized antenna can also be applied for receiving purpose. A few literatures are published on GPS antenna on planar surfaces and working at the single band with narrow operating bandwidth. A cylindrical conformal antenna array for GPS in L_1 band

with 20 MHz bandwidth and a gain of 1.65 dBi is proposed in [19].

Although a wideband GPS Antenna has been reported [20], but it is designed on flat surface. In [21], two elements conformal antenna is designed for multi-GNSS reception with narrow bandwidth. A proximity coupled fed circular patch with a cross-slot on the patch has been demonstrated on the flat surface with less bandwidth [22]. So with the rapid development of wireless communication systems and increase in their applications, wideband antenna design has become a challenging topic.

In this paper, a novel high performance cross-slot wideband conformal antenna is proposed. The proposed conformal antenna exhibits wideband bandwidth. The simulation and measurement results showed that the proposed GPS antenna offers overly good performance.

II. DESIGN METHODOLOGY OF ANTENNA AND PARAMETRIC STUDY

A square patch antenna as shown in Fig. 1, fed by a microstrip line feed is considered in the proposed design initially. The width of square patch can be calculated as follows:

$$W = \frac{c}{2f_r\sqrt{\frac{\varepsilon_r+1}{2}}}. \tag{1}$$

Where c is the velocity of light, f_r is the resonant frequency of the antenna and ε_r is the relative permittivity of the substrate.
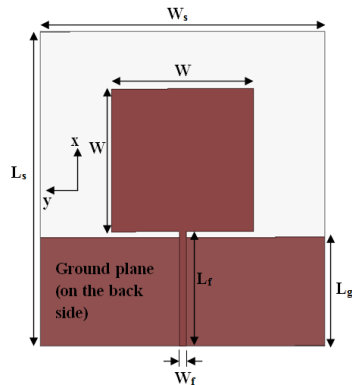
Fig. 1. Geometry of planar antenna: L_s=110 mm, W_s= 100 mm, W=50 mm, L_g=38 mm, L_f=40 mm, W_f=2.4 mm.

For designing this antenna, thermally stable substrate like Rogers RT/duroid 5880 of permittivity (ε_r) 2.2 and thickness of 0.787mm with microstrip line feed of 50 Ohm impedance matching is used. The dimension of substrate is 100×110×0.787 mm³ and dimension of the patch is 50×50 mm². In order to achieve wide operating bandwidth and omnidirectional coverage, partial ground concept is selected. The bandwidth is increased because

of suppression of surface wave propagation. The geometry of the proposed planar antenna is shown in Fig. 1. The planar antenna in Fig. 1 is transformed to the conformal one on a cylinder of radius 60 mm, which is shown in Fig. 2.
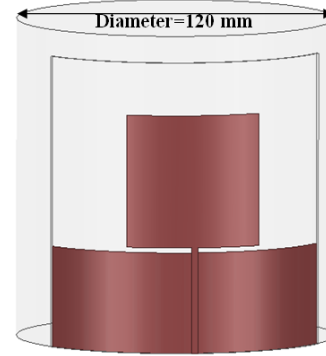
Fig. 2. Configuration of conventional conformal antenna.

The effect of length of the feed-line on the impedance matching is observed. It can be referred that better impedance matching is achieved by increasing the length of feed-line. The optimized value for L_f in the proposed conformal antenna is 40 mm. However, if the length is further increased more than 40 mm value, the variation of bandwidth can be observed in Fig. 3.
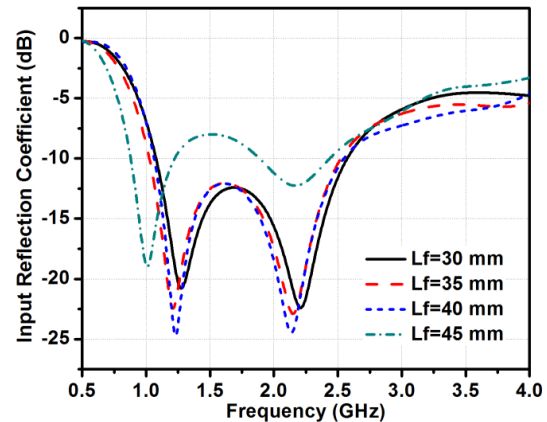
Fig. 3. Input reflection coefficient (dB) of the conformal antenna for different L_f.

Different shapes of slots like rectangular, square, circular can be introduced on the radiating patch antenna. These slots introduce capacitance, which counters the feed inductance and additional resonances introduced by slot combines with the patch resonance which produces wideband response. A horizontal dumbbell shaped slot is introduced on the patch initially. The use of circle on the dumbbell shaped slot is the best case among the other geometries. The circle makes the fields on the slots more uniform than the other cases. The cylindrical conformal antenna with horizontal dumbbell shaped slot on 60 mm

radius of curvature is shown in Fig. 4.
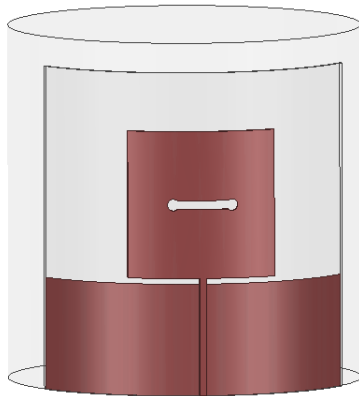
Fig. 4. Configuration of conformal antenna with horizontal dumbbell shaped slot.

The effect of length of horizontal dumbbell shaped slot on the impedance matching is observed in Fig. 5. The optimized dimension of L_h is 20 mm. If the length is increased, there is small change in impedance bandwidth.
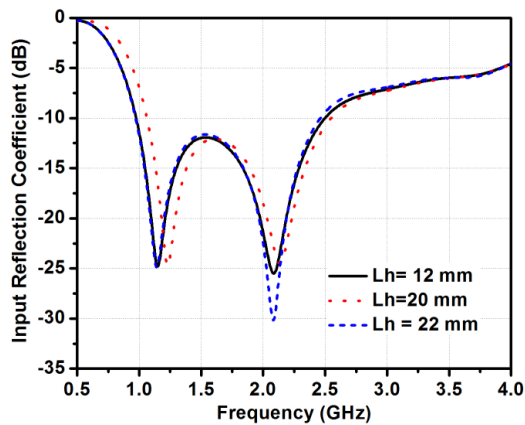
Fig. 5. Input reflection coefficient (dB) of the conformal antenna for different L_h.

A dumbbell shaped cross slot on the patch is shown in Fig. 6. Although there is not much difference in the impedance bandwidths for the designs in Figs. 2, 4 and 6, but better impedance matching for cross slot is obtained when compared with horizontal slot and without slot which is shown in Fig. 7.

The simulated return loss of the planar and proposed cylindrical conformal antennas with a 60mm radius of curvature are compared in Fig. 7. It shows that the return loss of all antennas are obtained below -10dB which indicates a good impedance matching condition. The proposed cylindrical antenna achieves 10dB impedance bandwidth of 1434 MHz, covering the frequency range 1.09-2.524 GHz with 79.28% fractional bandwidth indicating wide bandwidth.

A slight change in resonant frequency can be observed from planar to cylindrical conformal antenna in Fig. 7. This is because of increase in the effective resonant length of conformal antenna due to bending of the planar microstrip antenna structure. The resonant frequency of the cylindrical conformal antenna is shifted towards right. Also there is a change in return loss between conformal antenna without any slot, with only horizontal dumbbell shape slot and cross dumbbell shaped slot. It indicates that the resonant frequency also depends on slot's length. The matching performance of antenna is improved incorporating modification in cross-slot structure.
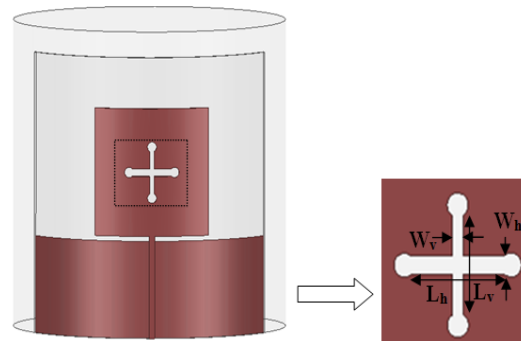
Fig. 6. Top view of conformal antenna with cross-slot: L_h=20 mm, W_h=3 mm, L_v=20 mm, W_v=2 mm; radius of circle=2mm.
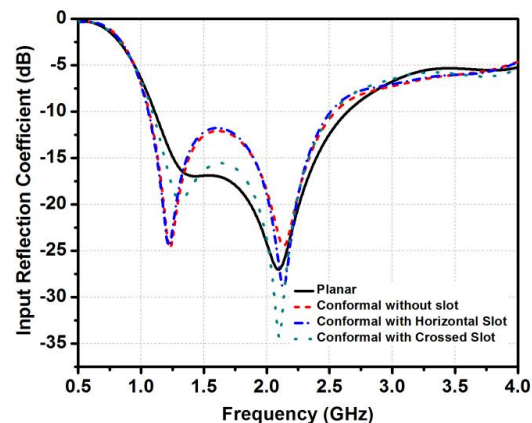
Fig. 7. Input reflection coefficient (dB) of the conformal antenna.

III. RESULTS AND DISCUSSION

The proposed antenna is designed and simulated using CST STUDIO SUITE 2016. A prototype planar antenna is fabricated on RT/duroid 5880 substrate with thickness of 0.787 mm. By using LPKF milling machine S100, the antenna is fabricated on a planar surface as shown in Figs. 8 (a) and 8 (b), and it is rolled up to form a cylindrical shape on foam of radius of 60 mm as shown in Fig. 8 (c). The foam material is used as mechanical

support for making 60 mm radius cylinder which has negligible radiation effect on the antenna. Both simulated and experimental input reflection coefficient (S_{11}) in dB of the proposed conformal antenna with 60 mm radius cylinder are demonstrated in Fig. 9. The input reflection coefficient is measured utilizing HP vector network analyzer within the frequency range of 130 MHz to 13 GHz. It is investigated that the designed cylindrical conformal patch antenna has a wide bandwidth of 79.28%, operating from 1.09-2.524 GHz. It can also be investigated that the experimental reflection coefficient (dB) slightly deviates from the impedance bandwidth achieved by using commercially available CST software may be due to tolerances in fabrication and SMA connector.

The radiation patterns at 1.17645, 1.2276 and 1.57542 in both E- and H-planes are illustrated in Fig. 10. The two dimensional patterns of the antenna are obtained in an anechoic chamber. It is investigated that, the two dimensional patterns at various frequencies are similar, which is expected from a wideband antenna. From Fig. 10 it can be referred that, the designed cylindrical conformal patch antenna has symmetrical radiation patterns. A figure of eight pattern and circular pattern are obtained in E-plane and H-plane respectively.

Fig. 9. Input reflection coefficient of the proposed conformal antenna.

Fig. 8. Photograph of prototype fabricated antennas: (a) front view of the proposed planar antenna, (b) back view of the proposed planar antenna, and (c) front view of a proposed cylindrical conformal antenna with 60 mm radius of curvature.
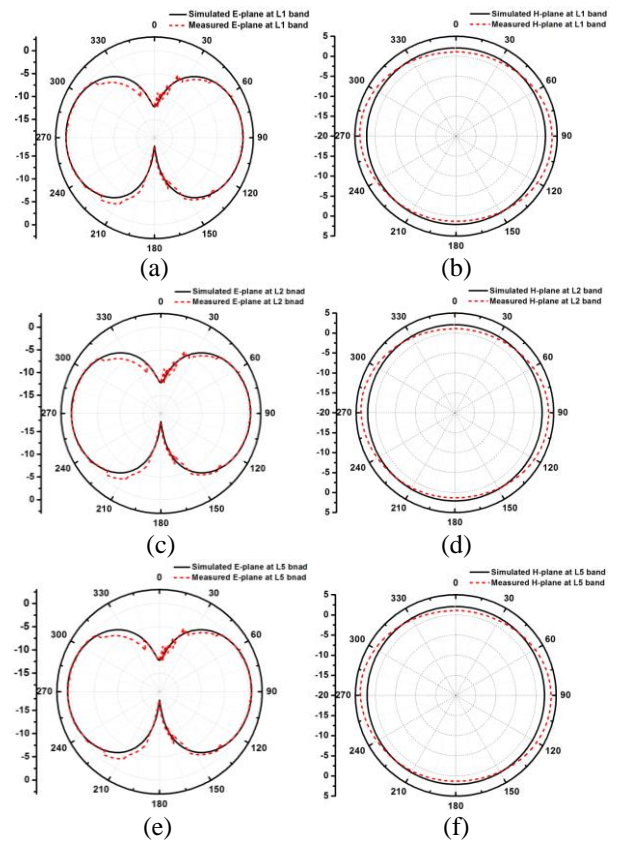
Fig. 10. Radiation pattern of proposed cylindrical conformal antenna at: (a) E-plane at L_1 band (1.57542 GHz), (b) H-plane at L_1 band (1.57542 GHz), (c) E-plane at L_2 band (1.2276 GHz), (d) H-plane at L_2 band (1.2276 GHz), (e) E-plane at L_5 band (1.17645 GHz), and (f) H-plane at L_5 band (1.17645 GHz).

The surface current distribution of the proposed conformal antenna at 1.575 GHz is shown Fig. 11. A strong surface current distribution around the dumbbell shape of the cross slot can be observed.

The gain of the cylindrical conformal antenna and planar antenna are compared in Fig. 12. The antenna gain is varying from 2.37 to 5.33 dBi over the operating frequency band. The gain of conformal antenna is more than the planar antenna. The simulated and measured gain of the proposed cylindrical conformal antenna are compared in Fig. 13.

The overall performance of the proposed cylindrical conformal antenna is compared with those of previously reported planar antennas at GPS frequency in [13-15] and given in Table 1. In spite of the fact that the proposed cylindrical conformal antenna is more size, yet it gives competitively wide bandwidths. Moreover, the gain is also more than the antennas existing in the literature [3],[5].
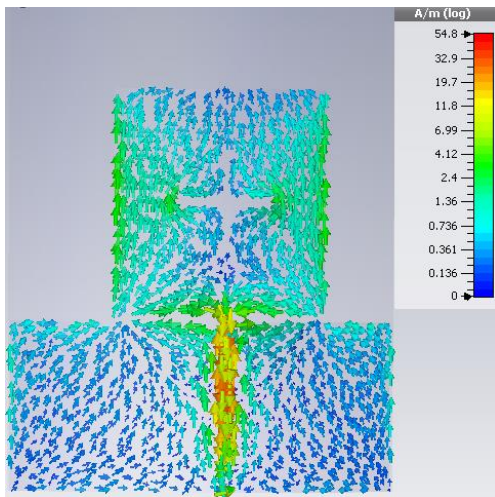
Fig. 11. Surface current distribution of the proposed conformal antenna at 1.575 GHz.
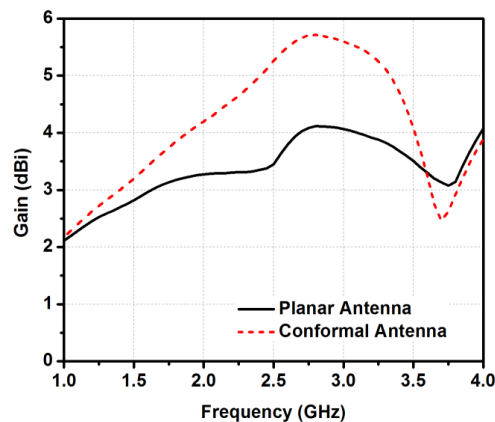
Fig. 12. The simulated gain of the planar and conformal antenna.
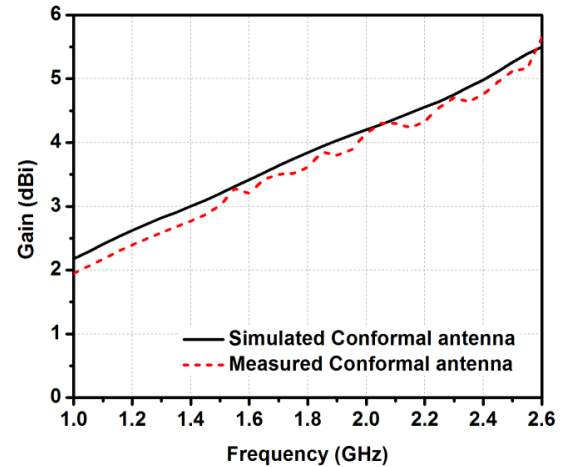
Fig. 13. The gain of conformal antenna.

Table 1: Performance of the proposed conformal antenna compared with planar one existing in the literature

Antenna	Perimeter (mm)	Frequency (GHz)	-10 dB Bandwidth	Gain (dBi)
Proposed work	420	L_1, L_2, L_3, L_4, L_5 BAND	79.28%	5.33
[15]	314.15	L_1	2.1%	-11
[16]	395.84	L_1	20 MHz	6.5
[17]	240	L_1	20 MHz	4

IV. CONCLUSION

This paper presents the design of cross-slot wideband cylindrical conformal antenna with 60 mm radius of curvature. The antenna is designed for planar and curved cylindrical configurations with well maintained radiation characteristics. The designed cylindrical conformal antenna offers a good wideband fractional bandwidth of about 79.28% and covering the bandwidth requirements of the modernized GPS application which can be used to guide the anti-tank guided missile (ATGM). Furthermore, the antenna has an omnidirectional radiation pattern in H-plane with a gain of about 2.37 to 5.33 dBi within the operating frequency range of 1.09 to 2.525 GHz.

REFERENCES

[1] R. Sahoo, D. Vakula, and N. V. S. N. Sarma, "Printed cross-slot wideband conformai antenna for GPS application," *2018 International Applied Computational Electromagnetics Society Symposium (ACES)*, Denver, USA, pp. 1-2, Mar. 2018.

[2] L. Josefsson, and P. Persson, *Conformal Array Antenna Theory, and Design*. *IEEE Press*, 2006.

[3] Z. Li, L. Tan, et al., "A novel wideband end-fire conformal antenna array mounted on a dielectric cone," *Applied Computational Electromagnetics Society Journal*, vol. 31, pp. 933-942, 2016.

[4] R. Bala, R. Singh, et al, "Wearable graphene based

curved patch antenna for medical telemetry applications," *Applied Computational Electromagnetics Society Journal*, vol. 31, pp. 543-550, 2016.

[5] N. Herscovici, "New considerations in the design of microstrip antennas," *IEEE Trans. Antennas Propagat.*, vol. 46, pp. 807-812, 1998.

[6] K. M. Luk, et al., "L-probe proximity fed U-slot patch antenna," *Electronics Letters*, vol. 34, pp. 1806-1807, 1998.

[7] Y.-X. Guo, et al., "Analysis and design of L-probe proximity fed-patch antennas," *IEEE Trans. Antennas Propagat.*, vol. 49, pp. 145-149, 2001.

[8] M. A. Gonzalez de Aza, J. Zapata, and J. A. Encinar, "Broadband cavity-backed and capacitively probe-fed microstrip patch arrays," *IEEE Trans. Antennas Propagat.*, vol. 48, pp. 784-789, 2001.

[9] K.-L. Wong and Y.-F. Lin, "Small broadband rectangular microstrip antenna with chip-resistor loading," *Electronics Letters*, vol. 33, pp. 1593-1594, 1997.

[10] T. Huynh and K.-F. Lee, "Single-layer single-patch wideband microstrip antenna," *Electronics Letters*, vol. 31, pp. 1310-1312, 1995.

[11] C.-K. Wu and K.-L. Wong, "Broadband microstrip antenna with directly coupled and parasitic patches," *Microwave and Optical Technology Letters*, vol. 22, pp. 348-349, 1999.

[12] E. Chang, S. A. Long, and W. F. Richards, "An experimental investigation of electrically thick rectangular microstrip antenna," *IEEE Trans. Antennas Propagat.*, vol. 34, pp. 767-772, 1986.

[13] F. Yang, et al., "Wide-band E-shaped patch antennas for wireless communications," *IEEE Trans. Antennas Propagat.*, vol. 49, pp. 1094-1100, 2001.

[14] H. F. Pues and A. R. Van De Capelle, "An impedance-matching technique for increasing the bandwidth of microstrip antennas," *IEEE Trans. Antennas Propagat.*, vol. 37, pp. 1345-1354, 1989.

[15] H.-M. Chen, Y.-F. Lin, C.-H. Chen, C.-Y. Pan, and Y.-S. Cai, "Miniature folded patch GPS antenna for vehicle communication devices," *IEEE Trans. Antennas Propagat.*, vol. 63, pp. 1891-1898, 2015.

[16] M. M. Bilgic and K. Yegin, "Modified annular ring antenna for GPS and SDARS automotive applications," *IEEE Antenna and Wireless Propagation Letters*, vol. 15, pp. 1442-1445, 2016.

[17] E. Wang and Q. Liu, "GPS patch antenna loaded with fractal EBG structure using organic magnetic substrate," *Progress in Electromagnetics Research Letters*, vol. 58, pp. 23-28, 2016.

[18] V. Pathak, S. Thornwall, M. Krier, S. Rowson, G. Poilasne, and L. Desclos, "Mobile handset system performance comparison of a linearly polarized GPS internal antenna with a circularly polarized antenna," *IEEE Antennas and Propagation Society International Symposium*, Columbus, OH, USA, vol. 3, pp. 666-669, June 2003.

[19] Z. Xiangjun, M. Xiaoping, and G. Xueyuan, "Design of cylindrical conformal microstrip GPS antenna arrays," *2009 Microwave Technology and Computational Electromagnetics (ICMTCE 2009)*, Beijing, China, pp. 105-108, Nov. 2009.

[20] F. Scire-Scappuzzo and S. N. Makarove, "A low-multipath wideband GPS antenna with cutoff or non-cutoff corrugated ground plane," *IEEE Trans. Antennas Propagat.*, vol. 57, pp. 33-46, 2009.

[21] J.-H. Bang, W.-J. Kim, and B.-C. Ahn, "Two-element conformal antenna for multi-GNSS reception," *IEEE Antenna and Wireless Propagation Letters*, vol. 16, pp. 796-799, 2017.

[22] M. Albooyeh, N. Kamjani, and M. Shobeyri, "A novel cross-slot geometry to improve impedance bandwidth of microstrip antennas," *Progress in Electromagnetics Research Letters*, vol. 4, pp. 63-72, 2008.

Ratikanta Sahoo received his M.Tech. in Communication System Engineering from VSSUT, Burla, India in the year 2012. He is currently a Ph.D. student at the Department of Electronics and Communication Engineering, National Institute of Technology, Warangal. His research interests include conformal antenna design, and metamaterial.

Damera Vakula received her Bachelor's degree in Electronics and Communication Engineering from Nagarjuna University, AP, India and M.Tech. from Birla Institute of Technology, Mesra, India, with Microwave specialization in the year 1992 and 1994, respectively. She obtained Ph.D. on Fault Diagnostics of Antenna Arrays from National Institute of Technology, Warangal, in the year 2010. She is working as an Associate Professor at National Institute of Technology, Warangal, India since 2006. She has published 31 papers in international Conferences and Journals. Her areas of interests include phase array antennas, conformal antenna, ultrawideband antennas, multiband antennas, fault diagnostics, and neural network.

N.V.S.N Sarma obtained his Bachelors degree with specialization in Electronics and Communications Engineering from Jawaharlal Nehru Technological University in the year 1984. His Master's and Doctoral degrees are from the Indian Institute of Technology, Kharagapur, India in the year 1985 and 1992, respectively. He worked at Tata Institute of Fundamental Research, Mumbai for a short period from February 86 to July 87. He has been with the Department of Electronics and Communications Engineering at National Institute of Technology, Warangal, India at various positions since 1990. About 70 papers are to his credit in International and National Journals and Conferences. His area of interest includes numerical electromagnetics, adaptive antenna arrays, and energy efficient routing protocols in wireless sensor networks.